



**US Army Corps  
of Engineers**

Engineer Research and  
Development Center

Technical Report SL-99-11  
September 1999

# **Development of a Constitutive Model for Numerical Simulation of Projectile Penetration into Brittle Geomaterials**

*by J. Donald Cargile*

Approved for Public Release; Distribution Is Unlimited

**DTIC QUALITY INSPECTED 2**

Prepared for Headquarters, U.S. Army Corps of Engineers

**19991213 014**

The contents of this report are not to be used for advertising, publication, or promotional purposes. Citation of trade names does not constitute an official endorsement or approval of the use of such commercial products.

The findings of this report are not to be construed as an official Department of the Army position, unless so designated by other authorized documents.



PRINTED ON RECYCLED PAPER

# **Development of a Constitutive Model for Numerical Simulation of Projectile Penetration into Brittle Geomaterials**

by J. Donald Cargile

U.S. Army Engineer Research and Development Center  
Waterways Experiment Station  
3909 Halls Ferry Road  
Vicksburg, MS 39180-6199

Final Report

Approved for Public Release; Distribution Is Unlimited

Prepared for U.S. Army Corps of Engineers  
Washington, DC 20314-1000

#### **Engineer Research and Development Center Cataloging-in-Publication Data**

Cargile, James D.

Development of a constitutive model for numerical simulation of projectile penetration into brittle geomaterials / by J. Donald Cargile ; prepared for Headquarters, U.S. Army Corps of Engineers.

228 p. : ill. ; 28 cm. — (Technical report ; SL-99-11)

Includes bibliographic references.

1. Projectiles — Mathematical models. 2. Projectiles — Simulation methods. 3. Penetration mechanics — Mathematical models. 4. Penetration mechanics — Simulation methods. 5. Geotextiles. I. United States. Army. Corps of Engineers. II. U.S. Army Engineer Research and Development Center. III. Structures Laboratory (U.S.) IV. Title. V. Series: Technical report SL ; 99-11.

TA7 W34 no.SL-99-11



## TABLE OF CONTENTS

	Page
PREFACE .....	xiii
CHAPTER 1 - INTRODUCTION .....	1
1.1 Background .....	1
1.2 Analysis Techniques .....	2
1.3 Objectives and Scope .....	7
CHAPTER 2 - PROJECTILE IMPACT AND PENETRATION .....	8
2.1 Introduction .....	8
2.2 Impact .....	11
2.3 Deep Penetration .....	15
2.4 Perforation .....	21
2.5 Summary and Conclusions .....	24
CHAPTER 3 - MATERIAL PROPERTIES .....	28
3.1 Introduction .....	28
3.2 Hydrostatic Pressure .....	37
3.3 Deviatoric Loading .....	45
3.3.1 Compression .....	49
3.3.2 Tension .....	53
3.3.3 Effect of Confinement .....	54
3.3.4 Effect of Strain Rate .....	61
CHAPTER 4 - NONLINEAR, INELASTIC FRACTURE MODEL .....	71
4.1 Modeling of Brittle Geomaterials .....	71
4.2 NIF Model Development .....	73
4.2.1 Volumetric Response .....	78
4.2.2 Deviatoric Response .....	83
4.3 Model Fitting .....	92
4.4 Model Driver .....	101

CHAPTER 5 - FINITE-ELEMENT CODE IMPLEMENTATION AND EVALUATION .....	115
5.1 Finite-Element Code Implementation .....	115
5.1.1 Calculation of Strain and Stress .....	117
5.1.2 NIF Model Subroutine .....	119
5.2 Model Implementation Evaluation .....	121
CHAPTER 6 - PENETRATION EXPERIMENTS AND NUMERICAL SIMULATIONS .....	129
6.1 Penetration Experiments .....	129
6.1.1 WES 83-mm Ballistic Range .....	129
6.1.2 Penetration Experiments .....	133
6.1.3 Perforation Experiments .....	140
6.2 Numerical Simulations .....	151
6.2.1 Penetration Experiments .....	153
6.2.2 Perforation Experiments .....	165
CHAPTER 7 - CONCLUSIONS AND RECOMMENDATIONS .....	177
7.1 Conclusions .....	177
7.2 Recommendations .....	179
LIST OF REFERENCES .....	181
APPENDIX .....	187

## LIST OF TABLES

Table	Page
2.1 Classification of impact response by velocity (after Zukas 1982) .....	9
3.1 Values for the crushable solids model parameters fit to CSPC concrete .....	32
4.1 Ingredients and mixture proportions for CSPC concrete .....	93
4.2 Summary of NIF model constants for the CSPC concrete .....	102
4.3 Ingredients and mixture proportions for WES5000 concrete .....	103
4.4 Summary of NIF model constants for the WES5000 concrete .....	104
6.1 Summary of penetration experiments for the AP projectile into CSPC concrete .....	137
6.2 Summary of perforation experiments for the SAP projectile into WES5000 concrete .....	144

## LIST OF FIGURES

Figure	Page
1.1 Projectile response after impact .....	3
2.1 Impact regimes based on impact pressure and material strength (Wilbeck 1985) .....	10
2.2 Projectile impact into brittle and non-brittle targets .....	13
2.3 High-velocity impact of a steel projectile into a concrete target showing formation of the ejecta cloud .....	14
2.4 Cross section of a granite or limestone target impacted by a steel sphere (Ahrens and Rubin 1993) .....	16
2.5 Penetration of a high-velocity projectile into a brittle geomaterial .....	17
2.6 Target response regions during projectile penetration (Forrestal 1986) .....	18
2.7 Rock failure during penetration (Livingston and Smith 1951) .....	20
2.8 Failure modes in impacted plates (Backman 1976) .....	22
2.9 Comparison of impact and exit craters for three thicknesses of unreinforced concrete perforated by similar projectiles at similar impact velocities .....	23
2.10 High-speed movie images showing backface of an unreinforced concrete target being perforated by a steel projectile .....	25
2.11 Sequence that occurs during perforation of a brittle geomaterial target .....	26
3.1 Description of elastic-perfectly plastic crushable solids material model in EPIC .....	30
3.2 Fit to recommended mechanical properties using the current model in EPIC for crushable solids .....	33

Figure	Page
3.3 Stress-paths at a depth of 1.8 in. (46 mm) .....	34
3.4 Stress-paths at a depth of 4.8 in. (122 mm) .....	35
3.5 Stress-paths at a depth of 25 in. (635 mm) .....	36
3.6 Initial and deformed rectangular shape of a specimen .....	40
3.7 Volumetric strain calculated using Equations 3.2 and 3.8 .....	41
3.8 Response of concrete to hydrostatic pressure .....	43
3.9 Material changes during application of hydrostatic stress .....	44
3.10 Principal stresses during triaxial experiments .....	46
3.11 Stress paths in the triaxial plane for typical mechanical property experiments (after Desai and Siriwardane 1984) .....	48
3.12 Results from a uniaxial compression test on CSPC concrete .....	50
3.13 Typical stress-strain behaviors for range of height-to-diameter ratio (Jansen and Shah 1995) .....	52
3.14 Results from a direct pull tension experiment on a concrete specimen .....	55
3.15 Failure modes in compression, (a) and (d) slabbing when one or a few cracks propagate parallel to the principal compression, (b) failure by aggregation of cracks to form a shear zone, and (c) near-homogeneous deformation by distribution microcracking (Ashby and Hallam 1986) .....	57
3.16 Effect of confining pressure on results from TC tests on concrete specimens .....	58
3.17 Results from TC experiments at 25 MPa after pre-stresses of 0, 100, and 400 MPa .....	59
3.18 Results from TC experiments at 100 MPa after pre-stresses of 0 and 400 MPa .....	60
3.19 Compression strength of concrete at different strain rates (Bischoff and Perry 1986) .....	63

Figure	Page
3.20 Strain rate effects on concrete tensile strength (Hughes, et. al. 1993) .....	64
3.21 Effect of pressure on dynamic strength of concrete .....	65
3.22 Effect of confining pressure on the dynamic strength of CSPC concrete .....	66
3.23 Effect of strain rate on the unconfined compression stress-strain response of concrete .....	68
3.24 Effect of confining pressure on the static and dynamic stress-strain response of CSPC concrete .....	69
3.25 Rate effect on load-deformation curve in tension (Kormeling, et. al. 1987 in Weerheijm, et. al. 1993) .....	70
4.1 Hydrostatic tension part of volumetric response .....	80
4.2 Hydrostatic compression part of volumetric response .....	82
4.3 Ultimate strength envelope .....	84
4.4 Maximum strength envelope for the cohesion subpart .....	87
4.5 Load/unload/reload under constant pressure .....	89
4.6 Friction and cohesion subparts and combined response for a constant pressure shear test .....	91
4.7 NIF model fit for hydrostatic tension and test data from Nichols and Ko (1996) .....	95
4.8 Recommended hydrostatic compression response of CSPC concrete .....	96
4.9 NIF model fit and recommended hydrostatic compression response .....	98
4.10 NIF model fit and recommended ultimate strength envelope .....	99
4.11 NIF model shear modulus and values obtained from the recommended CSPC concrete properties .....	100
4.12 Comparison of NIF model driver and recommended response for hydrostatic compression .....	106

Figure	Page
4.13 Comparison of NIF model driver and recommended responses for CTC experiments .....	107
4.14 Comparison of NIF model driver and experiment results for an unconfined compression experiment .....	109
4.15 Comparison of NIF model driver and recommended responses for uniaxial strain loading .....	110
4.16 Uniaxial strain stress paths for experiments conducted on a clayey sand (Cargile 1986) .....	111
4.17 Comparison of NIF model driver and experiment results for TC experiments at 25 MPa after pre-stresses of 0, 100, and 400 MPa .....	113
4.18 Comparison of NIF model driver and experiment results for TC experiments at 100 MPa after pre-stresses of 0 and 400 MPa .....	114
5.1 Computational technique used in EPIC (Johnson, et. al. 1978) .....	116
5.2 Single element configuration and loading history used in EPIC to check the NIF model for hydrostatic compression .....	122
5.3 Comparison of the hydrostatic compression from EPIC and the NIF model driver .....	123
5.4 Single element configuration and loading used in EPIC to check the NIF model for unconfined compression .....	124
5.5 Comparison of unconfined compression from EPIC and the NIF model driver .....	126
5.6 Single element configuration and loading used in EPIC to check the NIF model for uniaxial strain .....	127
5.7 Comparison of uniaxial strain loading from EPIC and the NIF model driver .....	128
6.1 WES projectile penetration research facility .....	130
6.2 Section of film from the streak camera showing the projectile (Frew et. al. 1993) .....	132

Figure	Page
6.3 Information from diagnostic systems that can be used during projectile penetration tests (Frew, et. al. 1993) .....	134
6.4 Dimensions of AP projectile launched into CSPC concrete targets .....	136
6.5 Depth of penetration for AP projectiles impacting CSPC concrete .....	138
6.6 Crater and penetration path profiles for AP projectiles impacting CSPC concrete .....	139
6.7 Posttest photographs of CSPC concrete targets penetrated by AP projectiles .....	141
6.8 Posttest photographs of AP projectiles used in penetration experiments into CSPC concrete .....	142
6.9 Dimensions of SAP projectile launched into WES5000 concrete slabs .....	143
6.10 Pre- and posttest photographs from a typical perforation experiment .....	146
6.11 Ratio of exit velocity to impact velocity versus target thickness for a SAP projectile perforating WES5000 concrete slabs .....	147
6.12 Selected images showing the front of a 254-mm-thick WES5000 concrete slab being impacted by a SAP projectile .....	148
6.13 Selected images showing the back of a 254-mm-thick WES5000 concrete slab being perforated by a SAP projectile .....	149
6.14 Selected images showing the back of a 127-mm-thick WES5000 concrete slab being perforated by a SAP projectile .....	150
6.15 Impact (left) and exit (right) crater profiles for the perforation experiments .....	152
6.16 Close-up of initial grid and materials used in simulation of the AP projectile impacting CSPC concrete (axis units are inches) .....	154
6.17 Initial grid for simulating the AP projectile penetrating CSPC concrete (axis units are inches) .....	155
6.18 Comparison of simulation and experiment results for an AP projectile impacting CSPC concrete .....	157



Figure	Page
6.19 Deformed grid for an AP projectile impacting CSPC concrete at 277 m/s (time is in seconds; axis units are inches) .....	158
6.20 Deformed grid for an AP projectile impacting CSPC concrete at 499 m/s (time is in seconds; axis units are inches) .....	159
6.21 Deformed grid for an AP projectile impacting CSPC concrete at 642 m/s (time is in seconds; axis units are inches) .....	160
6.22 EBAR (strain ratio) contours for an AP projectile impacting CSPC concrete at 277 m/s (time is in seconds; axis units are inches; contours are dimensionless) .....	162
6.23 EBAR (strain ratio) contours for an AP projectile impacting CSPC concrete at 499 m/s (time is in seconds; axis units are inches; contours are dimensionless) .....	163
6.24 EBAR (strain ratio) contours for an AP projectile impacting CSPC concrete at 642 m/s (time is in seconds; axis units are inches; contours are dimensionless) .....	164
6.25 Close-up of initial grid and materials used in simulation of the SAP projectile impacting WES5000 concrete slabs (axis units are inches) .....	166
6.26 Deformed grid for a SAP projectile impacting a half-space of WES5000 concrete (time is in seconds; axis units are inches) .....	167
6.27 Initial grids for simulating the SAP projectile perforating 127-, 216-, and 254-mm-thick (5.0-, 8.5-, and 10.0-inch-thick) WES5000 concrete slabs (axis units are inches) .....	168
6.28 Comparison of simulation and experiment results for a SAP projectile perforating WES5000 concrete slabs .....	170
6.29 Deformed grid for a SAP projectile perforating a 127-mm-thick WES5000 concrete slab (time is in seconds; axis units are inches) .....	171
6.30 Deformed grid for a SAP projectile perforating a 216-mm-thick WES5000 concrete slab (time is in seconds; axis units are inches) .....	172
6.31 Deformed grid for a SAP projectile perforating a 254-mm-thick WES5000 concrete slab (time is in seconds; axis units are inches) .....	173

Figure	Page
6.32 EBAR (strain ratio) contours for a SAP projectile perforating a 127-mm-thick WES500 concrete slab (time is in seconds; axis units are inches; contours are dimensionless) .....	174
6.33 EBAR (strain ratio) contours for a SAP projectile perforating a 216-mm-thick WES500 concrete slab (time is in seconds; axis units are inches; contours are dimensionless) .....	175
6.34 EBAR (strain ratio) contours for a SAP projectile perforating a 254-mm-thick WES500 concrete slab (time is in seconds; axis units are inches; contours are dimensionless) .....	176

## PREFACE

The work reported herein was funded by Headquarters, U.S. Army Corps of Engineers, under the Survivability and Protective Structures Research Program, Hardened Construction Materials Work Package, Work Unit AT22-HS-008, "Performance of Projectiles Impacting Geologic/Structural Targets." This report was prepared by Dr. J. Donald Cargile, Geomechanics and Explosion Effects Division (GEED), Structures Laboratory (SL), U.S. Army Engineer Waterways Experiment Station (WES), Vicksburg, MS, a complex of five laboratories of the U.S. Army Engineer Research and Development Center (ERDC). It is essentially a thesis submitted to the faculty of Purdue University in partial fulfillment of the requirements for the degree of Doctor of Philosophy in the Department of Civil Engineering.

The assistance of Ms. Tracey Waddell for her preparation of many of the figures, the Projectile Penetration Research Facility staff (Messrs. Richard Cooper, Belton Dent, and Mike Keene) and the Geodynamics Research Facility staff (Messrs. James McCaskill, Paul Reed, Leroy Peeples, and John Rhodes) is gratefully acknowledged. The author acknowledges the review and comments provided by Dr. Behzad Rohani, GEED, Professors Philippe Bourdeau, Richard Dechamps, and Rodrigo Salgado, Purdue University, and Professor Jean-Lou Chameau, Georgia Institute of Technology. The research was conducted under the general supervision of Mr. A. E. Jackson, Jr., Acting Chief, GEED. Dr. Bryant Mather was Director, SL.

Commander of ERDC during the conduct of this research was COL Robin R. Cababa, EN. This report was prepared and published at the WES complex of ERDC.

## CHAPTER 1

### INTRODUCTION

#### 1.1 BACKGROUND

Projectile impact and penetration problems can include the attack of a military target with penetrating weapons, propellant embedded anchors, storm launched debris impacting a structure, etc. Analysis of these problems requires knowledge of (1) the impact conditions (velocity and projectile orientation relative to the target) (2) characteristics of the projectile (geometry, mass, and strength) and (3) the properties of the target (dimensions and mechanical properties). Within the limits of the conventional impact velocities of interest, less than about 1 km/s, the depth of penetration increases when the kinetic energy of the projectile increases. This can be accomplished by increasing either the impact velocity or the projectile mass. Deformation of the projectile can also influence penetrability. A heavy, essentially non-deformable projectile, such as an armor-piercing (AP) projectile, will penetrate deeper into a target than a deformable projectile. An oblique impact results in a highly asymmetrical stress distribution on the projectile that can cause it to either breakup or result in a lower penetration depth than a normal impact. Strong geomaterials such as concrete or rock have greater mass, modulus, and strength characteristics than soil and will therefore have a greater resistance to penetration. The interaction of these three categories of parameters is complex and at times leads to difficulties in interpreting and analyzing impact and penetration events.

In general, depending on the complex interaction of all the variables, any of the following situations could prevail when a projectile impacts a target. The projectile could either (1) break up, deform significantly, and be "defeated" by the target, (2) ricochet, (3)

initially penetrate into the target and then broach, (4) perforate the target, or (5) penetrate and come to rest in the target (Figure 1.1). The response of target materials to projectile impact will depend on many variables such as the material properties, impact velocity, projectile shape, and target size. Material may be ejected from the target due to spalling or scabbing. Spalling is a tensile failure that results from the reflection of the initial compressive wave from the rear surface of a finite thickness target. Scabbing is similar in appearance to spalling but is formed by the fracturing and break up of target material due to large deformations. These conditions may exist under high impulse loadings due to intense impacts into materials that are stronger in compression than in tension, like most geomaterials. Under the impact and subsequent loading conditions of interest here, most of the target response near free surfaces is described by scabbing and fracture.

## 1.2 ANALYSIS TECHNIQUES

Projectile penetration events are generally analyzed by three approaches: empirical curve fitting, analytic models, and numerical methods. The selection of a predictive method is usually dictated by the level to which the penetration event is to be analyzed. If only depth of penetration is of interest, then any of the three predictive methods may be used. If the depth of penetration as well as the state of stress within the target is of interest, some analytical methods and any of the numerical methods can be used. Detailed description of the stresses and the deformations of the target require the use of the numerical approaches.

The degree to which the target materials are characterized generally increases with each approach. In-depth analyses must account for the geometry of the target, large finite strains and deflections, strain rate effects, work hardening, heating or frictional effects, and the initiation and propagation of fracture (Jonas and Zukas 1978). The empirical techniques (Young 1972, Bernard 1977, and Pahl 1989) involve curve fitting of penetration test data to relate depth of penetration and projectile deceleration to projectile

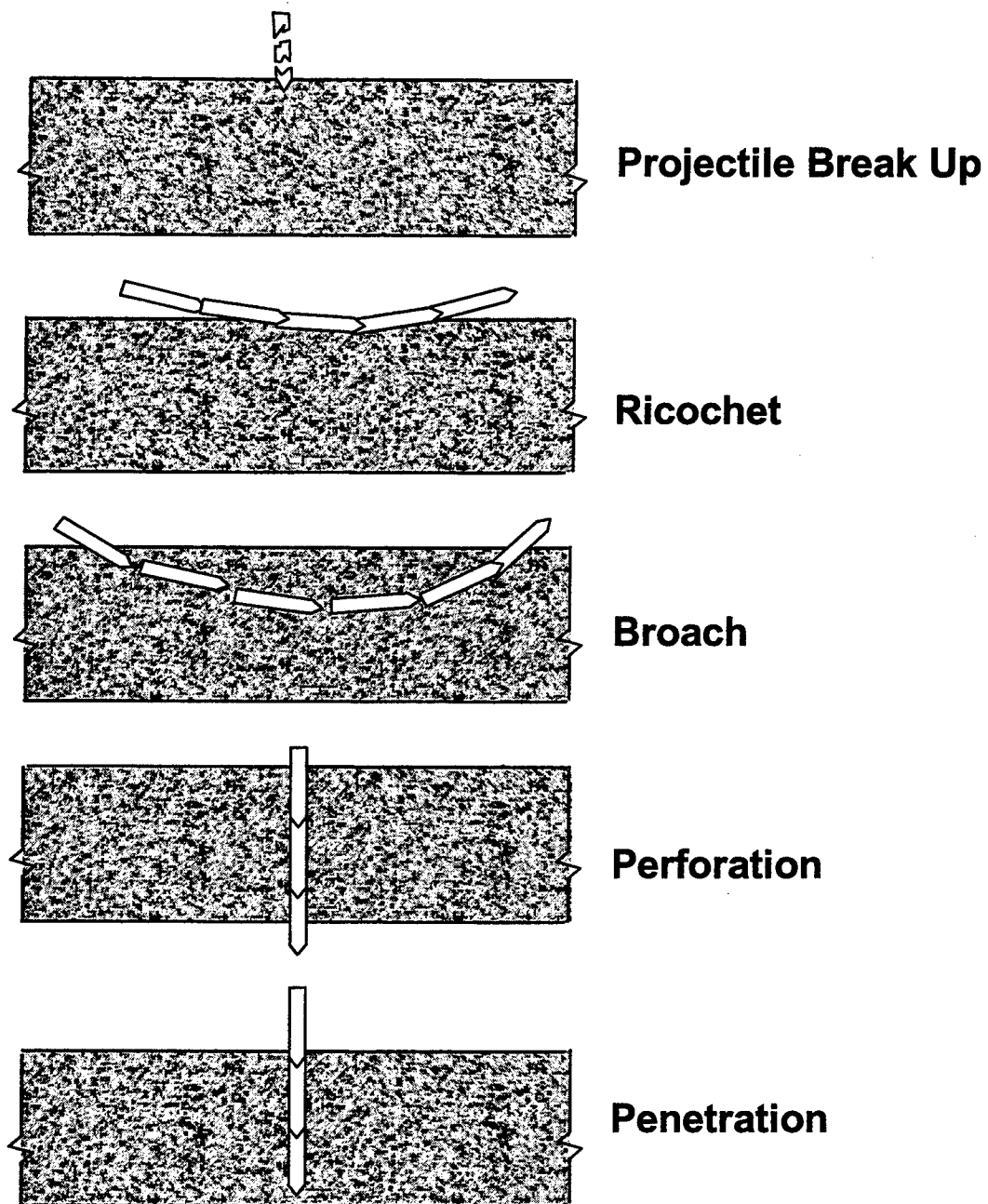


Figure 1.1. Projectile response after impact.

geometry, impact velocity, and target material type. The empirical relations are the simplest to apply and are generally reliable within the range of conditions covered by the data set on which they are based. The projectile is assumed to be rigid and the target material is characterized by simple engineering parameters, e.g., density, unconfined compressive strength, penetrability index (such as S-number; Young 1972). The trajectory of the projectile is assumed to follow a straight line. The empirical techniques offer no insight to the physics or mechanics of penetration and the response of the target material.

The analytic models offer a somewhat more fundamental approach in that they are based on the conservation and balance laws of continuum mechanics. Many of these models use dynamic cavity expansion techniques (CET) to determine the resistance of the target material to projectile penetration (Bernard and Creighton 1976, Forrestal 1986, Forrestal and Luk 1992, and Forrestal and Tzou 1997). The models are often restricted by the assumptions made on the target material motion (one-dimensional spherical or cylindrical geometries) and stress response (compressive) in order to simplify the analysis. The simplified governing equations can usually be solved in closed form. The constitutive properties of the target materials required by a given model are determined from independent laboratory tests. The properties may include density, compressibility, strength, shear modulus, etc. Recently, CET has been used to develop algorithms to predict penetration into soil (Forrestal and Luk 1992), rock (Forrestal 1986), and concrete (Forrestal and Tzou 1997). A limitation on the CET is that it is only valid for normal impact, penetration beyond the cratering phase and into the tunneling phase, and penetration into thick targets where the back surface does not influence the penetration process. The model can be compared to test data and its predictive capability assessed. Disagreements between the predicted and actual penetration event may suggest that the model is not adequate, but may also suggest physical effects that can not be accounted for in the simplified analytical procedure.

Another analytic technique is the so-called differential area force law (DAFL) approach. The DAFL type of formulation (Henderson and Stephens 1972) divides the projectile longitudinally and then circumferentially into a mesh of elements, or differential areas, on the projectile surface. A normal stress is calculated on each element using stress formulations that may be empirical or analytic based. The stress is divided by the area of the element and the total force is obtained by summing over all the elements.

The most comprehensive approach to projectile penetration problems is the numerical approach using finite-element or finite-difference wave propagation codes. The numerical methods solve the continuity, momentum and energy balance equations of continuum mechanics in conjunction with an appropriate constitutive representation for the target materials of interest. These first-principles techniques can use a wide variety of initial and boundary conditions to simulate the penetration event. The complexity of the constitutive material models that can be used with most of the numerical methods has little restriction. However, for problems concerning geomaterials, fairly simple material flow (associated flow rules of plasticity) and fracture models (reduction of the intact properties of the material) are usually employed due to a lack of understanding of how these complex processes should be modeled. The material property data required for use in the numerical methods must be obtained from the appropriate independent laboratory tests on the target materials.

The material models used in the analysis of penetration problems must incorporate the physical phenomena controlling the process. Ideally, the model should account for compaction, cracking, shear dilation, water migration, phase transformation, thermal effects, inhomogeneity, etc. Geomechanical models (such as the Prandtl-Reuss model, CAP-type models, etc.; Chen 1982) that simulate elasto-plastic deformations, compaction, and failure are available, but the implementation must be applicable to the high-pressure, sub-millisecond loadings that occur during high-velocity projectile impact.



This may require that the model be rate-dependent and include an equation-of-state to define the pressure-volume relation for the very high, impulsive loading. Fracture and damage models based on the micromechanical approach that simulate the opening of existing cracks and the formation of new cracks have been developed, but they have not been applied to penetration problems involving geomaterials for several reasons. Most of these models are developed to simulate the response of materials at low pressures under static or quasi-static loading conditions. Interpretation of the model parameters can be obscure and difficult to obtain from laboratory experiments. If implemented into a finite-element code, computation time can be prohibitive due to the large number of cracks and the volume of damaged material that are produced during projectile penetration. A need, therefore, exists to improve the geologic material models used to analyze penetration into geomaterials to account for pertinent phenomena such as brittle failure, post-fracture material response, and pressure and rate effects, and to incorporate the models into numerical analysis codes.

As pointed out by Desai and Siriwardane (1994), formulation of a viable constitutive law involves the following steps: (1) develop the mathematical formulation, (2) identify the significant parameters, (3) determine the parameters from laboratory experiments, (4) successful prediction of a majority of observed laboratory data from which the model parameters were determined and prediction of material response to other loading paths, and (5) satisfactory comparisons between numerical simulations of relevant boundary value problems using the constitutive law and results from experiments. The relevant boundary value problems of interest in this research involve the penetration and perforation of brittle geomaterials by high-velocity projectiles. Perhaps a precursor to these steps should be the conduct of an experiment, for example a beam test, or a projectile penetration experiment, or a blast loading in a rock-type material, etc. Results from the experiments should be observed carefully as to how the materials responded. Does the material have a brittle or ductile response, or a combination of the two? Does the material contain many cracks and, if so, their size and

patterns? Is the material loose and friable after the test? Where within the material do these conditions exist? Step one above should then try to mimic these observations.

### 1.3 OBJECTIVES AND SCOPE

The objectives of the research reported herein were (1) develop a constitutive model for brittle geomaterials for numerical simulation of high-velocity projectile penetration and perforation problems, (2) determine the numerical values for the parameters of the model from a series of laboratory material property tests, (3) implement the model into an existing large-deformation finite-element computer program, (4) conduct a series of controlled laboratory ballistic experiments involving high-velocity penetration and perforation of plain concrete targets, and (5) perform an in-depth numerical analysis of the ballistic experiments and evaluate the capability of the constitutive model to capture the salient features of the penetration and perforation of brittle geomaterials.

Chapter 2 presents a review of relevant projectile impact and penetration phenomena with emphasis placed on brittle geomaterials. Chapter 3 contains the results of material property test programs and includes relevant information on testing, analysis of data, and stress paths of interest to penetration problems. Chapter 4 details the development of a constitutive model for brittle geomaterials and the determination of the numerical values of the parameters of the model for plain concretes used in ballistic programs. Implementation of the constitutive model into a large-deformation finite-element computer program is presented in Chapter 5. The ballistic program and the comparisons of the results for the penetration and perforation experiments with corresponding numerical simulations are documented in Chapter 6. Chapter 7 contains conclusions and recommendations for additional research related to the topic of interest.

## CHAPTER 2

### PROJECTILE IMPACT AND PENETRATION

#### 2.1 INTRODUCTION

The impact between a projectile and a target has been of interest for hundreds of years. Historically the interest has been towards military applications such as the penetration of hardened structures and armor. Civilian interests in impact have begun to receive more study. These interests include demolition, transportation safety, crashworthiness of vehicles, weather borne impacts, aircraft impacts, body armor, erosion and fracture of solids, etc. (Zukas, et.al. 1982). The phenomena associated with impact are many and include elastic and plastic deformation, wave propagation, fracture and damage, friction, and, at very high velocities, hydrodynamic flow. Attempts have been made to classify impact by various regimes using parameters such as striking velocity (Table 2.1; Zukas, et.al. 1982) and the strength of the projectile and target and the impact pressure (Figure 2.1; Wilbeck 1985). According to Zukas, the problems of interest here will fall into the low to intermediate range ( $<1$  km/s). These impacts will result in permanent damage where the strength and compressibility of the materials are important. Material loading and response times are on the order of milliseconds at low velocities and microseconds at the higher velocities. Based on Wilbeck's criteria, the impacts will generally involve conditions where the ratio of impact pressure to projectile strength is less than or approximately equal to one and the ratio of impact pressure to target strength is much greater than one. The projectiles should sustain only slight deformation, but the target will sustain significant deformations.

Table 2.1. Classification of impact response by velocity (after Zukas 1982).

Striking Velocity, km/s	Strain Rate, m/m/s	Effect	Loading Method
>12	$10^8$	Explosive impact; colliding solids vaporize	Two-stage guns
3 - 12	$10^7$	Hydrodynamic; material compressibility cannot be ignored	Explosive acceleration
1 - 3	$10^5$	Materials behave as fluids; pressures approach or exceed material strength; density a dominant property	Powder and gas guns
0.5 - 1	$10^4$	Material strength significant	Powder guns
0.05 - 0.5	$10^2$	Plastic deformations	Mechanical devices
< 0.05	$10^0$	Elastic; some local plasticity	Mechanical devices

	$\frac{P}{\sigma_p} < < 1$	$\frac{P}{\sigma_T} < < 1$	$\frac{P}{\sigma_T} \sim 1$	$\frac{P}{\sigma_T} > > 1$
$\frac{P}{\sigma_p} < < 1$	Elastic Impact: Impact of two billiard balls, collision of a ball and bat, tire rolling on pavement		Bombs penetrating concrete, explosively launched debris	Hard Penetrator Into Soft Target: Earth penetrators, torpedoes in water, flight of aircraft
$\frac{P}{\sigma_p} \sim 1$	Fruit pickers, head injury from windshield impact		Design of armor and armor penetrators, containment of turbine components, impact of hard objects on aircraft engine components	Containment of turbine components, bombs penetrating concrete
$\frac{P}{\sigma_p} > > 1$	Soft Penetrator Into Hard Target: Birds impacting aircraft canopies at low flight velocity, lead bullets impacting a steel plate		Tornado-driven missiles, bird and hail impacts, rain erosion	Significant Material Failure: Hypervelocity impacts, penetration by shaped charges

P - Impact pressures.

$\sigma_p$  - Projectile strength.

$\sigma_T$  - Target strength.

Figure 2.1. Impact regimes based on impact pressure and material strength (Wilbeck 1985).

The dissipation of the initial kinetic energy of the projectile depends on the characteristics of the projectile and target and the impact velocity. In the case of a brittle target, much of the projectile's energy will be used to fragment and pulverize the target (Goldsmith 1960). The impact and penetration of a projectile into a brittle geomaterial can be separated into three possible phases. First is the impact phase where the projectile penetrates the target material only enough to form an impact crater. The depth of the impact crater is typically only a couple of projectile diameters (calibers) or less. The second phase is the deep penetration where the projectile penetrates beyond the impact crater and begins to tunnel into the target material. The tunneling is characterized by the opening of a cylindrical cavity by the projectile. Penetration generally results in the embedment of the projectile in the target. The third and most complicated phase is the perforation which is the complete piercing of a target with finite thickness by the projectile. This event includes the formation of the impact crater, may include the tunneling phase, and then an exit condition that will include the formation of an exit crater. All of these phases can result in ejection of material from the impact face and the back face of the target (Bangash 1993) and involve formation of cracks, plastic deformation as well as fragmentation and pulverization. The three phases are discussed in detail below.

## 2.2 IMPACT

Impact can include the collision of a rigid projectile with an equally rigid target, a deforming projectile impacting a rigid target, impact of an essentially rigid projectile with a deforming target, or impact of a deforming projectile with a deforming target. In some cases the impact may be followed by a deeper penetration. A rigid impact can be analyzed using conservation of momentum (Sears, et.al., 1976)

$$m_p V_{pi} + m_t V_{ti} = m_p V_{pf} + m_t V_{tf} \quad 2.1$$

and conservation of energy

$$\frac{1}{2}m_p V_{pi}^2 + \frac{1}{2}m_t V_{ti}^2 = \frac{1}{2}m_p V_{pf}^2 + \frac{1}{2}m_t V_{tf}^2 \quad 2.2$$

where  $m_p$  and  $m_t$  are the mass of the projectile and target,  $V_{pi}$  and  $V_{ti}$  are the initial velocity of the projectile and target, and  $V_{pf}$  and  $V_{tf}$  are the final velocity of the projectile and target. Solving for the final velocities yields

$$V_{pf} = \frac{m_p - m_t}{m_p + m_t} V_{pi} + \frac{2m_t}{m_p + m_t} V_{ti} \quad 2.3$$

$$V_{tf} = \frac{2m_p}{m_p + m_t} V_{pi} + \frac{m_t - m_p}{m_p + m_t} V_{ti} \quad 2.4$$

If the target is not only rigid with respect to deformation but also with respect to movement,  $V_{ti} = V_{tf} = 0.0$  and the final velocity of the projectile is equal in magnitude to the impact velocity, but opposite in direction. This is the simplest impact problem to analyze. It can occur in several ways such as very low velocity impacts between a projectile and target of strong materials and moderate velocity impacts between a projectile and target of very strong materials. Once deformation begins to occur during the impact, energy is transformed and the analysis becomes increasingly more complicated.

Methods to account for the effect of deformation on the impact phase can range from the simple, such as including Newton's coefficient of restitution to account for a non-catastrophic deformation, to the complicated involving the use of numerical methods. Two distinctly different modes of response during impact of geomaterials are shown schematically in Figure 2.2. High-velocity impact into brittle geomaterials will generally result in significant target deformation involving fracture, fragmentation and pulverization. For non-brittle materials the target response is dominated by compaction and shear flow and is similar to that for driving a pile into soil or the bearing failure of a shallow foundation. Figure 2.3 shows several images taken during the high-velocity

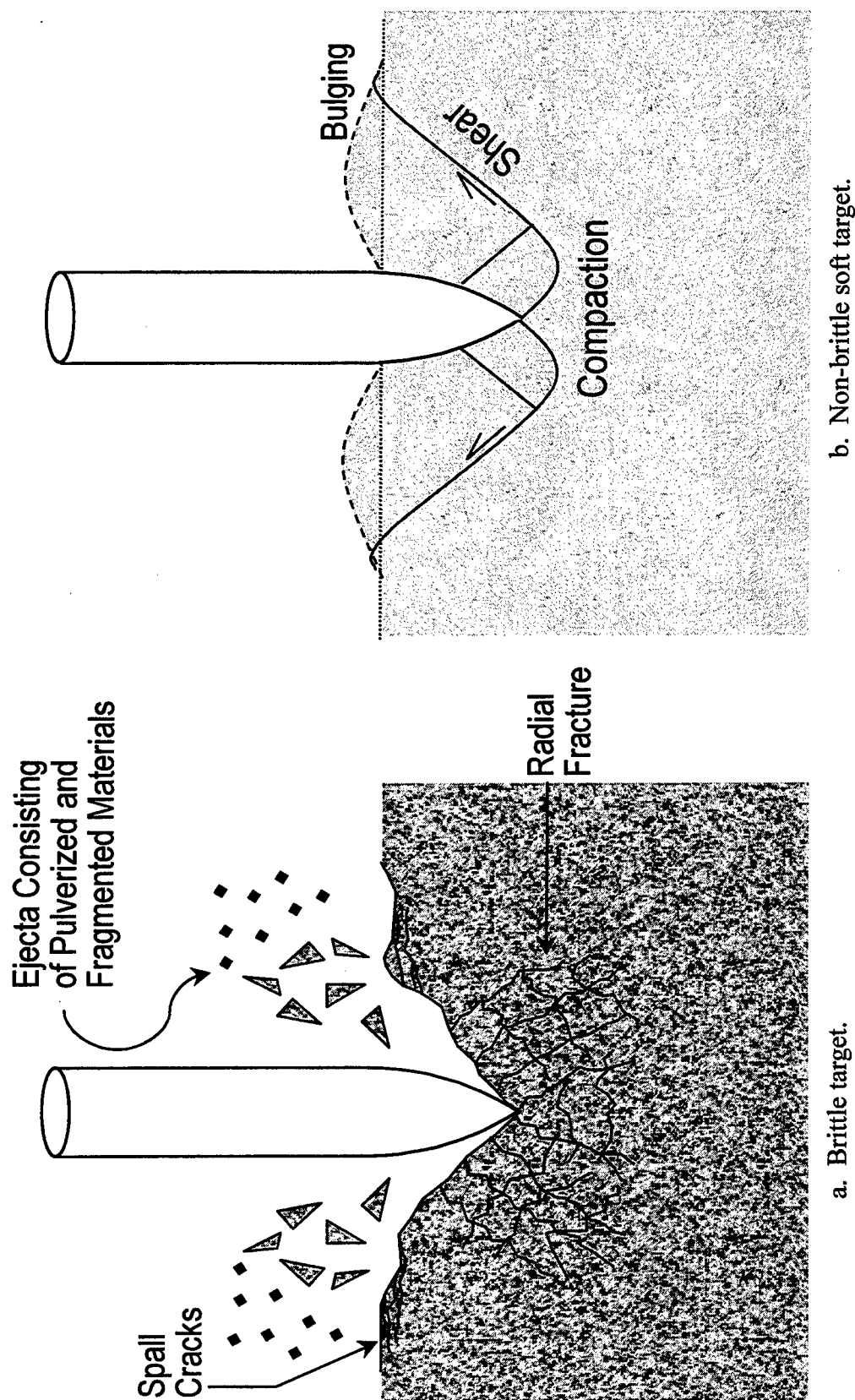
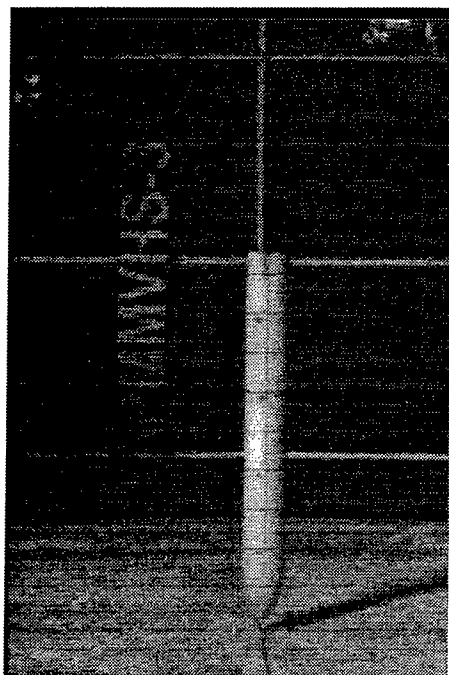
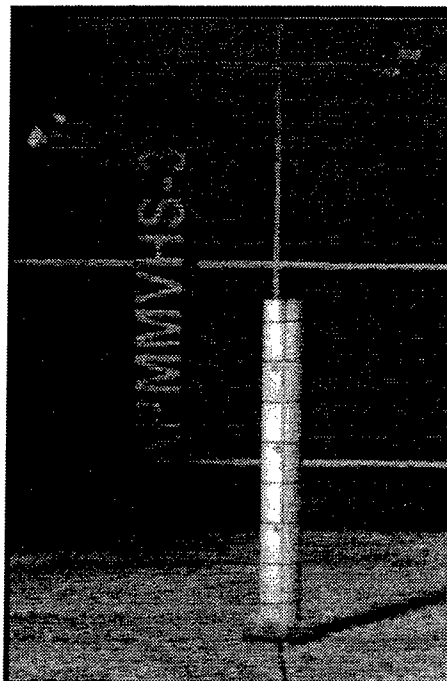


Figure 2.2. Projectile impact into brittle and non-brittle targets.

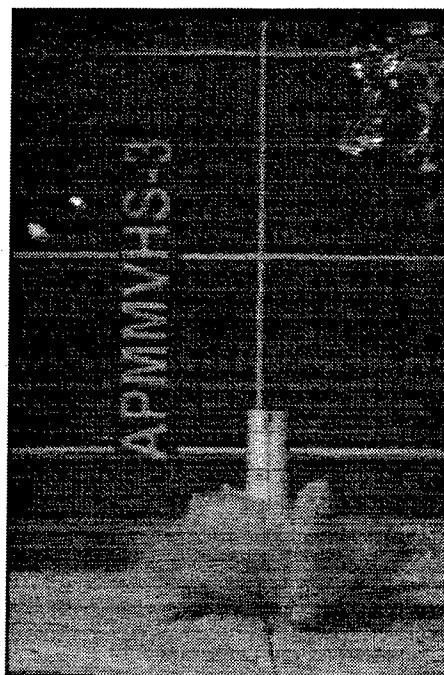




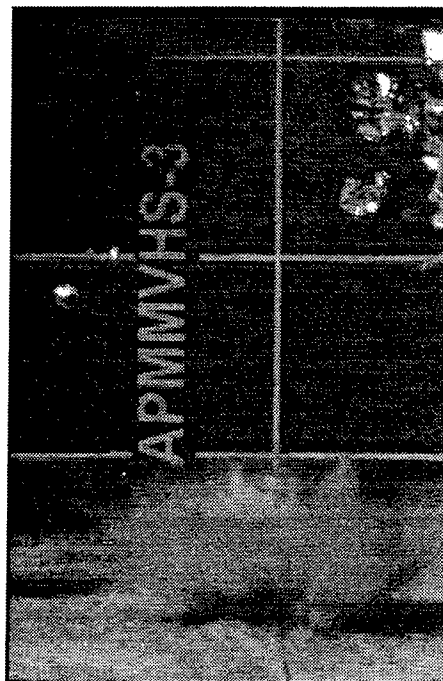
a.  $t_0$



b.  $t_1 > t_0$



c.  $t_2 > t_1$



d.  $t_3 > t_2$

Figure 2.3. High-velocity impact of a steel projectile into a concrete target showing formation of the ejecta cloud.

impact of a steel projectile into a concrete target. The figure shows the formation of the ejecta cloud, containing both the pulverized and fragmented materials, as the projectile enters the target. The damage to a granite target caused by the very high-velocity impact by a steel projectile is shown in Figure 2.4 (Ahrens and Rubin 1993). The figure illustrates and classifies the internal fractures radiating from the impact area and the highly fractured region near the impact crater. Concentric, radial, spall and near surface fractures are also illustrated. Pressures near the projectile tip are very high during the crater formation and cause the materials to be pulverized. The crater formation away from the projectile tip is primarily due to spall fracture and fragmentation which are controlled by the shearing strength and tensile capacity of the target material. As the bonds are broken due to pulverization and fragmentation, the material in these regions begins to respond more like a granular material than a cemented brittle material.

### 2.3 DEEP PENETRATION

Deep penetration into a semi-infinite target follows the impact crater formation and involves the opening of a cylindrical tunnel by the projectile. This phase is dominated by severe compaction and high-pressure shear flow. Friction can have some effect during this phase, particularly as the projectile slows down. The opening of the tunnel is illustrated in Figure 2.5. The resistance to penetration is primarily along the projectile nose. As penetration progresses, the material surrounding the nose of the projectile undergoes severe compaction and shear flow. Stresses near the nose of the projectile are extremely high, but dissipate rapidly by 80 percent or more only a couple of projectile diameters away from the penetration hole.

The different regions of material response during deep penetration are described in Figure 2.6 from the work by Forrestal (1986) for cavity expansion analysis. The cavity expansion theories put forth by Forrestal require that the projectile penetrate beyond the impact phase and into the tunneling phase. The target response during the tunneling

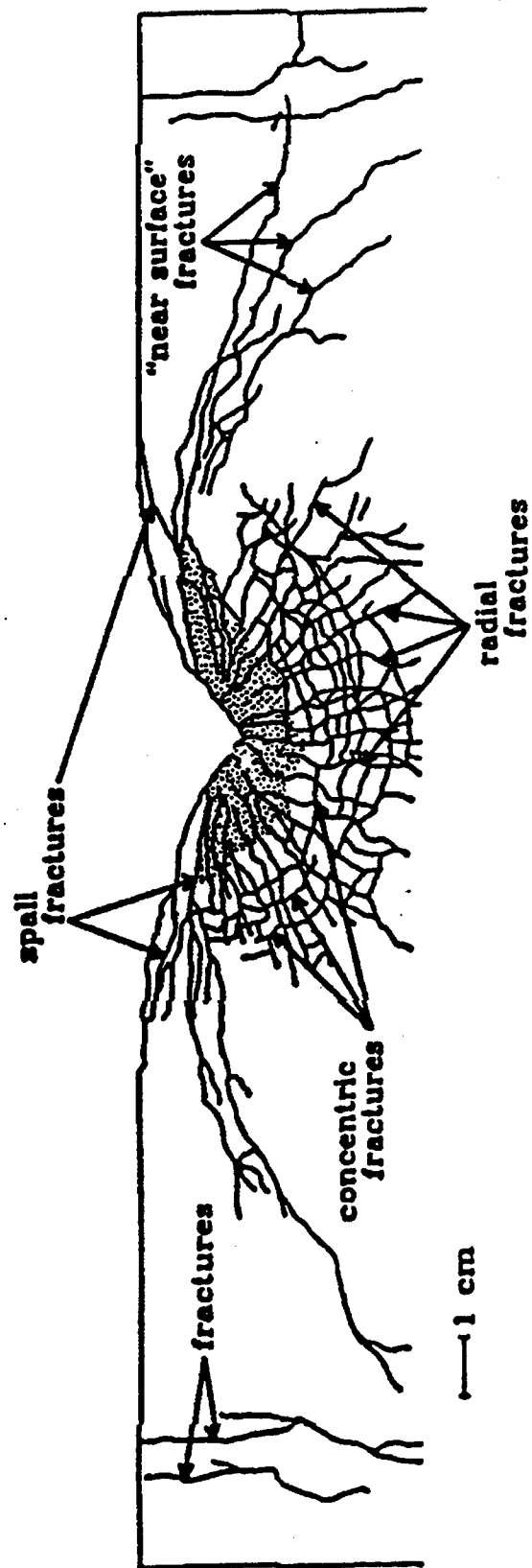


Figure 2.4. Cross section of a granite or limestone target impacted by a steel sphere (Ahrens and Rubin 1993).

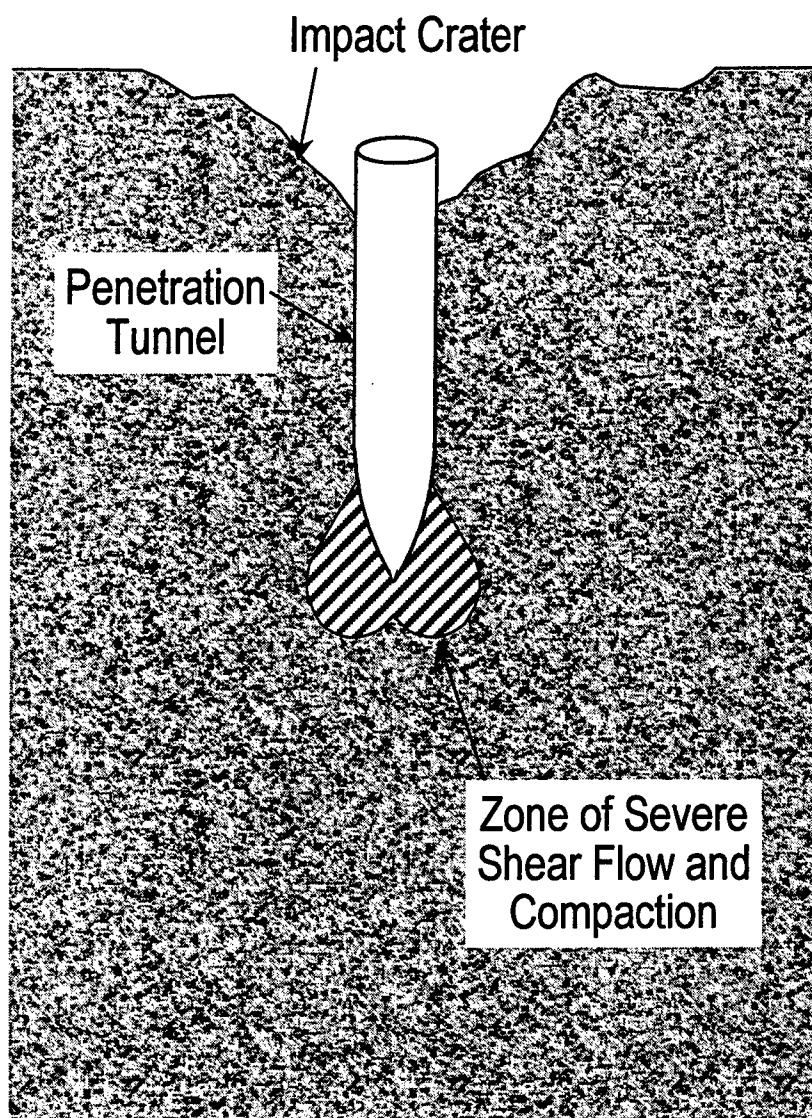


Figure 2.5. Penetration of a high-velocity projectile into a brittle geomaterial.

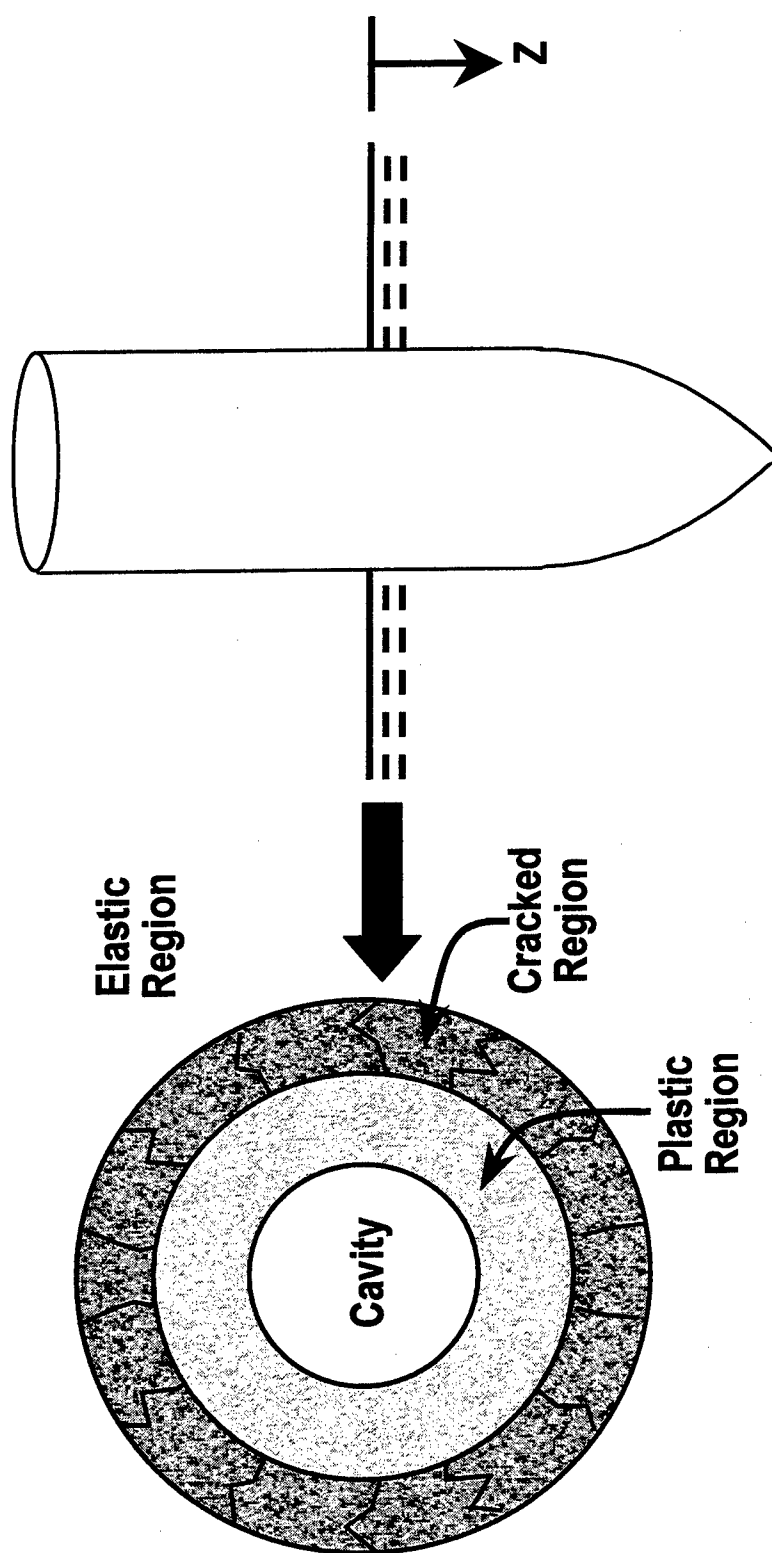


Figure 2.6. Target response regions during projectile penetration (Forrestal 1986).

phase is described as including two to three response regions (Forrestal 1986). At very high velocities, the target response is plastic near the penetration cavity where the stresses in the material have exceeded its shear strength and large deformations are occurring. Beyond the plastic region, the stresses are lower and the material response is elastic. At moderate velocities, a cracked region is added between the plastic and elastic region where the tensile strength of the material has been exceeded. At low velocities, where penetration into the tunneling phase is still possible, the plastic region is eliminated and the material response includes a cracked region followed by an elastic region.

Livingston and Smith (1951) conducted penetration experiments by air-dropping projectiles into granite and sandstone targets from aircraft at different altitudes. They proposed that the rock failure at impact is either by plastic flow or by crushing and fragmentation. The failure of the target material occurs in three zones shown in Figure 2.7. The zone of crushing occurs near the nose of the projectile and is characterized by the amount of fine material found near the nose. The amount of crushing depends on the kinetic energy of the projectile, the sharpness and cross-sectional area of the projectile, and the properties of the rock. The size of the zone is greatest near the surface where the kinetic energy of the projectile is greatest and the confinement of the target material is lowest. As penetration progresses, the size of the zone decreases since the kinetic energy of the projectile is decreasing and the confinement of the target material is increasing. The increase in confinement results in higher target strength. The zone of shearing begins at the zone of crushing and extends to the zone of tension slabbing. The shearing occurs because of the high compressive stresses imparted to the target material by the projectile, but the rapid release of these stresses as the projectile passes can cause the material to "burst" into the cavity behind the projectile. The zone of tension slabbing begins at the zone of shearing and extends to the surface. The extent of this zone decreases as penetration progresses. The observations by Livingston and Smith (1951) illustrate the importance of the compressibility, shear strength, and tensile strength of the target material and that the results from a single material response test, for example an

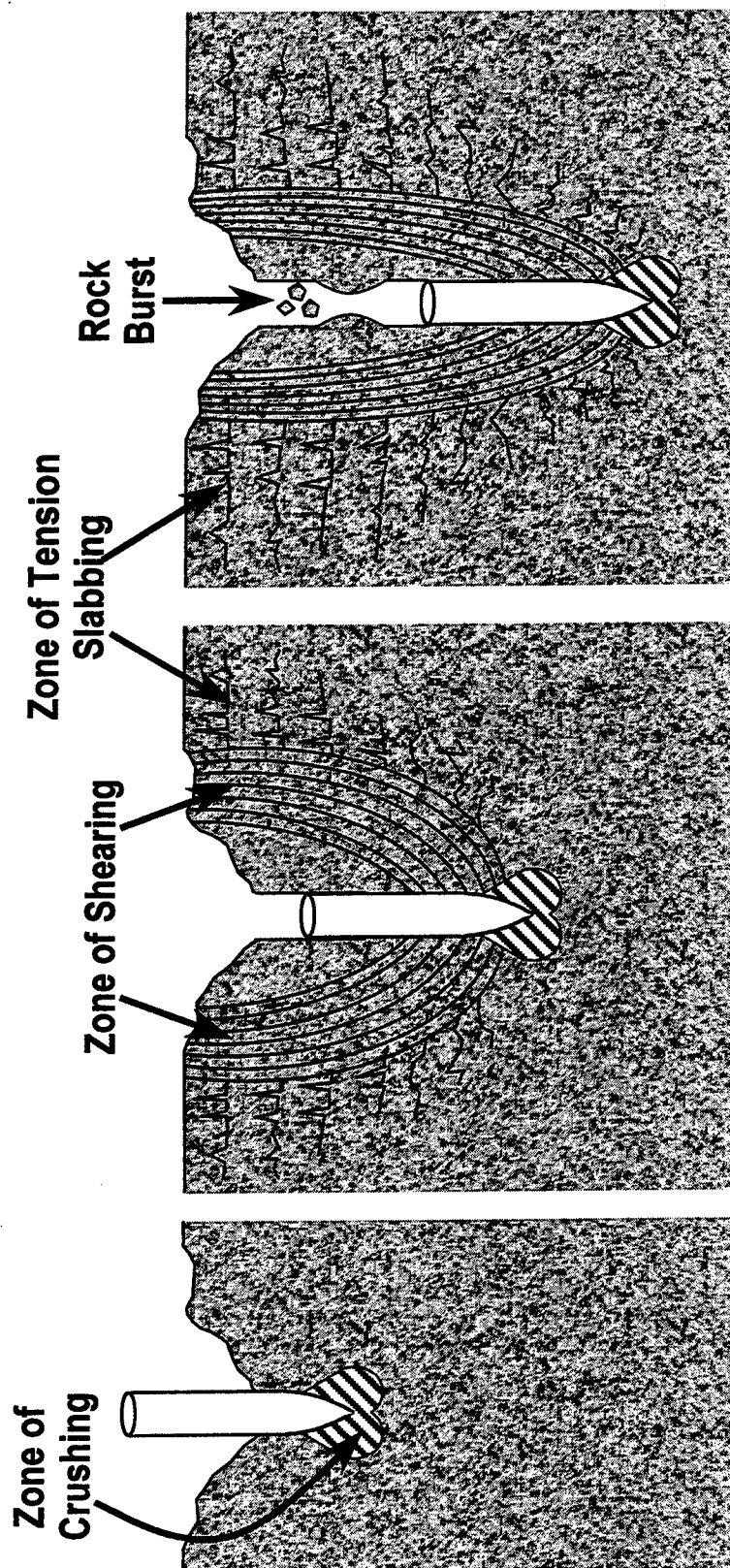


Figure 2.7. Rock failure during penetration (Livingston and Smith 1951).

unconfined compression test, cannot be used alone to describe a target materials response during the penetration process.

The primary effect of friction between the projectile and target in high-velocity projectile impact is near the end of the penetration event. The penetration tunnel has a tendency to close and grab the cylindrical aftbody of the projectile at this point and bring the projectile to a sudden stop. The influence of friction on the penetration to this point is believed to be insignificant when compared to the resistance offered by the target on the nose of the projectile as it creates a tunnel for the projectile to go through.

## 2.4 PERFORATION

Target perforation involves the formation of impact and exit craters, and may include a tunneling phase depending on the thickness of the target. Perforation will occur in finite thickness targets where the projectile maintains sufficient velocity through the impact phase and the tunnel phase, if applicable, to exit the target. Formation of the exit crater is a function of the shear resistance and tensile strength of the target material. Various failure modes during perforation of finite thickness plates are shown in Figure 2.8 (Zukas, et. al. 1982). The perforation process may include one of these modes as the dominant mode, but frequently includes a combination of several. In brittle geomaterials, only petaling is unlikely to occur. Brittle fracture will likely occur throughout the perforation event. As the projectile nears an exit surface, radial cracking, and fracture may occur. The plug formation is unlikely to occur as shown in Figure 2.8, but a cone of material may be formed and pushed out from the exit surface by the protruding projectile. Fragmentation is likely if the projectile has sufficient velocity to pass through and break up the cone.

Figure 2.9 shows the profiles of the impact and exit craters for several experiments using similar projectiles and impact velocities, but progressively thinner



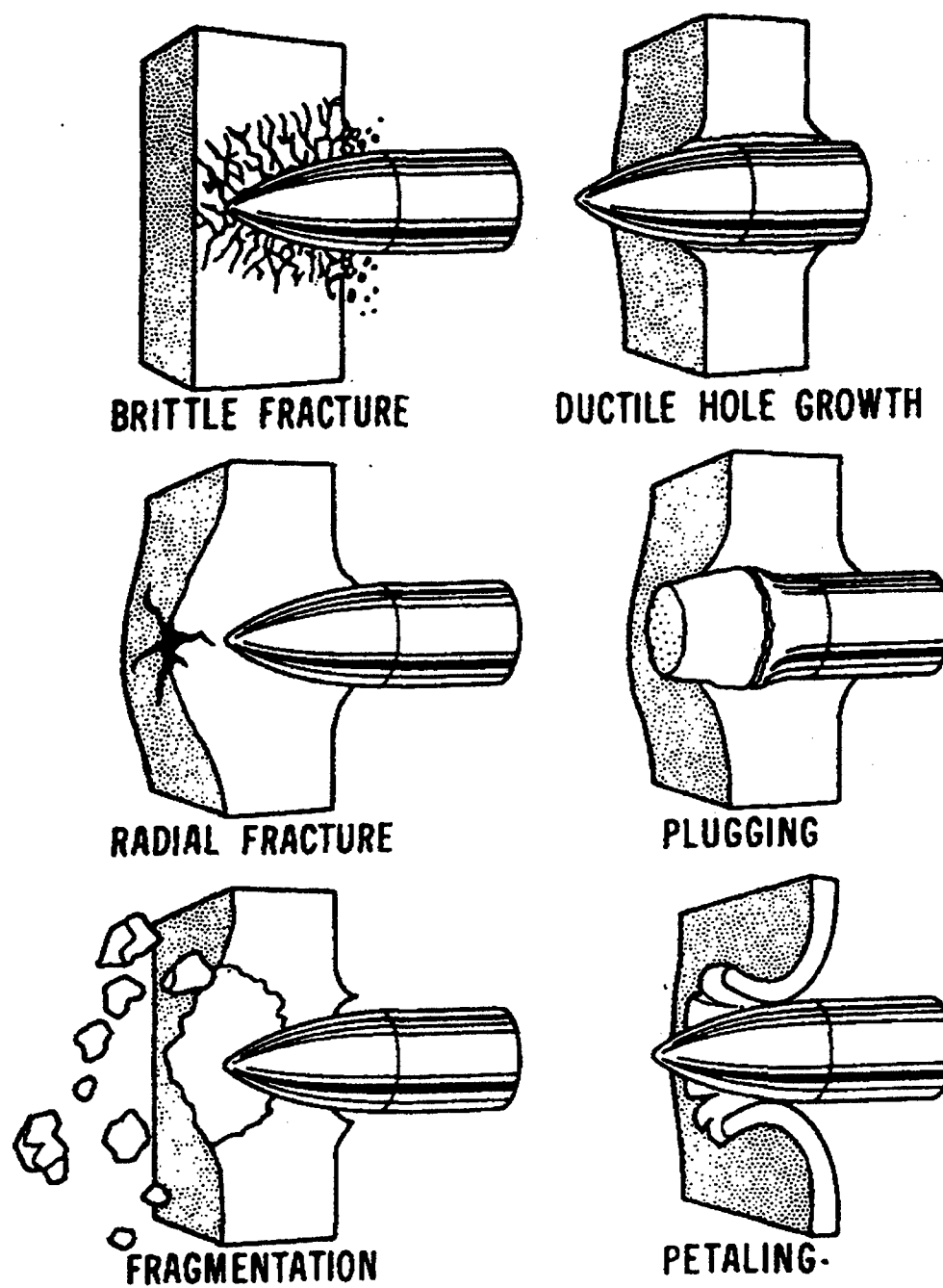


Figure 2.8. Failure modes in impacted plates (Backman 1976).

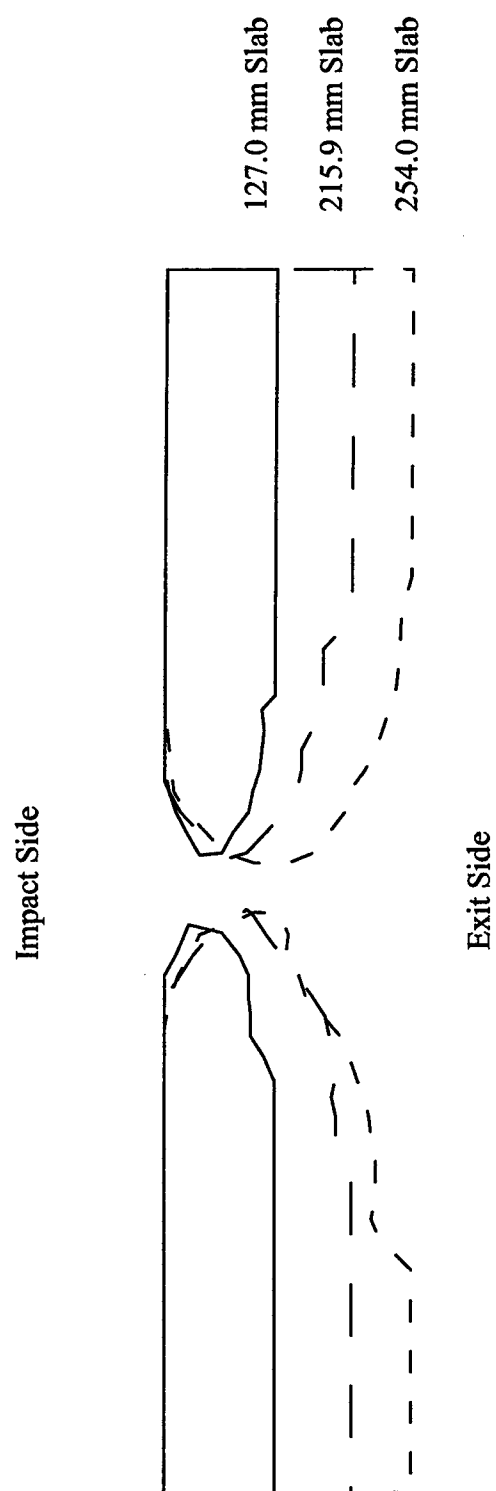


Figure 2.9. Comparison of impact and exit craters for three thicknesses of unreinforced concrete perforated by similar projectiles at similar impact velocities.

unreinforced concrete targets. The impact craters are conical in shape and very similar in depth and width for all experiments. The exit craters are also conical in shape, but their depth and width decreases as the target thickness decreases. Figure 2.10 shows captured images from a high-speed movie of the back of a concrete slab being perforated by a steel projectile. Radial cracking can be seen at time  $t_1$  as the cone that was formed ahead of the projectile is being pushed out through the back of the concrete slab. The projectile then passes through the cone fracturing it into pieces of various sizes. Figures 2.9 and 2.10 indicate that the modes of failure include combinations of brittle fracture, radial cracking, and fragmentation as described in Figure 2.8.

Figure 2.11 illustrates a hypothesis for perforation of brittle materials and the formation of the exit crater. The projectile first creates the impact crater and continues to tunnel through the target. The tunneling phase ends as soon as the concentrated force on the tip of the protruding projectile exceeds the resistance offered by a conical section of the target material (referred to as the shear cone). The resistance offered by the cone is essentially the integral of the shearing strength of the target material over the surface area of the cone. At this point the shear cone is formed and it separates from the back face of the target forming the exit crater. The pushing out of the cone from the back of the target results in a significant drop in target resistance (Pahl 1989). The existence of a tunnel and depth of the exit crater is determined by the target thickness and the strength of the target material. For very thick targets the impact crater is followed by a tunnel and an exit crater. As the target becomes thinner, the extent of the tunnel diminishes. At some point, the tunnel disappears completely and the impact and exit meet.

## 2.5 SUMMARY AND CONCLUSIONS

A synopsis of the three types of impact/penetration events has been presented. The simplest is the rigid impact which can be studied using momentum and energy principles. The impact of a hard projectile into a softer target will likely result in the

a.  $t_1$ b.  $t_2 > t_1$ c.  $t_3 > t_2$ d.  $t_4 > t_3$ 

Figure 2.10. High-speed movie images showing backface of an unreinforced concrete target being perforated by a steel projectile.

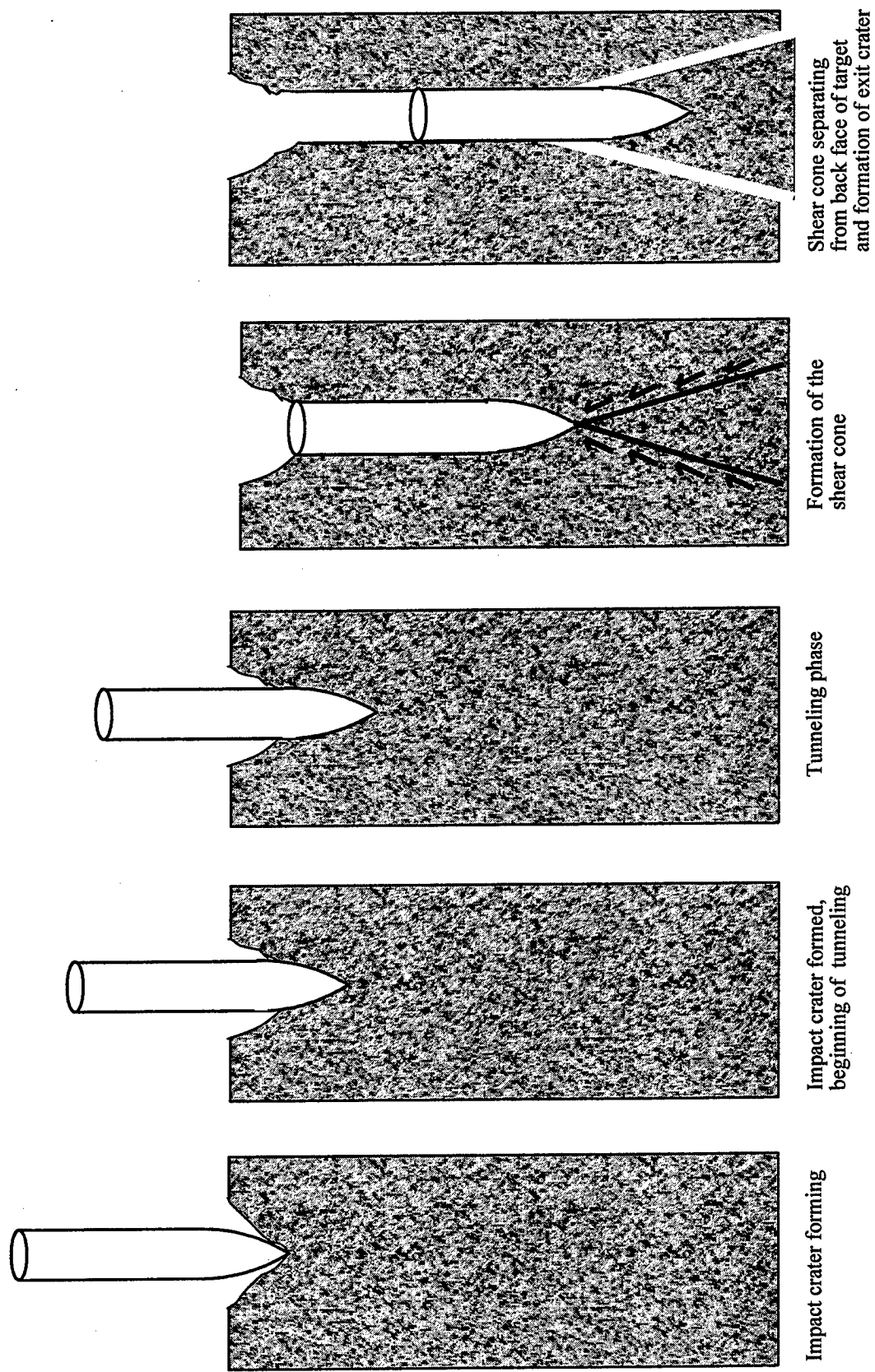


Figure 2.11. Sequence that occurs during perforation of a brittle geomaterial target.

formation of an impact crater. For brittle geomaterials, the depth of the crater is approximately two to four projectile diameters. The formation is primarily controlled by the shear and tensile strength of the target material. If the impact conditions and the extent of the target are sufficient the formation of a tunnel phase may result. The compressibility and strength of the target determine the formation of the tunnel. For finite thickness targets, an exit crater may form as the projectile perforates the target.

Much more research has been conducted to investigate deep penetration than to investigate impact and perforation of brittle geomaterials. This illustrates the complexity of the problem that requires modeling of the target materials response to complex loading paths in compression, tension, and shear.

## CHAPTER 3

### MATERIAL PROPERTIES

#### 3.1 INTRODUCTION

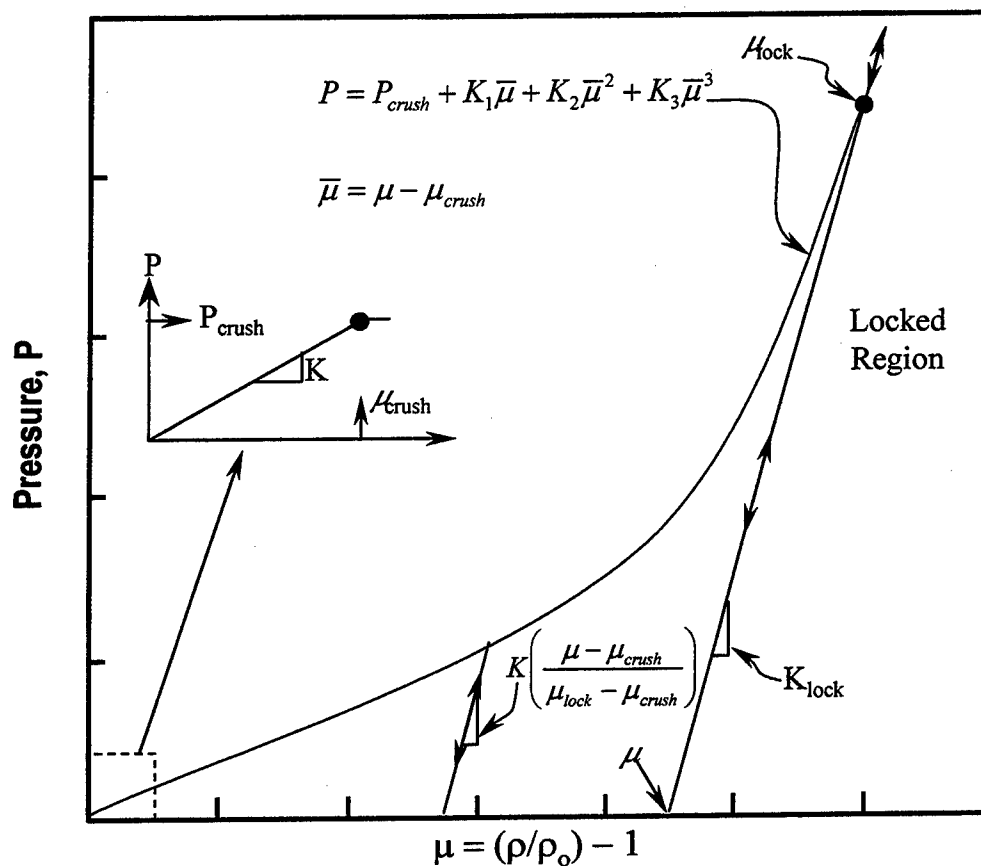
In the previous chapter, the different phases of impact, penetration and perforation were discussed. The material property required for a particular method of analysis is dictated by the type and complexity of the model being used to describe the target material during a penetration event. For the impact velocity range of interest ( $< 1$  km/s), the projectile is assumed to be rigid so that only the target response is closely modeled. The empirical, analytical and numerical methods of analysis each require different levels of target material description. The empirical methods require a minimal amount of information about the target. The information required by the analytic methods ranges from a minimal amount similar to that required by the empirical methods to a more detailed description requiring several specialized mechanical property tests. The numerical methods require detailed descriptions of the material response that are typically defined from results of many specialized mechanical property tests.

The detailed descriptions of the material properties are manifested in the numerical methods through mathematical constitutive models often referred to as material models. The material models will typically include a volumetric relation, shear or deviatoric relation, and failure criteria, and may include sophisticated hardening laws, fracture criteria, temperature effects, and strain rate effects. The principal obstacles to the use of numerical methods are time, cost, adequate description of the problem, and availability of adequate constitutive models. Time and cost are becoming manageable with the continued improvement of computational hardware and software. The finite-

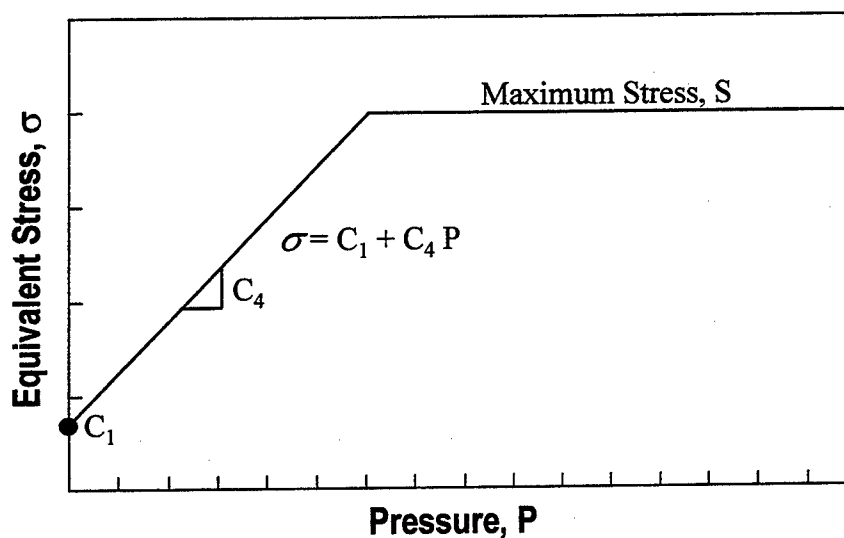
element codes use either Eulerian or Lagrangian descriptions to discretize the problem to be simulated. Eulerian codes, such as CTH (McGlaun, Thompson, and Elrick 1990), are considered to be better suited to problems involving large deformations, but sophisticated algorithms are required to propagate the various materials through the fixed mesh, and simulations often require large amounts of computer time. Lagrangian codes, such as EPIC (Johnson, et al 1995), are more straightforward, generally require fewer computations per time step, and the material boundaries are easily defined. Impact problems simulated using Lagrangian codes require the use of sliding interface algorithms to ensure separation of the colliding materials. As the mesh distortions become significant, the accuracy of the computation decreases and the computational time grows considerably. Some codes allow for the highly distorted regions to be rezoned either manually or automatically. Some codes contain algorithms that "erode" the highly distorted elements based on the assumption that the highly distorted material is no longer contributing to the mechanics of the problem. Once the highly distorted elements have been eroded the computation can continue at a more reasonable pace. Although the response of the element material is removed from the calculation, its mass is conserved at the nodes. Material models often found in numerical codes used to simulate projectile penetration problems decouple the effects of volumetric and shear response. An equation of state or pressure-volume relation is used to describe the volumetric response and elastic-plastic models are used to describe the shear response.

The pressure levels developed during high-velocity impact are much higher than those encountered in conventional loadings. To illustrate the stress levels that may be encountered during the penetration event, numerical simulations were made for a steel projectile penetrating into a conventional-strength (unconfined compressive strength of approximately 36 MPa) concrete (CSPC) from Forrestal, et. al. (1994) using the EPIC finite-element code (Johnson, et al 1994). The simulations were made using an elastic-perfectly plastic crushable solids material model. Figure 3.1 shows the description of the pressure-volume relation and the strength relation for the model. Pressure is determined





a. Description of the pressure-volume relationship



b. Description of the strength relationship

Figure 3.1. Description of elastic-perfectly plastic crushable solids material model in EPIC.

in Figure 3.1.a based on the current volumetric strain and whether the material is being loaded, unloaded or reloaded. The equivalent stress  $\sigma$  is based on the Von Mises yield criterion and is defined as

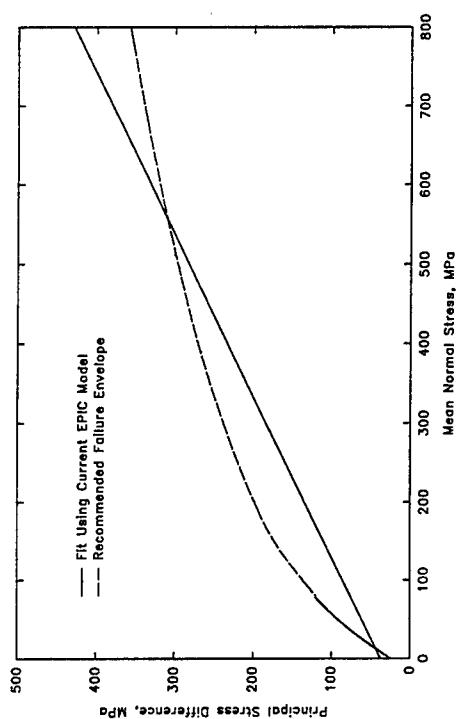
$$\sigma = \sqrt{\frac{1}{2}[(\sigma_x - \sigma_z)^2 + (\sigma_x - \sigma_\theta)^2 + (\sigma_z - \sigma_\theta)^2 + 6(\tau_{xz}^2 + \tau_{x\theta}^2 + \tau_{z\theta}^2)]} \quad 3.1$$

where  $\sigma_x$ ,  $\sigma_z$ ,  $\sigma_\theta$ ,  $\tau_{xz}$ ,  $\tau_{x\theta}$ , and  $\tau_{z\theta}$  are the six stress components. A constant shear modulus  $G$  is also used. Parameters used in the model to describe the CSPC concrete are summarized in Table 3.1. A comparison between the recommended material properties for the concrete (Cargile 1998) and the model fit is shown in Figure 3.2. Recommended properties are based on the results from many triaxial shear, hydrostatic compression, and specialized (such as uniaxial strain) experiments conducted on specimens of the concrete. They are an interpretation of the experiment results to provide a consistent set of responses that can be fit to mathematical models used in numerical simulations. The model matches the hydrostatic (or isotropic) compression response of the material fairly well, but, since the ultimate strength relation for the model is linear, the fits to the triaxial stress-strain relations are only approximate.

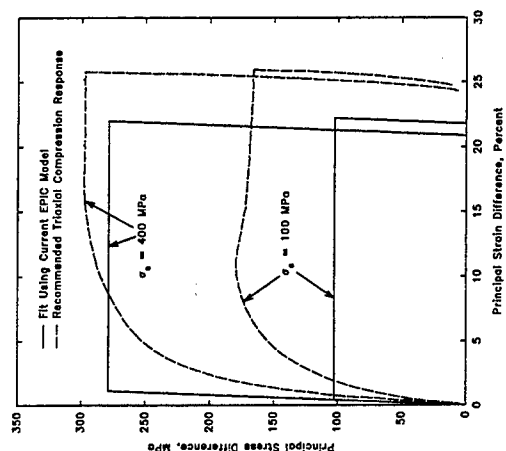
Plots of Von Mises Stress (VMS) versus pressure (referred to as the stress path) are presented in Figures 3.3, 3.4 and 3.5 for several elements at different ranges and at depths below the target surface of about 46, 122, and 635 mm, respectively, for an impact velocity of 610 m/s. The ranges from the impact point for each figure are 2.5, 10, 23, and 99 mm. Each stress path shows an initial increase in VMS with relatively little increase in pressure. The stress path then follows the failure surface. The peak pressures at these output stations range from about 840 MPa to about 3 MPa. Several of the stress paths indicate a tendency to enter the tensile (negative pressure) region as illustrated by the stress path "bumping into" the VMS axis. The calculations give some indication of the pressure levels at which material property tests must be conducted to adequately capture the material response during a numerical simulation of the penetration event.

Table 3.1. Values for the crushable solids model parameters fit to CSPC concrete.

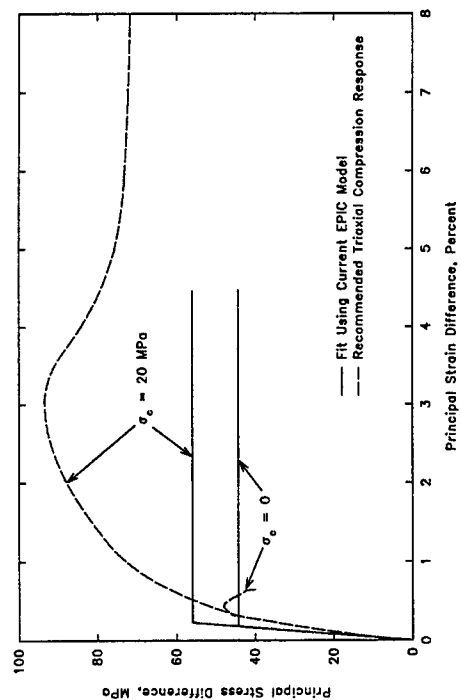
$P_{\text{crush}}$	27.0 MPa
$\mu_{\text{crush}}$	0.0015
$K_1$	10,504.3 MPa
$K_2$	-216,518.9 MPa
$K_3$	2,604,741 MPa
$\mu_{\text{lock}}$	0.0796
$K_{\text{lock}}$	76,000 MPa
$C_1$	37.1 MPa
$C_4$	0.49
$S$	1,057.5 MPa
$G$	19,600 MPa
Density	2.352 Mg/m <sup>3</sup>



a. Isotropic Compression



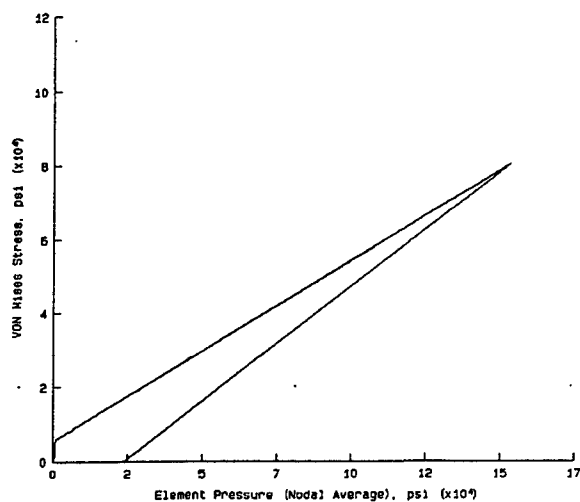
b. Triaxial Failure



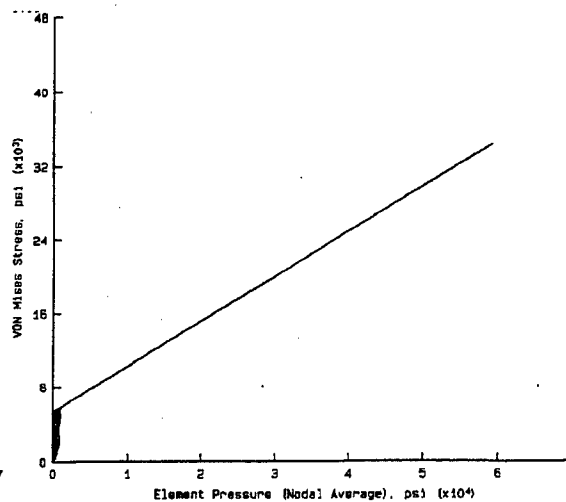
c. Low Pressure Shear

d. High Pressure Shear

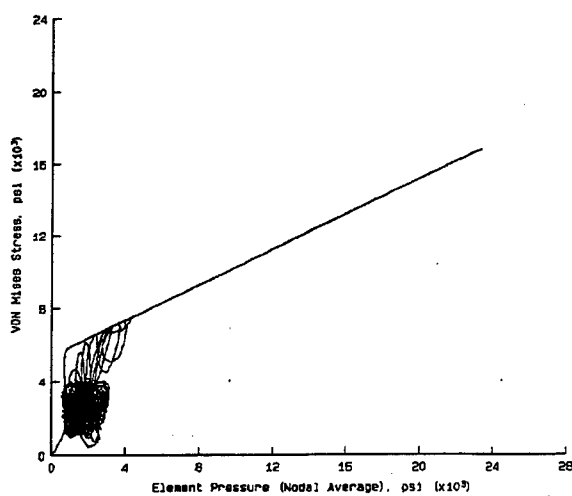
Figure 3.2. Fit to recommended mechanical properties using the current model in EPIC for crushable solids.



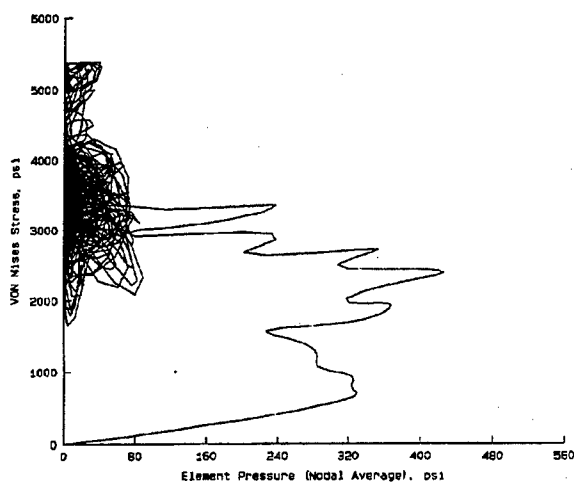
a. Range = 0.1 in. (2.5 mm)



b. Range = 0.4 in. (10 mm)

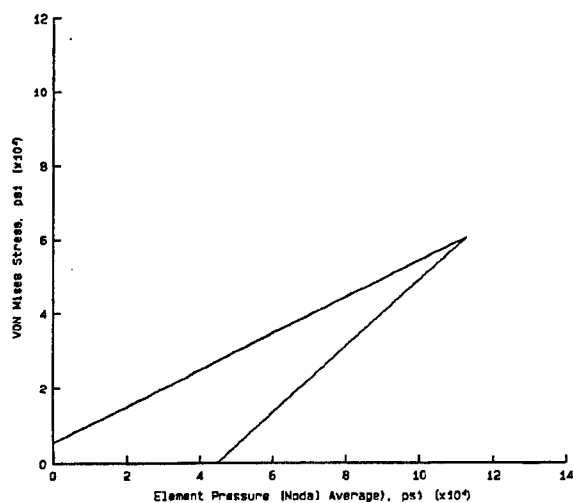


c. Range = 0.9 in. (23 mm)

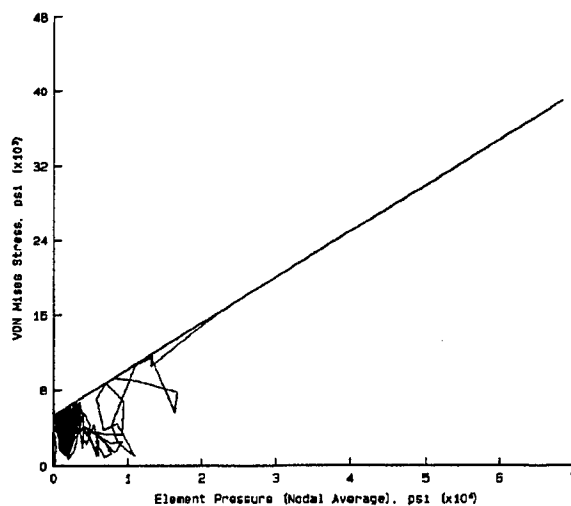


d. Range = 3.9 in. (99 mm)

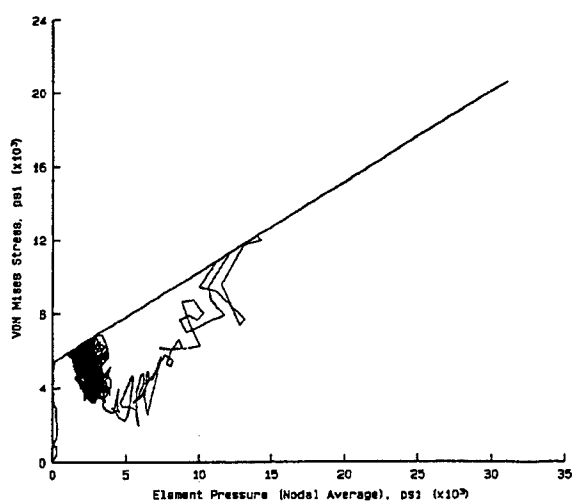
Figure 3.3. Stress-paths at a depth of 1.8 in. (46 mm).



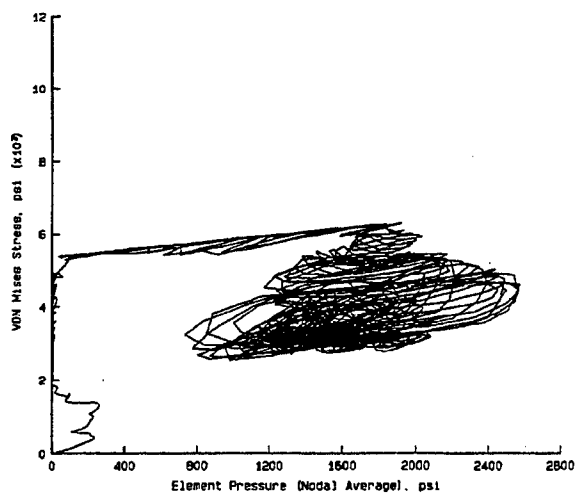
a. Range = 0.1 in. (2.5 mm)



b. Range = 0.4 in. (10 mm)

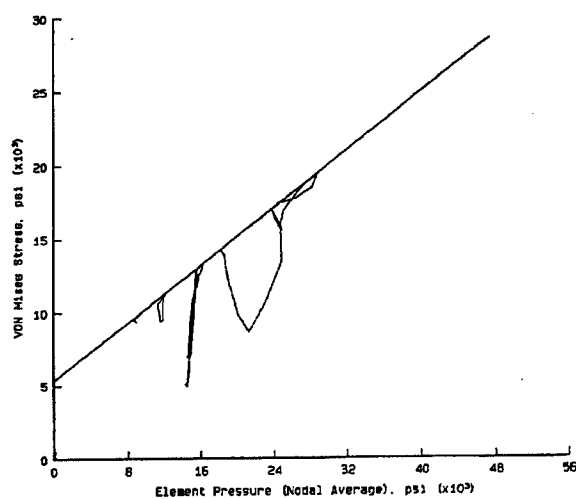


c. Range = 0.9 in. (23 mm)

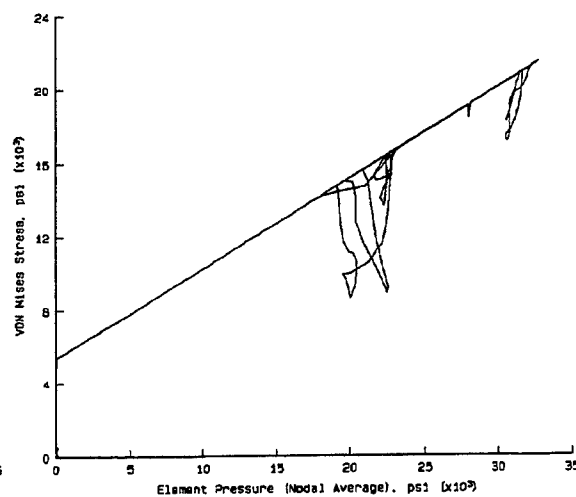


d. Range = 3.9 in. (99 mm)

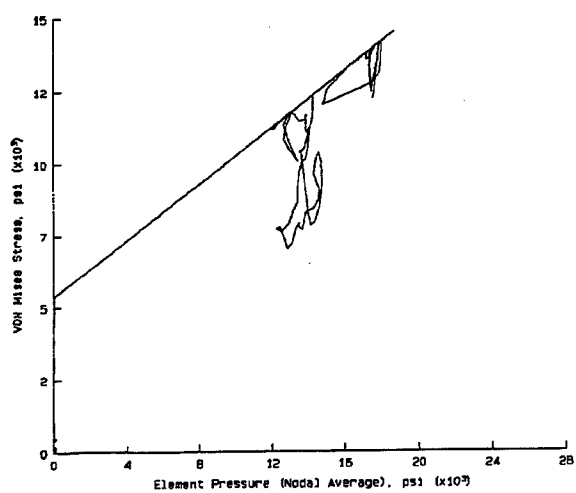
Figure 3.4. Stress-paths at a depth of 4.8 in. (122 mm).



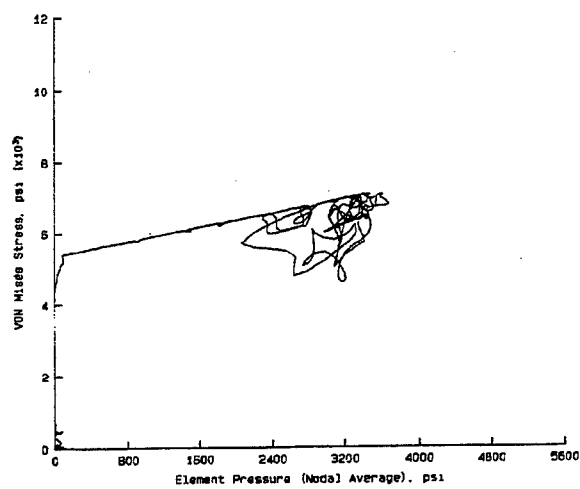
a. Range = 0.1 in. (2.5 mm)



b. Range = 0.4 in. (10 mm)



c. Range = 0.9 in. (23 mm)



d. Range = 3.9 in. (99 mm)

Figure 3.5. Stress-paths at a depth of 25 in. (635 mm).

The true properties of a material are directly linked to its structure at the macro-level, meso-level, and micro-level. The properties are the response of the material to mechanical, physical or chemical influences. To determine the properties, an experiment must be conducted on a specimen of given size and geometry, under an appropriate loading condition with specific boundary conditions. The loading condition should be representative of the conditions that are expected to exist in the system as a whole that is to be analyzed, such as a structure, foundation, dam, etc. (Hordijk, et.al. 1989).

The shear response of geomaterials is pressure dependent. As pressure increases, the ductility and strength of the material changes. Under certain loading conditions volumetric strains occur during shear thus implying a coupling between the volumetric and deviatoric response. In the following sections, the response of brittle geomaterials to hydrostatic and deviatoric states of stress will be discussed. The influences of pressure, loading path, and strain rate will be included.

### 3.2 HYDROSTATIC PRESSURE

The pressure-volumetric strain response of a geomaterial is typically determined by applying hydrostatic, or equal all-around, pressure to a specimen of material and determining the resulting volumetric strain. The pressure applied to the specimen is the true (or Cauchy) stress. The hydrostatic pressure and volumetric strain provide the bulk response of the material from which the bulk modulus  $K$  is determined, usually as a tangent to the pressure-volumetric strain curve. In fully-saturated materials, the volumetric strain is determined under drained conditions by monitoring the amount of pore fluid being forced out of the specimen. Under undrained conditions the change in volumetric strain is zero if the compressibility of the pore fluid is neglected. The geomaterials of concern here are generally partially saturated. Volumetric strain for these materials is determined by combining measurements of the sample deformations based on an assumed shape. The method used to calculate volumetric strain must be understood so



that consistency is maintained between the mathematical model and the method used to characterize the material property. Here and throughout this chapter, Lagrangian, or total, notation is used to define strain, i.e., strain is equal to the change in dimension divided by the original dimension, and compression is taken to be positive.

Most mathematical models assume small strain, at least in the increment, and therefore the most common method for calculating volumetric strain is

$$\epsilon_v = \epsilon_x + \epsilon_y + \epsilon_z \quad 3.2$$

where  $\epsilon_v$  is the volumetric strain and  $\epsilon_x$ ,  $\epsilon_y$ , and  $\epsilon_z$  are the axial strains in the three orthogonal directions assuming cartesian coordinates. In cylindrical coordinates the individual strains are  $\epsilon_r$ ,  $\epsilon_\theta$ , and  $\epsilon_z$ , with  $\epsilon_r$  and  $\epsilon_\theta$  often assumed to be equal.

Other methods for calculating volumetric strain based on an assumed shape were presented by Ehrgott (1971) for cylindrical specimens. The shape of the specimen during hydrostatic compression is influenced by the end restraint. If the specimen does not move freely at the ends, then the shape is similar to a double truncated cone and the volumetric strain is calculated as

$$\epsilon_v = \epsilon_z + \epsilon_r - \epsilon_z \epsilon_r + \frac{\epsilon_r^2}{3} (\epsilon_z - 1) \quad 3.3$$

If the specimen ends are free to move, the shape is more like that of a cylinder and the volumetric strain is calculated as

$$\epsilon_v = \epsilon_z + 2 \epsilon_r - 2 \epsilon_r \epsilon_z + \epsilon_r^2 (\epsilon_z - 1) \quad 3.4$$

If the higher order terms of Equation 3.4 are removed, it reduces to Equation 3.2 for small strains.

Given a right rectangular shape as in Figure 3.6, the original volume  $V_o$  can be written as

$$V_o = L R P \quad 3.5$$

and the current volume  $V_i$  can be defined as

$$\begin{aligned} V_i &= (L - \Delta L) (R - \Delta R) (P - \Delta P) \\ &= L R P (1 - \epsilon_L) (1 - \epsilon_R) (1 - \epsilon_P) \end{aligned} \quad 3.6$$

where  $L$ ,  $R$  and  $P$  are the lengths of each side,  $\Delta$  is the change in dimension and  $\epsilon$  is the total strain. Defining  $\epsilon_v$  as

$$\epsilon_v = \frac{\Delta_v}{V_o} = 1 - \frac{V_i}{V_o} \quad 3.7$$

and substituting Equations 3.5 and 3.6 gives

$$\begin{aligned} \epsilon_v &= 1 - \frac{L R P (1 - \epsilon_L) (1 - \epsilon_R) (1 - \epsilon_P)}{L R P} \\ &= \epsilon_L + \epsilon_R + \epsilon_P - \epsilon_L \epsilon_R - \epsilon_L \epsilon_P - \epsilon_R \epsilon_P + \epsilon_L \epsilon_R \epsilon_P \end{aligned} \quad 3.8$$

Equation 3.8 is similar to Equation 3.4 and, if the higher order terms are removed, is the same as the small strain definition in Equation 3.2. Figure 3.7 shows a calculation of volumetric strain using Equation 3.2 for the small strain assumption and Equation 3.8 for the large strain assumption, and assuming isotropic deformation such that the axial strains are equal. Most brittle geomaterials will exhibit a volumetric strain during hydrostatic compression of less than 10 percent, and certainly less than 20 percent. Figure 3.7 shows that the  $\epsilon_v$  using the small strain assumption is only 3 percent larger than the  $\epsilon_v$  using the large strain assumption at an axial strain of about 0.03, and only 7 percent larger at an axial strain of about 0.07. These axial strains correspond to volumetric strains of about 0.1 and 0.2 (10 and 20 percent), respectively.

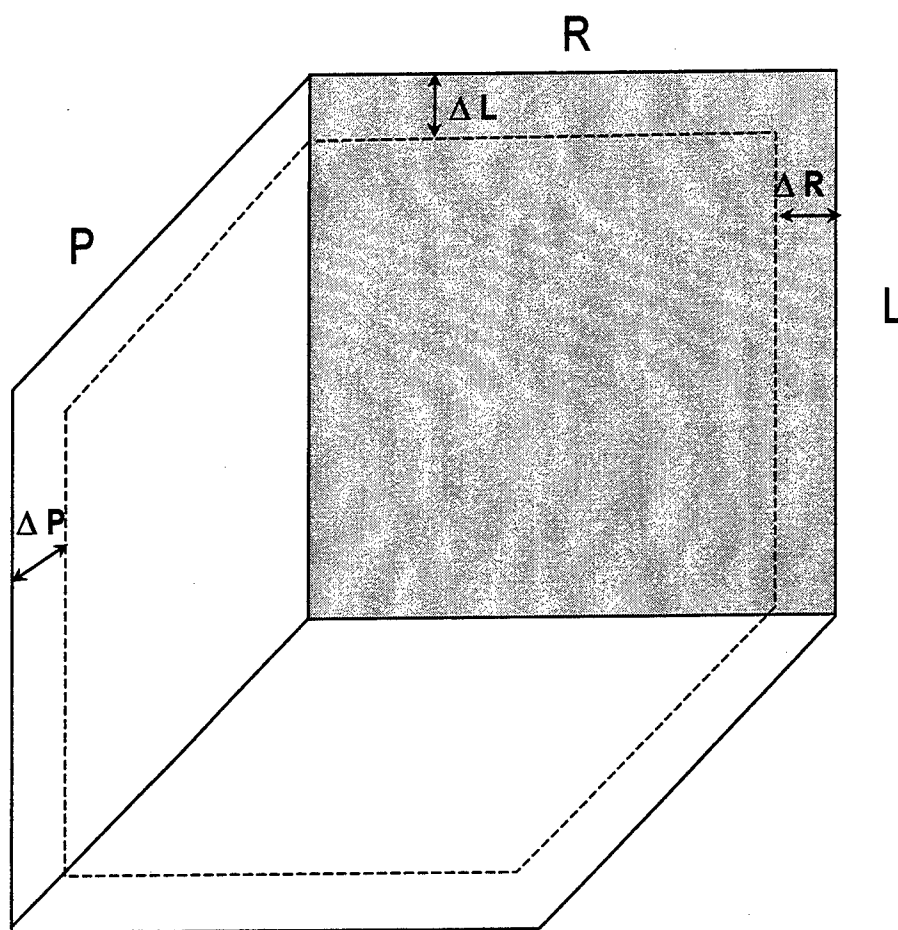


Figure 3.6. Initial and deformed rectangular shape of a specimen.

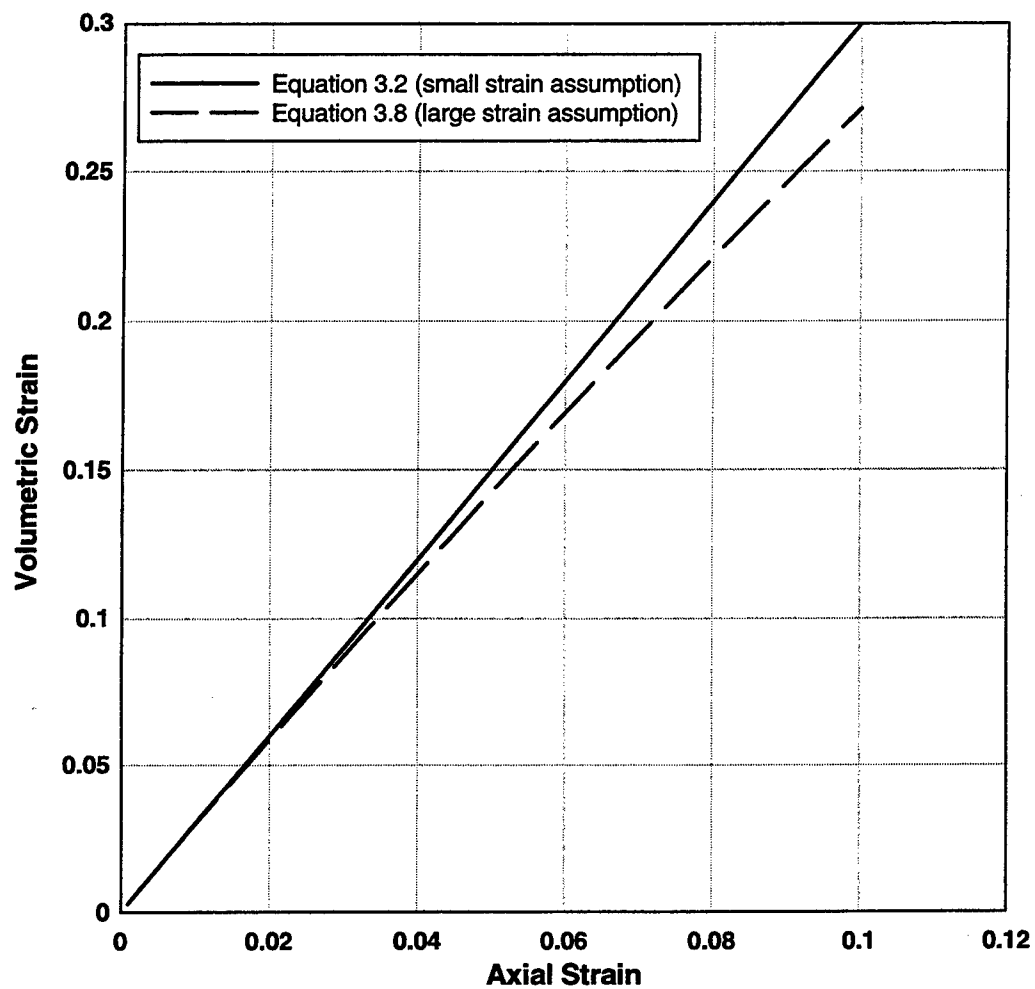
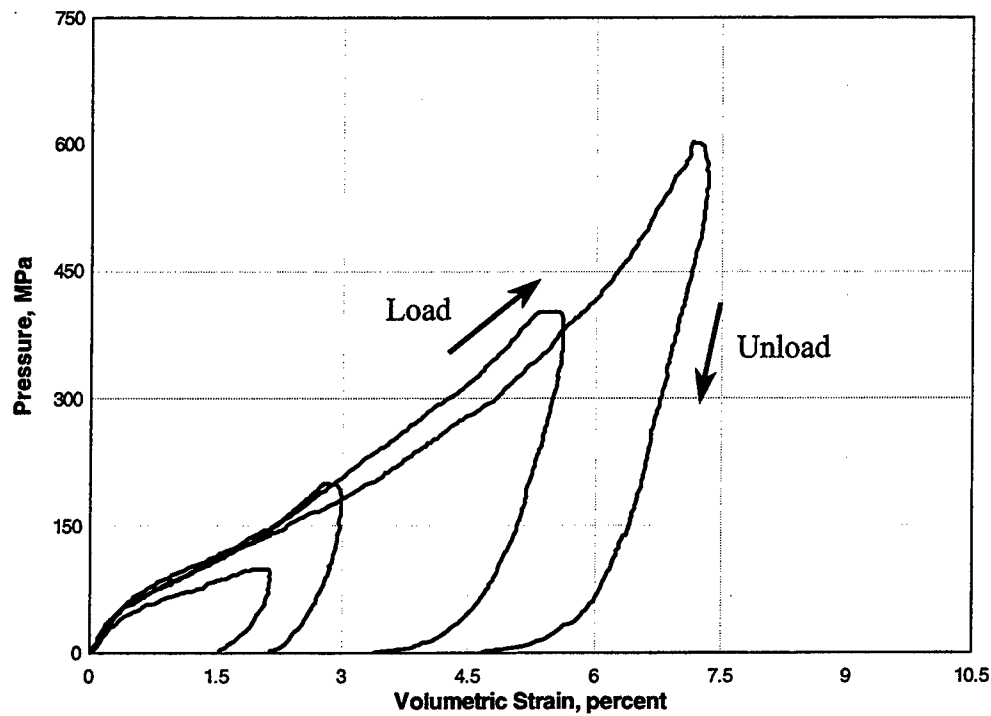


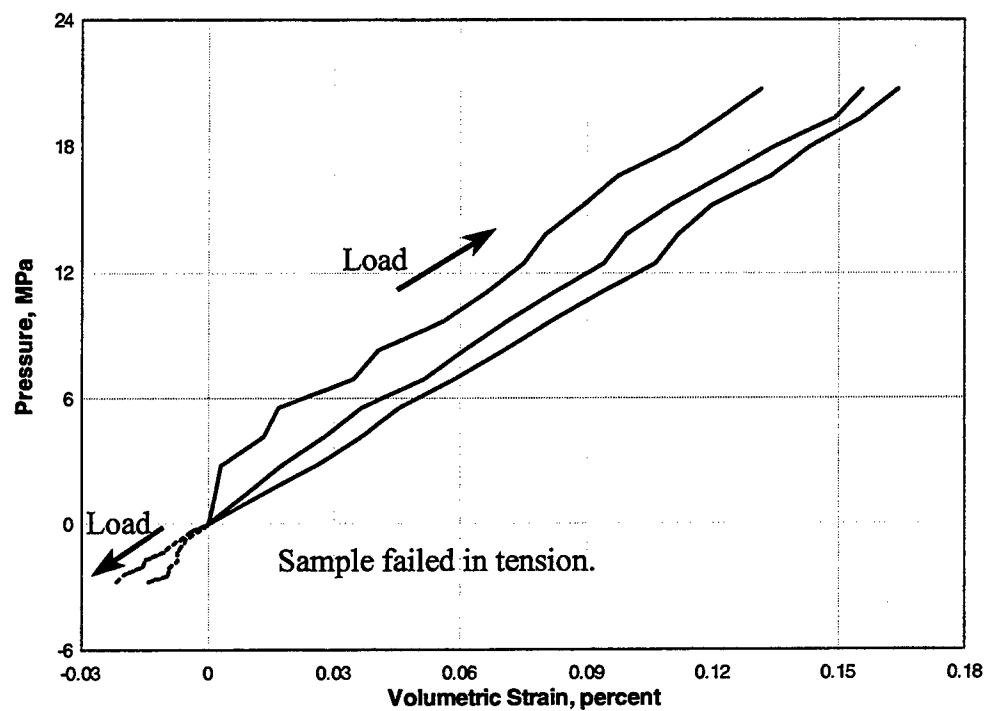
Figure 3.7. Volumetric strain calculated using equations 3.2 and 3.8.

Brittle geomaterials exhibit nonlinear stress-strain behavior during application of hydrostatic pressure as shown in Figure 3.8, where volumetric strain is calculated using Equation 3.2 and the pressure is the true stress being applied to the concrete specimen. In Figure 3.8.a shows the results from hydrostatic compression tests on four concrete specimens. The initial compression slope of the hydrostatic response is fairly constant and the material is essentially elastic. The response then becomes concave to the strain axis, but then reverses to become concave to the stress axis. This behavior indicates a change is occurring within the material, but it is not failing, i.e., when pressure is removed the material retains a shape with no easily visible cracks or damage. During unloading, the slope is nearly constant initially, but becomes concave to the stress axis as pressure approaches zero, which is another indication that the material has experienced some internal change. Figure 3.8.b shows the results from hydrostatic tension tests on two concrete samples and hydrostatic compression tests on three samples. In tension, the initial slope is a linear extension of the initial compressive slope. As the tensile stress increases, the curve becomes more concave to the strain axis and the material begins to experience more internal changes. In tension, an easily visible failure occurs when the material separates. Little information is available to describe "unloading" during hydrostatic tension because the failure of the material is sudden and catastrophic and control of the test is often lost.

The idealized brittle geomaterials here are assumed to consist of relatively hard granular particles cemented together by a weaker paste, whether introduced by man as with concrete or by nature as in cemented sands and rocks, with other inclusions such as micro- and macrocracks and voids. The voids may be filled with liquid such as water or gas such as air. During application of the hydrostatic pressure the brittle geomaterial specimen undergoes several physical changes. These changes are illustrated in Figure 3.9 where compression is positive. In region A of Figure 3.9, the material is essentially elastic and the stresses are not sufficient to cause slippage, significant coalescence of cracks, or significant damage to the paste or particles. The pressure being applied to the



a. Hydrostatic compression



b. Hydrostatic compression and tension

Figure 3.8. Response of concrete to hydrostatic pressure.

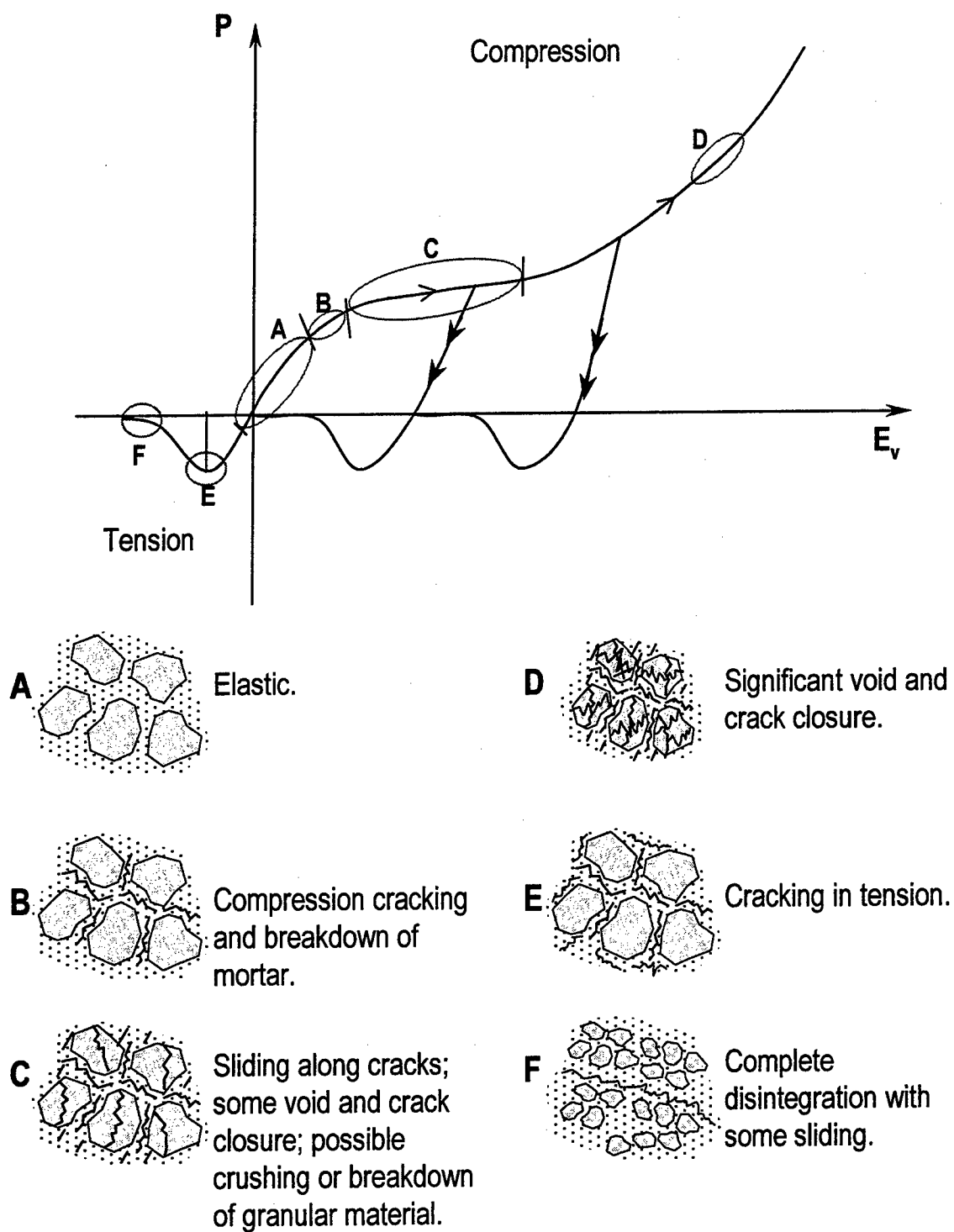


Figure 3.9. Material changes during application of hydrostatic stress.

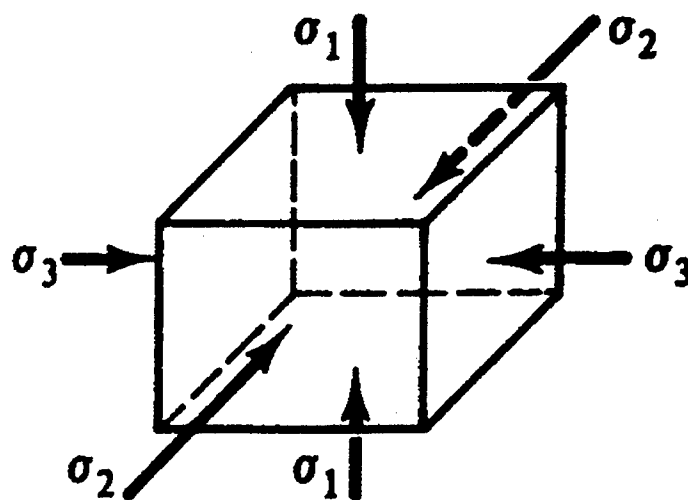
specimen is easily carried by the material constituents. In region B, crack formation and coalescence of cracks within the paste begins to occur. The cracks formed and extended in region B, along with the existing voids, will allow for the sliding and particle rearrangement that occurs in region C and additional breakdown of the paste. As the pressure increases in region C, some void and crack closure is possible and cracking and breakdown of the granular particles may begin. In region D, as pressure increases, less particle rearrangement occurs while void and crack closure becomes significant. At the extreme high pressures in region D, the voids and openings from the cracks are closed or filled with fluid such that the applied pressures are being carried by the pore fluid and not the skeleton of the material.

During the application of all around tensile stresses, the response of the material, regions E and F in Figure 3.9, can be dramatic in that, unlike compression, catastrophic failure of the test specimen may occur. Region E is similar to region B in compression except that the majority of the changes to the material are due to crack propagation and coalescence. At some level of tension, significant cracks will form and the material will fail with rapid, but not immediate, loss of capacity (region F). The loss is not immediate because the loss of strength will begin prior to complete separation at the significant crack. Since complete separation ultimately occurs, the specimen cannot retain a residual strength.

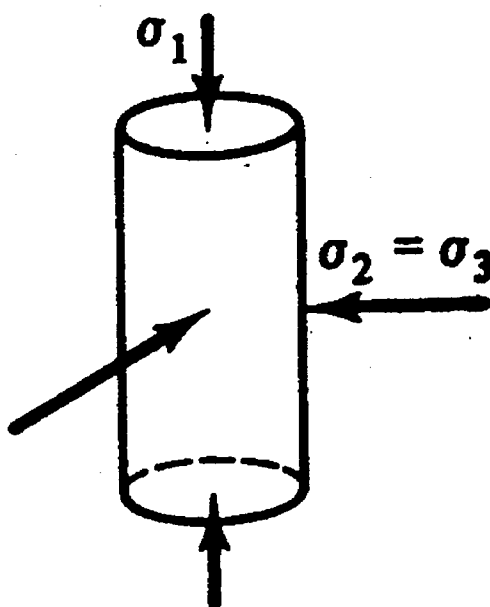
### 3.3 DEVIATORIC LOADING

A deviatoric, or shear, loading is often applied to a test specimen after some level of compressive (HC) or tensile hydrostatic (HT) pressure has been applied. The load, or deformation, is changed while the response of the material is monitored. Desai and Siriwardane (1984) describe several of the different types of loading paths that might be applied. The states of principal stress for triaxial experiments on cubic and cylindrical specimens are shown in Figure 3.10. In experiments on cylindrical specimens the stresses





a. True triaxial.



b. Cylindrical triaxial.

Figure 3.10. Principal stresses during triaxial experiments.

$\sigma_2$  and  $\sigma_3$  are assumed to be equal. Stress-paths for typical mechanical property experiments are illustrated in the triaxial plane in Figure 3.11. In most triaxial tests the specimen is subjected to an initial confining stress such that the principal stresses are all equal,  $\sigma_c = \sigma_1 = \sigma_2 = \sigma_3$ . In the conventional triaxial compression (CTC) test two of the stresses, usually  $\sigma_2$  and  $\sigma_3$ , are held constant while  $\sigma_1$  is increased until failure of the specimen occurs. The deviator stress and hydrostatic pressure both increase during the loading. In the reduced triaxial compression (RTC) test,  $\sigma_2$  and  $\sigma_3$  are reduced while  $\sigma_1$  is held constant so that the shear stress increases while the pressure decreases. In the triaxial compression (TC) test, the stress is applied so that the pressure remains constant while the shear stress increases. Similar loadings can be applied so that the shear stress decreases to conduct experiments in extension (RTE, CTE, and TE). In the simple shear (SS) test, the stresses are applied such that the mean pressure is kept constant. In a proportional loading (PL) test, the loading of the specimen is conducted while maintaining a constant ratio between  $\sigma_1$ ,  $\sigma_2$  and  $\sigma_3$  to give a particular loading path.

The stress reported from experiments involving deviatoric loads can either be the true stress or the total stress (conjugate stress to strain based on the original dimensions). The total stress may be provided when some deformation measurements are not recorded. On cylindrical specimens, if the lateral deformations are not recorded during an unconfined compression test, the load applied to the specimen may be divided by the original cross-sectional area to give the total stress for the material response. In tests where pressure (a true stress) is applied to the specimen, the lateral deformations are generally recorded and the axial stress is calculated based on the current dimensions of the specimen to give a true stress. Throughout this chapter, stresses are assumed to be the true stresses based on the current dimensions of the specimen and strains are the engineering strains based on the original dimensions. The use of engineering strain allows the material response to be presented as a function of the total strain of the specimen.

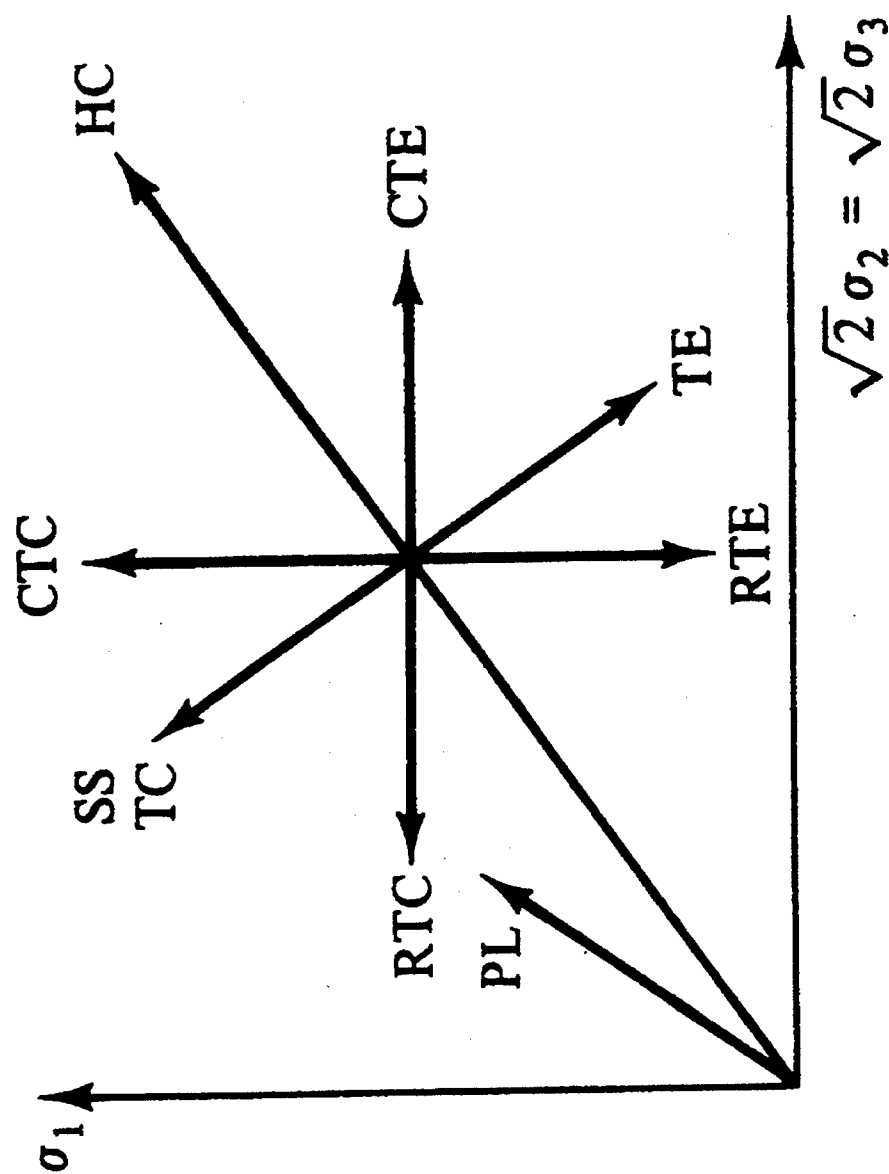


Figure 3.11. Stress paths in the triaxial plane for typical mechanical property experiments (after Desai and Siriwardane 1984).

The amount of data on the response of brittle geomaterials to the pressures experienced during projectile penetration (see Figures 3.3 through 3.5) is very limited and most of the available data is in compression. The majority of these tests are conducted as conventional triaxial compression because they provide a straightforward determination of the elastic constants (shear modulus  $G$ , Young's modulus  $E$ , and Poisson's ratio  $\nu$ ) and they are easy to perform.

### 3.3.1 Compression

Chen (1982) gives a description for the typical response of a concrete to uniaxial compression. A typical stress-strain curve for CSPC concrete in uniaxial compression is shown in Figure 3.12. The response is nearly linear elastic initially since the cracks and voids existing in the specimen are nearly unchanged. Between a stress of about 30 percent and 75 to 90 percent of the maximum compressive strength the response curves gradually increase in curvature. Above this region the response curves bend sharply and the specimen approaches its peak strength. Bond cracks caused by tensile stress concentrations between binder and aggregate (van Vliet and van Mier 1996) start to extend at stresses between 30 to 50 percent of the peak. The crack propagation is stable in that the crack lengths quickly reach their final values if the applied stress is kept constant. At stresses between 50 to 75 percent of the peak some cracks begin to bridge into the binder while some bond cracks continue to grow. Above about 75 to 90 percent of the peak stress, the largest cracks reach their critical lengths and the available internal energy of the system is greater than the required crack-release energy, or the energy required to propagate a crack. The system is unstable and complete failure can occur even if the load is kept constant. In Figure 3.12 at this point the lateral deformation is expanding more rapidly than the axial compression and the specimen begins to dilate. A posttest description of the test specimen describes a diagonal shear across the specimen from top to bottom.

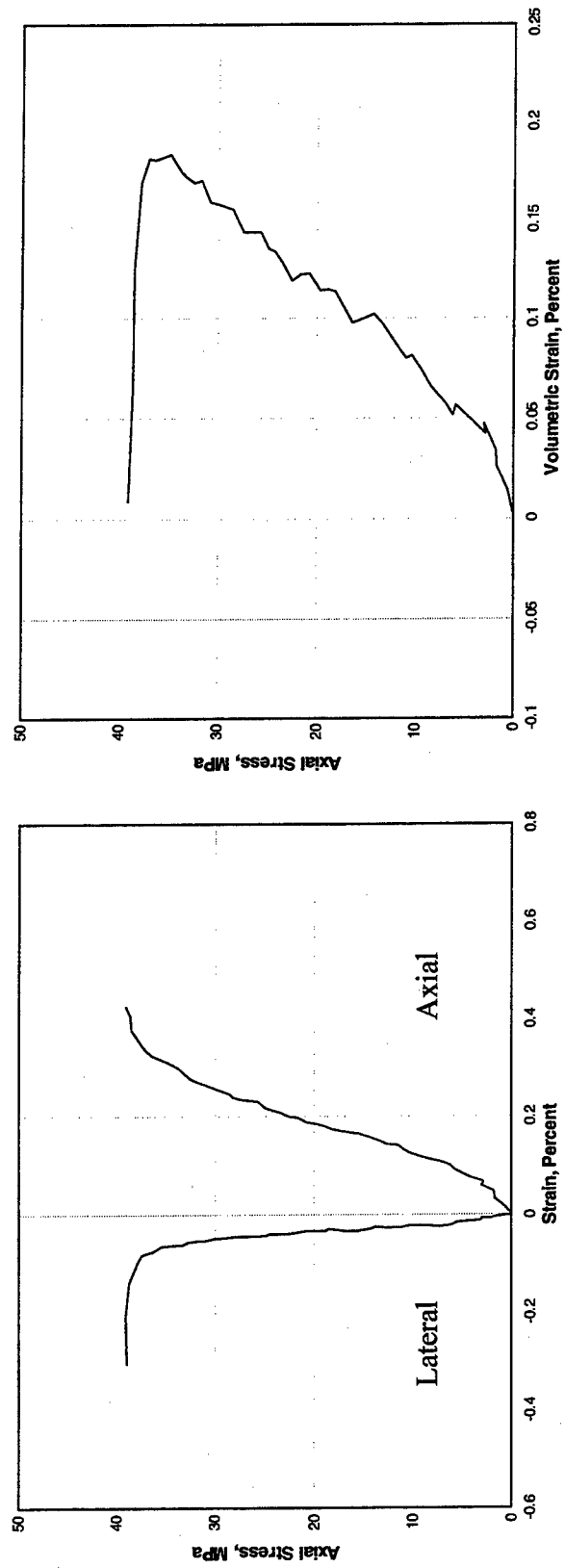


Figure 3.12. Results from a uniaxial compression test on CSPC concrete.

The softening, or descending, portion of the stress-strain curve is greatly influenced by specimen size and boundary conditions. Softening occurs when the microcracks that began forming during the pre-peak portion of the experiment coalesce to form a damage zone that greatly weakens the specimen (Jansen and Shah, 1995). Since localization occurs within the damage zone, the post-peak portion of the stress-strain curve is a material property, but dependent on the specimen length over which the deformation is measured. Van Vleet and van Mier (1996) conclude that softening is a combined material and structural property. If the length is confined to the area of the localization, the effect of specimen length-to-diameter ratio on the post-peak energy is removed for ratios between 2.0 to 5.5. Results from the experiments by Jansen and Shah showed that the fracture zone is 200 mm or more long for 100 mm diameter specimens. Figure 3.13 shows the stress-strain behavior for different length-to-diameter ratio specimens for a normal concrete with an average UC strength of about 48 MPa. The ascending portion of the curves are the same for all ratios. The descending portion of the curve is steeper for the high ratio specimens since the strain is based on the original length of the specimen, but the deformation is occurring within the 200 mm long damage zone. During softening, the cracks and shear bands will grow to a size comparable to the characteristic dimension of the specimen (van Vleet and van Mier, 1996).

Experiments by van Vleet and van Mier (1996) also showed that a specimen length at least twice the lateral dimension is required to avoid size effects in peak strength with high friction end restraints, and that the post-peak deformation is independent of size for ratios from 0.5 to 2.0. A length to width ratio of at least 2.0 should be used to avoid influencing the pre-peak and ultimate strength of the material. Strain calculated in the softening branch of the response should be based on the characteristic length for the specimen, which ideally is the same as the specimen height. In order to capture the pre-peak and post-peak response and the peak strength, a length to lateral dimension of two should be used for conventional concrete.

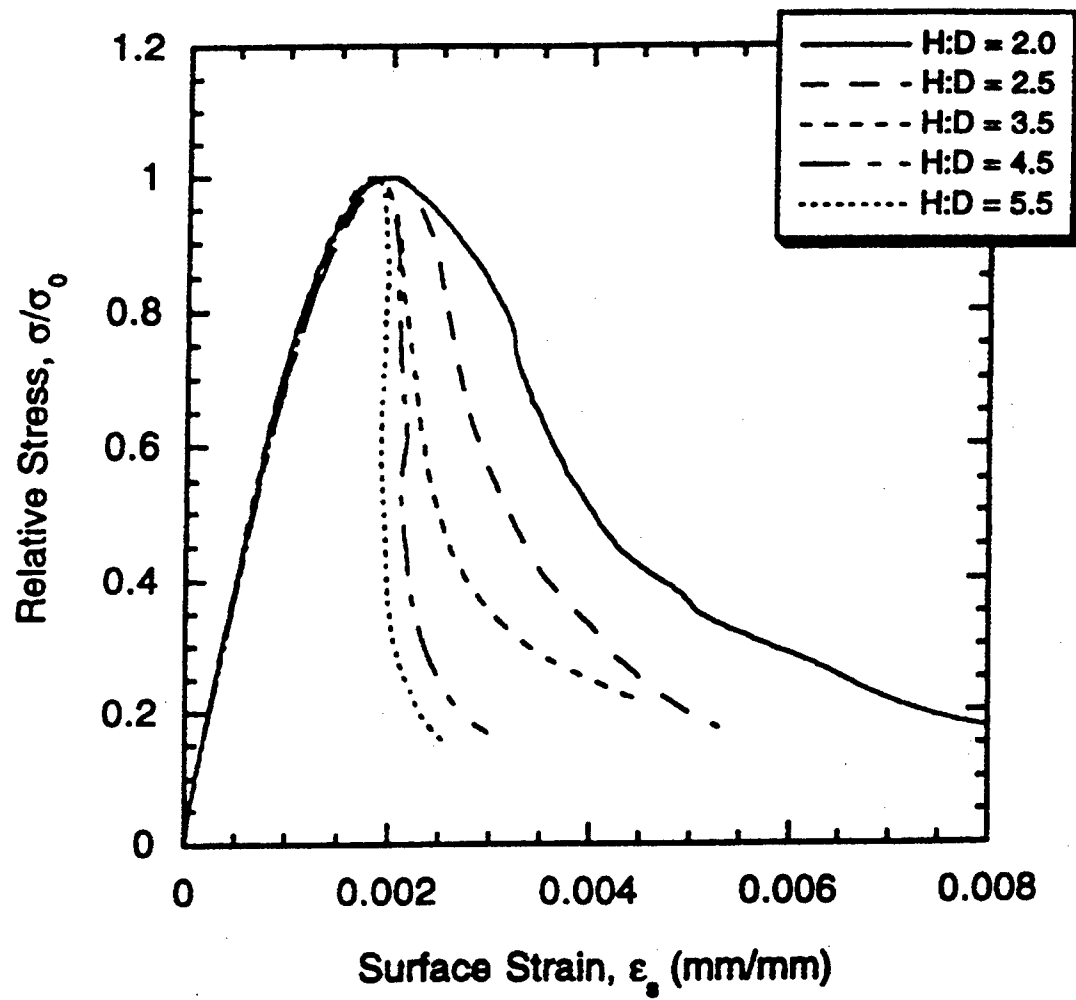


Figure 3.13. Typical stress-strain behaviors for range of height-to-diameter ratio (Jansen and Shah 1995).

Additional experimental results by Lee and Willam (1995) further illustrate the effects of specimen size. They conducted uniaxial compression experiments on cylindrical concrete specimens with aspect ratios of 1.8, 1.2, and 0.6 under deformation control. The ultimate strength of the 1.8 and 1.2 aspect ratio specimens was the same and the strength of the 0.6 aspect ratio specimen was about 30 percent greater. They measured both axial and radial deformation and note that the initial Poisson's ratio of 0.18 in the prepeak region increased to about 12 (based on deformation) in the post-peak regions. This "fictitious Poisson's effect" was the same for all specimen heights and was constant in the post-peak regime. The post-peak response is the result of localized splitting that initiates at the peak strength, and the energy dissipation is the combined effect of axial splitting and shear dissipation. The characteristic length for the test specimens was estimated to be 0.095  $h$  based on fracture energies for mode I and mode II type failures and 0.27  $h$  to 0.44  $h$  based on analytic solutions of fracture mechanics, where  $h$  is the specimen height.

Similar observations have been made for rock (Bruno and Nelson, 1991; Desai, et al, 1990; Sulem and Vardoulakis, C&D). Large rock masses contain faults, joints, and changes in lithology across bedding planes that separate the different strata. Individual specimens of rock are a complex assembly of crystals, grains, smaller matrix materials, cementing material, and porespace (Bruno and Nelson, 1991). The observed inelastic deformations in material property experiments are the result of microstructural damage and fracturing and are similar to the results from experiments on concrete.

### 3.3.2 Tension

The tensile response of a material generally provides the basic input for fracture mechanics models (Hordijk, et.al. 1989). Like in compression, the crack evolution cannot be obtained directly, but must be derived from the complete stress-displacement relation. The ultimate tensile strength is determined by the strength and stiffness of the



particles and the cementing material and the bond strength between the two. In cases when the particles and cement are similar in strength, the crack paths pass through the aggregate particles. This results in a more brittle response than if the crack path is more tortuous and must travel around particles instead of through them.

Rossi, et al (1994) present results from direct tensile experiments on cylindrical specimens of concrete with different diameters but all with a height-to-diameter ratio of two. They note a size effect in that the strength for the smaller specimens is higher than that for the larger specimens. Specimens of the same size also exhibited a Young's modulus that was equal to the modulus in compression. The scale effect is hypothesized to be a function of the specimen volume and the total volume of the coarsest aggregate. The basis is that the weakest link in the material is the cement paste that contains faults such as bubbles, microcracks, initial stresses, etc., so that crack initiation begins in the paste.

Results from a direct pull tension experiment on a concrete specimen with height/diameter ratio of about 2 are shown in Figure 3.14. The experiment was conducted under load control therefore the catastrophic failure of the specimen resulted in no post-peak data. In uniaxial tension, bond microcracks begin to grow in concrete at stresses above about 60 percent of the ultimate tensile strength. The onset of unstable crack propagation occurs at about 75 percent of the ultimate strength and the stress-strain response becomes more concave. The crack direction is generally perpendicular to the direction of loading. The ultimate strength of concrete in uniaxial tension is about 5 to 10 percent of the strength in compression (Chen, 1982).

### 3.3.3 Effect of Confinement

Confinement has a significant effect on the response of brittle geomaterials to deviatoric loads. Figure 3.15 schematically shows the gross effect of confinement on

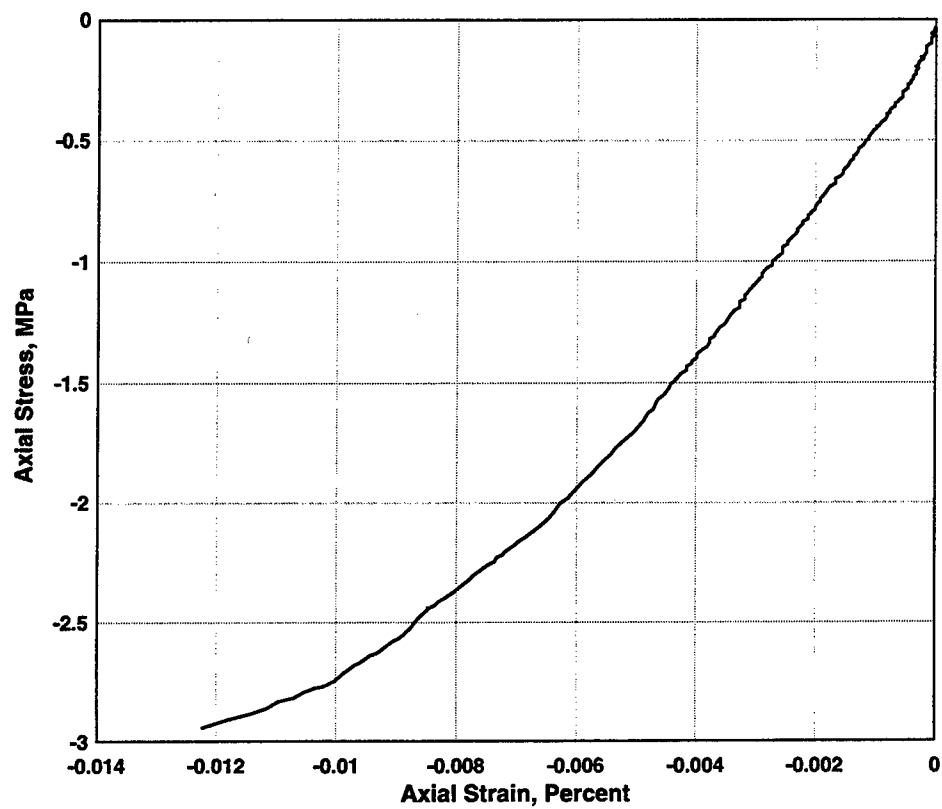


Figure 3.14. Results from a direct pull tension experiment on a concrete specimen.

material response in compression. As discussed above, at low confining pressures these materials behave in a brittle manner where the propagation of unstable cracks leads to their coalescence and the eventual formation of failure planes (Ladanyi and Aubertin, 1990; Lubada, et.al., 1996; Ashby and Hallam, 1986). The failure plane formation is illustrated by dilation in the overall response of the material. As confining pressure increases, the material response to shear loading transitions through a brittle to ductile regime where dislocation motion and fracture propagation processes interact and the formation of a shear band and strain softening are suppressed. Microcracks still occur and produce dilation, but ductile processes at the crystalline scale are also influencing the material response (Ladanyi and Aubertin, 1990). Increasing confining pressure results in increasing strength. At high confining pressures deformation occurs at the intercrystalline level resulting in a ductile response. The effect of confining pressure on the TC response of concrete specimens is shown in Figure 3.16. As confining pressure increases, the response transitions from a brittle response at low confining pressure to a ductile response at high confining pressure. Posttest descriptions of the test specimens are similar to those in Figure 3.15.b and c.

As discussed in Section 3.2 and illustrated in Figure 3.9, as pressure is applied to brittle cemented geomaterials it is hypothesized that the material is altered through the creation and propagation of dislocations, rearrangement of particle orientation, and compaction. To test this hypothesis, TC experiments were conducted on concrete specimens at two different confining pressures where some of the specimens were hydrostatically pre-stressed prior to the TC experiment. Results from TC experiments at confining pressures of 25 and 100 MPa are shown in Figures 3.17 and 3.18, respectively. For the 25 MPa experiments, one pre-stress was conducted to 100 MPa, or at about the knee of the HC pressure-volume response where breakdown and cracking in the matrix is beginning, and one pre-stress was conducted to 400 MPa, or at a level of pressure where the material has undergone significant changes. The shear response of the specimen pre-stressed to 100 MPa is similar to the response of the specimen with no pre-stress, but

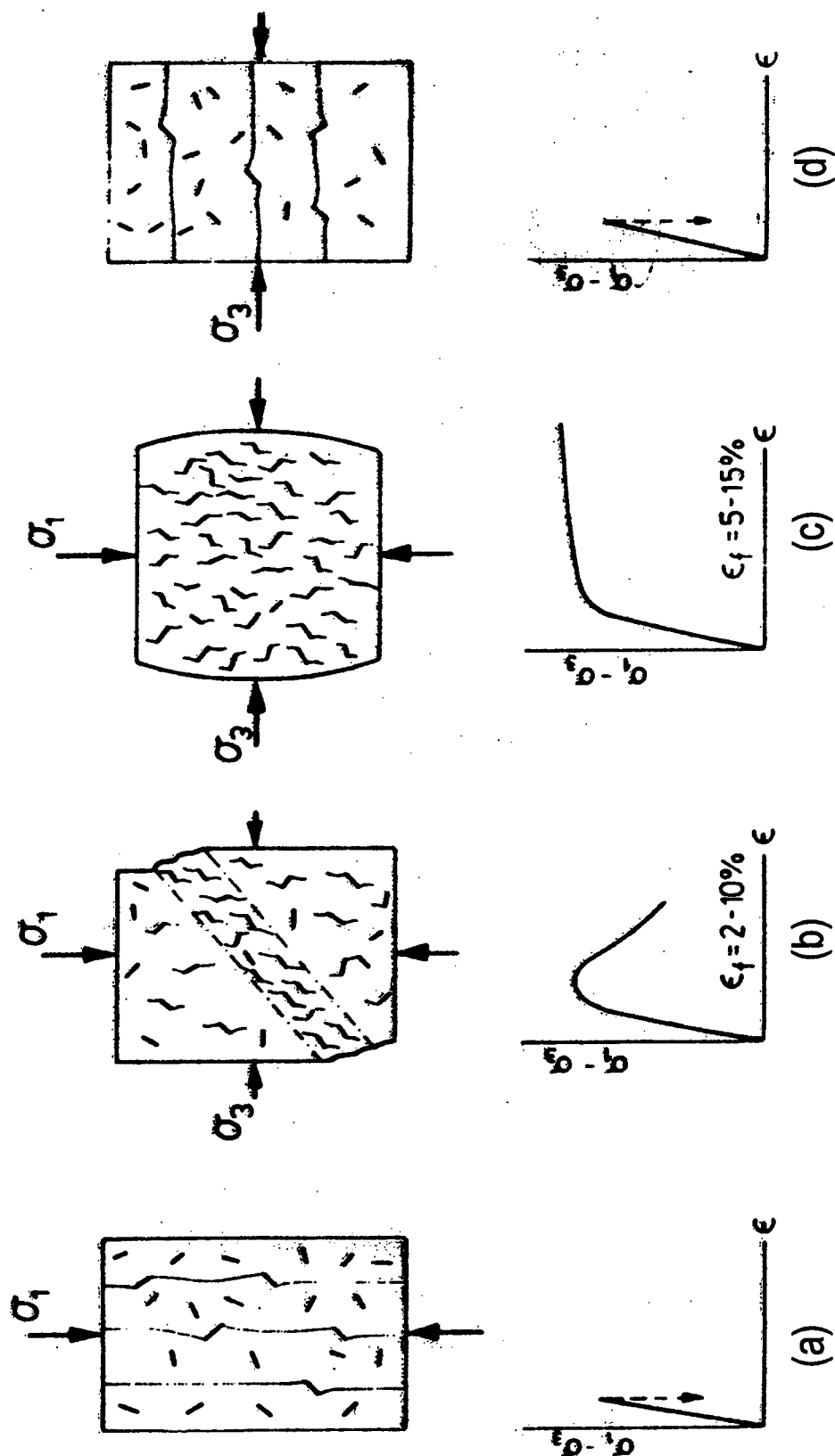


Figure 3.15. Failure modes in compression, (a) and (d) slabbing, when one or a few cracks propagate parallel to the principal compression, (b) failure by aggregation of cracks to form a shear zone, (c) near-homogeneous deformation by distribution microcracking (Ashby and Hallam 1986).

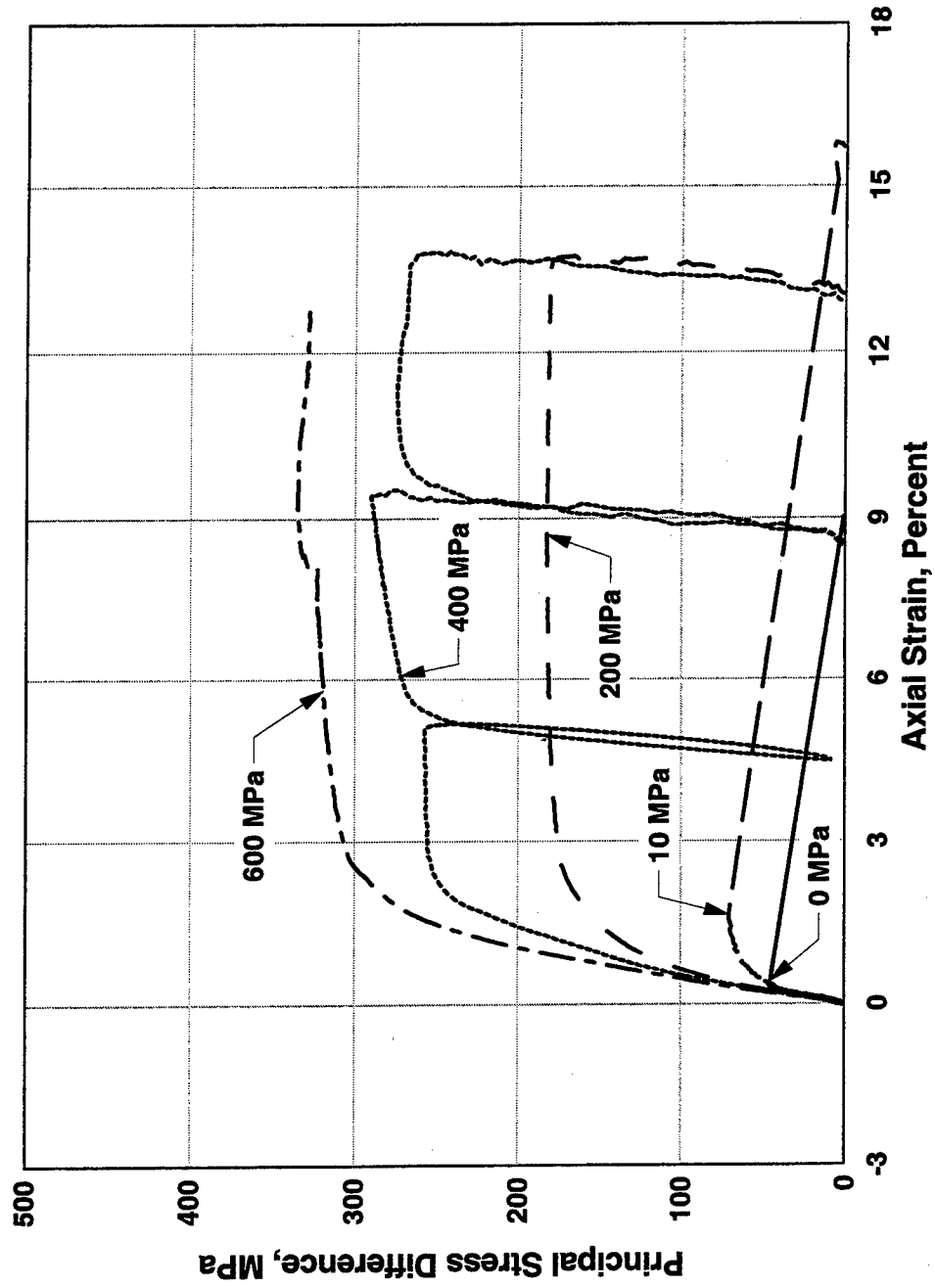


Figure 3.16. Effect of confining pressure on results from TC tests on concrete specimens.

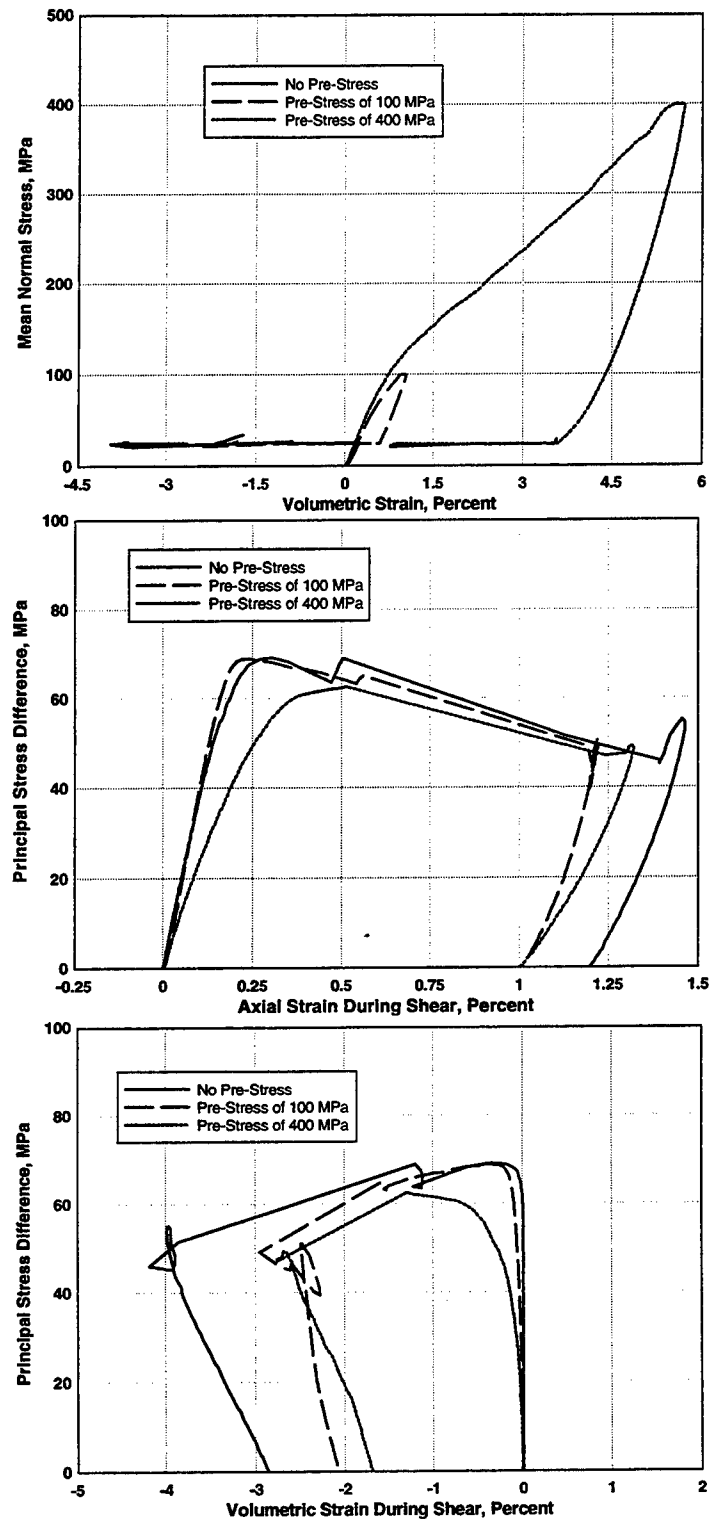


Figure 3.17. Results from TC experiments at 25 MPa after pre-stresses of 0, 100, and 400 MPa.

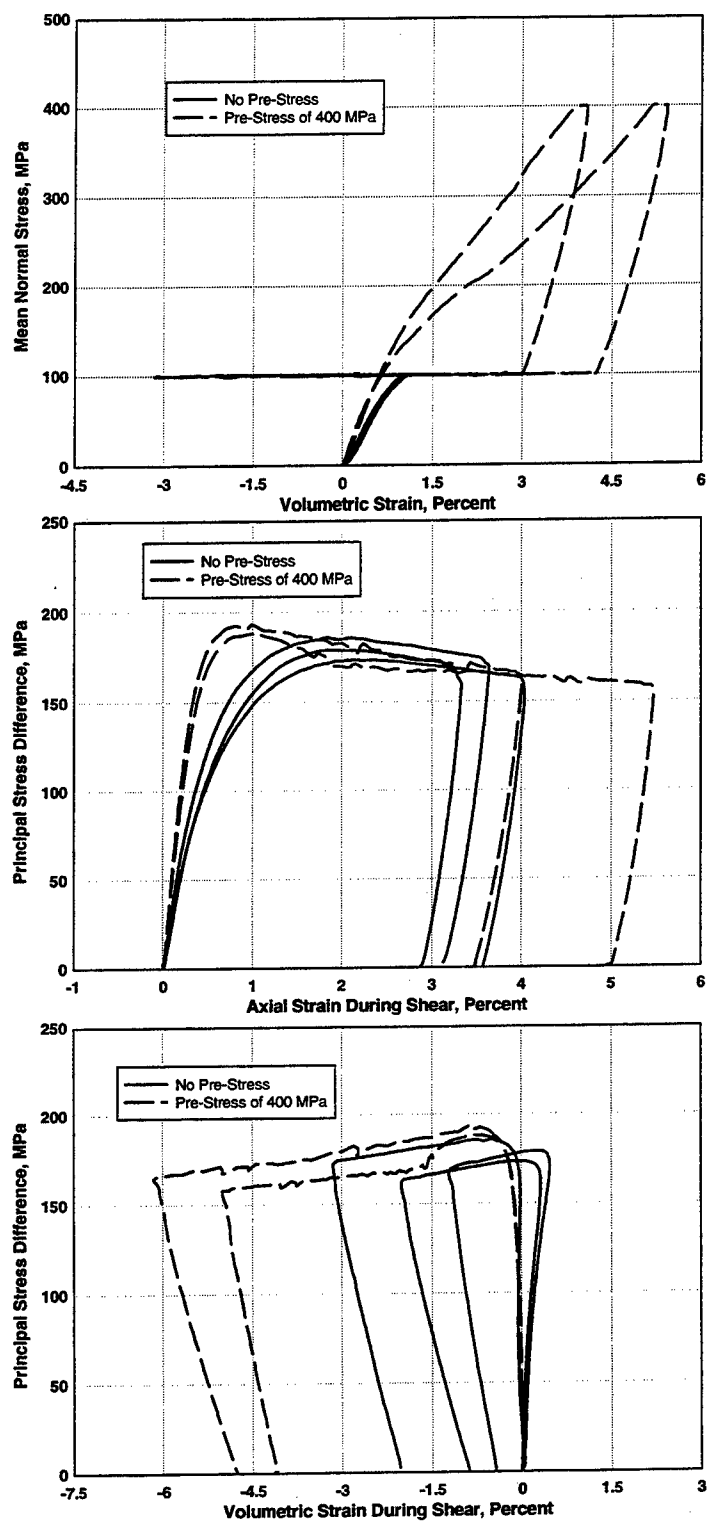


Figure 3.18. Results from TC experiments at 100 MPa after pre-stresses of 0 and 400 MPa.

does show a tendency toward dilation earlier in the shear loading. The shear response of the specimen pre-stressed to 400 MPa is much softer than the specimen with no pre-stress, has a strength slightly lower, and shows significant dilation during shear that begins almost as soon as the shear loading is applied. The appearance of the specimens after the TC experiment was similar for all pre-stresses. For the 100 MPa experiments (Figure 3.18), a pre-stress to 400 MPa was applied to two specimens. The shear response of the pre-stressed specimens is stiffer than the specimens with no pre-stress and has an ultimate strength that is slightly higher. The pre-stressed specimens begin to dilate soon after the shear loading is applied. Test specimens that had been pre-stressed to 400 MPa exhibited slightly more bulging near the midheight and a more visible shear plane after the TC experiment.

### 3.3.4 Effect of Strain Rate

The dynamic response of the target materials is of interest since the stress field within the target during the penetration process is being applied over a period of only a few milliseconds. Conventional testing equipment using pressure chambers and loading rams can be used to test materials at strain rates to about 10 /s. These devices typically use fast opening valves or explosives to drive rams that apply the stresses to the test specimen. Measurements are made using mechanical based systems such as strain gages, linear variable differential transformers (LVDTs), coiled wire pressure gages, etc. Drop hammers and anvils can also be used to conduct experiments to strain rates of about 10 /s. Above this rate of loading wave propagation effects between the specimen and test device must be taken into account (Sierakowski 1984). Pressure bars such as the split Hopkinson bar have been used to obtain data at strain rates up to about  $10^3$  /s. Data from the experiments must be analyzed using wave propagation theories in order to deduce the stress and strain within the test specimen. Another wave propagation experiment that can provide data at strain rates greater than  $10^3$  /s is the flyer plate test.



The test methods have been applied by many researchers to investigate the dynamic response of brittle geomaterials to compressive and tensile states of stress. Results from dynamic compression experiments conducted by several researchers were summarized by Bischoff and Perry (1986). The ratio of dynamic to static compressive strength is shown versus the log of strain rate in Figure 3.19. Quasi-static loading is generally taken to be about  $10^{-5}$  to  $10^{-6}$  /s. The data show a gradual increase in strength to a strain rate between  $10^{-1}$  and 1 /s, where the dynamic strength begins to increase rapidly as the strain rate increases to a ratio of almost 2 at a rate of  $10^2$  /s. Hughes, et.al. (1993) show the effects of strain rate on the tensile strength of concrete in Figure 3.20. Comparison of Figures 3.19 and 3.20 indicates that the increase in strength with strain rate is more dramatic in tension than in compression.

Confinement of the test specimen has been shown to influence the increase in strength as strain rate increases (Gran, et. al. 1989). Results by Gran, et. al. (1989) in Figure 3.21.a for a concrete with static unconfined compressive strength of about 100 MPa indicate that the ratio between the static and dynamic strength (1.3 to 1.4) is nearly constant as pressure increases for dynamic strain rates of about 1.3 /s to 5 /s. Results by Yamaguchi, et. al. (1989) in Figure 3.21.b for a concrete with unconfined compressive strength of about 20 MPa indicate that the dynamic strength increases gradually from the static strength as pressure increases for strain rates of 0.254 /s and lower. Results from static and dynamic triaxial compression experiments conducted at WES on CSPC concrete are shown in Figure 3.22 where strain rate (approximately 0.1 /s) is the axial strain at peak stress divided by the time to peak, all adjusted to the start of the shear phase of the experiment. The data show the ratio between dynamic and static strength decreasing slightly as the confining pressure increases, but, at this dynamic strain rate, the data are within the scatter of the data in Figure 3.19.

Loading rate also affects the shape of the stress-strain response of brittle geomaterials. Figure 3.23 shows the effect of strain rate on the unconfined compression

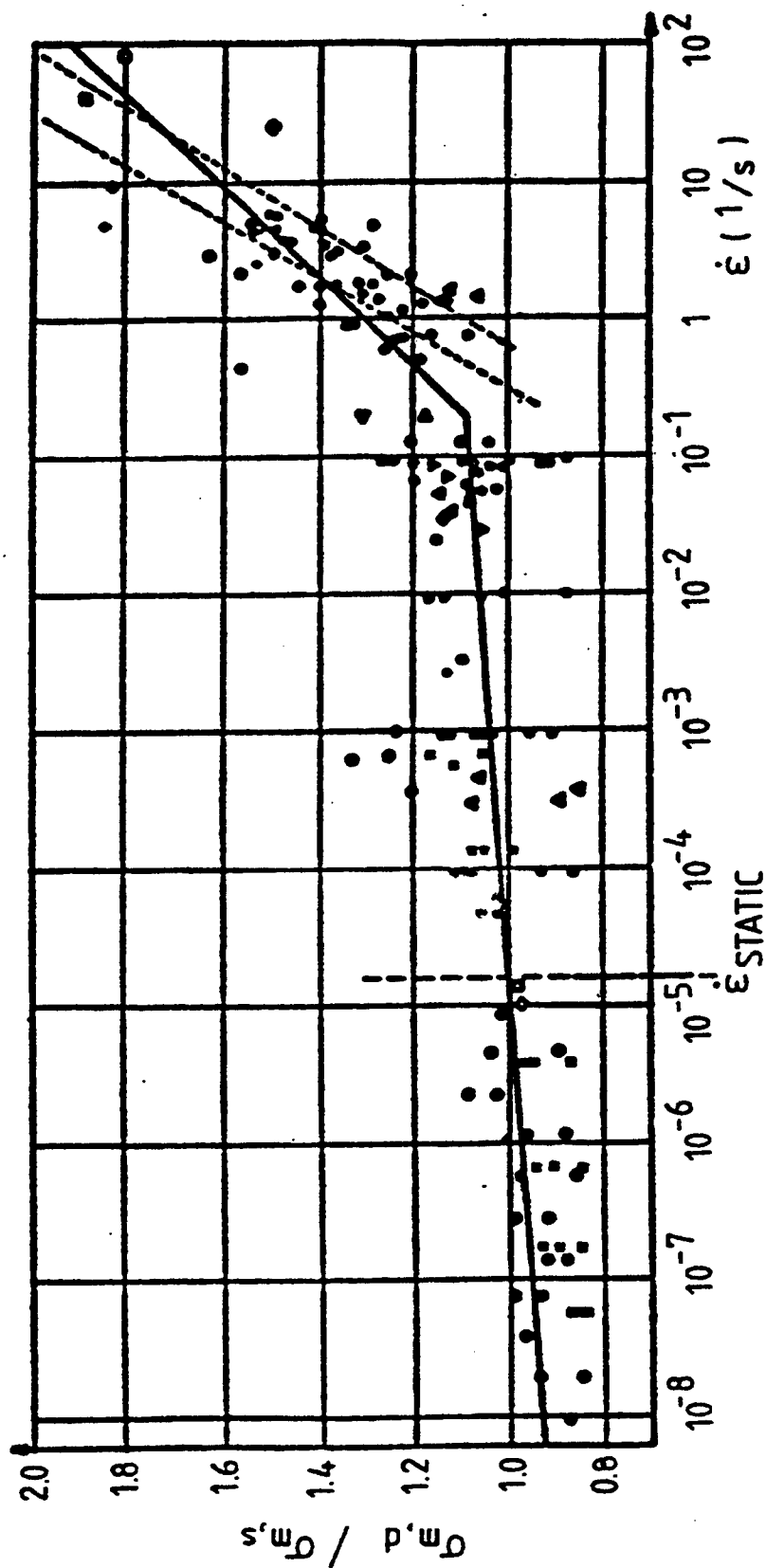


Figure 3.19. Compression strength of concrete at different strain rates (Bischoff and Perry 1986).

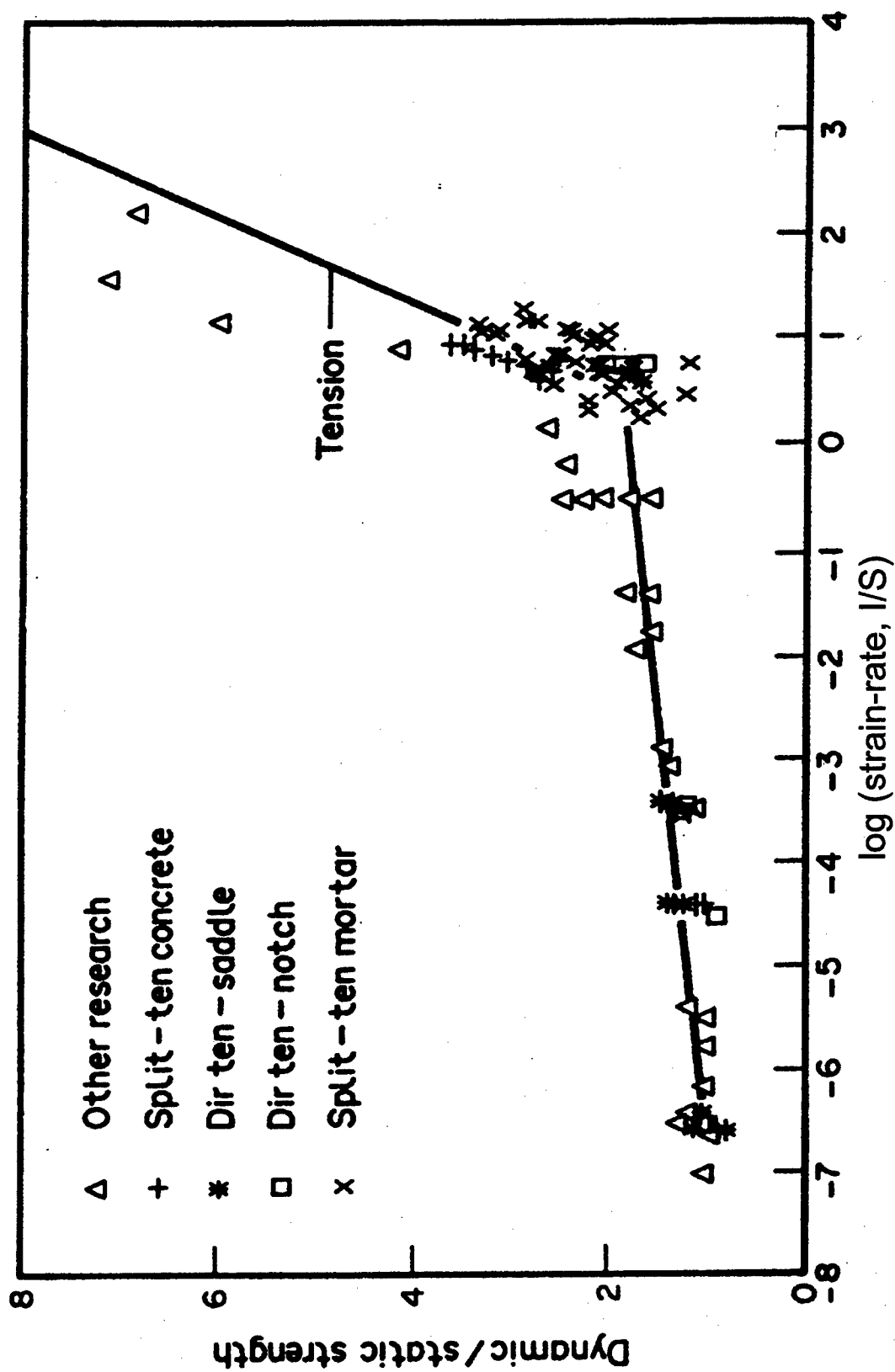
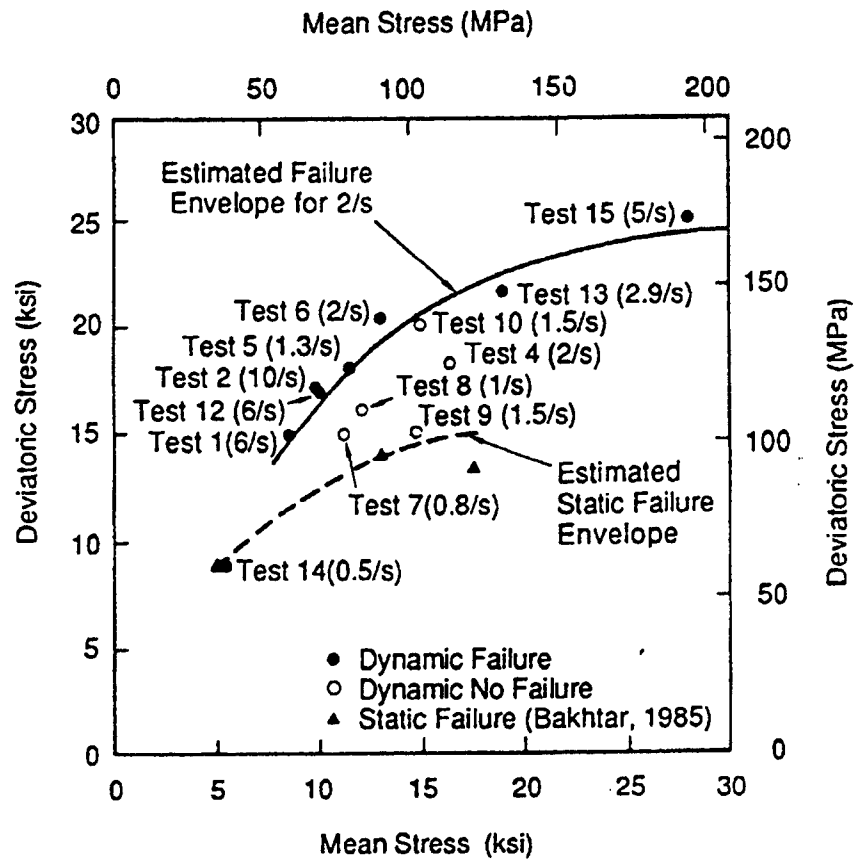
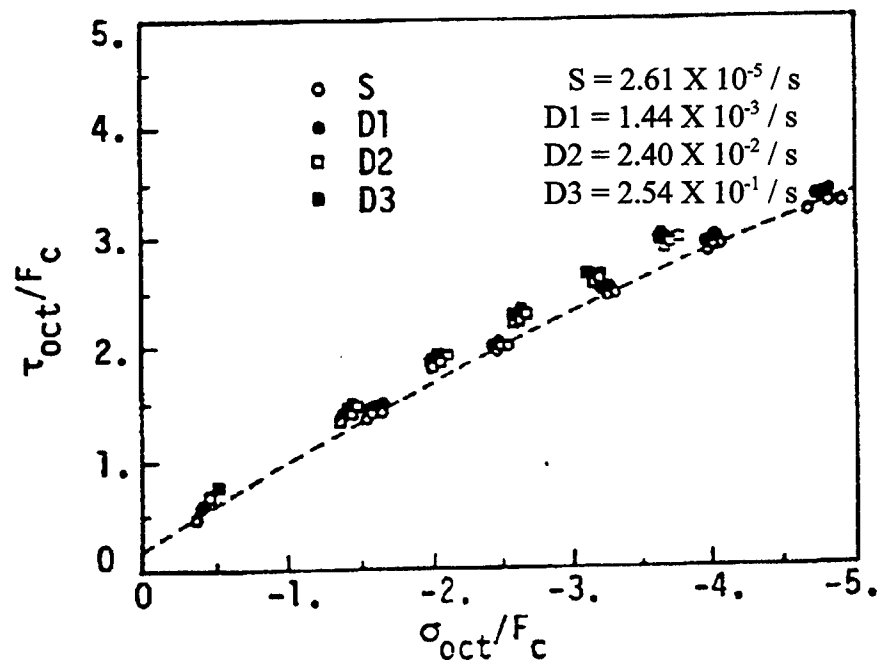


Figure 3.20. Strain rate effects on concrete tensile strength (Hughes, et. al 1993).



a. Gran, et. al. 1989



b. Yamaguchi, et. al. 1989

Figure 3.21. Effect of pressure on dynamic strength of concrete.

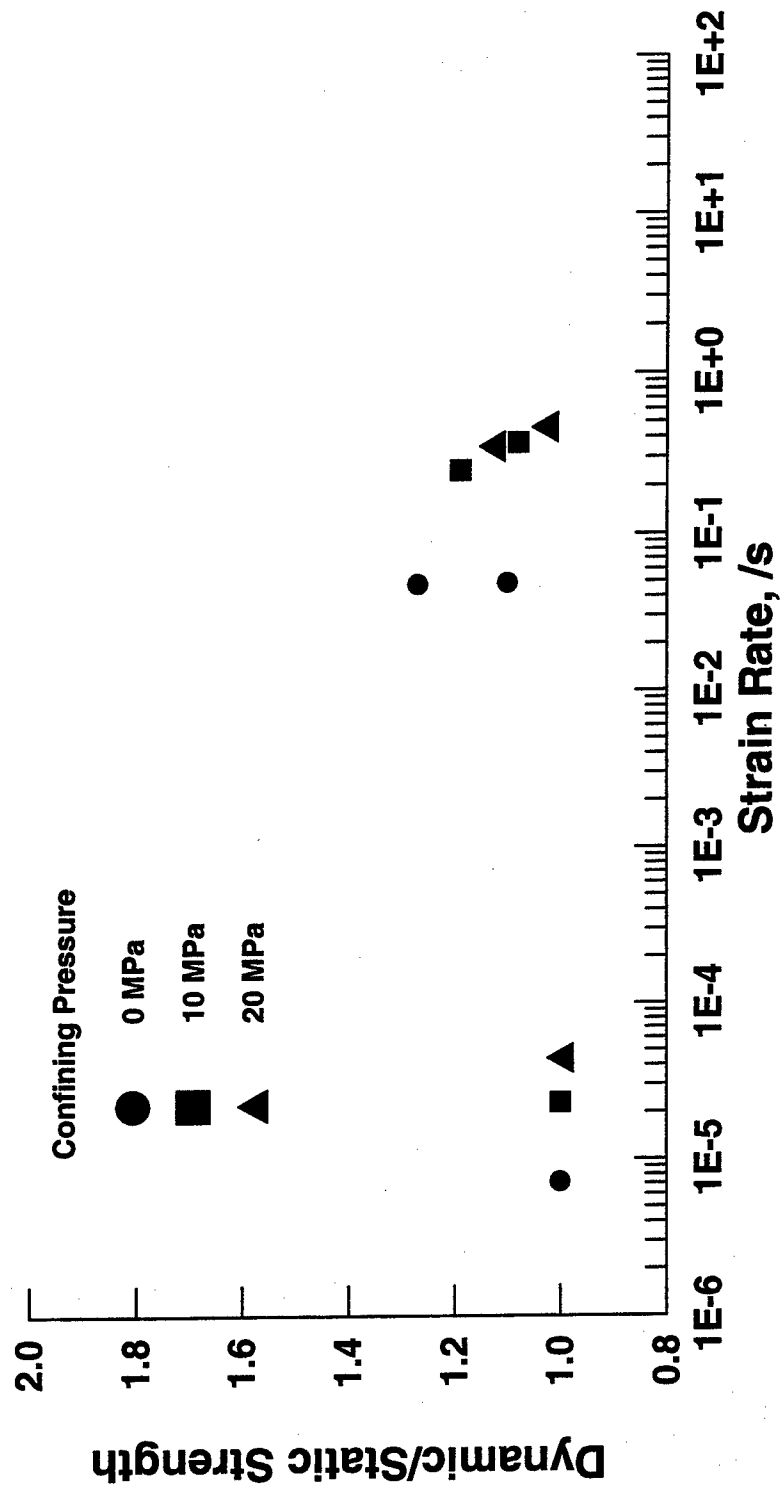
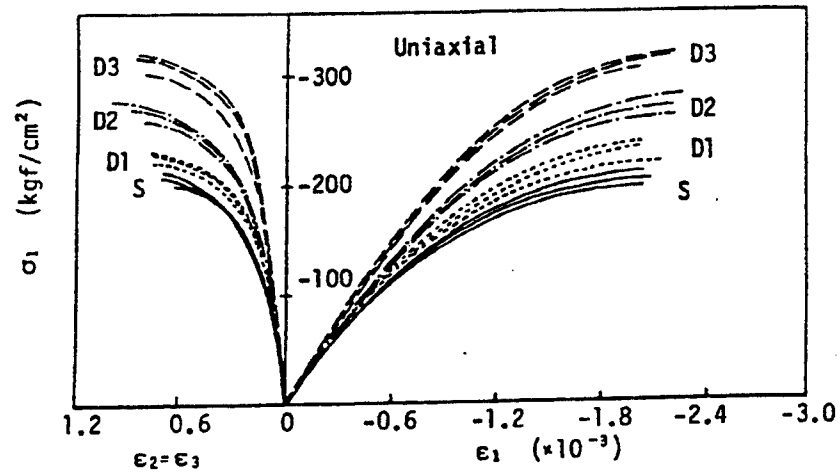


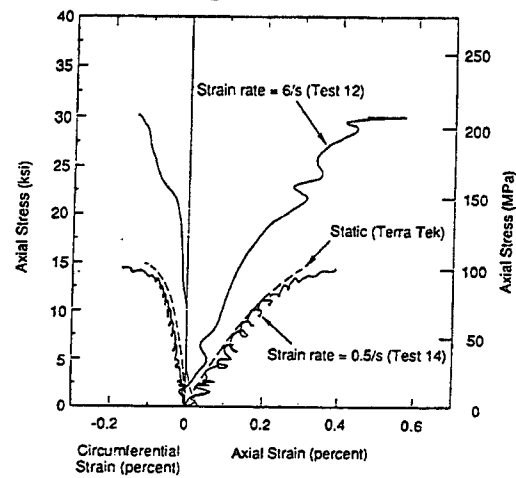
Figure 3.22. Effect of pressure on the dynamic strength of CSPC concrete.

stress-strain response of three concretes. Figure 3.24 shows the effect of strain rate on the stress-strain response of CSPC concrete at confining pressures of about 0, 10, and 20 MPa. The pre-peak portion of the dynamic responses are generally stiffer than the static response, but the post-peak softening response tends to become softer (more gradual) as the strain rate increases. The strain at peak strength does not change significantly as the strain rate increases. Similar observations can be made for the tensile response of concrete (Figure 3.25).

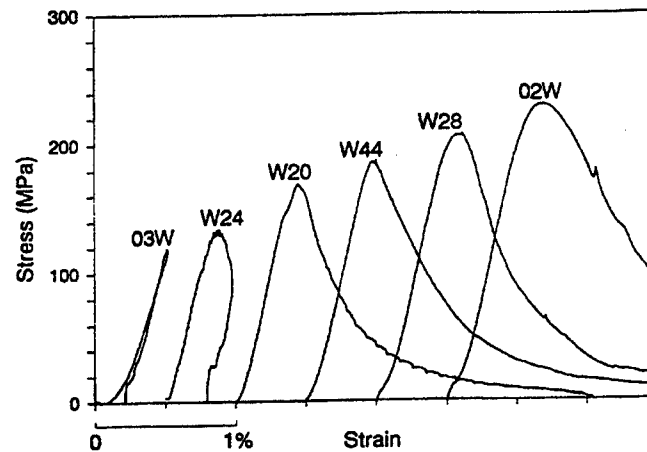
It has been suggested that the enhanced performance of brittle geomaterials during dynamic loading is due to lateral inertial confinement of the interior of the specimen. Tang, et. al. (1992) conducted analyses that showed the magnitude of this confinement is only about 0.1 to 0.2 percent of the applied axial stress and could not account for the significant strength increase. The development of internal microcracks is responsible for the increasing non-linearity of brittle geomaterials when loaded quasi-statically. The resistance of these cracks to propagate during increased loading rate is believed to be the cause of the increased strength (Bischoff and Perry 1986). During high loading rates the internal cracks do not have time to follow the path of least resistance and are forced to propagate along paths that go through aggregate and paste that would normally be avoided. Higher strength concretes do not show as significant an increase in strength as loading rate increases since cracks are often forced to propagate through aggregate even during quasi-static loading. As shown in Figures 3.19 and 3.20, a wide scatter exists in the data. The discrepancies are caused by several factors including the inherent heterogeneity of concrete, the concrete mix proportions, aggregate type, curing conditions, age at testing, specimen geometry, and boundary conditions during the experiment (Fu, et. al. 1990). Many of these same observations can also be applied to other brittle geomaterials such as rock.



a. Yamaguchi, et. al. 1989

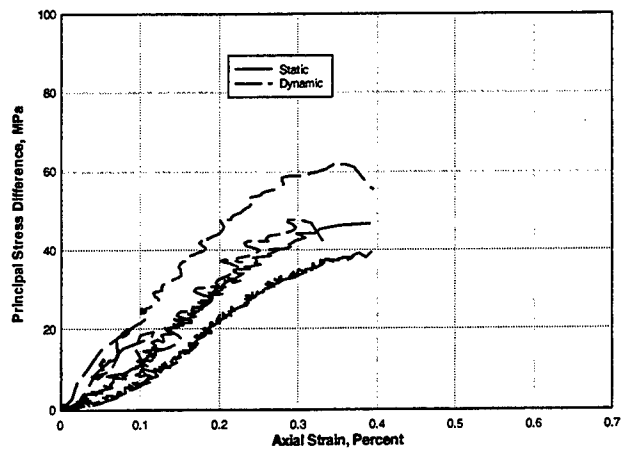


b. Gran, et. al. 1989

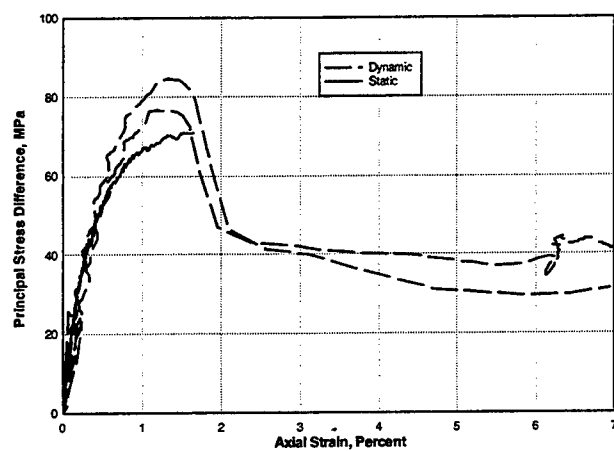


c. Tang, et. al. 1992

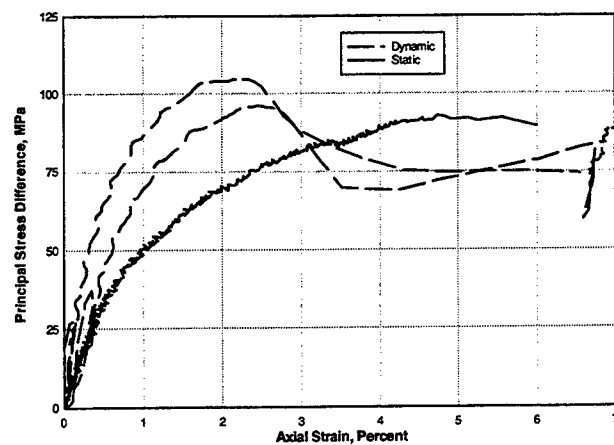
Figure 3.23. Effect of strain rate on the unconfined compression stress-strain response of concrete.



a. No confining pressure



b. 10 MPa confining pressure



c. 20 MPa confining pressure

Figure 3.24. Effect of confining pressure on the static and dynamic stress-strain response of CSPC concrete.



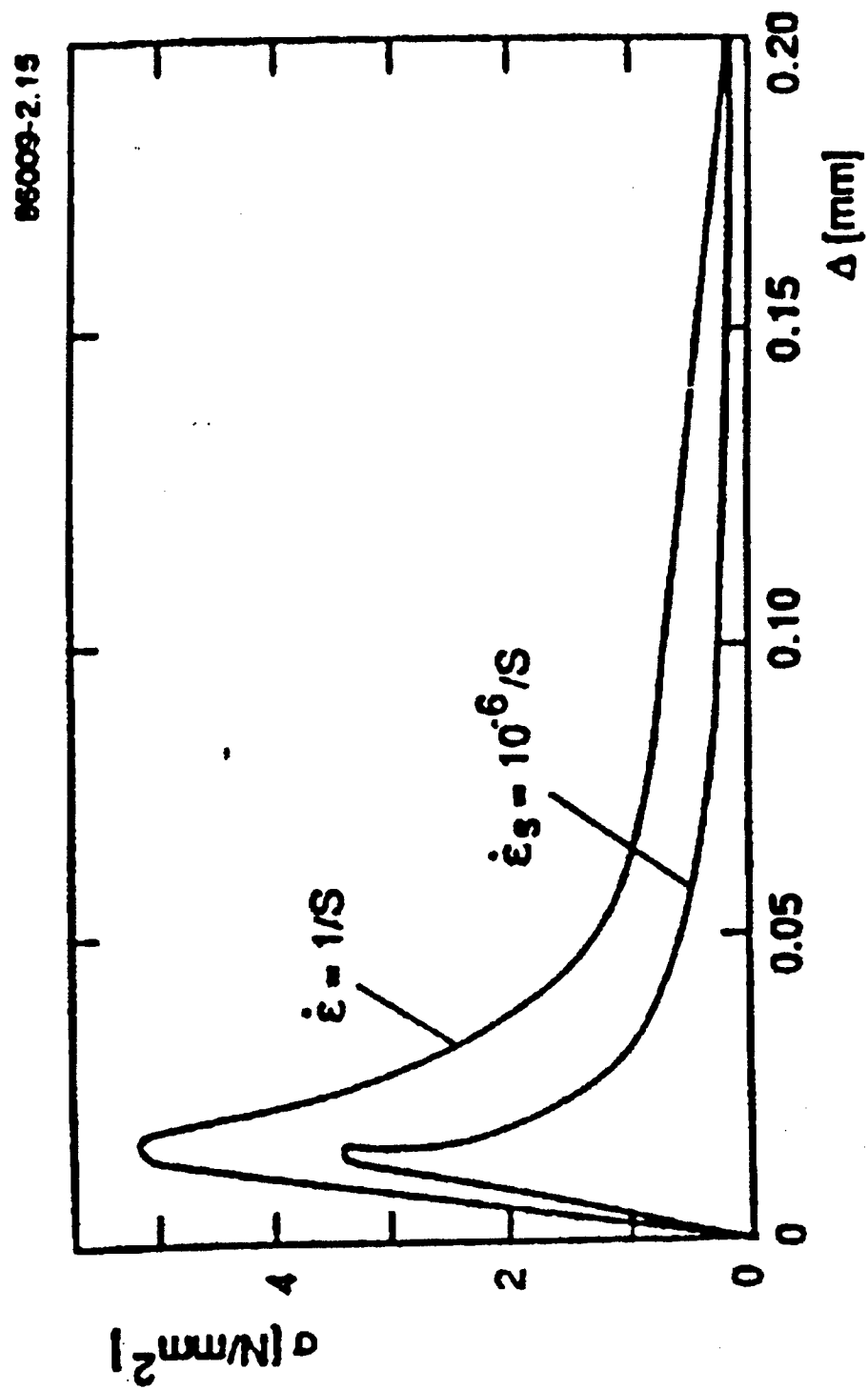


Figure 3.25. Rate effect on load-deformation curve in tension (Kormeling, et. al. 1987 in Weerheijm, et. al. 1993).

## CHAPTER 4

### NONLINEAR, INELASTIC FRACTURE MODEL

#### 4.1 MODELING OF BRITTLE GEOMATERIALS

Two procedures are generally employed to formulate constitutive theories for the nonlinear stress-strain response of materials (Rohani and Thompson 1970). One procedure seeks to find a physical phenomena that is the outcome of a framework of elaborate mathematics. Although the mathematics is complete, it may be difficult to find actual materials whose response is simulated by the predicted stress-strain curves. The other procedure, often referred to as the physical approach, seeks to find the appropriate mathematical forms needed to model the observed physical behavior of actual materials. The essential material responses are incorporated into the theory at the beginning. One pleasing feature of this approach is that new criteria or mathematical forms can be incorporated into the theory as appropriate. Since no one approach or theory can be expected to describe the response of a material under all conditions, the approach taken may come down to the preferences of the model developer. Also, the desirable features of both approaches might be used in the model development.

Desai and Siriwardane (1984) provide seven axioms that the constitutive model must obey. The axiom of determinism states that current state of stress and strain due to an external force is dependent on the history of forces that have been experienced. The axiom of causality states that a material response cannot occur without a cause. The axiom of objectivity states that the material properties cannot vary with the motion of the observer. The axiom of neighborhood states that the response at a point is not affected by conditions that are far away. The axiom of memory states that the constitutive variables

are not affected by the values of the constitutive variables in the distant past. The axiom of equipresence states that the variables identified for a material should be present in all of the constitutive equations for that material. The axiom of admissibility states that the constitutive equations must be consistent with the physical laws, such as continuity, motion, momentum, entropy, etc. Since a constitutive model is intended to relate a physical response to applied loads, the model must obey the above axioms that govern the response.

The various approaches used to model geomaterials can be found in several texts (Chen 1982, Chen and Saleeb 1982, Desai and Siriwardane 1984, Chen and Baladi 1985). The approaches include linear and nonlinear elasticity with and without failure criteria and with and without fracture, hypoelasticity, hyperelasticity, and plasticity with and without fracture, as well as endochronic, viscoelastic, and viscoplastic methods. The linear elastic models are widely used in practice because they are relatively easy to use and understand and the model constants are usually easy to obtain. The stress-strain relationships for most geomaterials however can be better modeled by using nonlinear elasticity equations. The elastic methods work well when the loading is monotonic and well below failure. If the effects of unloading and reloading are significant then a separate criteria for these conditions may be included. The plasticity based methods use yield surfaces and flow criteria to determine the material response incrementally. They can range from the simple elastic-perfectly plastic model to complicated with multiple response surfaces and flow criteria.

In recent years, efforts to use fracture and damage mechanics methods, both alone and in conjunction with elasticity and plasticity, to describe the response of brittle geomaterials have increased (Elfgren 1989). Fracture mechanics evolved as a result of failures in metal structures built in the 19<sup>th</sup> century through World War II (Ewalds and Wanhill 1984). Investigations revealed that material deficiencies could initiate cracking and fracture at flaws and stress concentrations. Similarly, brittle geomaterials contain

microcracks, pores, voids, and stress concentrations where fractures can initiate. The pre-failure stress-strain behavior is often characterized by models based on the elasticity and plasticity theories of continuum mechanics (Yamaguchi and Chen 1987), but the tensile and compressive failures are primarily due to macroscopic crack propagation (Jenq and Shah 1987) which cannot be explained by using only these theories. Fracture mechanics is concerned almost entirely with the fracture-dominant behavior characterized by highly localized plasticity and essentially macroscopic sized defects (Ewalds and Wanhill 1984).

A damage model is one that contains a specific internal variable that qualifies the state of damage locally and a kinetic equation that defines the evolution of the damage with the applied load or time (Krajcinovic 1984). The internal variable is tracked during loading and used to calculate or trigger the calculation of a damage variable. The damage variable usually varies from zero to one and is applied to the stiffness of the material. The damage variable can be either a scalar for inducing isotropic damage or a vector for inducing anisotropic damage. As the damage is accumulated, the stiffness of the material is softened to effectively induce a strain-softening effect. Individual models can vary on the internal variable that is tracked and how the damage is calculated and applied.

## 4.2 NIF MODEL DEVELOPMENT

A non-linear, inelastic fracture (NIF) model will be developed to capture some of the response characteristics of brittle geomaterials to the severe loading conditions that occur during high-velocity projectile impact. In this sense, the model will be developed following the physical approach to replicate the responses presented in the previous chapter assuming a true stress-total strain representation. The state of stress in the model will be determined uniquely by the current state of strain. The model will be nonlinear and inelastic, include the tensile characteristics of the material, and capture the brittle shear response at low pressures, the ductile shear response at high pressures and the transition between the brittle and ductile behavior.

The behavior of a material is modeled mathematically using constitutive equations. The general form of a constitutive equation under isothermal conditions for the stress tensor as a function of the strain tensor and the deformation-rate tensor may be expressed as (Rohani and Thompson 1970)

$$\sigma_{ij} = f_{ij}(\epsilon_{mn}, d_{rs}) \quad 4.1$$

where  $\epsilon_{mn}$  is the strain tensor and  $d_{rs}$  is the deformation-rate tensor. The response function  $f_{ij}$  must be form invariant with respect to rigid motion of a spatial frame of reference and invariant with respect to coordinate transformations. For a kinematically linear system, the strain rate tensor  $\dot{\epsilon}_{ij}$  is generally assumed to be the same as the deformation-rate tensor. A polynomial of two symmetric second rank tensor variables can represent  $f_{ij}$  in Equation 4.1 resulting in the following equation:

$$\begin{aligned} \sigma_{ij} = & \eta_0 \delta_{ij} + \eta_1 \epsilon_{ij} + \eta_2 \epsilon_{im} \epsilon_{mj} + \eta_3 \dot{\epsilon}_{ij} + \eta_4 \dot{\epsilon}_{im} \dot{\epsilon}_{mj} \\ & + \eta_5 (\epsilon_{im} \dot{\epsilon}_{mj} + \dot{\epsilon}_{im} \epsilon_{mj}) + \eta_6 (\epsilon_{im} \epsilon_{mn} \dot{\epsilon}_{nj} + \dot{\epsilon}_{im} \epsilon_{mn} \epsilon_{nj}) \\ & + \eta_7 (\epsilon_{im} \dot{\epsilon}_{mn} \dot{\epsilon}_{nj} + \dot{\epsilon}_{im} \dot{\epsilon}_{mn} \epsilon_{nj}) \\ & + \eta_8 (\epsilon_{im} \epsilon_{mn} \dot{\epsilon}_{np} \dot{\epsilon}_{pj} + \dot{\epsilon}_{im} \dot{\epsilon}_{mn} \epsilon_{np} \epsilon_{pj}) \end{aligned} \quad 4.2$$

The response coefficients  $\eta_0$  through  $\eta_8$  are scalar-valued functions of the ten joint invariants of  $\epsilon_{ij}$  and  $\dot{\epsilon}_{ij}$  given as

$$\begin{aligned} I_1 &= \epsilon_{ss} & \dot{I}_1 &= \dot{\epsilon}_{ss} \\ I_2 &= \epsilon_{ts} \epsilon_{st} & \dot{I}_2 &= \dot{\epsilon}_{ts} \dot{\epsilon}_{st} \\ I_3 &= \epsilon_{ts} \epsilon_{tr} \epsilon_{sr} & \dot{I}_3 &= \dot{\epsilon}_{ts} \dot{\epsilon}_{tr} \dot{\epsilon}_{sr} \\ M &= \epsilon_{ts} \dot{\epsilon}_{st} & R &= \epsilon_{ts} \dot{\epsilon}_{tr} \dot{\epsilon}_{sr} \\ N &= \epsilon_{ts} \epsilon_{tr} \dot{\epsilon}_{sr} & Q &= \epsilon_{ts} \epsilon_{sk} \dot{\epsilon}_{kr} \dot{\epsilon}_{rt} \end{aligned} \quad 4.3$$

and  $\delta_{ij}$  is the Kroneker delta. The response coefficients can have various forms and must be determined from experiments. All response coefficients are not required for all materials.

Based on the information presented in Chapter 3, the proposed constitutive relationship should include a nonlinear pressure-volume relation, nonlinear shear stress-strain relation, effect of pressure on the shear response, failure, and fracture as well as unloading and reloading criteria. A mathematical model incorporating these response characteristics will include expressions of the form

$$\sigma_{nn} = f_1(\epsilon_{nn}) \quad 4.4$$

or the hydrostatic response, and

$$\tau_{oct} = f_2(\gamma_{oct}, \sigma_{nn}) \quad 4.5$$

for the deviatoric response, where  $f_1$  and  $f_2$  are continuous scalar functions. The volumetric strain  $\epsilon_{nn}$  and octahedral shear strain  $\gamma_{oct}$  are expressed in terms of the principal invariants of strain tensor as

$$\epsilon_{nn} = I_1 = \epsilon_{11} + \epsilon_{22} + \epsilon_{33} \quad 4.6$$

and

$$\begin{aligned} \gamma_{oct} &= 2\sqrt{\frac{2}{3} I_2} \\ &= \frac{2}{3} \left[ (\epsilon_{11} - \epsilon_{22})^2 + (\epsilon_{22} - \epsilon_{33})^2 + (\epsilon_{33} - \epsilon_{11})^2 + 6(\epsilon_{12}^2 + \epsilon_{13}^2 + \epsilon_{23}^2) \right]^{\frac{1}{2}} \end{aligned} \quad 4.7$$

where the tensorial shear strains ( $\epsilon_{12}$ ,  $\epsilon_{13}$ , and  $\epsilon_{23}$ ) are equal to one-half of the engineering shear strains ( $\gamma_{12}$ ,  $\gamma_{13}$ , and  $\gamma_{23}$ ).

Strain rate will not be included directly in the development of the current model. It is clear from the discussion in Chapter 3 that brittle geomaterials are affected by loading rate. The majority of available data however are concentrated at or near the unconfined regime. The problems of interest here include dynamic loading at high pressures. The influence of loading rate as confinement increases is unclear. The

available information on the effect of strain rate on the ultimate strength indicates two approaches. One is that the increase in dynamic ultimate strength is a percentage of the static ultimate strength, while the other is that the increase in dynamic ultimate strength is essentially a shift in the static ultimate strength envelope (that is, a constant increase at all pressure levels). An indirect approach to account for the dynamic effects will be used here by increasing the static ultimate strength envelope by a percentage without introducing strain rate effects explicitly.

Eliminating the rate effects and removing the higher order strain terms reduces Equation 4.2 to

$$\sigma_{ij} = \eta_0 \delta_{ij} + \eta_1 \varepsilon_{ij} \quad 4.8$$

The response coefficients  $\eta_0$  and  $\eta_1$  must now be selected so that the constitutive equation yields the same expression for mean stress and octahedral shear stress as Equations 4.4 and 4.5, respectively. Mean stress  $\sigma_m$  is defined as

$$\sigma_m = \frac{\sigma_{nn}}{3} \quad 4.9$$

Substituting into Equation 4.8 gives

$$\sigma_m = \frac{\sigma_{nn}}{3} = \frac{3\eta_0 + \eta_1 \varepsilon_{nn}}{3} \quad 4.10$$

The octahedral shear stress is defined as

$$\tau_{oct} = \sqrt{\frac{2}{3} J_2} \quad 4.11$$

where  $J_2$  is the second invariant of the deviatoric stress tensor and is defined as

$$J_2 = \frac{1}{6} [(\sigma_{11} - \sigma_{22})^2 + (\sigma_{22} - \sigma_{33})^2 + (\sigma_{11} - \sigma_{33})^2] + \sigma_{12}^2 + \sigma_{23}^2 + \sigma_{13}^2 \quad 4.12$$

As stated before,

$$\gamma_{oct} = 2\sqrt{\frac{2}{3} I_2} \quad 4.13$$

where  $I_2$  is the second invariant of the deviatoric strain tensor (Equation 4.7). In view of Equations 4.8, 4.11 and 4.13,

$$\tau_{oct} = \frac{\eta_1 \gamma_{oct}}{2} \quad 4.14$$

Solving Equation 4.14 for  $\eta_1$  gives

$$\eta_1 = 2 \frac{\tau_{oct}}{\gamma_{oct}} \quad 4.15$$

Substituting into Equation 4.10 and solving for  $\eta_0$  gives

$$\eta_0 = \frac{\sigma_{nn}}{3} - \frac{2}{3} \frac{\tau_{oct}}{\gamma_{oct}} \epsilon_{nn} \quad 4.16$$

Substituting Equations 4.15 and 4.16 into Equation 4.8 and rearranging gives the general form of the constitutive equation relating the stress tensor with the invariants  $\sigma_m$ ,  $\tau_{oct}$ ,  $\gamma_{oct}$  and  $\epsilon_{nn}$  as

$$\sigma_{ij} = \sigma_m \delta_{ij} + 2 \frac{\tau_{oct}}{\gamma_{oct}} \left( \epsilon_{ij} - \frac{\epsilon_{nn}}{3} \delta_{ij} \right) \quad 4.17$$

The task now is to determine appropriate mathematical relations for  $\sigma_m$  and  $\tau_{oct} / \gamma_{oct}$ .

The model has two basic premises: (1) the material response can be decoupled into hydrostatic and deviatoric parts and (2) the deviatoric response can be further separated into cohesive and frictional parts. Assuming the response to be decoupled implies that the hydrostatic (volumetric) and deviatoric (shear) parts can be treated



separately. In general, some coupling does exist since the response of a material to pure shear can result in volumetric deformation. In Equation 4.17 the term to the left of the + sign represents the volumetric part and the term to the right of the + sign represents the deviatoric part. A hydrostatic state of stress will result in volumetric deformation only and a state of stress characterized by pure shear will result in shear deformation only. Therefore, each part can be fit separately to the volumetric and shear response of the material.

#### 4.2.1 Volumetric Response

The volumetric response defines the relationship between pressure and volumetric strain. In the NIF model, this response is separated into five segments as a function of the current volumetric strain and whether loading, unloading, or reloading is taking place. The volumetric response is described by a tension portion modeled with a single equation and a compression portion modeled by three loading equations and one unload/reload equation. Under hydrostatic tension, the response of the material has the same initial modulus  $K_e$  as the compression portion. With increasing tension, the material reaches a maximum level of stress  $\sigma_{mc}$  where it begins to soften and eventually breakup. The "loading" response in tension is modeled using the following equation developed by Elwi and Murray (1979)

$$\sigma_m = - \frac{K_e \epsilon_{vt}}{1 + \left( R + \frac{K_e}{K_s} - 2 \right) X - (2R - 1)X^2 + RX^3} \quad 4.18$$

where,

$$R = \frac{K_e(\sigma_{mc}/\sigma_{mf} - 1)}{K_s(\epsilon_{vf}/\epsilon_{vc} - 1)^2} - \frac{\epsilon_{vc}}{\epsilon_{vf}}$$

$$K_s = \frac{\sigma_{mc}}{\epsilon_{vc}}$$

$$\epsilon_{vo} = \epsilon_v \text{ at } \frac{\sigma_m}{3} = 0$$

$$\epsilon_{vt} = \epsilon_v - \epsilon_{vo}$$

$$X = \frac{\epsilon_{vt}}{\epsilon_{vc}}$$

The material constants are  $K_e$ ,  $\epsilon_{vc}$ ,  $\epsilon_{vf}$ ,  $\sigma_{mc}$ , and  $\sigma_{mf}$  and are shown graphically in Figure 4.1. "Loading" in tension occurs if (a) the volumetric strain is negative and increasing in magnitude, or (b) an unloading from a compression state (positive stress) into a negative state of stress and the volumetric strain is decreasing. No data is available on which to base unloading and reloading in hydrostatic tension. "Unloading" from a state of tension should imply an increase of pressure. Unloading/reloading could be viewed as elastic and follow the loading response, but this is not physically realistic once softening has begun. The unload/reload could also be "elastic" by following a straight line from the start of the unload/reload to zero volumetric strain. This approach is reasonable, but adds another history variable, the volumetric strain at the start of unloading, that must be tracked. An intermediate unloading slope could be used but it is not known what the response should be once zero pressure is reached. The last option is to assume that softening does not occur during hydrostatic tension such that the pressure remains constant once  $\sigma_{mc}$  is reached. Unloading/reloading is then treated as elastic and follows the loading response. For projectile penetration problems, it is believed that the details of the unload/reload in hydrostatic tension is not relevant and only the limiting value of the hydrostatic tensile stress (referred to as the tension cutoff) defined by  $\sigma_{mc}$  is important.

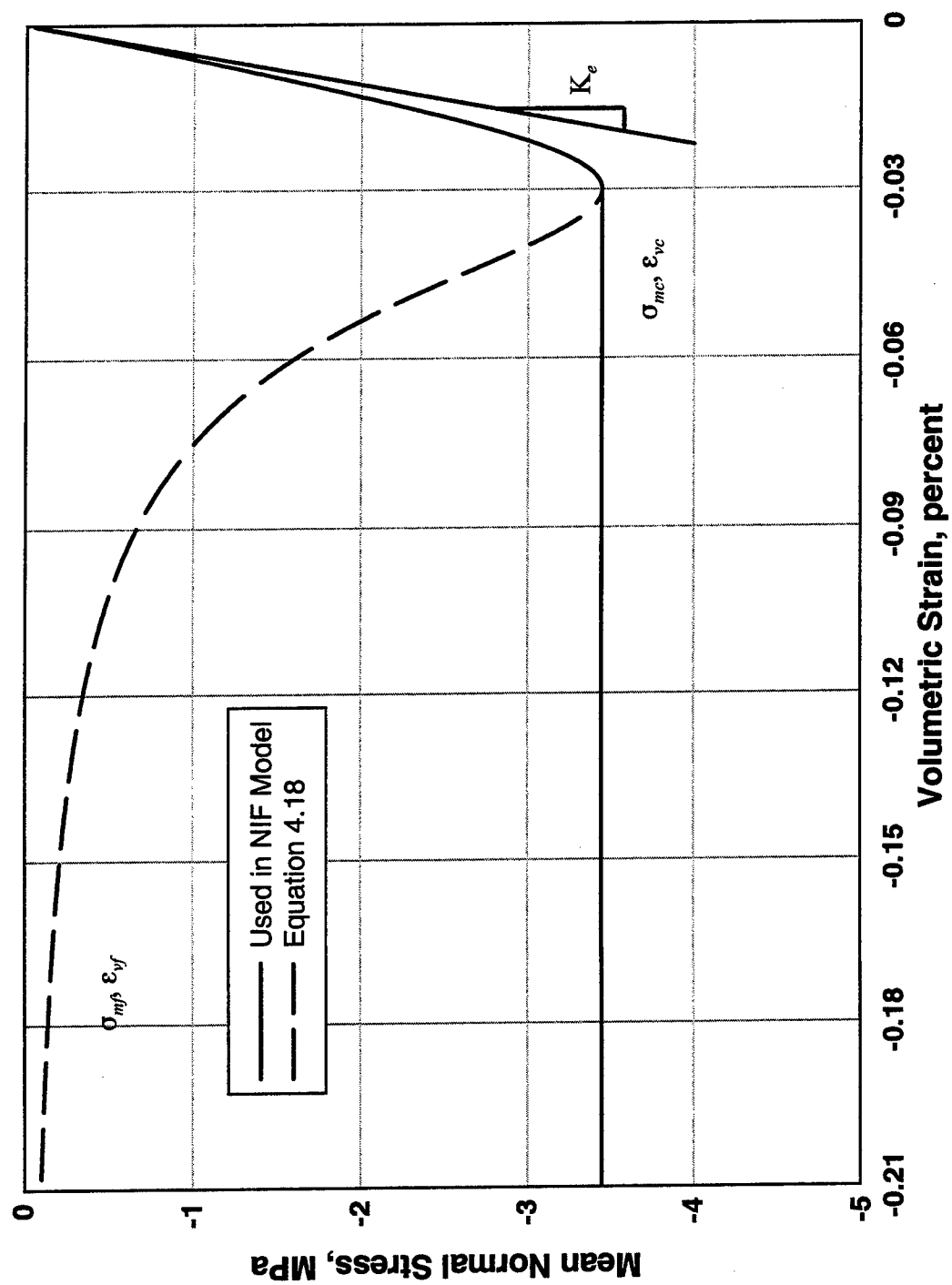


Figure 4.1. Hydrostatic tension part of volumetric response.

The loading and unloading portion of hydrostatic compression response is the same as that described in Johnson, et. al. (1994). Initial loading in compression is defined as

$$\sigma_m = K_e \epsilon_v \quad \text{for } \epsilon_v \leq (\epsilon_v)_{crush} \quad 4.19$$

$$\sigma_m = (\sigma_m)_{crush} + a \epsilon_v' + b (\epsilon_v')^2 + c (\epsilon_v')^3 \quad \text{for } (\epsilon_v)_{crush} < \epsilon_v \leq (\epsilon_v)_{lock} \quad 4.20$$

$$\sigma_m = (\sigma_m)_{lock} + K_{lock} \epsilon_v'' \quad \text{for } \epsilon_v > (\epsilon_v)_{lock} \quad 4.21$$

where,  $\epsilon_v$  is the volumetric strain,  $(\sigma_m)_{crush}$  is the pressure at  $(\epsilon_v)_{crush}$ ,  $\epsilon_v' = \epsilon_v - (\epsilon_v)_{crush}$ ,  $\epsilon_v'' = \epsilon_v - (\epsilon_v)_{lock}$  and  $K_e$ ,  $(\epsilon_v)_{crush}$ ,  $a$ ,  $b$ ,  $c$ ,  $K_{lock}$ , and  $(\epsilon_v)_{lock}$  are material constants.

Unloading in the compression regime occurs if (a) the volumetric strain is decreasing and (b) it is less than the previous maximum volumetric strain. Currently, only linear unloading/reloading is used. If the unloading begins at a volumetric strain less than  $(\epsilon_v)_{crush}$  then the unloading/reloading follows  $K_e$ . If the unloading begins at a volumetric strain greater than  $(\epsilon_v)_{lock}$  then the unloading/reloading follows  $K_{lock}$ . If the unloading begins at a volumetric strain between  $(\epsilon_v)_{crush}$  and  $(\epsilon_v)_{lock}$ , the unloading/reloading will follow a slope given by

$$K_{unl/rel} = K_e + (K_{lock} - K_e) \frac{[(\epsilon_v)_{max} - (\epsilon_v)_{crush}]}{[(\epsilon_v)_{lock} - (\epsilon_v)_{crush}]} \quad 4.22$$

If the unloading extends into the tension (negative pressure) region Equation 4.18 is used to define the response, but the value of  $K_e$  will depend on where the unloading originated. If the unloading originated at a strain less than  $(\epsilon_v)_{crush}$ , Equation 4.18 is used as is. If the unloading originates at a strain between  $(\epsilon_v)_{crush}$  and  $(\epsilon_v)_{lock}$ ,  $K_{unl/rel}$  is used in Equation 4.18 instead of  $K_e$ ; if the unloading originates at a strain greater than  $(\epsilon_v)_{lock}$ ,  $K_{lock}$  is used in Equation 4.18 instead of  $K_e$ . Each section of the compression pressure-volumetric strain response and the corresponding equation are shown in Figure 4.2.

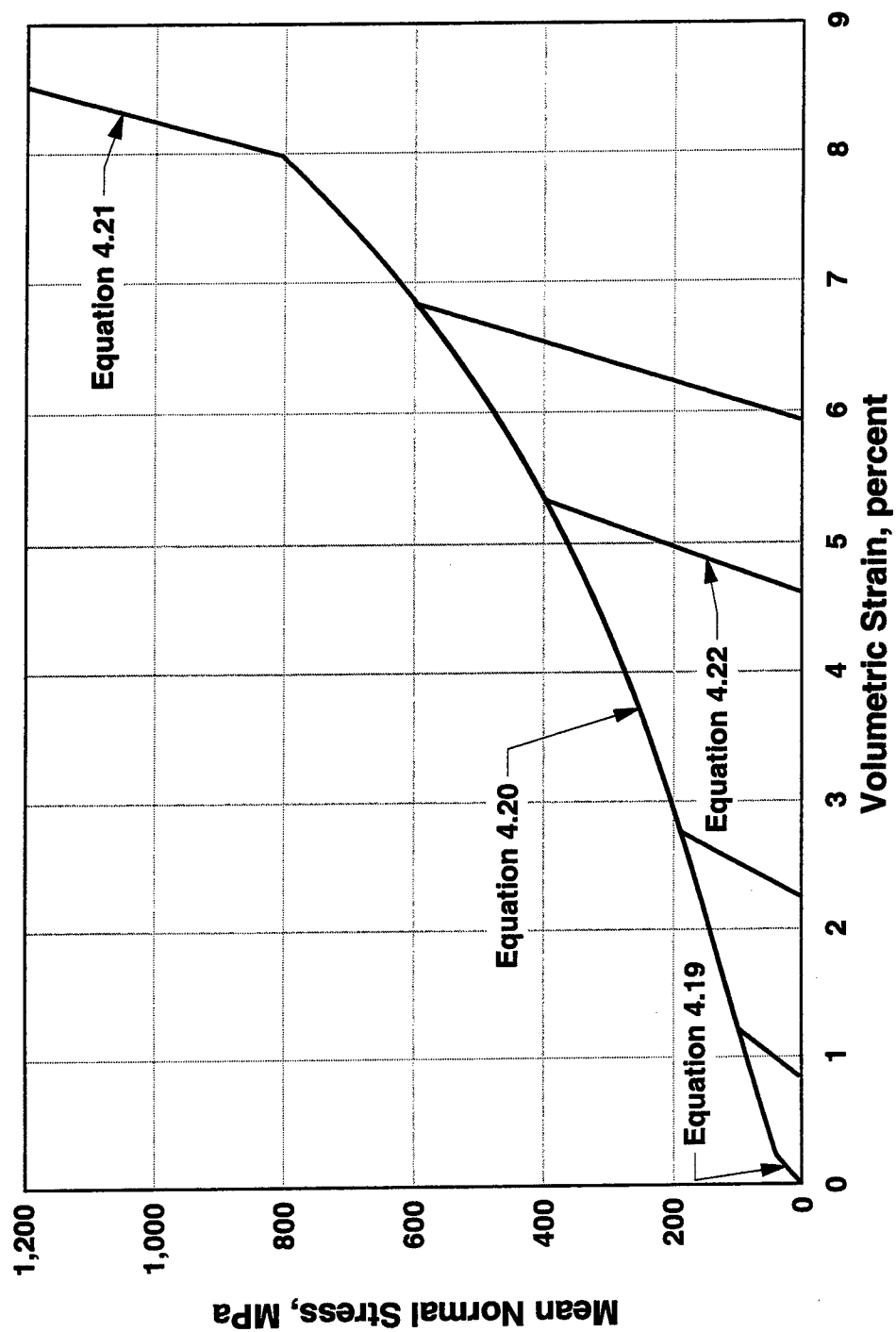


Figure 4.2. Hydrostatic compression part of volumetric response.

#### 4.2.2 Deviatoric Response

The deviatoric stress-strain response is separated into friction and cohesion subparts. The octahedral shear stress for the friction subpart increases with increasing strain (strain hardening) and is a function of the superimposed hydrostatic state of stress. The friction subpart is described by an equation of the form  $\tau_{octf} = f(\gamma_{oct}, \sigma_m)$ . The following hyperbolic equation is used:

$$\tau_{octf} = \frac{\gamma_{oct} F (\tau_{ult} - \tau_{yc}) (b_2 + b_o(\sigma_m)^{b_1})}{F (\tau_{ult} - \tau_{yc}) + \gamma_{oct} (b_2 + b_o(\sigma_m)^{b_1})} \quad 4.23$$

where,  $\tau_{ult}$  is the ultimate strength surface containing both the frictional and the cohesive parts,  $\tau_{yc}$  is the cohesive part of the ultimate strength surface, and  $b_o$ ,  $b_1$  and  $b_2$  define the initial modulus of the  $\tau_{oct}$  vs  $\gamma_{oct}$  response. The parameter  $F$  will be described below. The ultimate strength  $\tau_{ult}$  of the material is defined using a two part curve in the  $\tau_{oct}$  vs  $\sigma_m$  space. For pressures greater than zero (compression), the curve is defined as

$$\tau_{ult} = A - C \exp(B \sigma_m) \quad 4.24$$

For pressures less than zero (tension), the curve is defined as

$$\tau_{ult} = (A - C) \left( 1.0 - \frac{\sigma_m}{\sigma_{m_c}} \right) \quad 4.25$$

In Equations 4.24 and 4.25,  $A$ ,  $B$  and  $C$  are material constants that define the nonlinear part of the compression side of the ultimate strength surface. Equation 4.25 is the linear part of the tension side of the ultimate strength surface, and it ensures that the ultimate strength of the material at the maximum hydrostatic tensile stress is zero. Equations 4.24 and 4.25 are shown graphically in Figure 4.3.

For the cohesion subpart, the stress increases with increasing strain until a strain is reached where the maximum cohesive strength of the material is exceeded. This

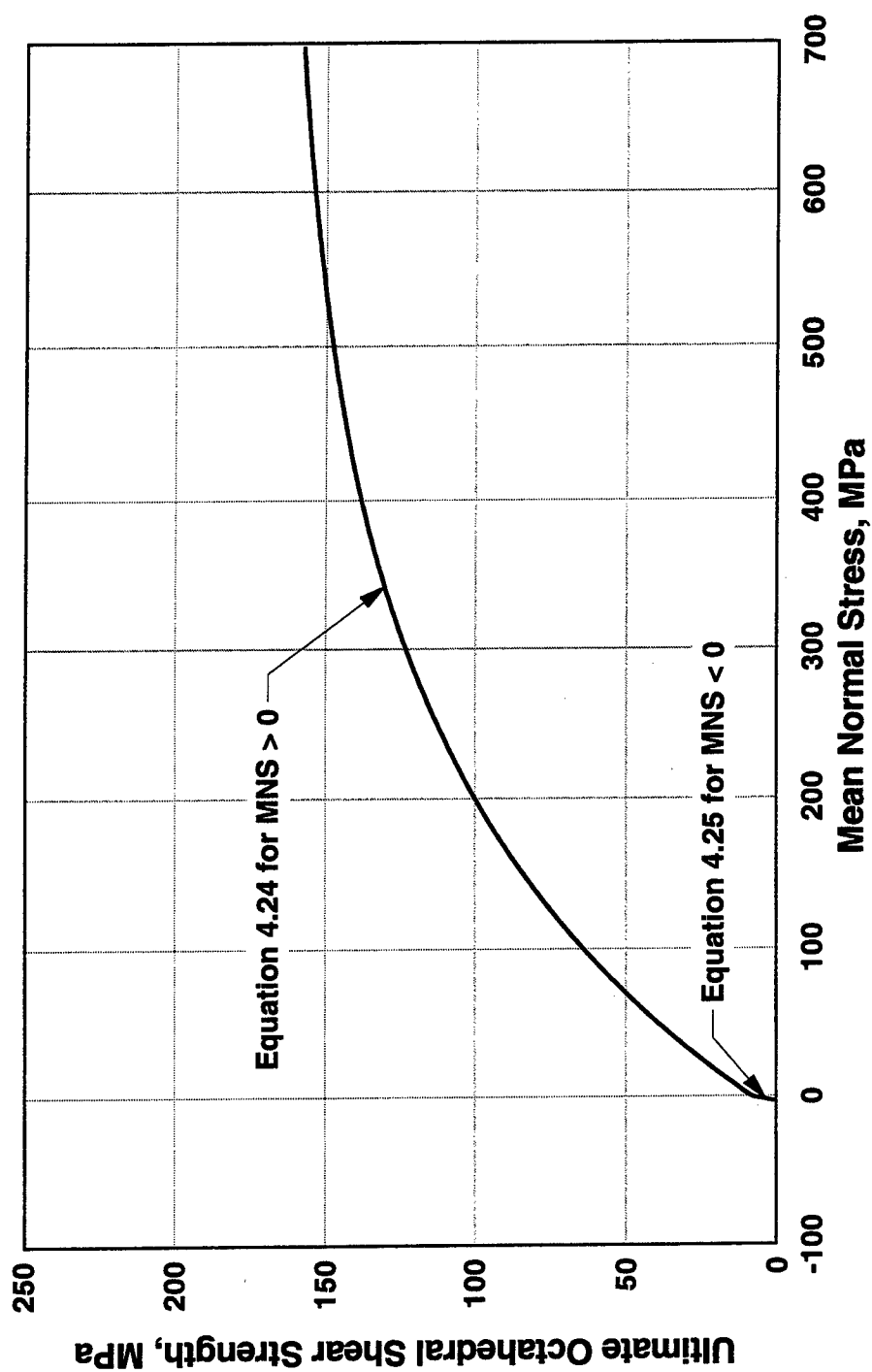


Figure 4.3. Ultimate strength envelope.

phenomenon is referred to as cohesive fracture. Beyond this strain, the stress will decrease with increasing strain (strain softening). The cohesive subpart is described by an equation of the form  $\tau_{octc} = f(\gamma_{oct})$  and is given as

$$\tau_{octc} = \frac{F \tau_{yc} \gamma_c \mu_c \gamma_{oct} R_{ed}}{F \tau_{yc} \gamma_c + (\mu_c \gamma_c - F \tau_{yc}) \gamma_{oct}} \quad 4.26$$

where, the parameter  $\gamma_c$  is the octahedral shear strain at which strain softening begins,  $\mu_c$  is the initial slope of the cohesion subpart of the deviatoric stress-strain response, and  $R_{ed}$  is a parameter that defines how the cohesive fracture will progress, i.e., for very brittle fracture the stress will decrease rapidly and for a more ductile fracture the stress will decrease more gradually. The parameter  $\gamma_c$  is dependent on the history of pressure that has been applied to the material. The maximum cohesive strength  $\tau_{yc}$  is dependent on the current pressure as well as the pressure history of the material. As was discussed in Chapter 3, brittle geomaterials will experience internal damage during the application of hydrostatic pressure. In compression, during the initial phase very little change occurs. As pressure increases the level of "damage" will also increase as bonds between the aggregates are broken. Eventually the grains will rearrange as the initial cementation breaks down. Defining the boundaries of each phase is based on the different regions of the pressure vs volumetric strain response as described in Figure 3.9. The onset of bond breakage is assumed to occur when  $(\sigma_m)_{crush}$  is reached using Equation 4.19. To this point in compression,  $\tau_{yc}$  is constant and is

$$\tau_{yc} = A - C \quad 4.27$$

which is the value of  $\tau_{ult}$  at  $\sigma_m$  equal to zero from Equation 4.24. At the pressure where the cohesion component is zero ( $\tau_{yc}$  is zero), the response is only frictional. This point is assumed to be the point of inflection of the pressure vs. volumetric strain response where it begins to stiffen rapidly. The value of  $(\sigma_m)_{fric}$  is defined by taking the second derivative of Equation 4.20, setting equal to zero and solving for  $\epsilon'_v$ . This value of  $\epsilon'_v$  ( $\epsilon'_v = -b/3c$ ) is then substituted into Equation 4.20 to obtain



$$(\sigma_m)_{fric} = K_e (\epsilon_{nn})_{crush} - \frac{ab}{3c} + \frac{2b^3}{27c^2} \quad 4.28$$

Between pressures of  $(\sigma_m)_{crush}$  and  $(\sigma_m)_{fric}$  the  $\tau_{yc}$  gradually decreases to zero using the following equation

$$\tau_{yc} = (A - C) \left( 1.0 - \frac{\sigma_m - (\sigma_m)_{crush}}{(\sigma_m)_{fric} - (\sigma_m)_{crush}} \right) \quad 4.29$$

The ultimate strength envelope of the cohesion subpart is shown graphically in Figure 4.4.

The octahedral shear strain at which softening begins,  $\gamma_c$ , should be reached when the total calculated octahedral shear stress  $\tau_{oct}$  is equal to the ultimate octahedral shear stress given by either Equation 4.24 or Equation 4.25. Equations 4.23 and 4.26 are hyperbolic equations and when combined provide the total deviatoric response of the material. To ensure that  $\tau_{oct}$  reaches  $\tau_{ult}$  within a reasonable value of  $\gamma_{oct}$  (discussed in Chapter 3), a factor  $F$  is applied in Equations 4.23 and 4.26 and is described below. The value for  $\gamma_c$  where  $\tau_{oct}$  equals  $\tau_{ult}$  can be determined from Equations 4.23 and 4.26 by (1) substituting  $\gamma_c$  for  $\gamma_{ocr}$  (2) adding the two equations, (3) setting  $R_{ed}$  equal to 1.0 since we are looking for the value of  $\gamma_c$  where strain softening just begins, (4) setting  $\tau_{oct}$  equal to  $\tau_{ult}$ , and (5) solving for  $\gamma_c$  to give

$$\gamma_c = \frac{F (\tau_{ult} - \tau_{yc}) (\tau_{ult} - F \tau_{yc})}{(b_2 + b_o (\sigma_m)^{b_1}) \tau_{ult} (F - 1)} \quad 4.30$$

In order to model brittle geomaterial response at low pressures and ductile response at high pressures with a transition from brittle to ductile in between, the following expressions were specified for  $F$

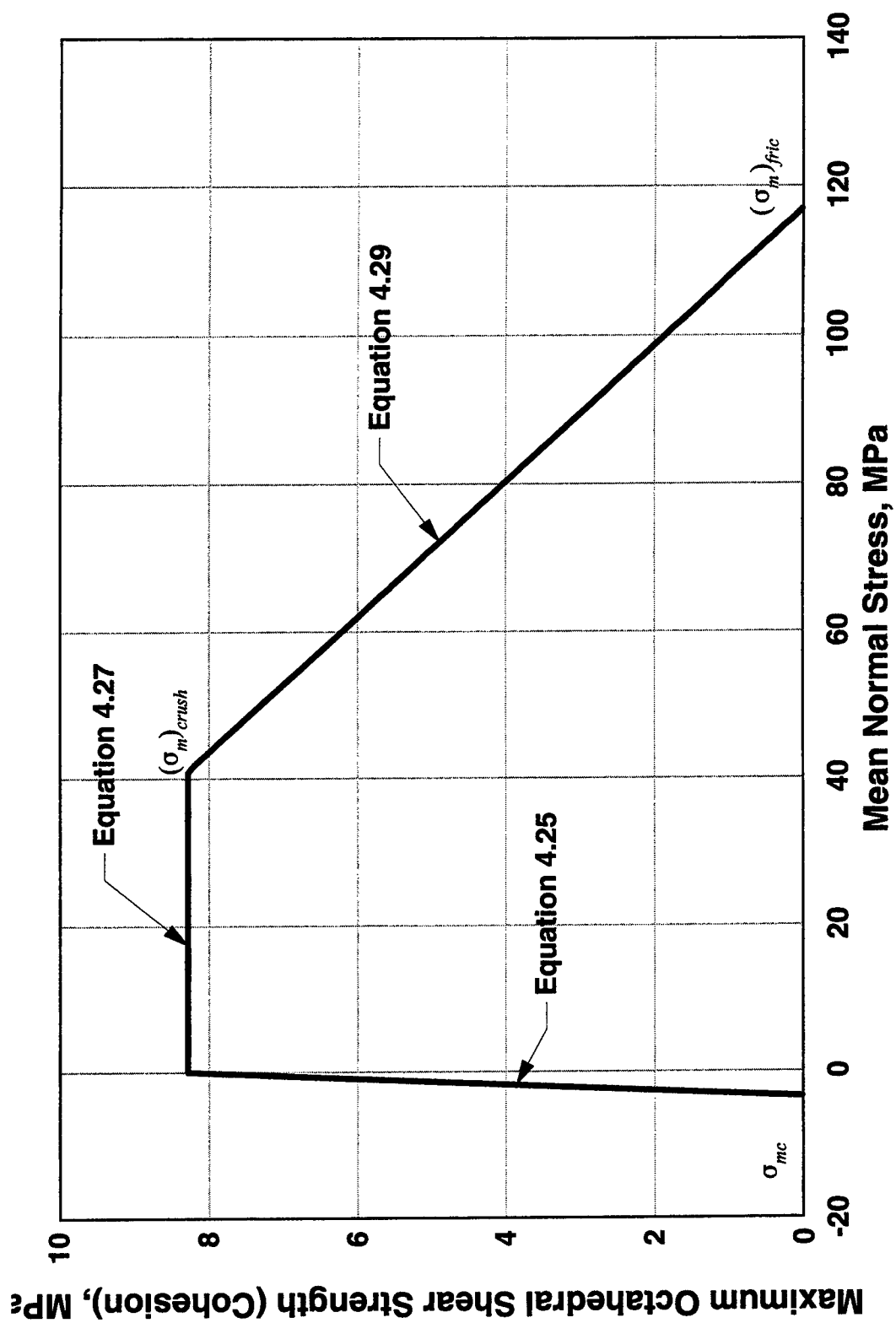


Figure 4.4. Maximum strength envelope for the cohesion subpart.

$$F = 1.325 \quad \text{for } \sigma_m < (\sigma_m)_{crush} \quad 4.31$$

$$F = 1.100 + 0.225 \left( 1.000 - \frac{\sigma_m - (\sigma_m)_{crush}}{(\sigma_m)_{fric} - (\sigma_m)_{crush}} \right) \quad \text{for } (\sigma_m)_{crush} \leq \sigma_m \leq (\sigma_m)_{fric} \quad 4.32$$

$$F = 1.100 \quad \text{for } \sigma_m > (\sigma_m)_{fric} \quad 4.33$$

The following equations are specified for  $R_{ed}$

$$R_{ed} = 1.0 \quad \text{for } \gamma_{oct} < \gamma_c \quad 4.34$$

$$R_{ed} = 1.0 - \frac{\gamma_{oct} - \gamma_c}{\gamma_c (N - 1.0)} \quad \text{for } \gamma_c \leq \gamma_{oct} \leq N \gamma_c \quad 4.35$$

$$R_{ed} = 0.0 \quad \text{for } \gamma_{oct} > N \gamma_c \quad 4.36$$

where  $N$  defines how far  $\gamma_{oct}$  is from  $\gamma_c$  when  $R_{ed}$  is zero.

Unloading and reloading in shear will be determined by the current value of the octahedral shear strain. If  $\gamma_{oct}$  is less than the largest value of  $\gamma_{oct}$  obtained thus far then the material is assumed to be either unloading or reloading. Load, unload, and reload cycles are illustrated in Figure 4.5. The unload response initially follows a slope equal to the initial total modulus of the  $\tau_{oct}$  vs  $\gamma_{oct}$  response associated with the pressure at the time unloading begins. If the value of  $\tau_{oct}$  implied by the total modulus and the current value of  $\gamma_{oct}$  becomes negative (see Figure 4.5), then the response is determined using Equations 4.23 through 4.33 with  $R_{ed} = 1.0$  so that no softening occurs. The value for  $\gamma_{oct}$  used in the equations is the difference between the point at which  $\tau_{oct}$  became zero and the current value of  $\gamma_{oct}$ . Reloading will retrace the unloading response until the current value of  $\gamma_{oct}$  exceeds the maximum value of  $\gamma_{oct}$  where the virgin loading of the material continues.

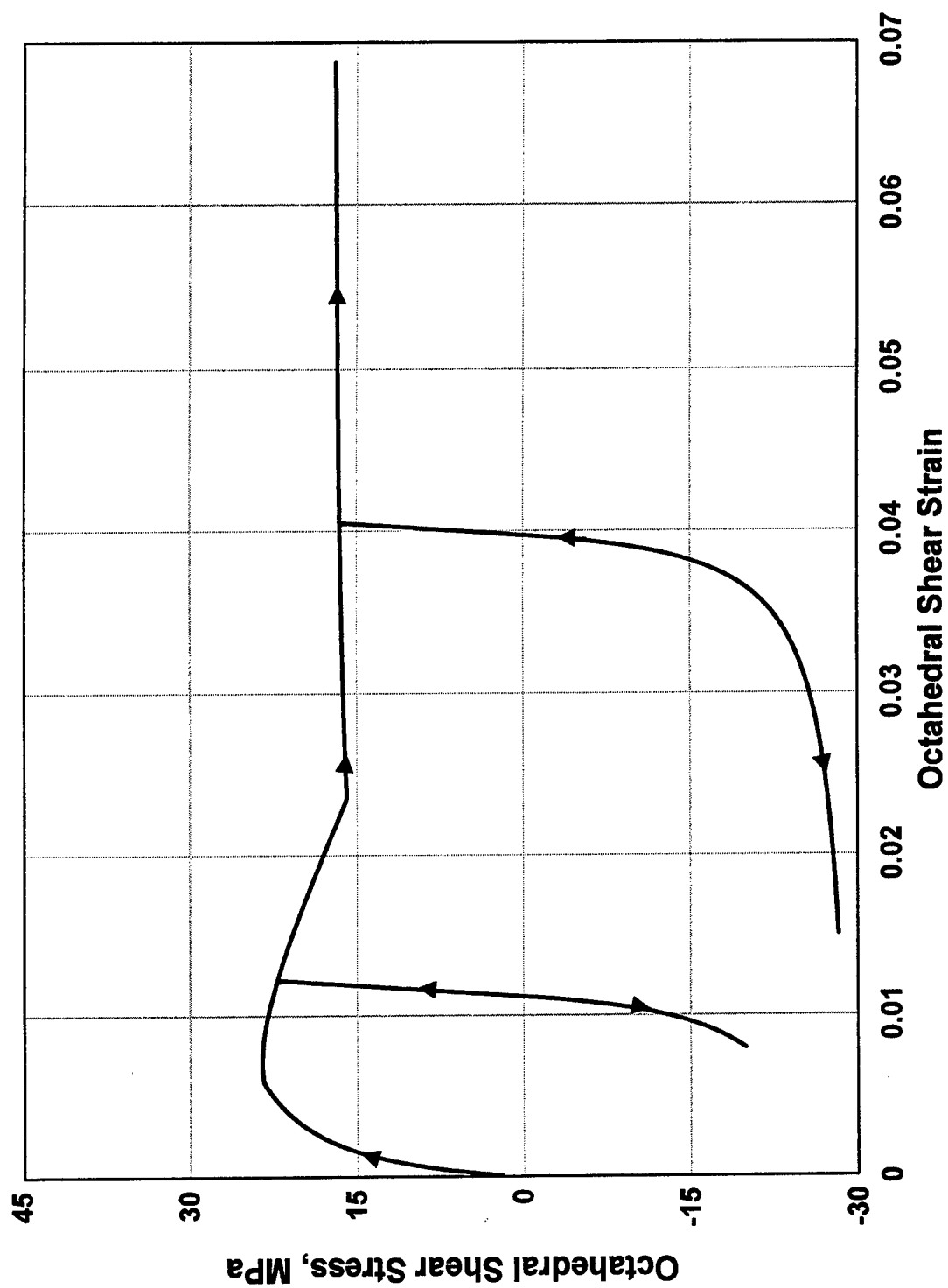


Figure 4.5. Load/unload/reload under constant pressure.

The model that has been developed to this point is rate independent. From Figures 3.19 and 3.20 the strength of conventional concrete increases as the strain rate increases. The ultimate strength in shear and hydrostatic tension is multiplied by a parameter DYN to indirectly account for rate effect. Currently, DYN is a constant that increases the ultimate strength by a percentage.

The total octahedral shear stress is obtained by adding the shear stresses from the friction (Equation 4.23) and cohesion (Equation 4.26) subparts as

$$\tau_{oct} = \tau_{octf} + \tau_{octc} \quad 4.37$$

For low pressures where the deviatoric part will be dominated by the cohesive subpart, a brittle, strain softening response will result. As pressure increases, the frictional subpart will begin to dominate and the response will become more ductile. Figure 4.6 shows the friction and cohesion subparts and the combined response for a constant pressure shear test. The stress associated with the friction subpart increases monotonically with strain. The stress associated with the cohesion subpart initially increases with strain but begins to decrease beyond  $\gamma_{oct} = 0.005$ . The combined response adds both subparts to result in softening behavior and a residual strength (corresponding to the frictional subpart) when the cohesive strength is completely lost.

The NIF model requires that five variables be stored as history variables for each element of the material. These variables record the current extremes that the material has experienced. The first variable is the maximum volumetric strain. This variable is always greater than or equal to zero. If the current value of volumetric strain is less than this value, the material is either in tension or in an unload/reload cycle with respect to pressure. The second variable is the maximum octahedral shear strain. This value will be used to determine if the material is in an unload/reload cycle with respect to shear. The third variable is the pressure at the start of an unload/reload cycle in shear. This pressure will be used to determine the initial total modulus of the  $\tau_{oct}$  vs  $\gamma_{oct}$  response when

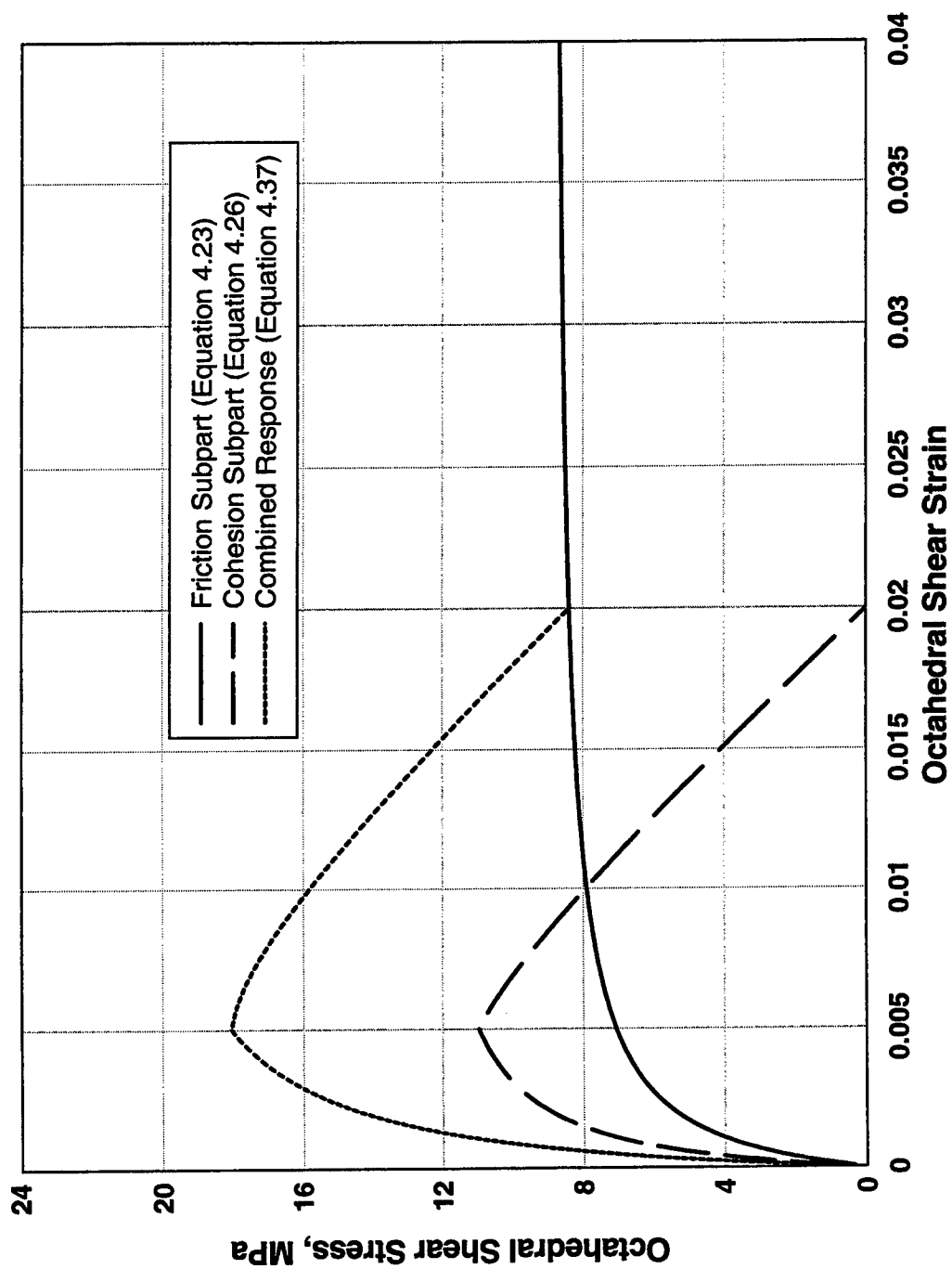


Figure 4.6. Friction and cohesion subparts and combined response for a constant pressure shear test.

unloading/reloading in shear. The fourth variable is the minimum value of  $\tau_{yc}$  thus far. The fifth variable is the maximum value of  $\gamma_c$  calculated thus far. The fourth and fifth variables imply that healing can not occur, i.e., a material that has been loading to the point where cohesion has been lost and then unloaded does not regain its brittle characteristics simply because it has been unloaded.

### 4.3 MODEL FITTING

The NIF model must now be fit to the results from laboratory tests. The model has nineteen constants that are defined by the user: eleven constants that define the pressure-volumetric strain response ( $K_e$ ,  $\epsilon_{vc}$ ,  $\epsilon_{vf}$ ,  $\sigma_{mc}$ ,  $\sigma_{mf}$ ,  $(\epsilon_v)_{crush}$ ,  $a$ ,  $b$ ,  $c$ ,  $K_{lock}$ , and  $(\epsilon_v)_{lock}$ ) and eight constants that define the  $\tau_{oct}$  vs  $\gamma_{oct}$  response ( $b_o$ ,  $b_1$ ,  $b_2$ ,  $A$ ,  $B$ ,  $C$ ,  $\mu_c$ , and  $N$ ). The numerical values of these constants must be determined from laboratory test data for the material of interest. To illustrate the fitting procedure, the model will be fit to the conventional-strength portland cement (CSPC) concrete whose mix proportions are presented in Table 4.1.

Constants that describe the tension portion of the pressure-volumetric strain response ( $K_e$ ,  $\epsilon_{vc}$ ,  $\epsilon_{vf}$ ,  $\sigma_{mc}$ , and  $\sigma_{mf}$ ) can be taken directly from a plot similar to Figure 4.1. Very little data is available for the hydrostatic tension response of brittle geomaterials. Nichols and Ko (1996) present data for a plain concrete under true triaxial tension (hydrostatic tension). Only the pre-peak loading portion of the response was captured. The average pressure at failure was about 2.9 MPa at a volumetric strain of 0.021 percent. They note that the stress at failure is the same as that from uniaxial tension experiments. Direct pull tension experiments on CSPC concrete provided an average strength of about 3.6 MPa at an axial strain of about 0.012 percent. Using this information an average value of 3.4 MPa will be used for  $\sigma_{mc}$ . The value for  $K_e$  is determined from the compression portion of the response that is described below. An initial bulk modulus  $K_e$  of 17,900 MPa agrees with the initial slope of the response. Assuming a linear response,

Table 4.1. Ingredients and mixture proportions for CSPC concrete.

Item	Mixture Proportions, Saturated Surface-Dry
Type II portland cement	328.0 kg/m <sup>3</sup>
9.5-mm limestone coarse aggregate	1,034.1 kg/m <sup>3</sup>
Limestone fine aggregate	806.3 kg/m <sup>3</sup>
Water	186.9 kg/m <sup>3</sup>
Water reducing admixture	1.3 l/m <sup>3</sup>
Air-detraining agent	0.33 kg/m <sup>3</sup>

w/c = 0.57



a value for  $\epsilon_{vc}$  of 0.019 percent corresponds to the above values for  $\sigma_{mc}$  and  $K_e$ . Since the response becomes nonlinear as the peak is approached, this value for  $\epsilon_{vc}$  will be too stiff, therefore, a value of 0.030 percent will be used. Values for  $\sigma_{mf}$  and  $\epsilon_{vf}$  in Equation 4.18 define a point on the “descending” portion of the response. Since no data exists on which to base this point, a value of  $\sigma_{mc}/4$  (0.9 MPa) will be used for  $\sigma_{mf}$  and  $4\epsilon_{vc}$  (0.12 percent) will be used for  $\epsilon_{vf}$ . Although the post-peak softening is not used, it is recommended to input  $\sigma_{mf}$  and  $\epsilon_{vf}$  since they do influence the pre-peak portion. The response from Equation 4.18 and the data from Nichols and Ko are shown in Figure 4.7.

The seven constants required to define the compression part of the pressure-volumetric strain response are  $K_e$  (also used in the tension part),  $(\epsilon_v)_{crush}$ ,  $a$ ,  $b$ ,  $c$ ,  $K_{lock}$ , and  $(\epsilon_v)_{lock}$ . The value for  $K_e$  is the initial slope of the response and is taken to be 17,900 MPa. The value for  $(\epsilon_v)_{crush}$  is determined as the point on the pressure-volumetric strain response where the material is no longer linear elastic and the bonds between the aggregate materials begin to break down. For the CSPC concrete, a value of 0.229 percent will be used. Values for  $K_{lock}$  and  $(\epsilon_v)_{lock}$  should be determined next. The recommended pressure-volumetric strain response shown in Figure 4.8 does not extend to a strain where the modulus is nearly constant. Since this constant modulus should occur when all of the air has been compressed out of the material, the air voids content should provide some assistance in determining these values. The locked modulus should extend to a point on the volumetric strain axis that is close to the air voids content. From the recommended properties in Figure 4.6, the highest unloading modulus is 74100 MPa. Extrapolating this modulus from a volumetric strain equal to an air voids content of 6.4 percent shows that the material has not reached the locked modulus. The pressure at which the material will reach the locked modulus is estimated to be about 800 MPa. This value for pressure will be used with the polynomial portion to obtain a value for  $(\epsilon_v)_{lock}$ . Parameters for the polynomial part of the response between  $(\epsilon_v)_{crush}$  and  $(\epsilon_v)_{lock}$  are determined with the aid of curve fitting software. Values for  $a$ ,  $b$ , and  $c$  are 6244.15 MPa, -47387.5 MPa, and 1212580.0 MPa, respectively. The value for  $(\epsilon_v)_{lock}$  is obtained by

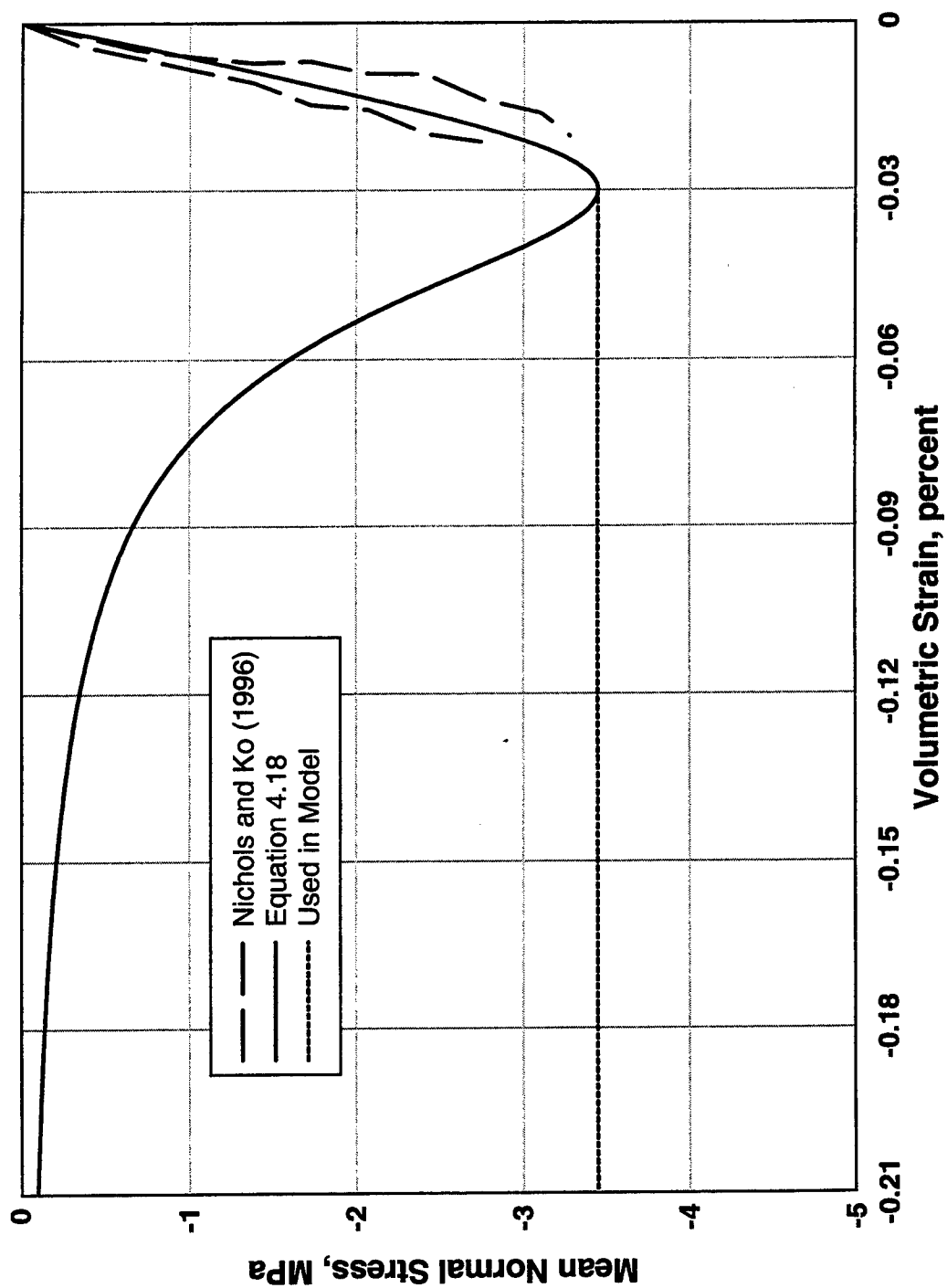


Figure 4.7. NIF model fit for hydrostatic tension and test data from Nichols and Ko (1996).

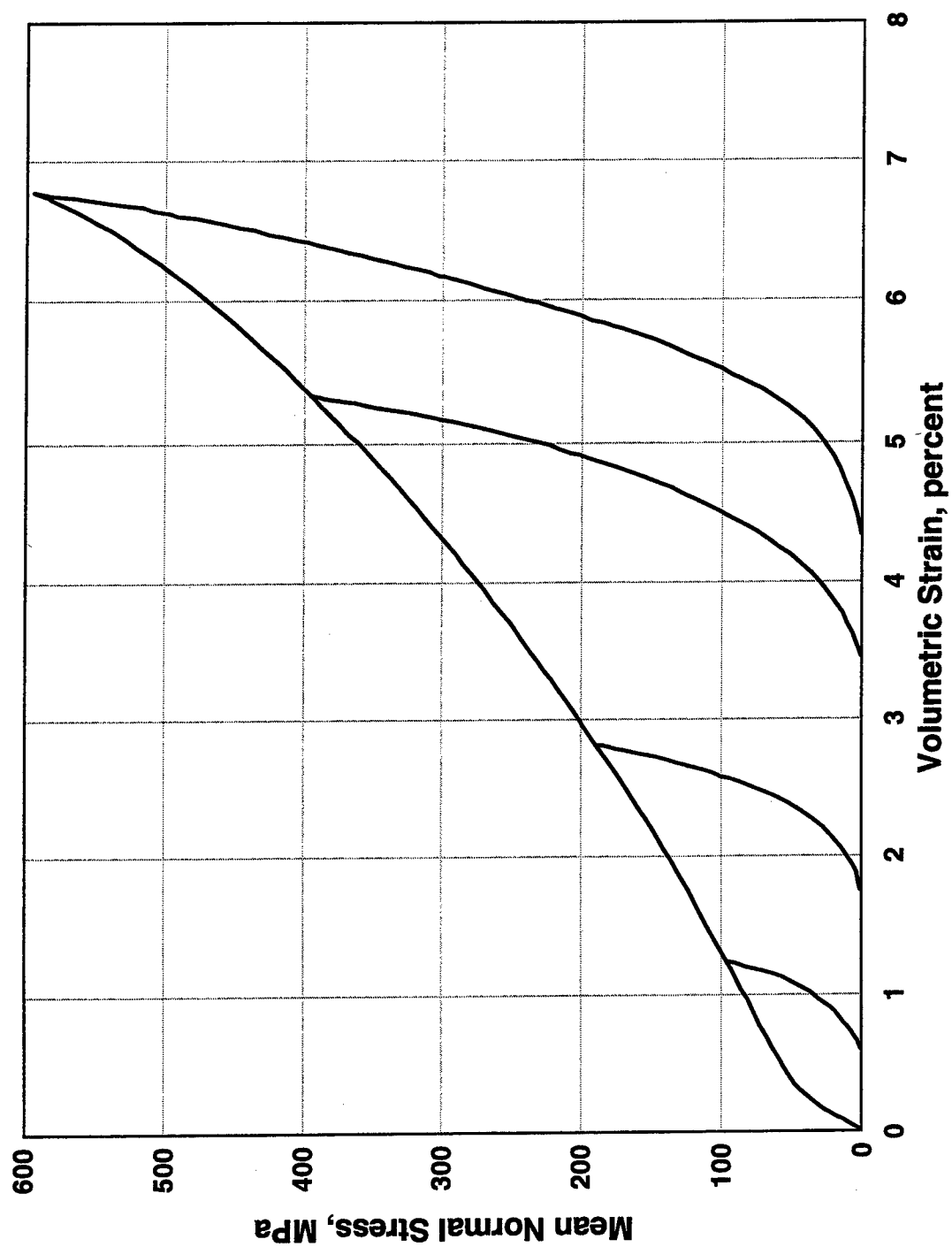


Figure 4.8. Recommended hydrostatic compression response for CSPC concrete.

determining the volumetric strain that coincides with a pressure of 800 MPa, and was calculated to be 7.98 percent. The model fit and recommended response are shown in Figure 4.9.

The recommended properties for the CSPC concrete do not include experiments conducted under constant pressure, which ideally is needed to fit the NIF model. The set of recommended properties does include the results from constant radial stress experiments, which can be used if the ultimate strength envelope is assumed to be path independent, i.e., the same envelope is obtained regardless of the loading path during the experiment. Constants that describe the deviatoric part of the model ( $b_o$ ,  $b_1$ ,  $b_2$ ,  $\mu_c$ ,  $A$ ,  $B$ ,  $C$ , and  $N$ ) are obtained from the results of shear experiments. Values for  $A$ ,  $B$ , and  $C$  are obtained by fitting Equation 4.24 to the peak strengths from the shear experiments plotted as  $\tau_{oct}$  vs  $\sigma_m$ . Using the curve fitting software, values for  $A$ ,  $B$ , and  $C$  were determined to be 165.197 MPa,  $-0.0044034265 \text{ MPa}^{-1}$ , and 156.913 MPa, respectively. A comparison of the model ultimate strengths (total, cohesion, and friction) and the recommended response is shown in Figure 4.10. The total envelope from the model agrees very well with the recommended surface. The cohesion part follows the total envelope in the negative pressure region, is equal to the octahedral shear stress intercept from zero pressure until  $(\sigma_m)_{crush}$  is reached, and then decreases to zero at  $(\sigma_m)_{fric}$ . The friction part is the difference between the total envelope and the cohesion part.

Values for  $b_o$ ,  $b_1$ , and  $b_2$  are determined by fitting the shear modulus part of Equation 4.23 to the initial shear modulus from the results of shear experiments conducted at several pressure levels. The data provided with the recommended properties can be used by noting that the shear modulus can be obtained from the plots of principal stress difference vs principal strain difference. Values selected for  $b_o$ ,  $b_1$ , and  $b_2$  are 2530.21, 0.192653, and 2758.62 MPa, respectively. A comparison of the model shear modulus and the data is presented in Figure 4.11. The shear modulus for the cohesion part  $\mu_c$  cannot be obtained from the data provided in the recommended properties since

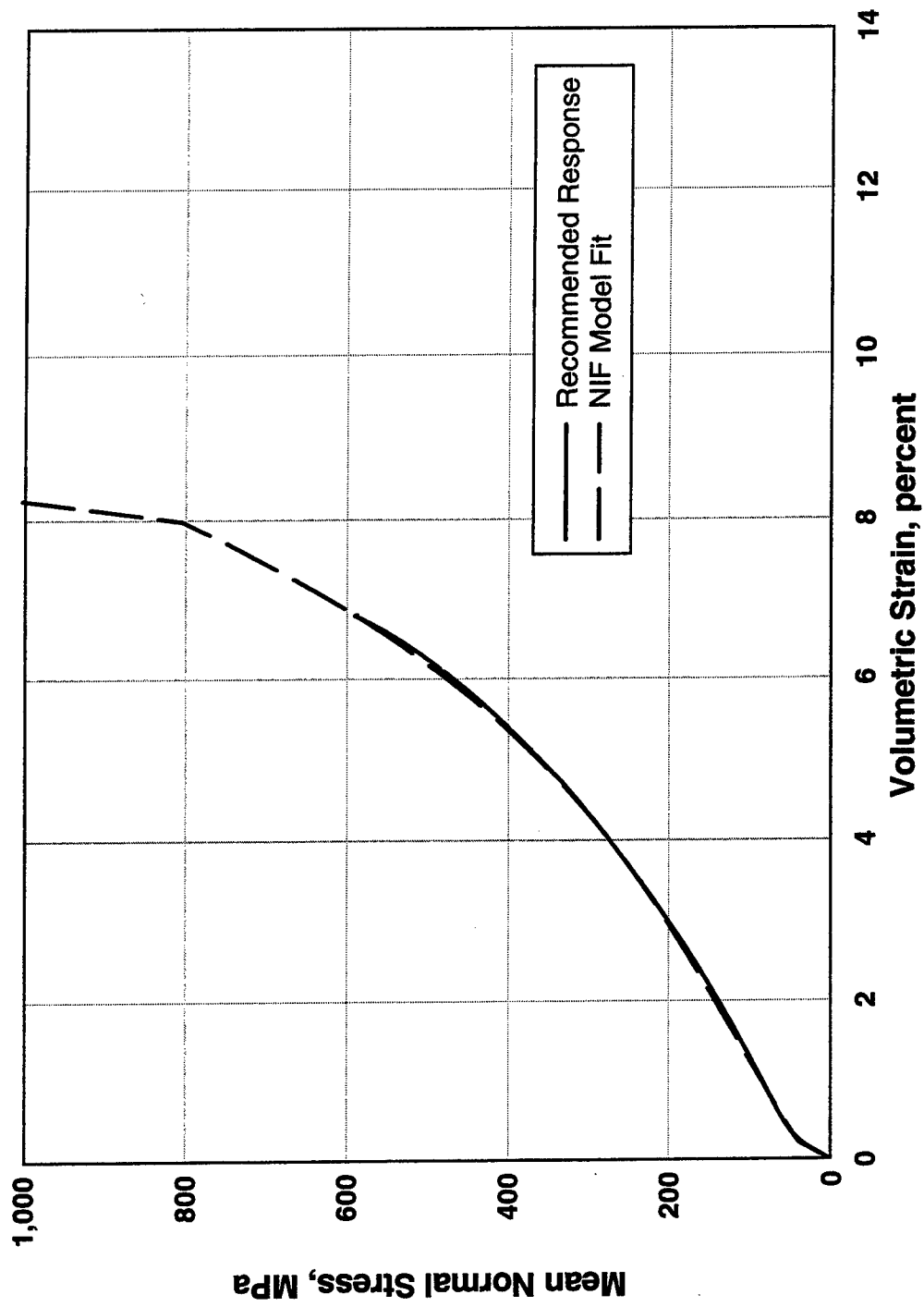


Figure 4.9. NIF model fit and recommended hydrostatic compression response.

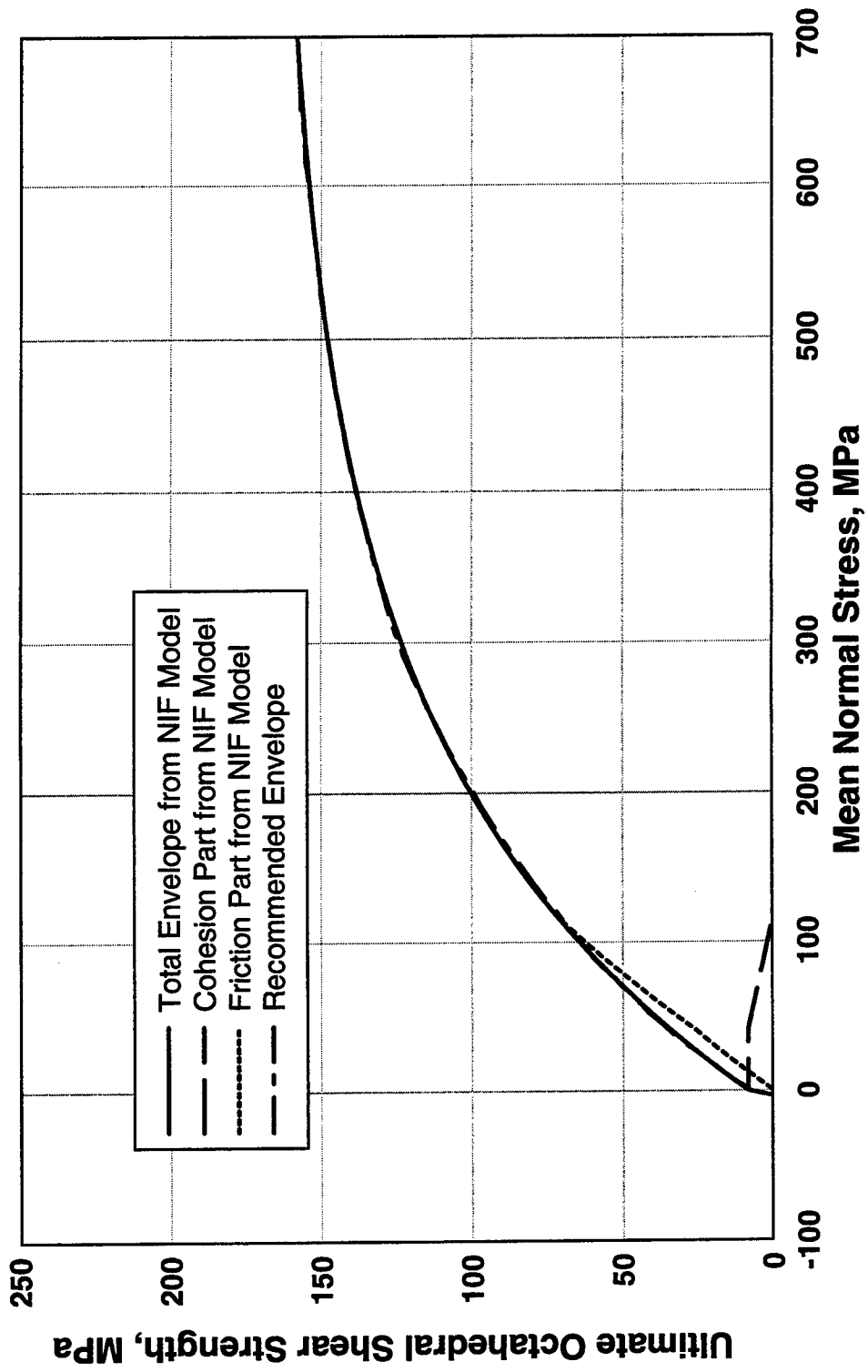


Figure 4.10. NIF model fit and recommended ultimate strength envelope.

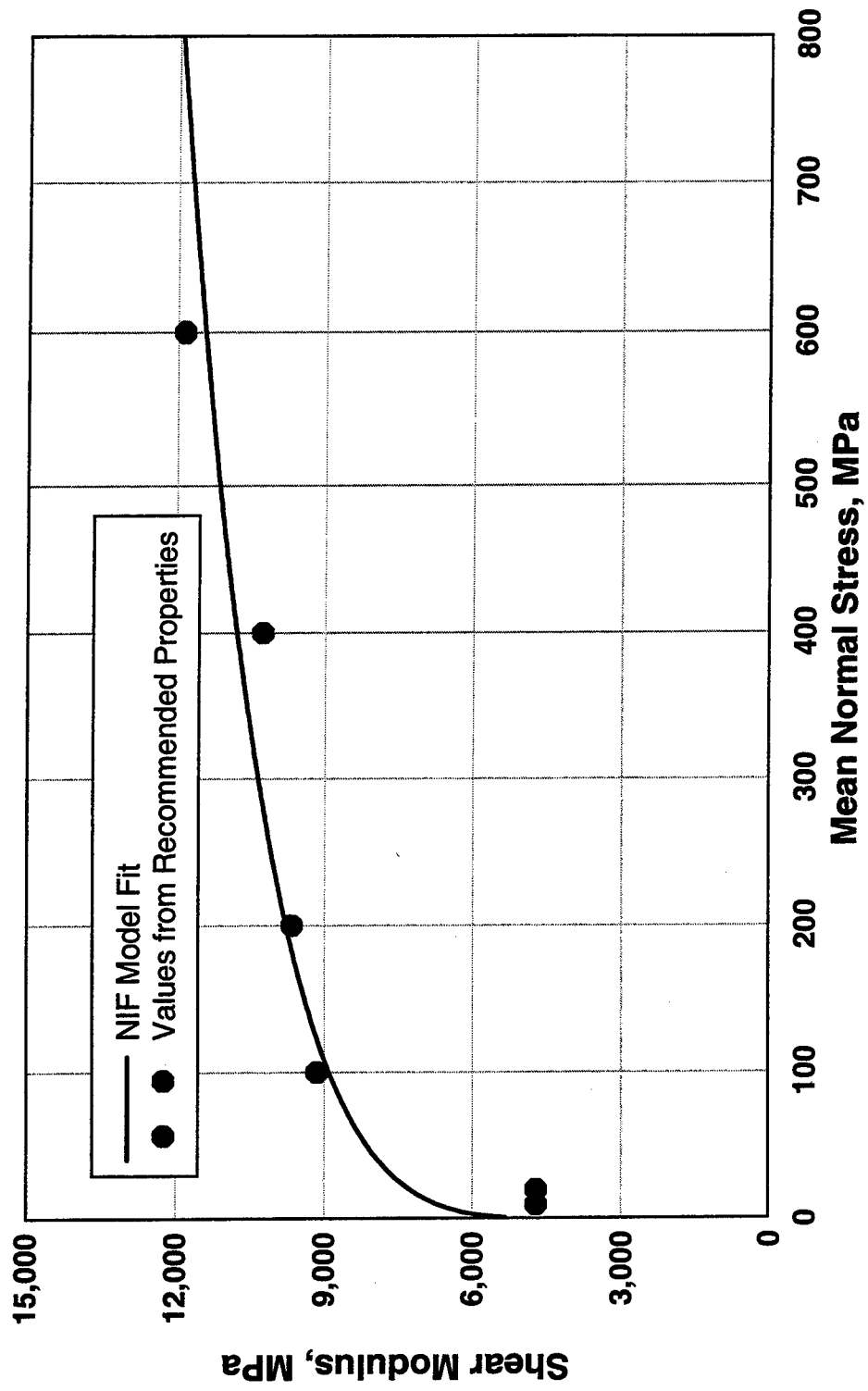


Figure 4.11. NIF model shear modulus and values obtained from the recommended CSPP concrete properties.

the friction part is included in all experiments for which recommended properties were provided. Using the shear modulus provided for the experiment at zero confining pressure (14000 MPa) should approximate this value. The last parameter required for the shear part of the model is  $N$ . The value of  $N$  should be based on the softening portion of a pure shear experiment conducted at zero pressure, for which little or no data exists. The recommended properties do not contain such data. An extrapolation for the softening portion of a dynamic unconfined compression experiment provided with the properties indicates that the strength is zero at about an  $N$  of 4. For lack of a better value, 4 will be used unless results from exercising the model indicate a change is needed. The nineteen constants for the NIF model fit to the CSPC concrete are summarized in Table 4.2.

A second concrete that was used in several projectile penetration experiments was also fit to the NIF model. The mix proportions for the WES5000 concrete are presented in Table 4.3. The procedure used to fit the model to this concrete are the same as those used to fit the model to the CSPC concrete. The nineteen constants for the NIF model fit to the WES5000 concrete are summarized in Table 4.4.

#### 4.4 MODEL DRIVER

The NIF model has now been "fit" to a set of recommended properties by determining the numerical values for each of the model constants. The next step in determining the adequacy of the model and the quality of the fit is to use a computer code containing the model (referred to as a model driver) to drive, or exercise, the model along loading paths to which the model has been fit, and paths which can demonstrate the level of robustness of the model. The driver can also be used to make adjustments to the model parameters to provide better agreement with the recommended properties. If a particular loading path has been found to be prominent in the problem for which the model will be used, adjustments can be made to appropriate model parameters to better replicate that path. The response along other loading paths may be sacrificed, if necessary, in doing this and must be checked for adequacy.



Table 4.2. Summary of NIF model constants for the CSPC concrete.

NIF Model Constant	Constant Value
$K_e$	17,900 MPa
$\epsilon_{vc}$	0.0003
$\epsilon_{vf}$	0.0012
$\sigma_{mc}$	3.4 MPa
$\sigma_{mf}$	0.9 MPa
$(\epsilon_v)_{crush}$	0.00229
$a$	6,244.15 MPa
$b$	-47,387.5 MPa
$c$	1,212,580.0 MPa
$K_{lock}$	74,100 MPa
$(\epsilon_v)_{lock}$	0.0798
$b_0$	2,530.21
$b_1$	0.192653
$b_2$	2,758.62 MPa
$A$	165.197 MPa
$B$	-0.0044034265 MPa <sup>-1</sup>
$C$	156.913 MPa
$\mu_c$	14,000 MPa
$N$	4

Table 4.3. Ingredients and mixture proportions for WES5000 concrete.

Item	Mixture Proportions, Saturated Surface-Dry
Type I portland cement	264.0 kg/m <sup>3</sup>
Fly ash	55.8 kg/m <sup>3</sup>
9.5-mm local unprocessed chert coarse aggregate	1,037.6 kg/m <sup>3</sup>
Local unprocessed chert fine aggregate	840.7 kg/m <sup>3</sup>
Water	145.9 kg/m <sup>3</sup>
Water reducing admixture "300N"	0.65 l/m <sup>3</sup>
High-range water reducing admixture "Rheobuild 716"	1.6 l/m <sup>3</sup>

w/c = 0.46

Table 4.4. Summary of NIF model constants for the WES5000 concrete.

NIF Model Constant	Constant Value
$K_e$	18,130 MPa
$\epsilon_{vc}$	0.00032
$\epsilon_{vf}$	0.00128
$\sigma_{mc}$	3.4 MPa
$\sigma_{mf}$	0.9 MPa
$(\epsilon_v)_{crush}$	0.0039
$a$	9,811.49 MPa
$b$	-64,658.8 MPa
$c$	772,978.9 MPa
$K_{lock}$	66,000 MPa
$(\epsilon_v)_{lock}$	0.14935
$b_0$	1,539.17
$b_1$	0.2175
$b_2$	2,758.62 MPa
$A$	298.831 MPa
$B$	-0.002423 MPa <sup>-1</sup>
$C$	287.568 MPa
$\mu_c$	12,750 MPa
$N$	4

The driver is a computer program that runs on a PC that can exercise the model along any prescribed stress or strain load/unload/reload path. An undocumented program obtained from Akers (1992) was modified for this purpose. The model has been developed to accept strains as input in order to obtain the corresponding stresses. The driver has been set up so that either stress or strain paths can be prescribed.

The total strain based on the original configuration of the material will be supplied to the model. The sequence of operation of the model is to first calculate the current pressure based on the current volumetric strain. In the driver, the volumetric strain is calculated using Equation 4.6. The criteria described above in Section 4.3 are followed to determine whether the material is loading, unloading or reloading. Once the pressure has been determined, the deviatoric part is calculated following the criteria for loading, unloading, and reloading described above. Equation 4.17 is then used to determine the individual stress components. The coding of the subroutine containing the NIF model that is used in EPIC (provided in the Appendix) is essentially the same as the coding used in the driver.

A comparison of the model driver and the recommended pressure-volumetric strain response for the CSPC concrete is shown in Figure 4.12. Results from the model driver compare well with the recommended response for initial loading. The unloadings from the model driver do not agree as closely since the model currently has no mechanism to allow for the hysteresis that occurs as the pressure approaches zero. A comparison of the model driver and the recommended response for constant confining pressure triaxial shear (CTC) experiments is shown in Figure 4.13.a as principal stress difference ( $\sigma_{diff}$ ) vs principal strain difference ( $\epsilon_{diff}$ ) and Figure 4.13.b as principal stress difference vs axial strain during the shear phase where

$$\sigma_{diff} = \sqrt{3J_2} \quad 4.38$$

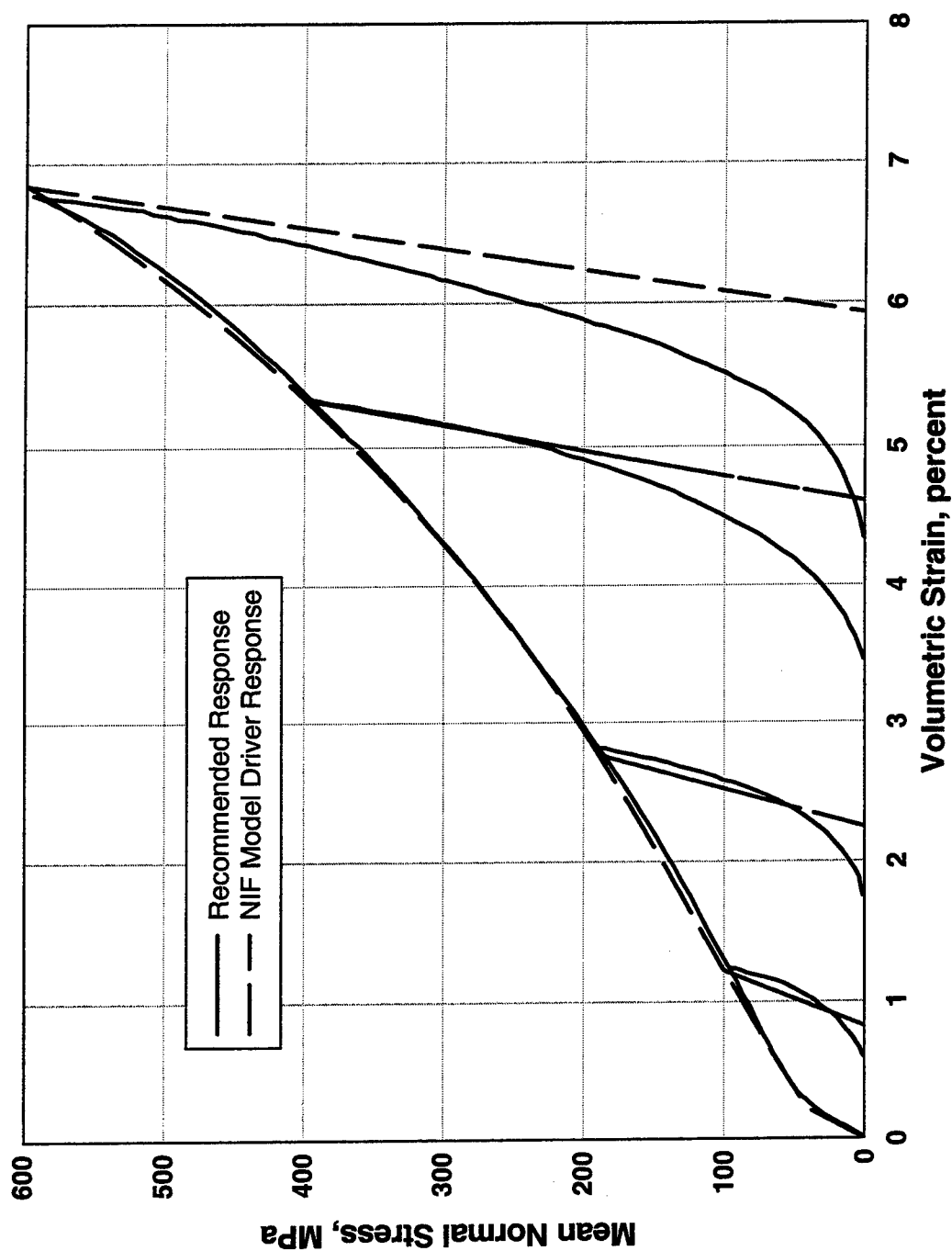


Figure 4.12. Comparison of NIF model driver and recommended response for hydrostatic compression.

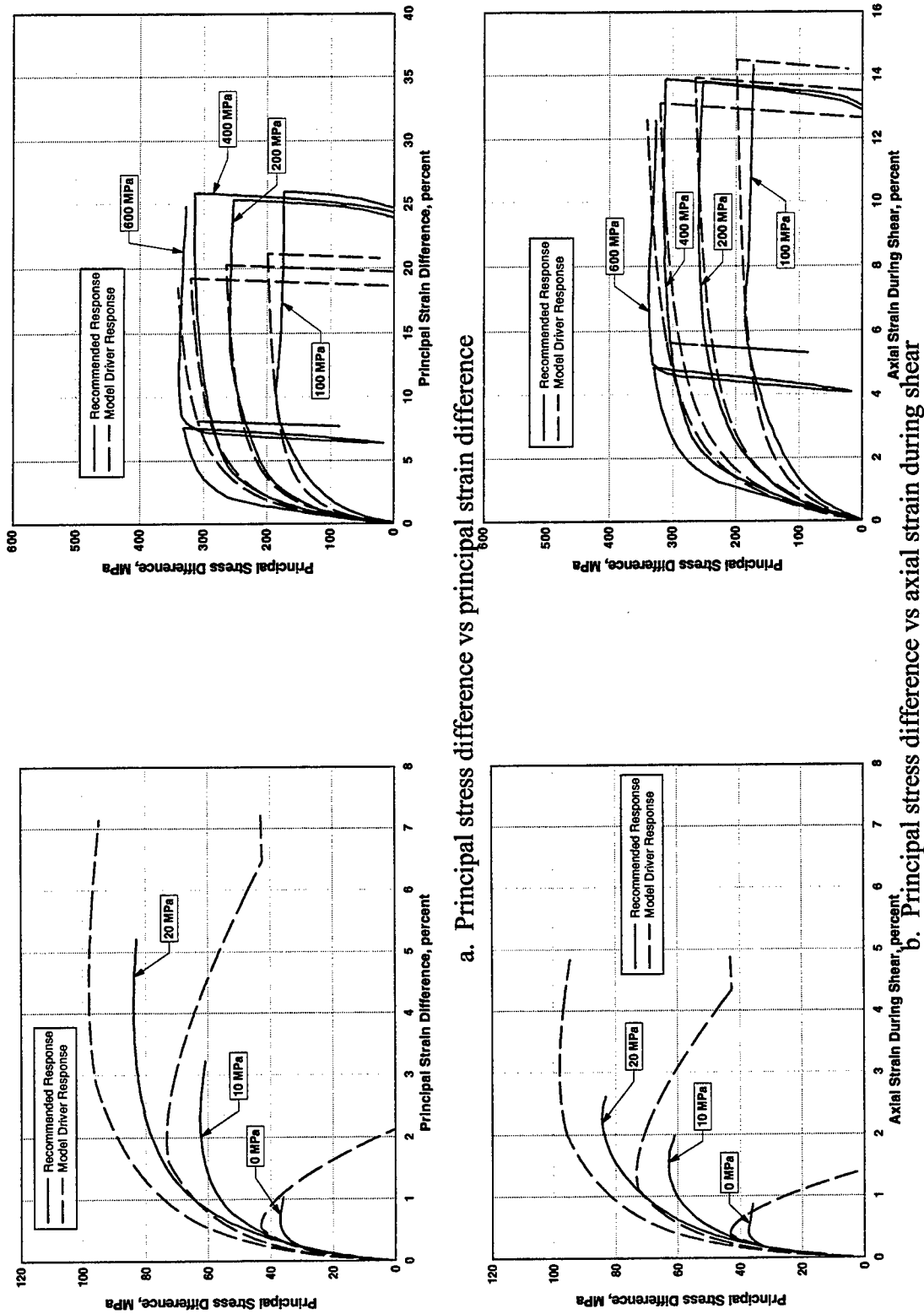


Figure 4.13. Comparison of NIF model driver and recommended responses for CTC experiments.

and

$$\epsilon_{diff} = \sqrt{3I_2} \quad 4.39$$

The model driver agrees reasonably well with the recommended responses. Figure 4.13 also illustrates the capacity of the model to simulate the transition from brittle to ductile response.

A comparison of the model driver response and the experiment results from Figure 3.12 are shown in Figure 4.14 for a uniaxial state of stress. The model agrees well with the axial stress versus lateral and axial strain to peak stress. The model also shows higher values of axial strain than radial strain similar to the experiment results. The model response then softens, but the softening portion from the experiment was not recorded. The axial stress versus volumetric strain from the model is stiffer than the experiment results and does not show a tendency to dilate near the peak. One explanation for this response is that the experiment is less "controlled" than the driver in that the driver adjusts the lateral strain in an attempt to maintain zero radial stress.

An additional loading path provided with the recommended responses is a uniaxial strain loading in compression. A comparison between the model driver and the recommended response is shown in Figure 4.15. The axial stress vs axial strain responses agree well, but the principal stress difference vs mean normal stress (pressure) response from the model driver is slightly below the recommended response. Unloading under uniaxial strain conditions results in unloading in both pressure and shear. This results in some hysteresis within the model since the shear modulus is changing as the pressure changes, particularly once the principal stress difference reaches zero. The model response shows continued unloading resulting in the "J-shape" of the stress path in the negative principal stress difference regime (obtainable since the specimen is assumed to be axisymmetric). Data to support this response is not available for CSPC concrete, but similar responses have been observed for clayey sands (Figure 4.16).

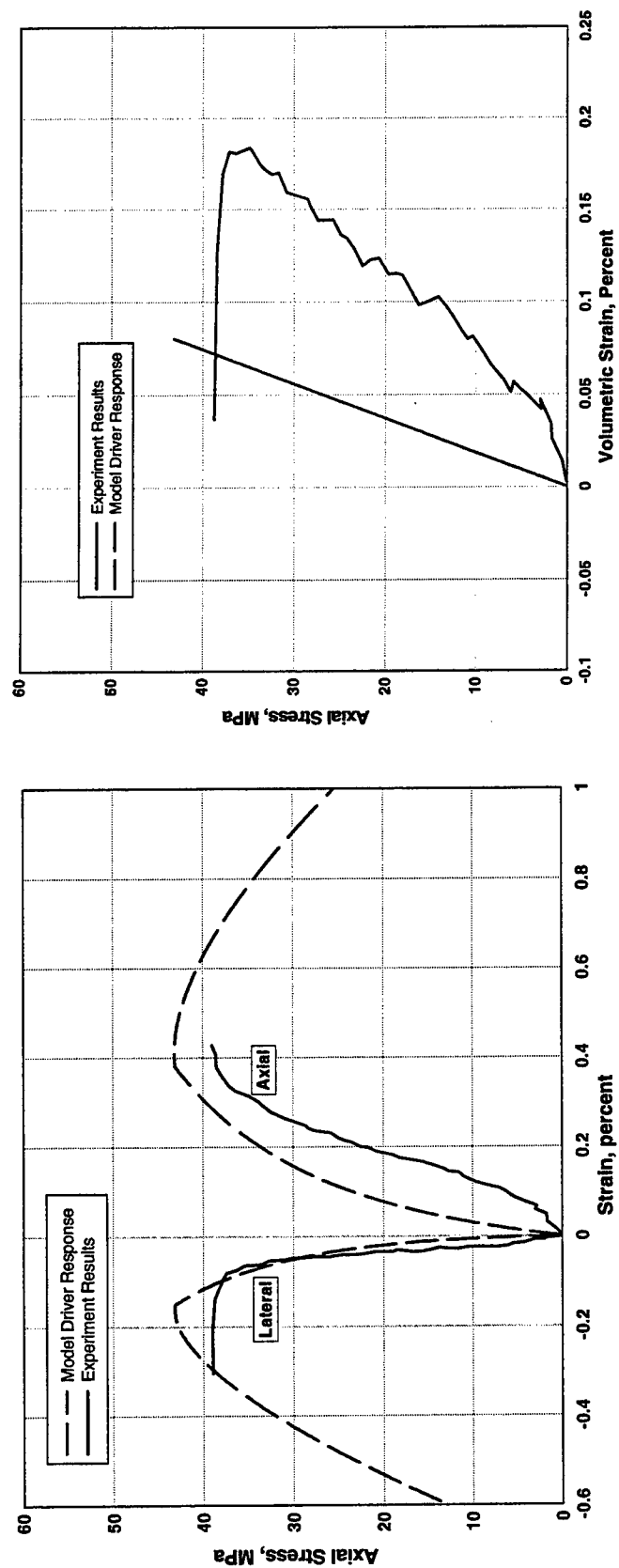


Figure 4.14. Comparison of NIF model driver and experiment results for an unconfined compression experiment.



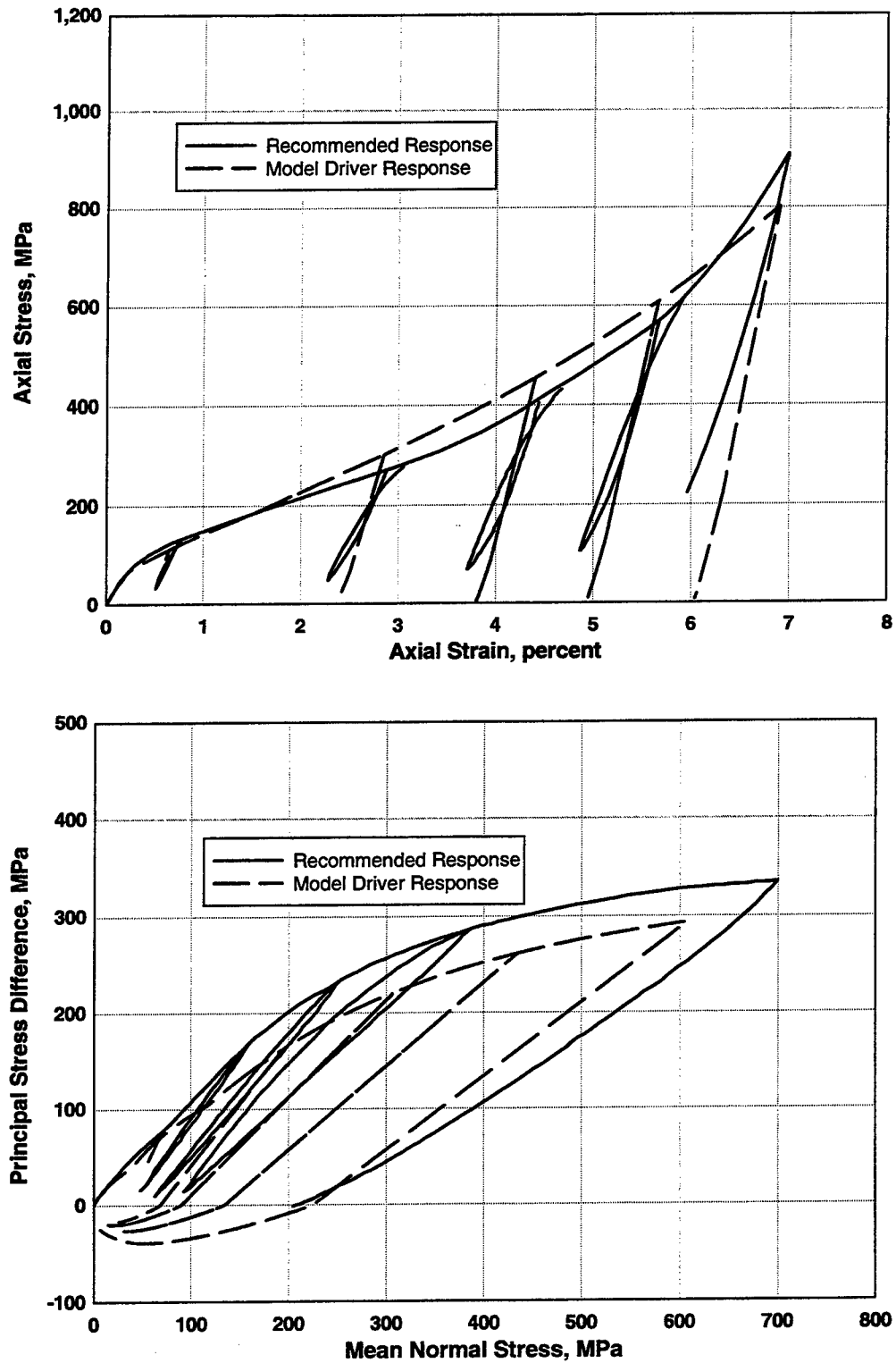


Figure 4.15. Comparison of NIF model driver and recommended responses for uniaxial strain loading.

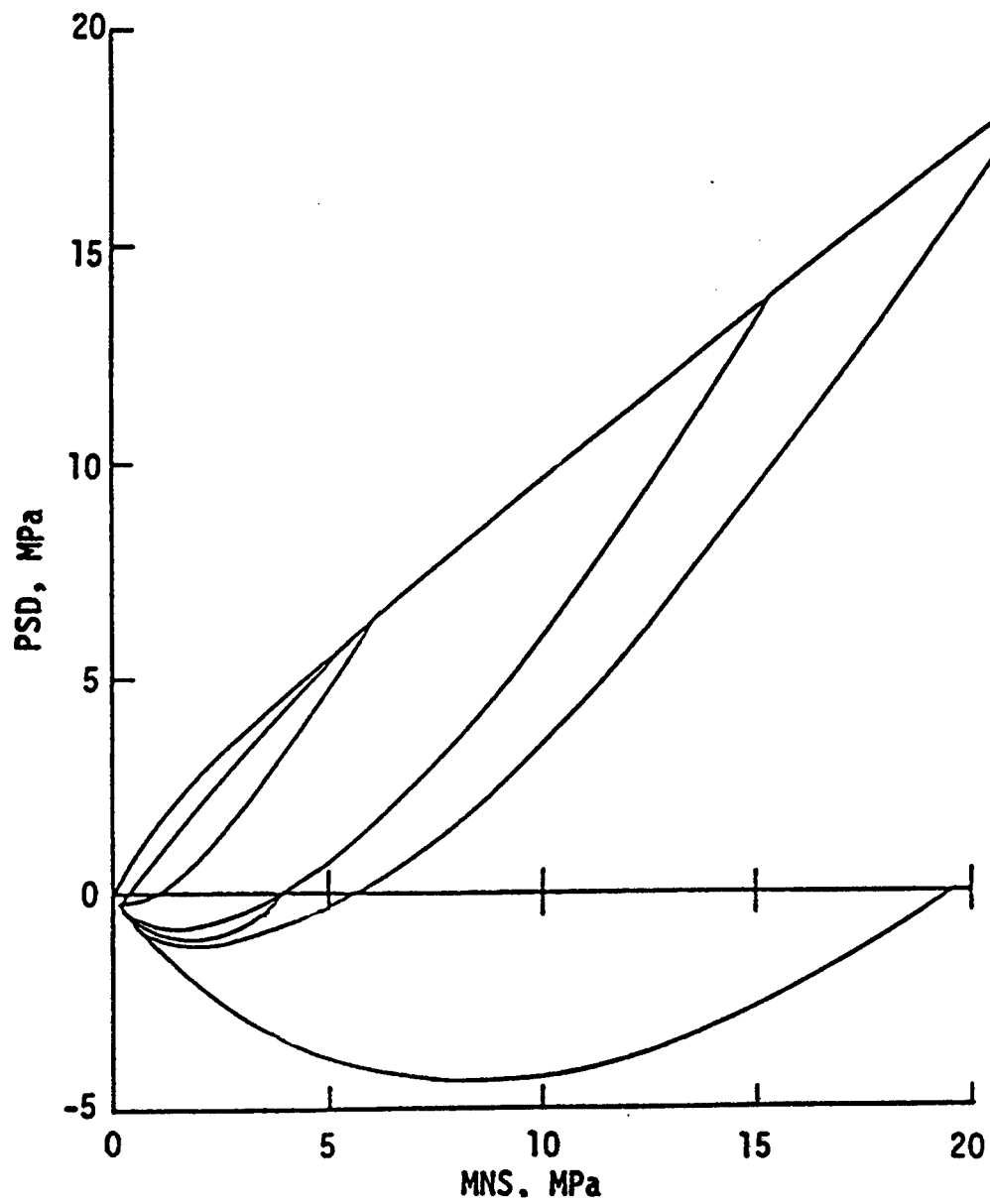
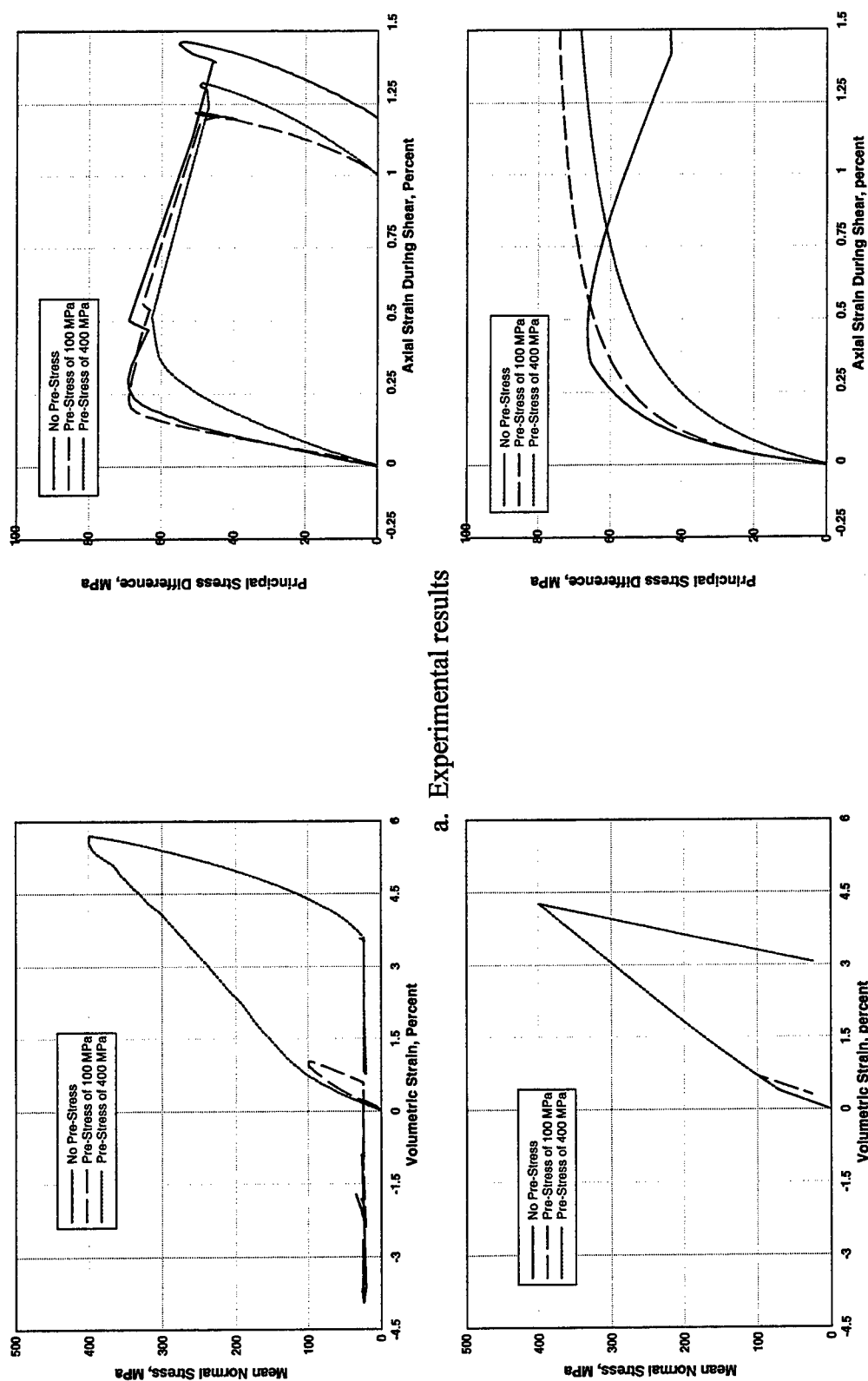


Figure 4.16. Uniaxial strain stress paths for experiments conducted on a clayey sand (Cargile 1986).

Although not used to fit the model, constant pressure (TC) experiments were conducted on specimens of the WES5000 concrete. Results from experiments and the model driver at constant pressures of 25 MPa after pre-stresses of 0, 100, and 400 MPa are shown in Figure 4.17. The experiment results show that a pressure of 25 MPa is below the crush pressure for these specimens, 100 MPa is close to the crush pressure, and 400 MPa is well beyond the crush pressure and may be close to or beyond the friction pressure. Results from pre-stress experiments of 0 and 100 MPa are similar. But the pre-stress of 400 MPa resulted in a softer shear response and slightly lower strength. The model driver indicates the pre-stress of 100 MPa is beyond the crush pressure and 400 MPa is beyond the friction pressure. The model driver therefore results in a softer shear response as the pre-stress increases, and a slightly higher ultimate strength since the value of  $\gamma_c$  increases as pressure. Unlike the experiment results, the model driver does not indicate dilation since the test boundary conditions imply zero change in volumetric strain for constant pressure. Results from experiments and the model driver at a constant pressure of 100 MPa after pre-stresses of 0 and 400 MPa are shown in Figure 4.18. The experiment results show a slightly stiffer response for the pre-stressed material. The pressure-volumetric strain response for the pre-stressed material is stiffer than the response for the non-prestressed material, which may explain the difference. The model driver shows a softer response for the pre-stressed material, which results from the loss of cohesion and increase in  $\gamma_c$  as the pressure increased, and the assumption that unloading does not "heal" the material.



b. NIF model driver

Figure 4.17. Comparison of NIF model driver and experiment results for TC experiments at 25 MPa after pre-stresses of 0, 100, and 400 MPa.

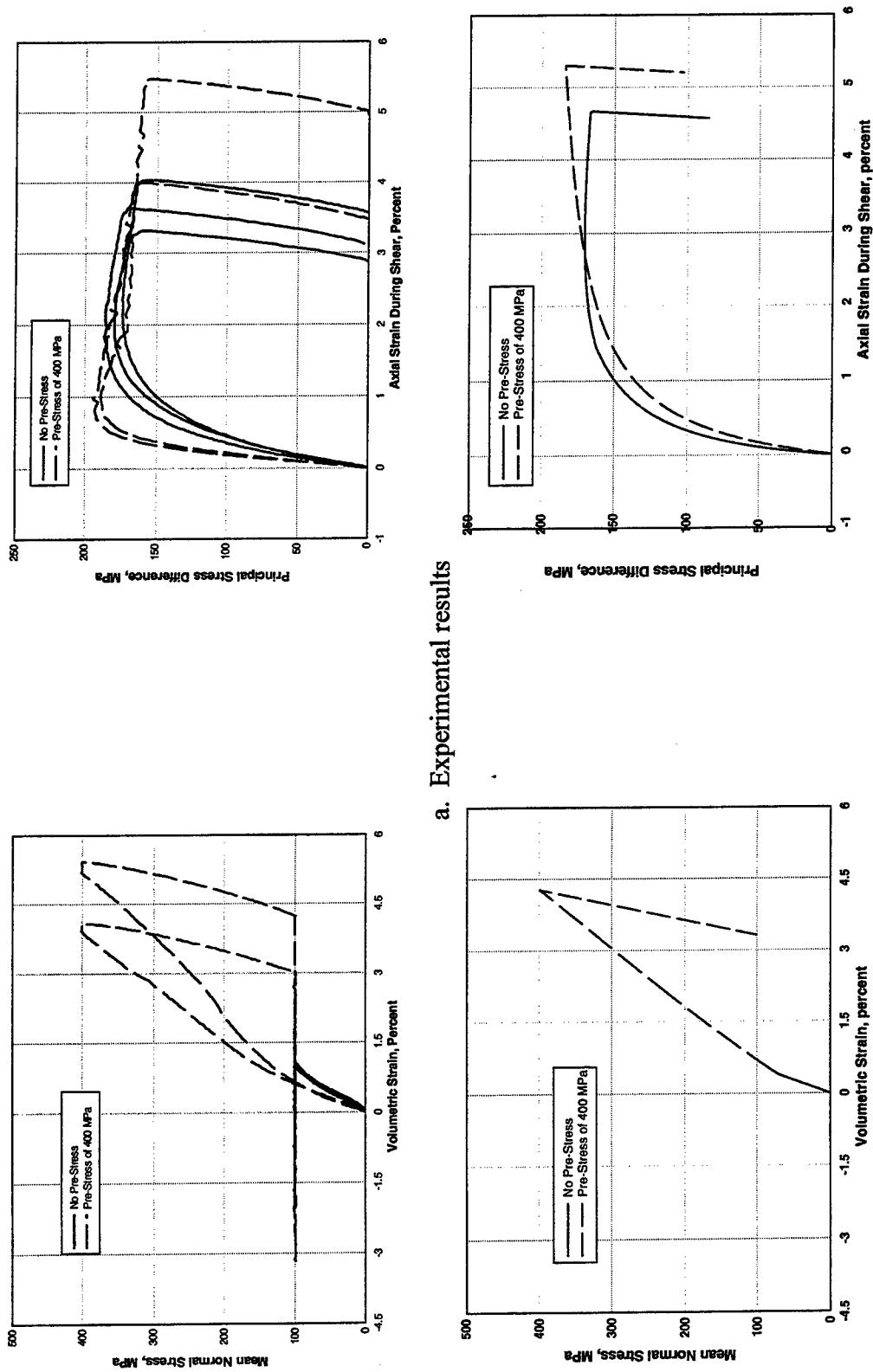


Figure 4.18. Comparison of NIF model driver and experiment results for TC experiments at 100 MPa after pre-stresses of 0 and 400 MPa.

## CHAPTER 5

### FINITE-ELEMENT CODE IMPLEMENTATION AND EVALUATION

#### 5.1 FINITE-ELEMENT CODE IMPLEMENTATION

The constitutive model developed in Chapter 4 must now be implemented into a numerical computer code in order to be a useful tool. The computer code selected for this purpose is the EPIC code (Johnson, et. al. 1994). This process involves the implementation of algorithms to calculate the correct strain input to the model and to convert the stress output by the model into a compatible form accepted by the code. The NIF model has been developed based on the assumption that the strain input to the model is the total strain related to the original configuration (total change in length/original length) and the output stress is the Cauchy stress aligned with the original configuration. The output stress will need to be rotated to the current configuration of the element to be compatible with the kinematics of the code. Other issues that will be addressed are the use of artificial viscosity and criteria for elimination of highly distorted elements from a simulation.

The EPIC code is capable of solving two- and three-dimensional projectile impact and penetration problems. The code has several element options and a material model library for several materials typically encountered in these types of problems. All of the available models for geomaterials are based on plasticity concepts. The code can account for the sliding interface between projectile and target and can erode highly deformed elements. The computational flow of the code is shown schematically in Figure 5.1 (Johnson, et. al. 1978). The geometry of the problem is first represented with elements. The mass of the material contained in each element is then lumped at the nodes and

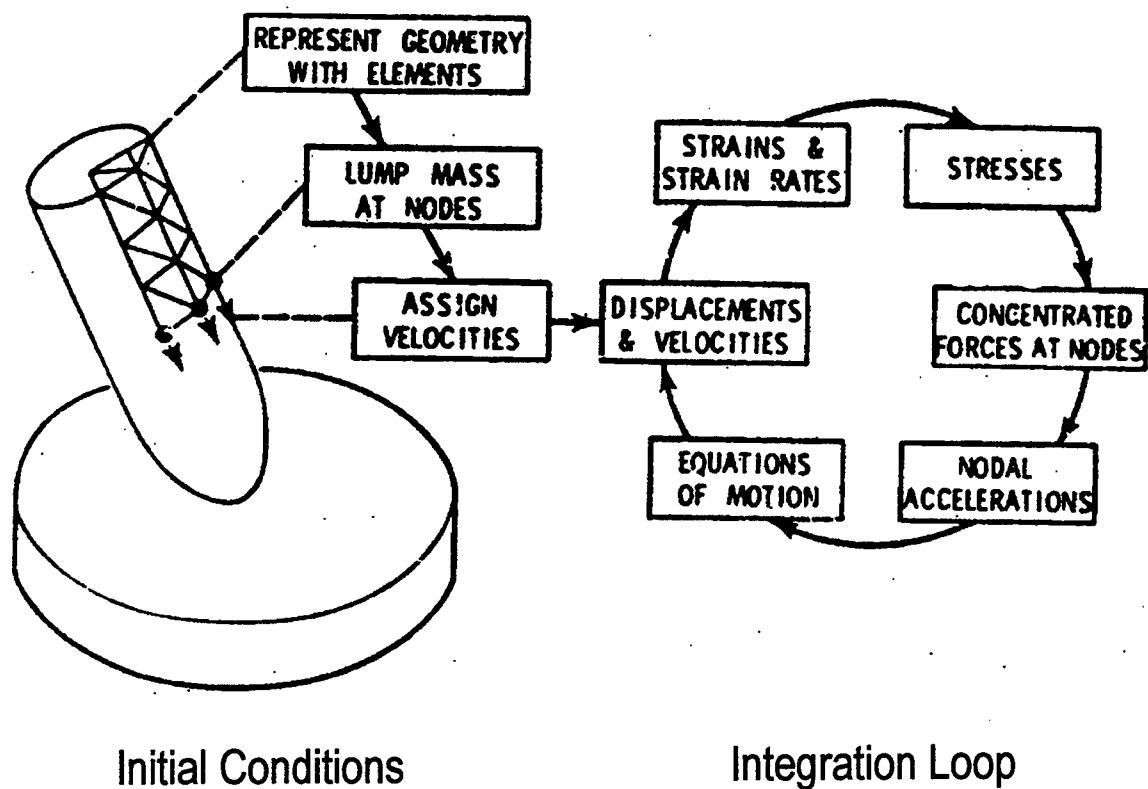


Figure 5.1. Computational technique used in EPIC (Johnson, et al. 1978).

velocities are assigned. The velocities are used to obtain the displacements and the strains and strain rates are calculated. The stresses within the element are then calculated using the mathematical material model. The stresses are converted into concentrated forces at the nodes and the nodal accelerations are calculated using Newton's equations of motion. The equations of motion are evaluated to determine the updated velocities at the nodes and the process is repeated until a termination criterion (maximum time) is met. In this scheme, the NIF model will be used in the computation of the stresses within the element consisting of a brittle geomaterial. Models used for computing stresses within the projectile will not be altered.

#### 5.1.1 Calculation of Strain and Stress

The EPIC code is based on an explicit Lagrangian finite-element formulation where the equations of motion are integrated directly. This eliminates the need for the traditional stiffness matrix approach. The general form of the code uses an updated Lagrangian-Jaumann kinematic formulation to account for the finite strains. This formulation uses the Cauchy stress ( $\sigma$ ) and the rate of deformation ( $\mathbf{D}$ ), respectively, as the stress and strain measure, and the Jaumann stress rate tensor as the objective stress rate. The frame of reference is the current configuration of the body.

The total Lagrangian kinematic formulation (Adley, et. al. 1996) that will be used to implement the NIF model into EPIC will use the Green-Lagrange strain as input to the model. The non-conjugate Cauchy stress associated with the original orientation ( $\sigma^R$ ) will be output by the model (Bazant 1996 and Bazant, et. al. 1996).

The Green-Lagrange strain required as input to the NIF model will be computed as follows using the rate of deformation tensor ( $\mathbf{D}$ ) and the spin tensor ( $\mathbf{W}$ ) that are calculated by the code. The spatial velocity gradient ( $\mathbf{L}$ ) is related to the deformation



gradient ( $F$ ) by

$$\dot{F} = L F \quad 5.1$$

where

$$L = D + W \quad 5.2$$

Assuming that  $L$  is constant during the current time step, Equation 5.1 has as a solution at the current time ( $t$ )

$$F(t) = F_n \exp[L(t - t_n)] \quad 5.3$$

where  $F_n$  is the value of  $F$  at the end of the preceding time step ( $t_n$ ). The exponential function in Equation 5.3 can be approximated by the Taylor series expansion as

$$\exp[L(t - t_n)] = I + L(t - t_n) + \frac{1}{2}L^2(t - t_n)^2 + \dots \quad 5.4$$

where  $I$  is the identity matrix and higher order terms are not considered since the time increment is very small for the problems of interest. The increment of  $F$  during the current time step ( $\Delta F$ ) is then calculated as

$$\Delta F = F(t) - F(t_n) = F_n \left( L \Delta t + \frac{1}{2} L^2 \Delta t^2 \right) \quad 5.5$$

where  $\Delta t = t - t_n$ . The Green-Lagrange strain ( $\epsilon$ ) at the current time can then be calculated as

$$\epsilon = \frac{1}{2}(F^T F - I) \quad 5.6$$

with  $F = F_n + \Delta F$  where  $F_n$  is the deformation gradient at the previous time. Note that the off-diagonal terms in  $\epsilon$  are the tensorial values of the shear strain, i.e.,  $\epsilon_{12} = \gamma_{12} / 2$ . These strains will be used in the NIF model to calculate the Cauchy stresses associated with the original configuration ( $\sigma^R$ ).

The stresses calculated by the NIF model must be rotated back to the current configuration before continuing within the EPIC code. The transformation used is

$$\sigma = R \sigma^R R^T \quad 5.7$$

The rotation matrix ( $R$ ) can be determined from information contained within EPIC using an equation based on the relationship between  $F$  and the left-hand stretch tensor ( $V$ ) ( $F = VR$ ) developed by Anderson, et. al. (1994) as

$$R_{t+\Delta t} = \left( I - \frac{1}{2} \Delta t W \right)^{-1} \left( I + \frac{1}{2} \Delta t W \right) R_t \quad 5.8$$

The spin tensor ( $W$ ) can be obtained in EPIC from the nodal velocity ( $v$ ) as

$$W_{ij} = \frac{1}{2} \left( \frac{\partial v_i}{\partial y_j} - \frac{\partial v_j}{\partial y_i} \right) \quad 5.9$$

The updated rotation tensor from Equation 5.8 is used in Equation 5.7 to calculate the Cauchy stress related to the current configuration of the element.

### 5.1.2 NIF Model Subroutine

The subroutine (NIF) used to implement the NIF model into the EPIC code is presented in the Appendix. The first part of the subroutine consists of the DIMENSION and PARAMETER statements required by the subroutine. Constants that will be used in the subroutine and the NIF model constants are then assigned to the code variables. All of the code variable names assigned to the material constants begin with an "A" only as a matter of convenience. The next section of the subroutine computes the total stresses and stress increments from the previous time for use in an energy calculation later in the subroutine. The next section of the subroutine uses the procedures outlined in Section 5.1.1 to calculate the Green-Lagrange strains and the rotation matrix.

The volumetric strain input to the model for calculation of the pressure is the volumetric strain calculated within the EPIC code based on the deformation of the element. An additional variable computed as part of the model is EBAR. This variable will be used to determine when an element has deformed to an extent that it no longer can provide meaningful resistance to the applied deformations, and may be controlling the computational speed of the simulation due to its small aspect ratio. The variable is calculated in shear as the ratio of the current value of  $\gamma_{oct} / \gamma_c$ . Since failure can also occur in hydrostatic tension, a similar quantity is calculated as  $\epsilon_v / \epsilon_{vc}$ . The maximum of the two quantities is assigned to EBAR. EBAR in essence tracks how far beyond the critical strain at the start of softening the material has strained. EBAR is checked against a user input ( $EBAR_{crit}$ ) to determine if the element is to be removed from the calculation by setting all stresses to zero, but retaining the mass of the element at the nodes. An advantage to this approach is that EBAR becomes dependant on the current state of stress within the element and is not simply a scalar value that checks the state of plastic strain within the element, which is commonly used. At high pressures, the use of plastic strain as the check may prematurely eliminate elements that are still providing a significant resistance to deformation. The above calculation of EBAR will result in a criterion at high pressures that is larger than the criterion at low pressures which makes more sense from a physical standpoint.

An artificial viscosity ( $Q$ ) is also used with the model. The artificial viscosity is applied to the normal stresses to damp out localized oscillations of the concentrated masses that might otherwise occur during wave propagation problems. The approach used is the original method contained in the EPIC code (Johnson, et. al. 1997). The equation for  $Q$  contains linear and quadratic components and is expressed as

$$Q = C_L \rho c_s h \left| \dot{\epsilon}_v \right| + C_Q \rho h^2 (\dot{\epsilon}_v)^2 \quad 5.10$$

where  $C_L$  and  $C_Q$  are the linear and quadratic dimensionless coefficients, respectively,  $\rho$  is the density,  $c_s$  is the sound velocity of the material, and  $h$  is the minimum altitude of the

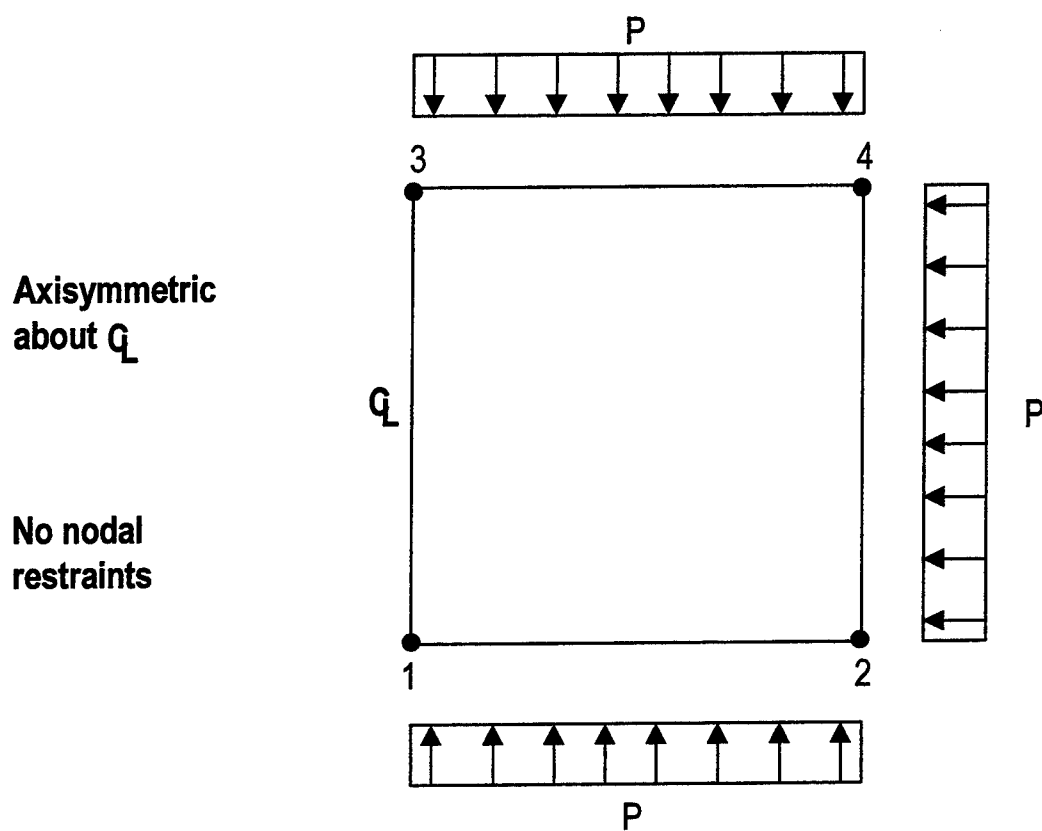
element. Equation 5.10 is only applied if the volumetric strain rate ( $\dot{\epsilon}_v$ ) is compressive. The value of  $Q$  is a pressure that is added to the total normal stresses output from the NIF model when the element is being compressed. When the element is expanding, no artificial viscosity is applied. Values of 1.75 for  $C_L$  and 14.0 for  $C_Q$  give smooth results for one-dimensional wave propagation calculations using the model.

## 5.2 MODEL IMPLEMENTATION EVALUATION

The NIF model as implemented into the EPIC code must be evaluated to ensure that the implementation yields the desired results. This evaluation will consist of exercising the model for a single element along prescribed boundary conditions to simulate a hydrostatic compression loading, an unconfined compression loading, and a uniaxial strain compression loading. Unload/reload cycles will also be included with some cycles proceeding into extension.

The element configuration and loading history for hydrostatic compression are shown in Figure 5.2. The simulation is for a single axisymmetric quad element with the integration point at the center of the element. Pressure applied to the three outer sides of the element varies with time to provide several unload/reload cycles to a maximum pressure of 600 MPa at a time of 0.00245 s. Results from the simulation are compared to the results from a similar loading using the NIF model driver in Figure 5.3. Both the EPIC simulation and the NIF model driver provide the same responses. Results from the EPIC simulation also show some of the unload cycles extending into the hydrostatic tension region where the pressure is limited to  $\sigma_{mc}$ .

The element configuration and loading history for unconfined compression are shown in Figure 5.4. The element configuration is the same as that for hydrostatic compression. The loading is applied by giving the nodes a compressive velocity equal to 101.6 mm/s over the duration of the simulation. Results from the EPIC simulation are



<u>t, s</u>	<u>P* 600 MPa</u>
0.00000	0
0.00030	0.16
0.00031	0
0.00050	0.33
0.00052	0
0.00100	0.50
0.00104	0
0.00245	1.0
0.00250	0

Figure 5.2. Single element configuration and loading history used in EPIC to check the NIF model for hydrostatic compression.

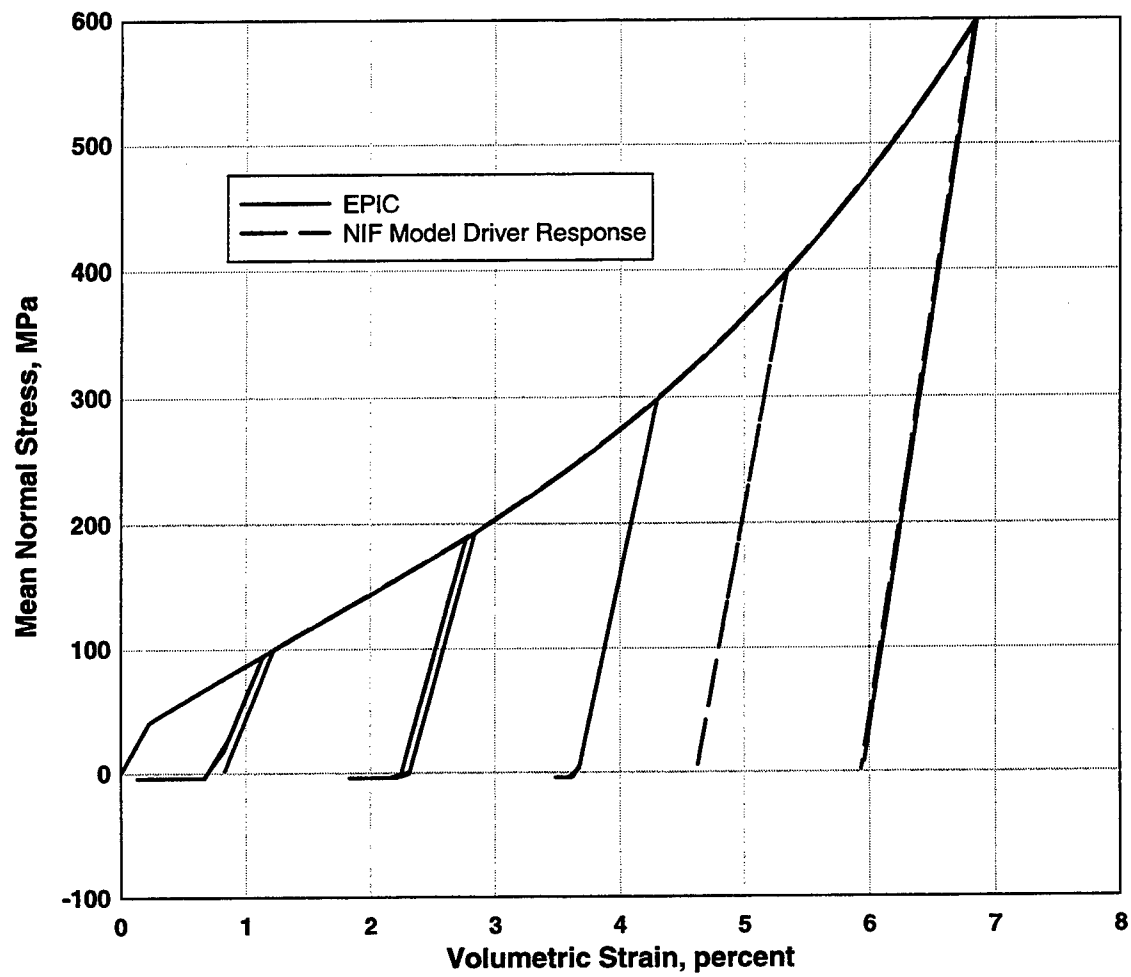


Figure 5.3. Comparison of the hydrostatic compression from EPIC and the NIF model driver.

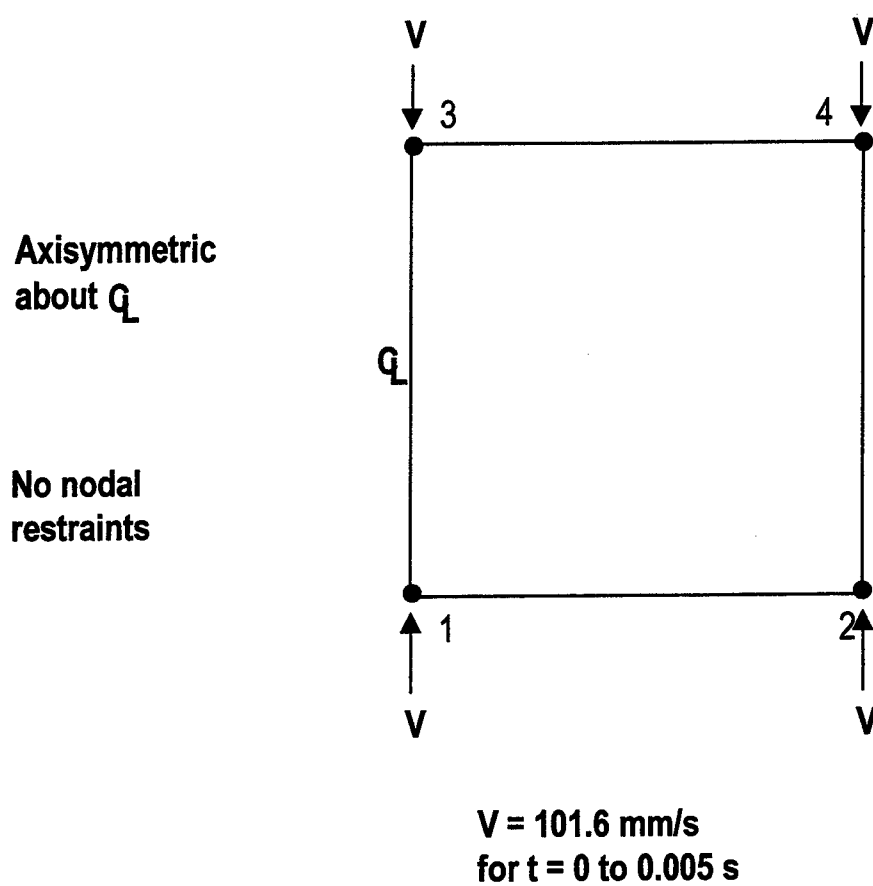


Figure 5.4. Single element configuration and loading used in EPIC to check the NIF model for unconfined compression.

compared to the results using the NIF model driver in Figure 5.5. Except for the point where the axial stress has reduced to zero during the softening phase, the results are very similar. The discrepancy at the end of the softening is believed to come from two sources. First is a small contribution by the artificial viscosity used in the EPIC simulation. Second is that the element is free to deform solely based on the resistance supplied by the model, but the applied velocity is constant in the vertical direction. This may act to introduce some "confinement" to the element.

The element configuration and loading history for uniaxial strain are shown in Figure 5.6. The element configuration is again a single axisymmetric quad, but the bottom nodes are constrained from moving and the top nodes are constrained in the lateral direction. The loading is applied by giving the top nodes a varying compressive velocity to provide unload/reload cycles to a maximum velocity equal to 30.4 m/s. Results from the EPIC simulation are compared to the results using the NIF model driver in Figure 5.7. Again, results from the EPIC simulation agree well with the results from the NIF model driver.

Based on the above simulations, the NIF model appears to be properly implemented into the EPIC code and functioning as expected. In the following chapter, simulations will be performed to evaluate using the NIF model in EPIC to simulate projectile penetration and perforation experiments.



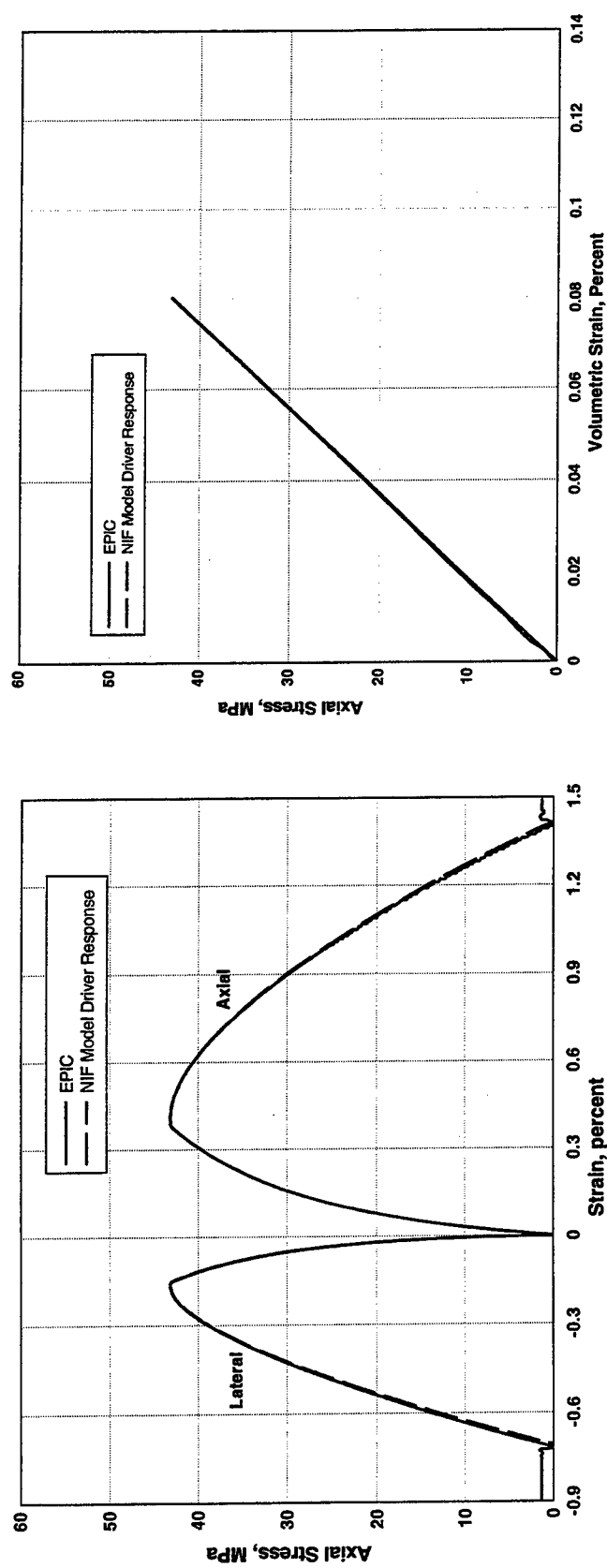
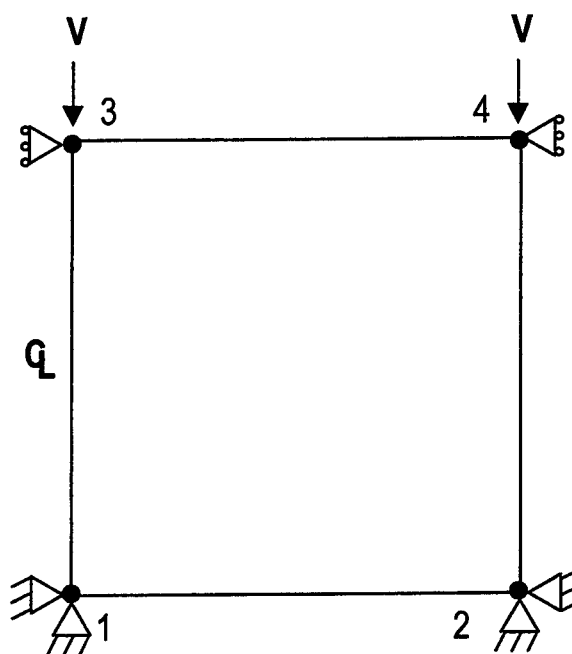


Figure 5.5. Comparison of unconfined compression from EPIC and the NIF model driver.

Axisymmetric  
about  $Q_L$



<u>t, s</u>	<u><math>V^* 3.8 \text{ m/s}</math></u>
0.00000	0.0
0.00020	1.0
0.00021	- 1.0
0.00040	2.0
0.00041	- 2.0
0.00075	4.0
0.00076	- 4.0
0.01490	8.0
0.01500	- 8.0

Figure 5.6. Single element configuration and loading used in EPIC to check the NIF model for uniaxial strain.

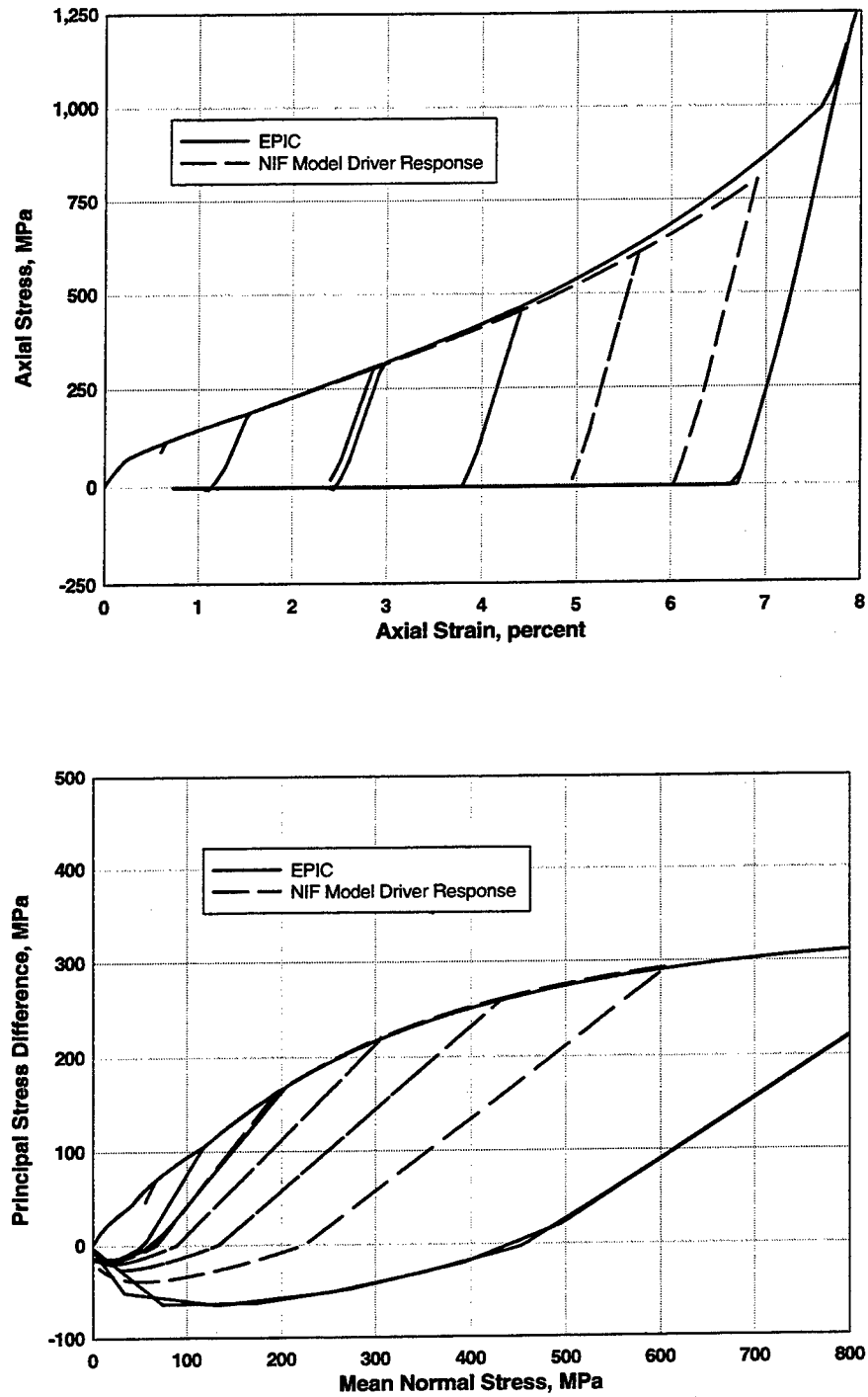


Figure 5.7. Comparison of uniaxial strain loading from EPIC and the NIF model driver.

## CHAPTER 6

### PENETRATION EXPERIMENTS AND NUMERICAL SIMULATIONS

#### 6.1 PENETRATION EXPERIMENTS

Performance of the NIF model in EPIC will be evaluated by comparing code simulations to the results from projectile penetration and perforation experiments. The experiments involved the launch of steel projectiles into concrete targets in the WES 83-mm ballistic range. Penetration experiments were conducted using a robust, thick-walled armor piercing (AP) projectile launched into semi-infinite (target thickness much greater than the penetration depth) CSPC concrete targets at impact velocities ranging from 277 to 800 m/s. Perforation experiments were conducted using a robust, semi-armor piercing (SAP) projectile launched into WES5000 concrete targets with thicknesses ranging from 127 to 284 mm. In both series of experiments the projectile sustained minimal damage. The following sections describe the WES 83-mm ballistic range and the results from the experiments.

##### 6.1.1 WES 83-mm Ballistic Range

The WES 83-mm Ballistic Range (Frew, et.al. 1993) consists of an 83-mm solid-propellant launcher, a mount to support and align the launcher, a blast tank, a sabot separator system, a drift tube assembly, and a target room as shown in Figure 6.1. The 83-mm "gun" is capable of launching projectiles with masses up to 2.8 kg at velocities in excess of 2 km/s and projectiles with masses of 12 kg or more at velocities of 1 km/s. At the downstream end of the launch tube a vented section extends into the blast tank. The vents (large ports cut into the tube wall) allow the accelerating gases to expand laterally

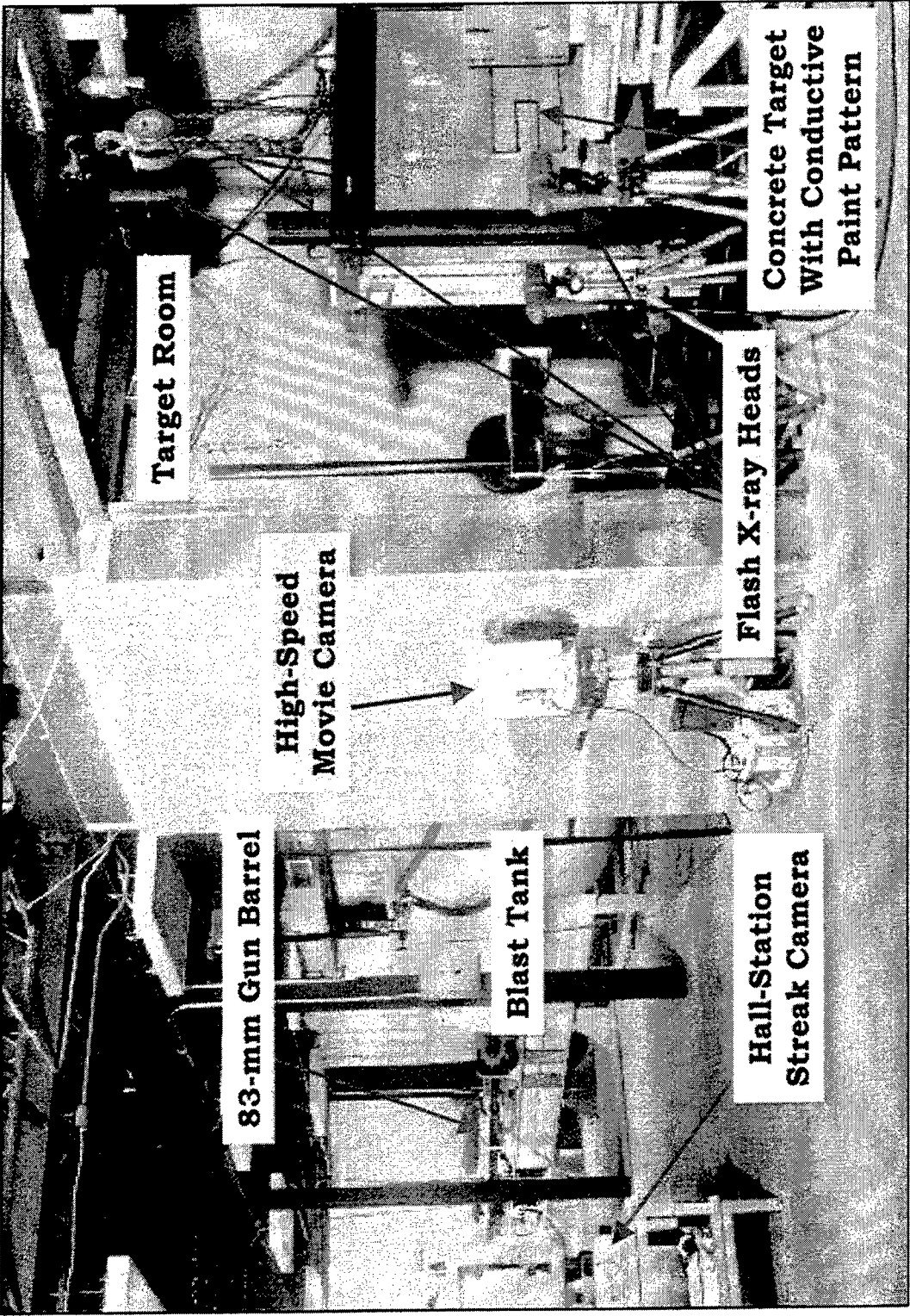


Figure 6.1. WES projectile penetration research facility.

into the blast tank. The effect of the vent section is to terminate projectile acceleration and muzzle the sound. The blast tank contains two central baffles used to break up large gas flows and is equipped with a ventilation system to remove the explosive gas after the test. The projectile travels down the launch tube in a hard plastic sabot. The sabot can either be stripped using a sabot separator system, stripped aerodynamically or left on the projectile. The sabot separator system consists of a gasdynamic tube and impact tank. The gasdynamic tube is an extension of the launch tube with provisions to seal each end of the tube. The gasdynamic tube can be operated at atmospheric pressure or pressurized at levels up to 2.0 atm. A sabot impact tank is used to intercept and pulverize oncoming sabots while allowing projectiles to pass through the drift tube and into the target room unimpeded. If stripped aerodynamically, the multi-piece sabot folds away from the projectile as it is traveling in the target room. The sabot can then be allowed to impact the target and be destroyed, usually without causing damage to the target, or steel plates can be used to pulverize and deflect the sabot before it impacts the target.

The velocity measurement system of the range consists of a Hall Intervalometer System which is located alongside the drift tube. It is used to determine both the projectile velocity and orientation. A pair of shadowgrams from orthogonal viewing angles are recorded by a streak camera as the projectile passes each of two stations along the drift tube. Figure 6.2 is an example of the type of photograph which is recorded with the streak camera. The photograph shows top and side views of the projectile at two stations that are 0.75 metres apart. A time reference is supplied by timing marks placed along the sides of the film using a time code generator. Measurements at each station are used to determine the velocity and yaw rate of the projectile in free flight with accuracies of 0.2 percent and  $\pm 1$  degree, respectively.

Targets are housed in a 5.6-m-long by 4.6-m-wide by 3.0-m-high reinforced-concrete enclosed target room. Viewing ports on the side and in the ceiling of the room permit high-speed motion pictures of projectile/target interaction; flash x-ray heads and breakscreens can be located freely within the room for additional experiment diagnostics.

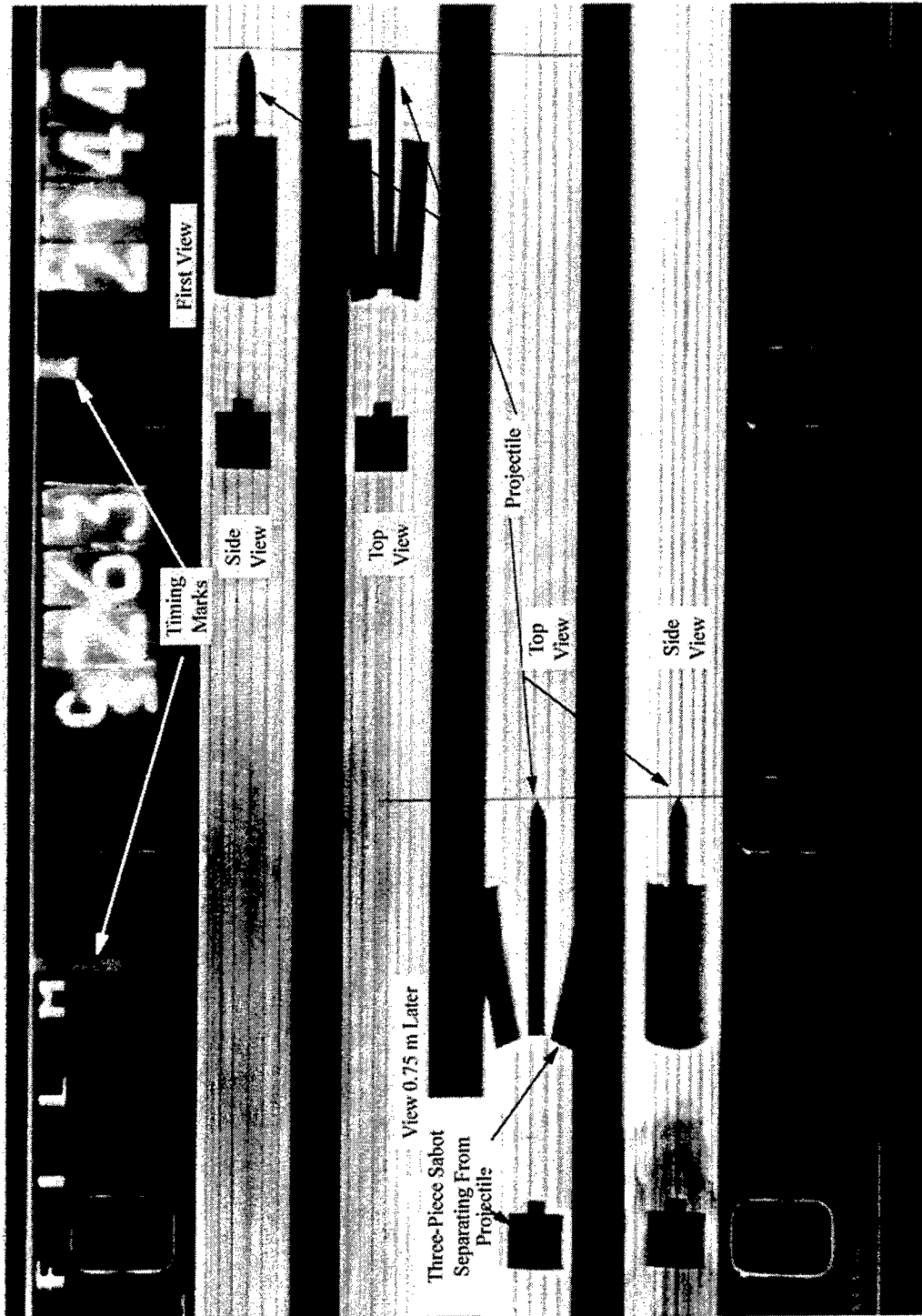


Figure 6.2. Section of film from the streak camera showing the projectile (Frew et. al 1993).

A penetration experiment typically involves the launch of a steel projectile into a target consisting of geologic and/or man-made materials contained within steel culverts. Projectiles are fabricated in the WES Machine Shop by machining the projectile to a slight oversize dimension from steel stock, heat treating it to the desired hardness and then remachining it to final dimensions. Complexity of the target can range from a simulated half-space of concrete, to a layered system of concrete and soil, to a subscale model of an actual structure or components of the structure. Targets can be fabricated by placing concrete that has been mixed by WES personnel, mixed at a local batch plant under supervision of WES personnel, or simply purchased from a local vendor; soil fills can be placed to desired specifications.

Basic information obtained during projectile penetration experiments includes impact velocity and projectile orientation from the Hall Station, depth of penetration, and target damage such as crater profile, crack patterns and photographs. Additional information can include high speed movies (Figure 6.3.a), flash x-rays (Figure 6.3.b), and instrumentation of the projectile using an accelerometer and miniature hardened data acquisition package to record the loading history (Figure 6.3.c) which can be integrated to determine the projectile's motion-time response during the penetration process. Concrete cylinders poured during target fabrication are broken on or within a few days of the impact test to determine the unconfined compressive strength of the concrete. Additional experiments to determine the mechanical properties of the concrete can be conducted on specimens cored from samples of the concrete that were obtained during target fabrication.

#### 6.1.2 Penetration Experiments

A series of penetration experiments were conducted by launching AP projectiles into targets consisting of CSPC concrete at impact velocities ( $V_i$ ) ranging from 277 to 800 m/s. All experiments were conducted at normal incidence to the target face. The CSPC



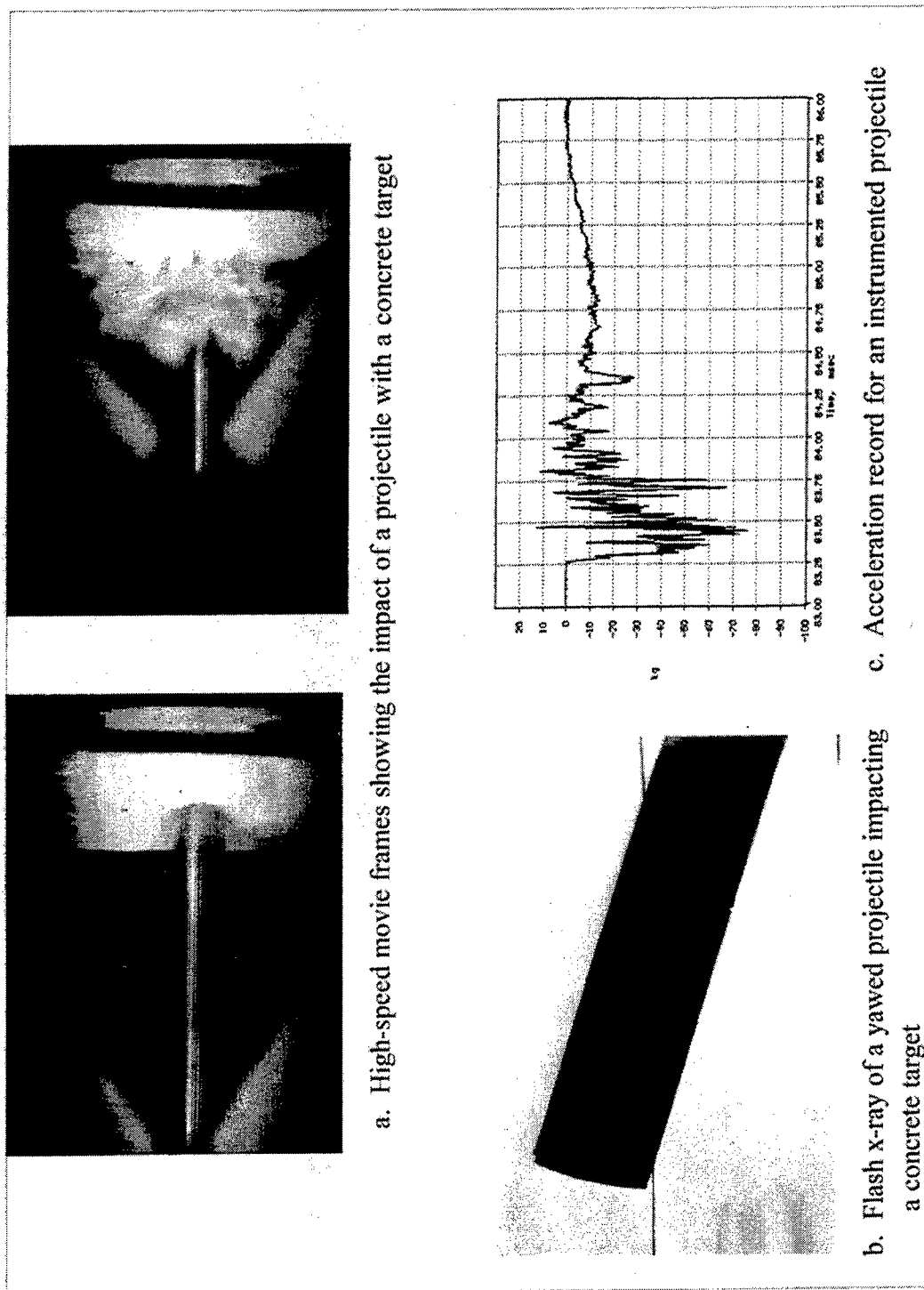


Figure 6.3. Information from diagnostic systems that can be used during projectile penetration tests (Frew et. al 1993).

concrete targets were cast in corrugated steel culverts approximately 1.37 m or 1.22 m in diameter. The diameter of the target should be greater than 25 projectile diameters (calibers) to eliminate edge effects during the penetration process. Target diameters for these experiments were a minimum of 45 calibers. The length of the targets varied depending on impact velocity, but all target lengths were greater than twice the depth of penetration to prevent backface effects on the projectile penetration. Cylinders measuring 152 mm in diameter by 305 mm in length were cast from the concrete placed in each target for subsequent unconfined compressive strength tests. Values of unconfined compressive strength for each target are given in Table 6.1. Penetration experiments and unconfined compressive strength tests were conducted at about 28 days after the targets were cast. Target strength was nominally 36 MPa and ranged from 32.4 to 40.1 MPa.

The AP projectiles were dimensioned as shown in Figure 6.4, and were machined from 4340 steel rods and heat treated to a Rockwell hardness,  $R_{c}$ , of 43 - 45. The inner cavity of the projectile was filled with either grout or sand at a density of approximately  $1.58 \text{ Mg/m}^3$ . The projectiles were fitted with plastic sabots and obturators that fit snugly into the gun bore. The sabots and obturators were stripped aerodynamically prior to impacting the targets. Pitch and yaw angles measured from the Hall Interferometer streak film were less than one degree. Data from the experiments is presented in Table 6.1.

The primary data from these experiments are depth of penetration and a mapping of the impact crater and penetration path. Except for the experiment at 277 m/s, all projectiles penetrated at least one projectile body length into the target. Experiment results are presented as depth of penetration in calibers (depth/projectile diameter) versus impact velocity in Figure 6.5. The data show a consistent trend, as expected, of increased depth of penetration with increasing impact velocity. The mapping of the impact crater and penetration path for the experiments conducted at impact velocities of 277, 499, and 642 m/s is shown in Figure 6.6. The impact crater enters the tunneling phase after a penetration of about 50 mm, or about 2 projectile diameters. Posttest photographs of the

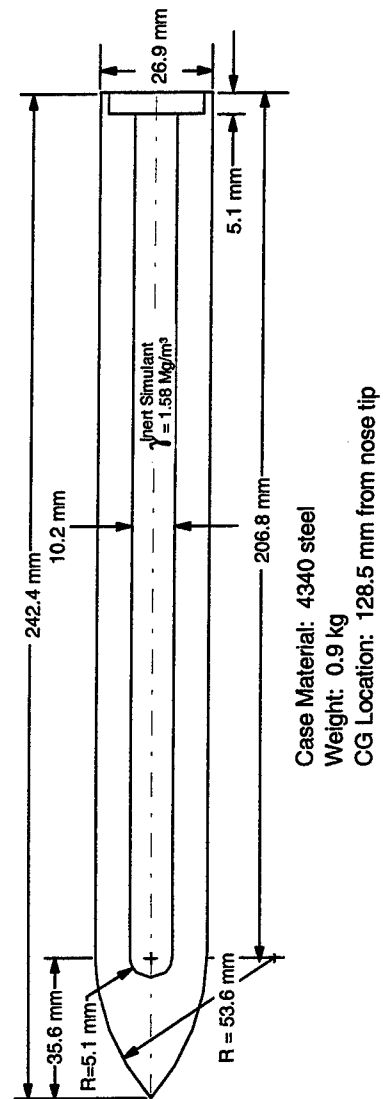


Figure 6.4. Dimensions of AP projectile launched into CSPC concrete targets.

Table 6.1. Summary of penetration experiments for the AP projectile into CSPC concrete.

Test No.	Projectile Mass, kg	Target Diameter, m	Target Length, m	Unconfined Compressive Strength, MPa	Impact Velocity, m/s	Penetration Depth, mm
14	0.906	1.37	0.76	35.2	277	173
13	0.910	1.37	0.91	37.8	410	310
15	0.907	1.37	0.91	38.1	431	411
11	0.912	1.37	0.76	33.5	499	480
12	0.910	1.37	1.07	38.4	567	525
1	0.901	1.22	1.83	40.1	591	513
3	0.903	1.22	1.83	35.4	631	607
4	0.905	1.22	1.83	34.7	642	620
5	0.901	1.22	1.83	36.0	773	866
6	0.904	1.22	1.83	32.4	800	958

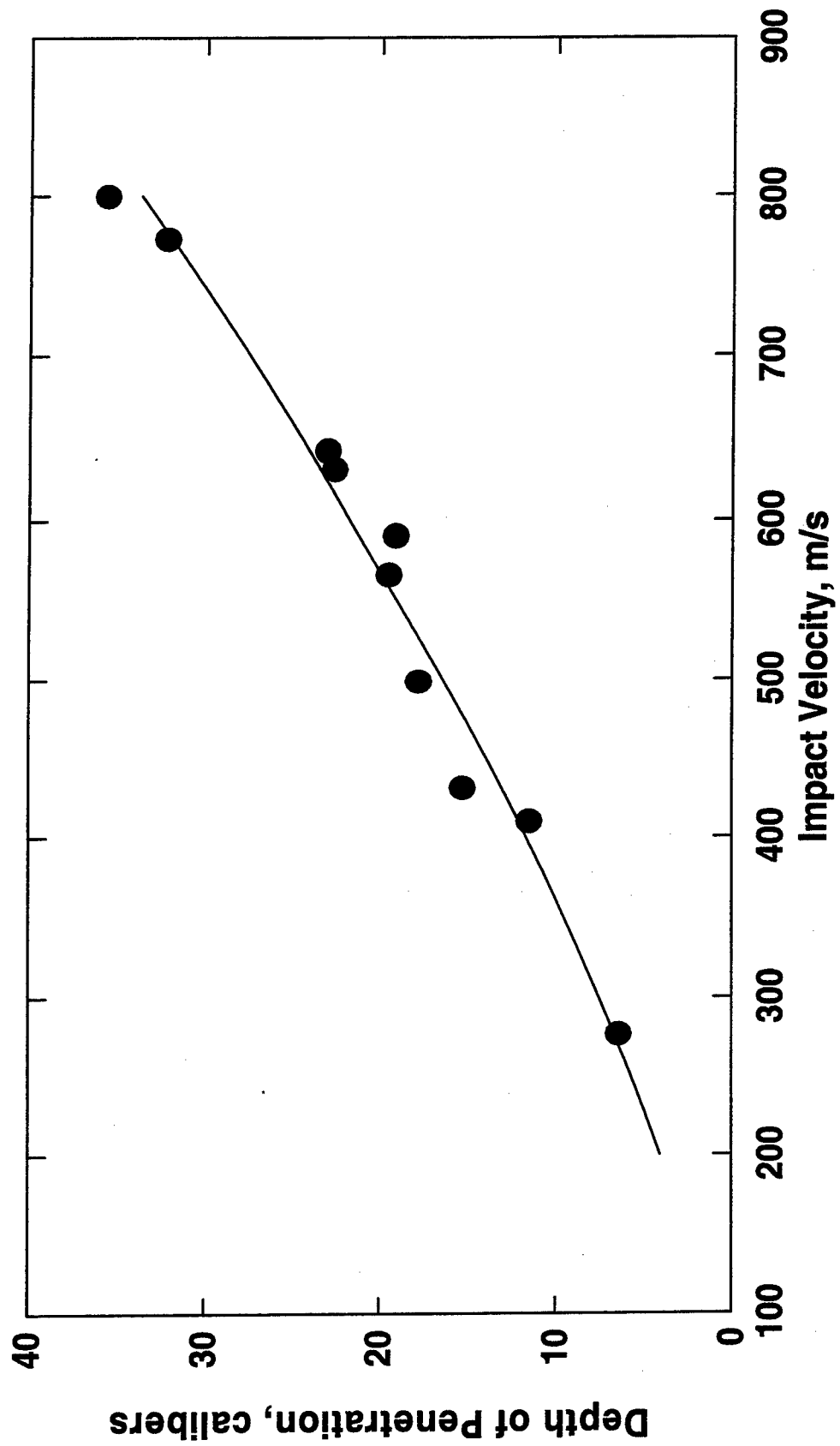


Figure 6.5. Depth of penetration for AP projectiles impacting CSPC concrete.

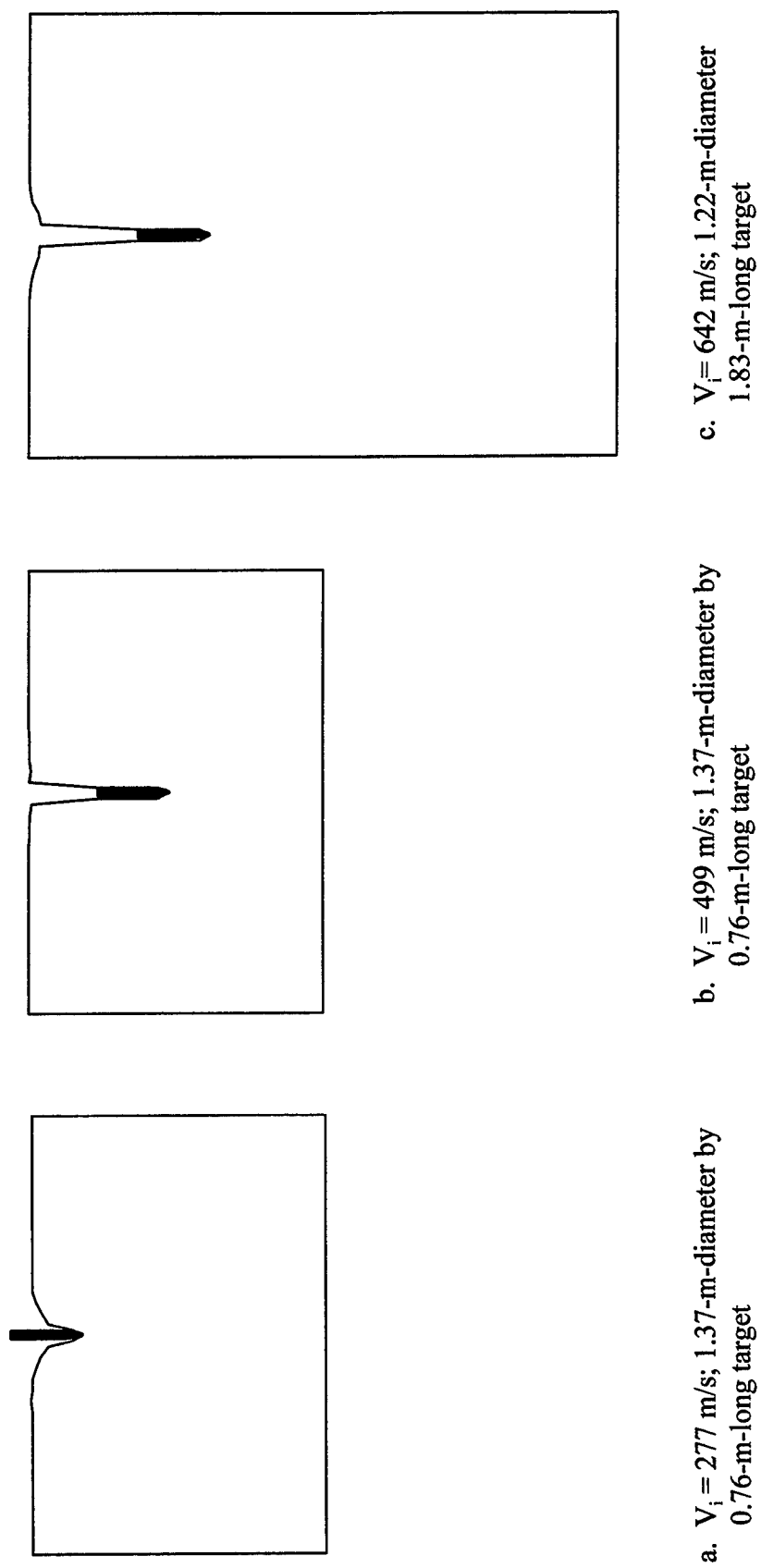


Figure 6.6. Crater and penetration path profiles for AP projectiles impacting CSPC concrete.

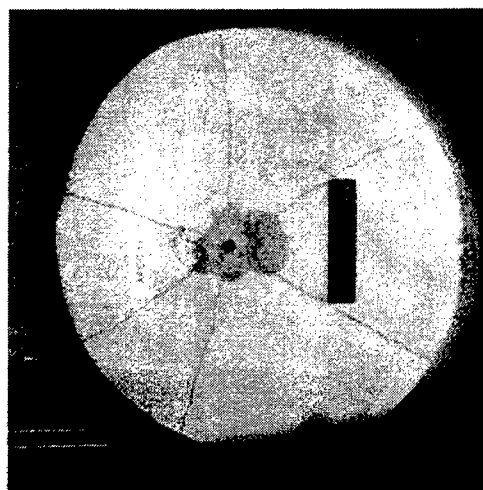
targets (Figure 6.7) illustrate that the craters are similar in appearance for all impact velocities, but the number of visible radial cracks increases as impact velocity increases. The cracks occur after the penetration event and do not influence the final depth of penetration.

The targets for the six experiments above were opened and the projectiles were removed to inspect their condition. Posttest photographs of the six projectiles are shown in Figure 6.8. Target material on the front half of the projectiles is believed to have adhered to the projectile after it had stopped. All of the projectiles show very little damage so that the projectiles can be modeled as being effectively rigid.

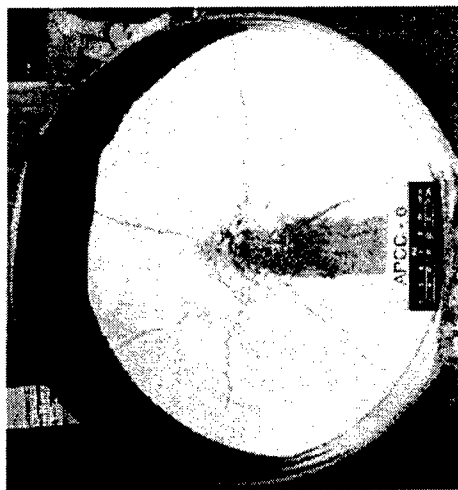
### 6.1.3 Perforation Experiments

The targets used in the perforation experiments consisted of WES5000 concrete having a nominal unconfined compressive strength of 38.2 MPa. The unreinforced concrete slabs had thicknesses of 284, 254, 216 and 127 mm. The concrete was poured into steel culverts having a nominal diameter of 1.52 m, vibrated to remove trapped air, and allowed to cure approximately 28 days prior to the perforation experiment. Water was ponded on the top surface of the slabs for approximately 7 days. The target diameter is 30 times the projectile diameter so that edge effects should not influence the experiment results.

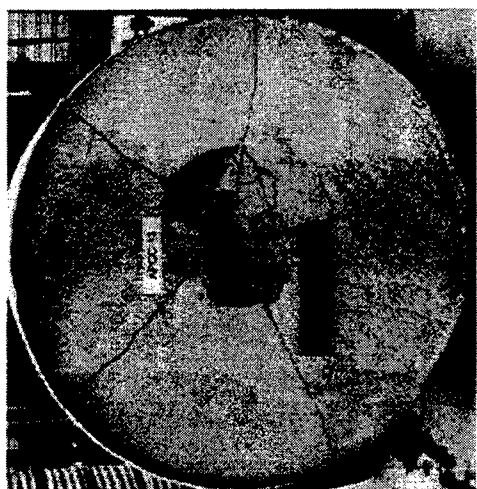
A drawing and the pertinent characteristics of the projectile used in the perforation experiments is presented in Figure 6.9. The projectile was machined from 4340 steel rods and then heat treated to a Rockwell hardness,  $R_c$ , of 43 - 45. The inner cavity of the projectiles was filled with sand. The masses of the test projectiles were similar (see Table 6.2). Impact velocity ( $V_i$ ) for all experiments was about 313 m/s.



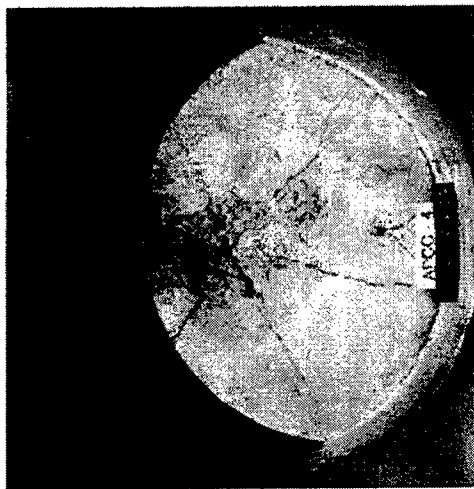
c.  $V_i = 499$  m/s



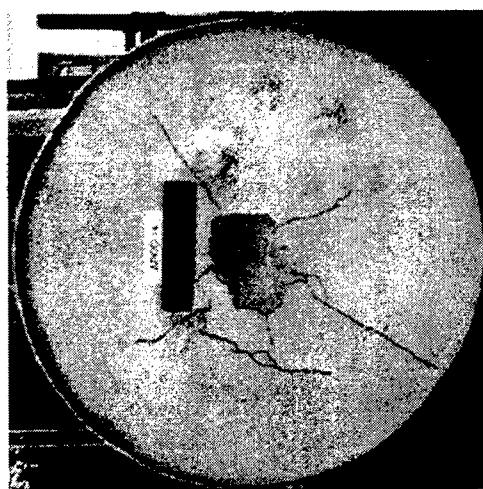
f.  $V_i = 800$  m/s



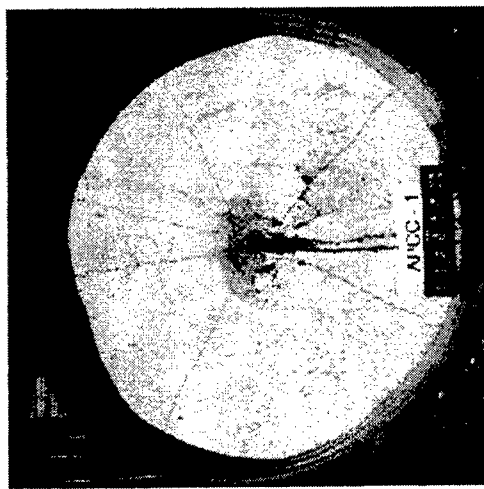
b.  $V_i = 410$  m/s



e.  $V_i = 642$  m/s



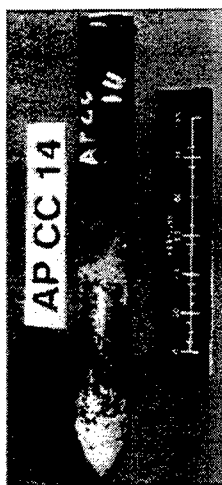
a.  $V_i = 277$  m/s



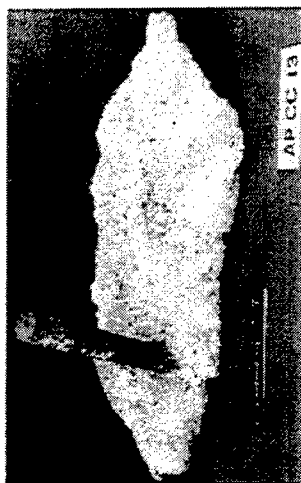
d.  $V_i = 591$  m/s

Figure 6.7. Posttest photographs of CSPC concrete targets penetrated by AP projectiles.

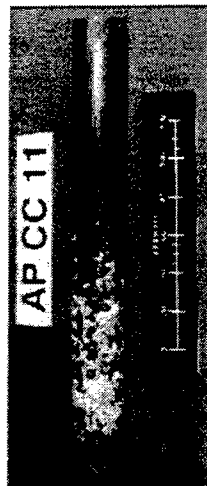




a.  $V_i = 277$  m/s



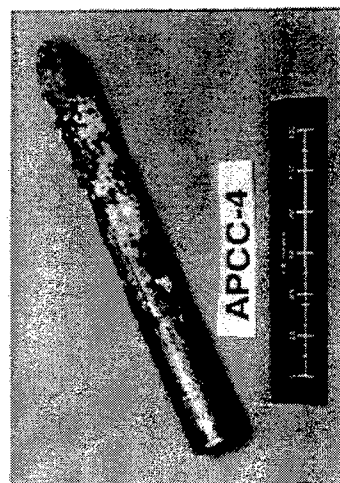
b.  $V_i = 410$  m/s



c.  $V_i = 499$  m/s



d.  $V_i = 591$  m/s

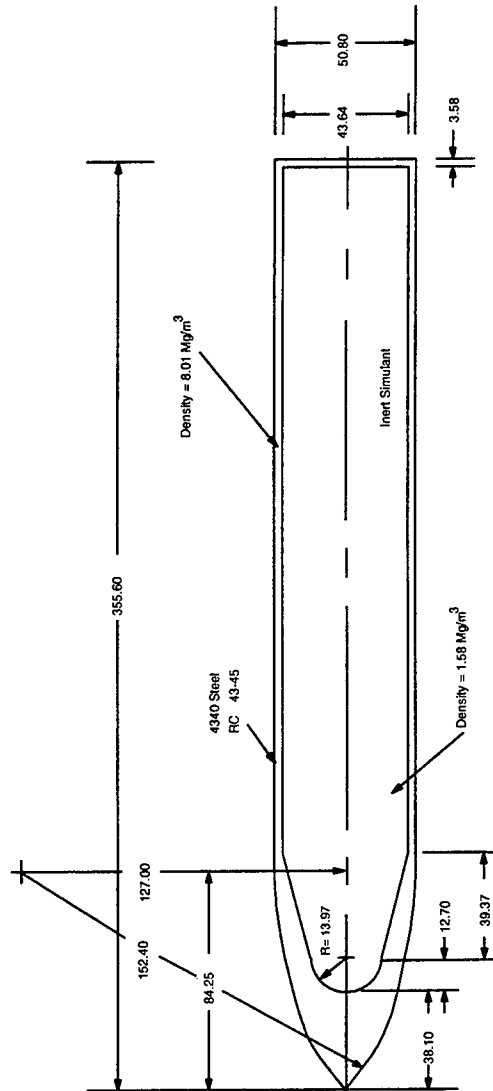


e.  $V_i = 642$  m/s



f.  $V_i = 800$  m/s

Figure 6.8. Posttest photographs of AP projectiles used in penetration experiments into CSPC concrete.



Case Material: 4340 steel  
 Weight: 2.343 kg  
 CG Location: 185.3 mm from nose tip

Figure 6.9. Dimensions of SAP projectile launched into WES5000 concrete slabs.

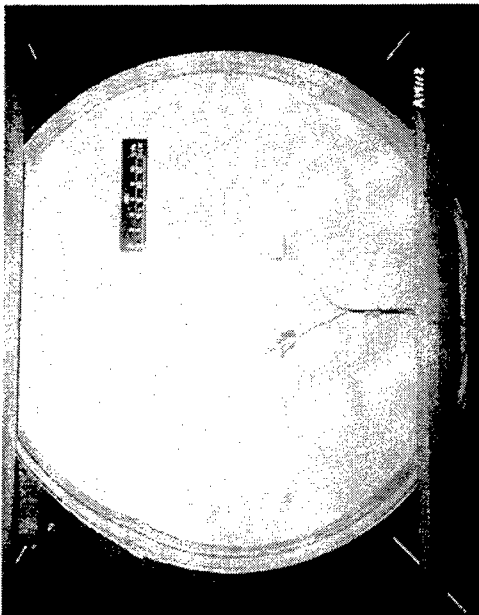
Table 6.2. Summary of perforation experiments for the SAP projectile into WE5000 concrete.

Test No.	Projectile Mass, kg	Slab Thickness, mm	Unconfined Compressive Strength, MPa	Impact Velocity, m/s	Exit Velocity, m/s
PERF-1	2.319	284	39.9	309	0
PERF-2	2.330	284	39.9	317	0
PERF-3	2.330	254	36.5	318	41
PERF-4	2.314	254	36.5	309	46
PERF-5	2.319	254	36.5	309	32
PERF-6	2.268	216	39.9	325	104
PERF-7	2.322	216	39.9	311	116
PERF-8	2.330	127	36.5	319	233
PERF-9	2.355	127	36.5	306	221
PERF-10	2.354	127	36.5	306	218

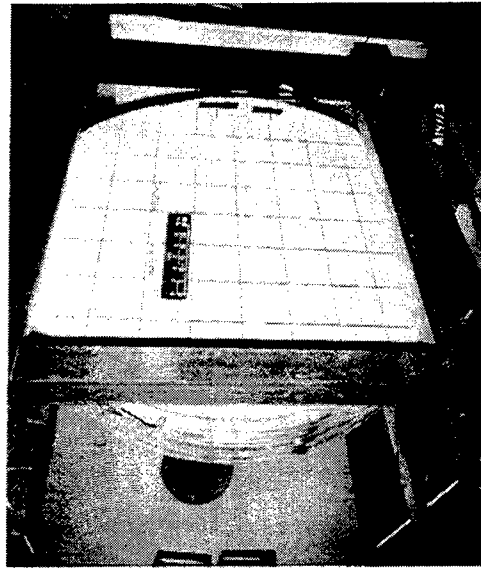
Primary data obtained from these experiments included high-speed movies of the slab impact viewed from the side at an angle of about 45 degrees, high-speed movies of the damage to the backface of the slab viewed using a mirror placed at an angle of 45 degrees to the backface, exit velocity ( $V_e$ ) from breakscreens and the high-speed movies, and mappings of the impact and exit craters. All experiments were conducted at normal incidence to the slab. From the high-speed movies of the impact face, the yaw at impact in the vertical plane was less than 1.3 degrees for all experiments except PERF-7 (2.1 degrees); yaw in the horizontal plane at impact is not known but is believed to be small. A typical target configuration is shown in Figure 6.10. Figure 6.10.a shows the frontface of the target with a break screen attached to determine the time of impact. Figure 6.10.b shows the backface of the target with a 152-mm-square grid painted on the surface to aid in viewing the breakup of the target as it is being perforated. Figures 6.10.c and 6.10.d show the posttest condition of the target. The impact crater is significantly smaller than the exit crater. Also, most of the cracks that were found on the front of the target were also found on the back of the target indicating that they extended through the target.

Projectile masses and impact and exit velocities are summarized in Table 6.2. In all of the experiments the projectile exited the backface of the slab. For experiments on the 284-mm-thick slab, the projectile was found on the floor just behind the slab and is believed to have simply fallen through the back of the slab due to gravity.

A plot of  $V_e/V_i$  versus slab thickness ( $T$ ) is shown in Figure 6.11. Assuming a constant deceleration while perforating the slabs, the thickness at which the projectile will just exit the target is about 260 mm. Selected images captured from the high-speed movies of the impact face of a target are shown in Figure 6.12. From these images, only a cloud of "pulverized" material and small pieces of concrete can be seen coming from the impact area. Selected images from the high-speed movies of the backface of the slab are shown in Figures 6.13 and 6.14 for 254- and 127-mm-thick slabs, respectively. These images indicate that damage begins with cracks radiating from the center of the backface.



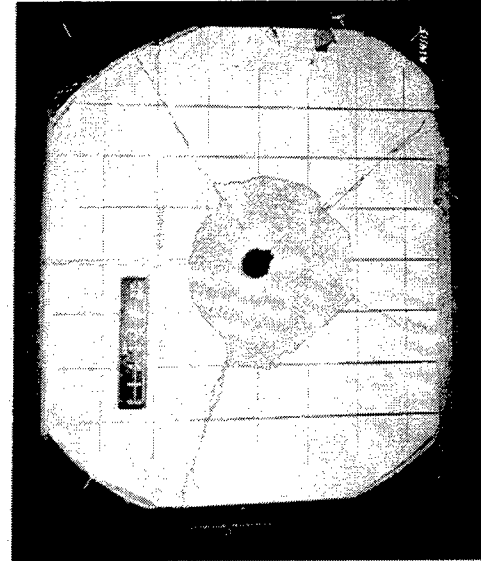
a. Pretest photo of frontface



b. Pretest photo of backface



c. Posttest photo of frontface



d. Posttest photo of backface

Figure 6.10. Pre- and posttest photographs from a typical perforation experiment.

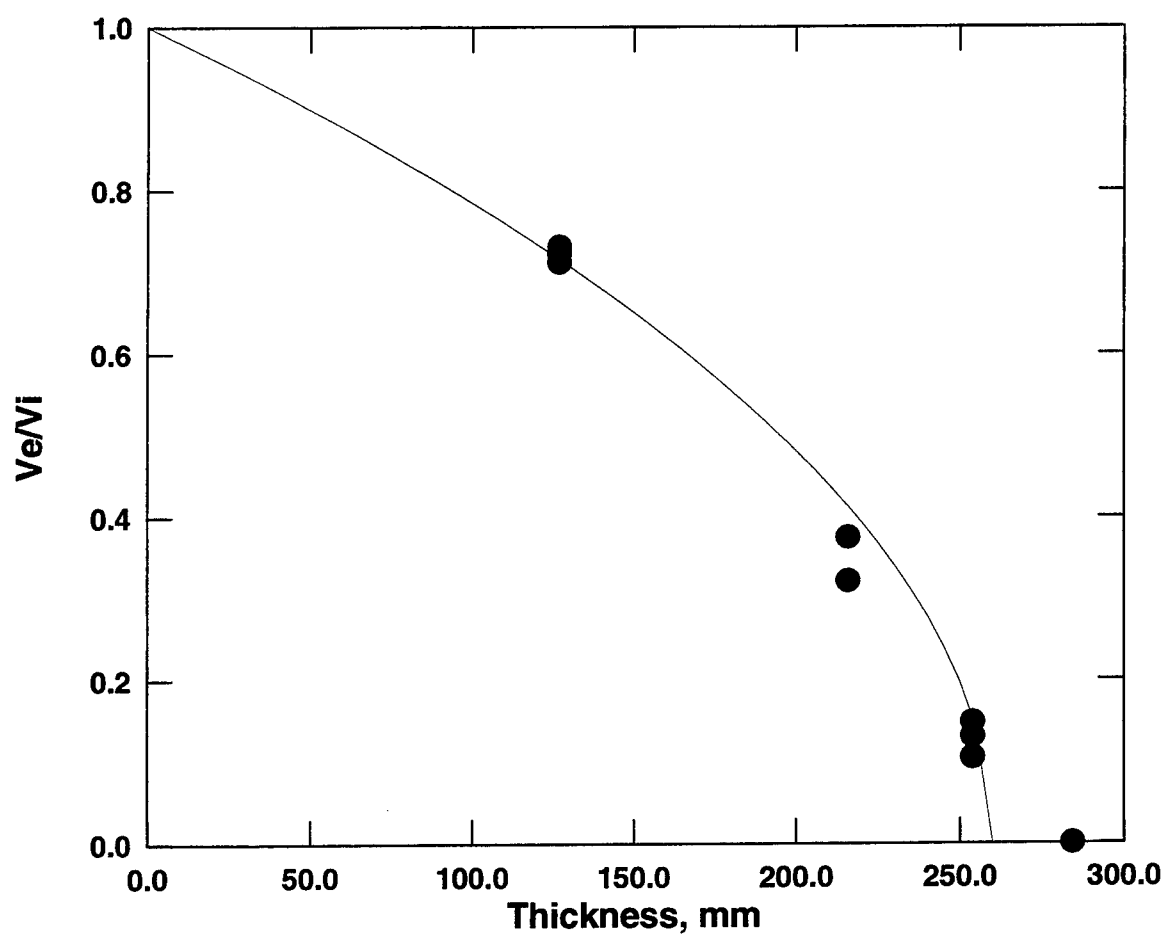


Figure 6.11. Ratio of exit velocity to impact velocity versus target thickness for a SAP projectile perforating WES5000 concrete slabs.

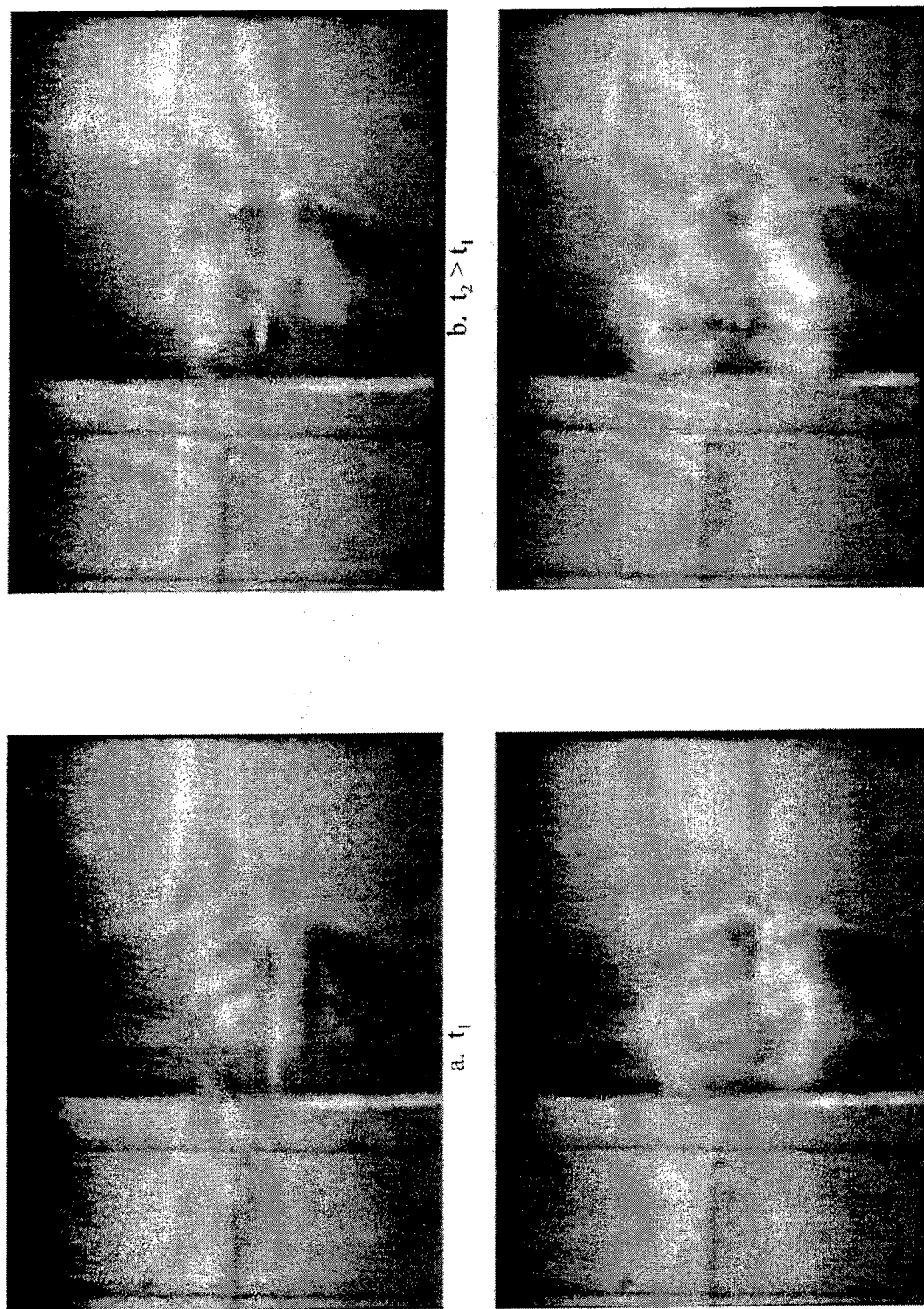


Figure 6.12. Selected images showing the front of a 254-mm-thick WES5000 concrete slab being impacted by a SAP projectile.

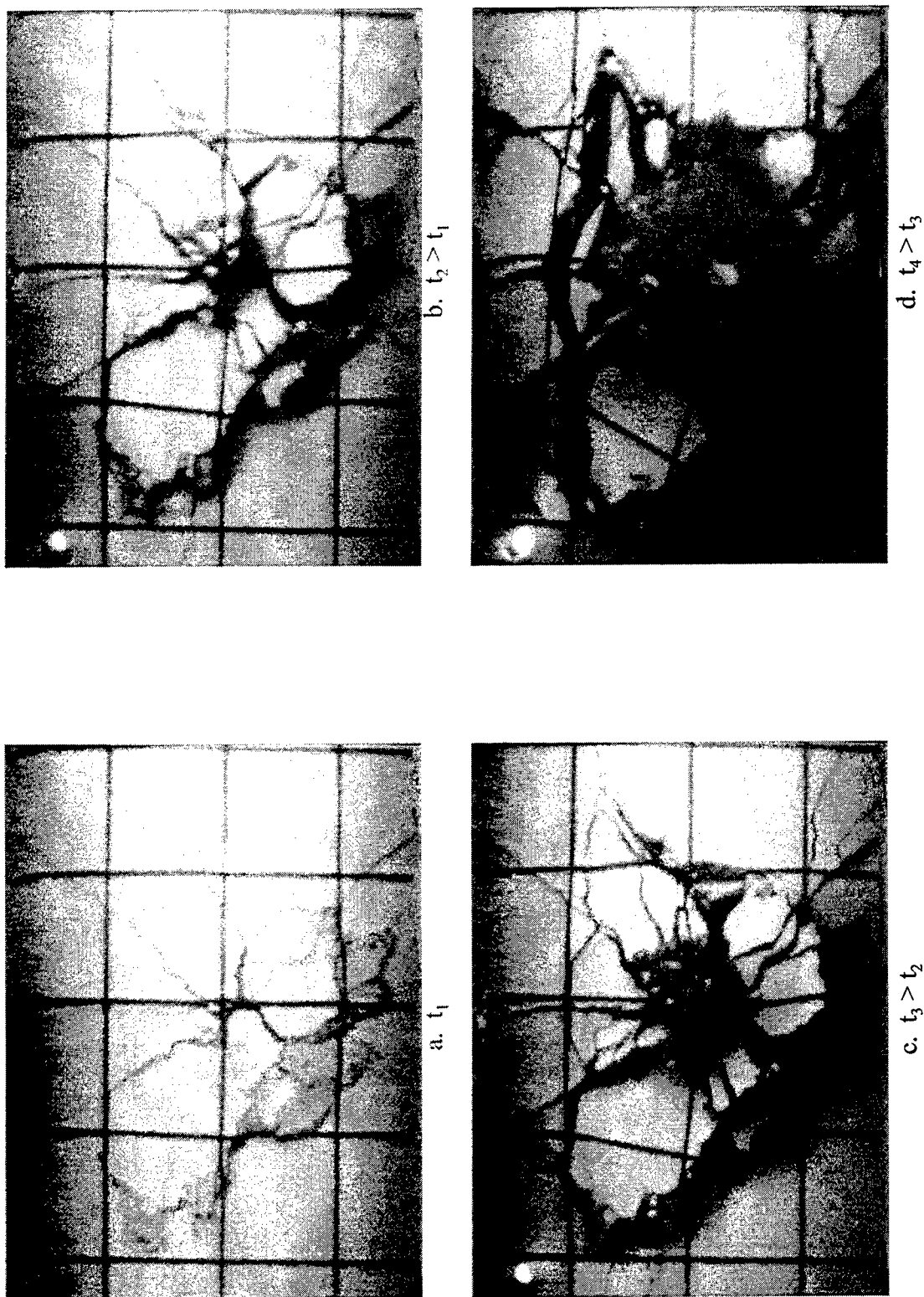


Figure 6.13. Selected images showing the back of a 254-mm-thick WES5000 concrete slab being perforated by a SAP projectile.



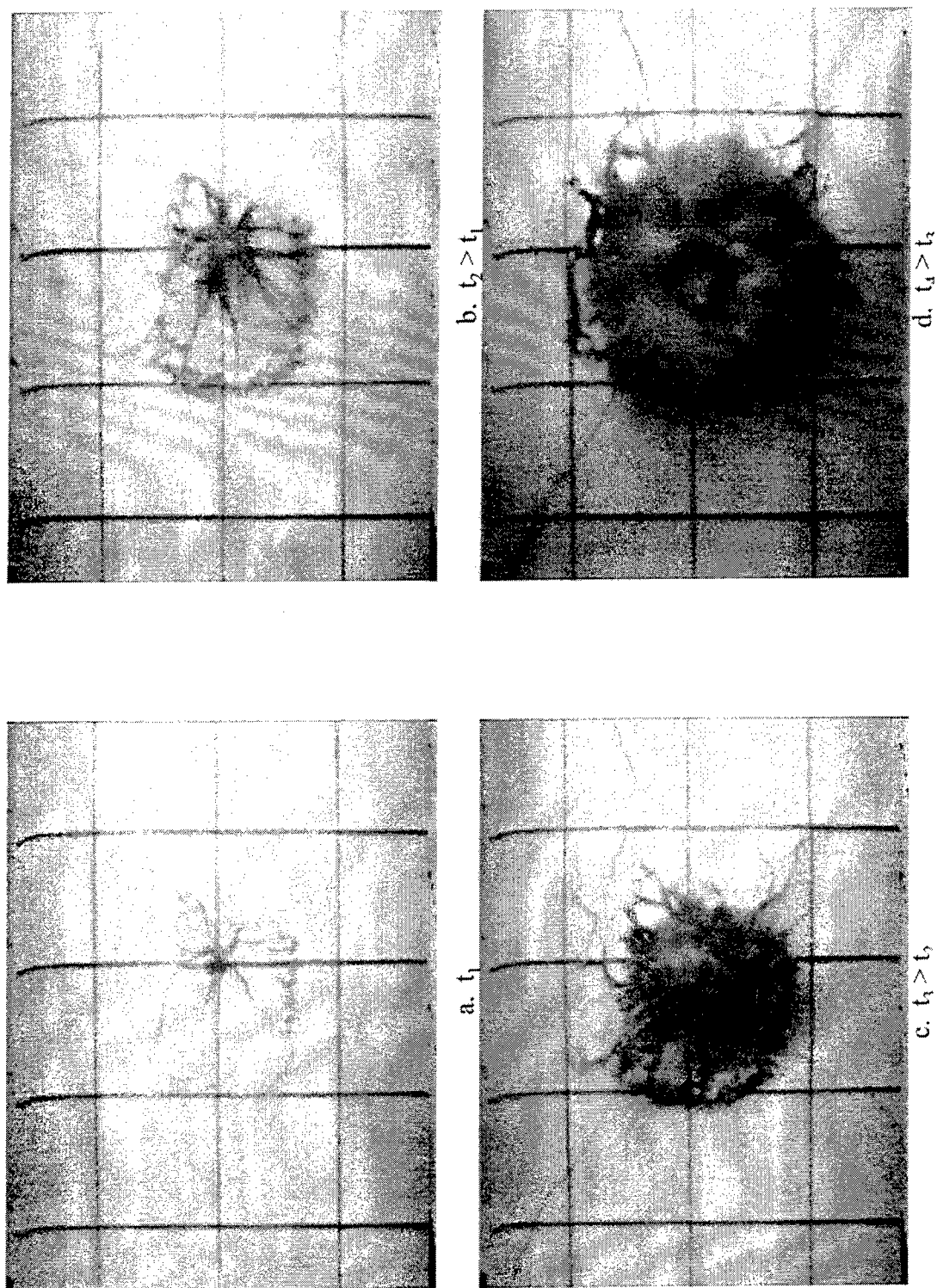


Figure 6.14. Selected images showing the back of a 127-mm-thick WES5000 concrete slab being perforated by a SAP projectile.

The outer edges of the exit crater begin to form as material is pushed out from the backface of the slab. As the tip of the projectile protrudes through the backface of the slab, the material ahead of the projectile is destroyed. The pieces being pushed from the backface of the slab were generally larger and fewer in number for the thicker slabs. Pieces of concrete seen in the movies and recovered after the experiment were relatively thick and showed no delamination of concrete near the backface that might result from a reflected tensile stress wave. Profiles showing the impact and exit craters for three slab thicknesses are shown in Figure 6.15. The size of the exit crater increases with increasing thickness of the slab. Several of the projectiles exited the slabs with significant yaw rates. Since the yaw at impact was small, the exit yaw rates were attributed to inhomogeneity of the concrete and interaction of the projectile with the pieces of concrete being pushed through the backface of the slab.

## 6.2 NUMERICAL SIMULATIONS

Simulations of the penetration and perforation experiments were conducted using the NIF model implemented in the EPIC code. Initial simulations of the penetration experiments indicated some instability that was traced to the hydrostatic tension and unloading/reloading portions of the model. In Figure 4.1, the hydrostatic tension response is nonlinear as the pressure  $\sigma_{mc}$  is approached. This response was altered to be linear with a slope equal to  $K_{unl/rel}$  as defined in Section 4.2.1 and a pressure limit equal to  $\sigma_{mc}$ . The shear unload/reload portion was altered to be linear with a slope equal to 1.20 times the initial loading slope of the corresponding  $\tau_{oct}$  vs  $\gamma_{oct}$  curve. All simulations were axisymmetric and used triangle elements. The simulations were performed on the WES Cray C90 super computer. Post-processing was performed using software supplied with EPIC and downloaded as encapsulated post-script files for insertion into the figures.

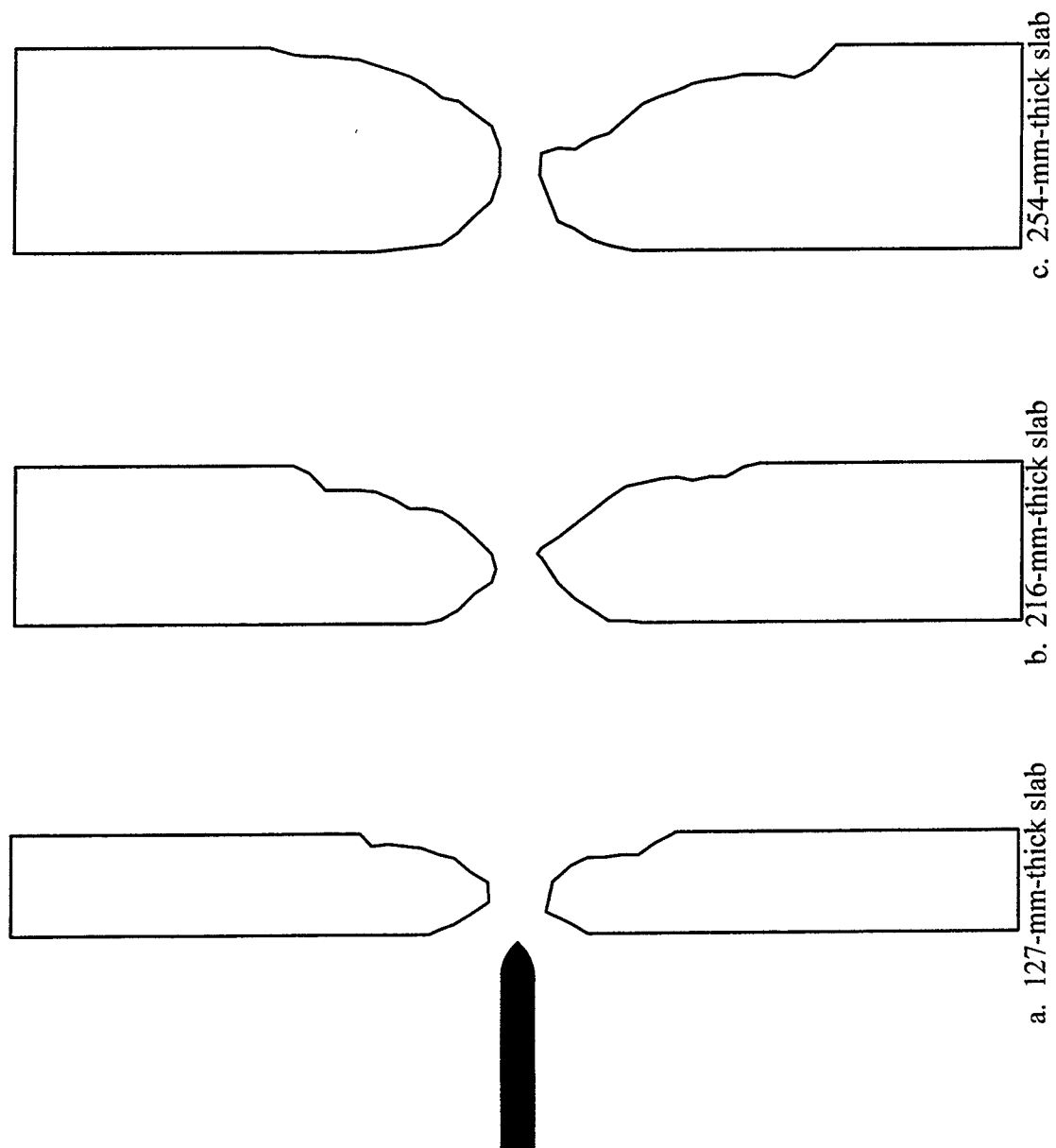


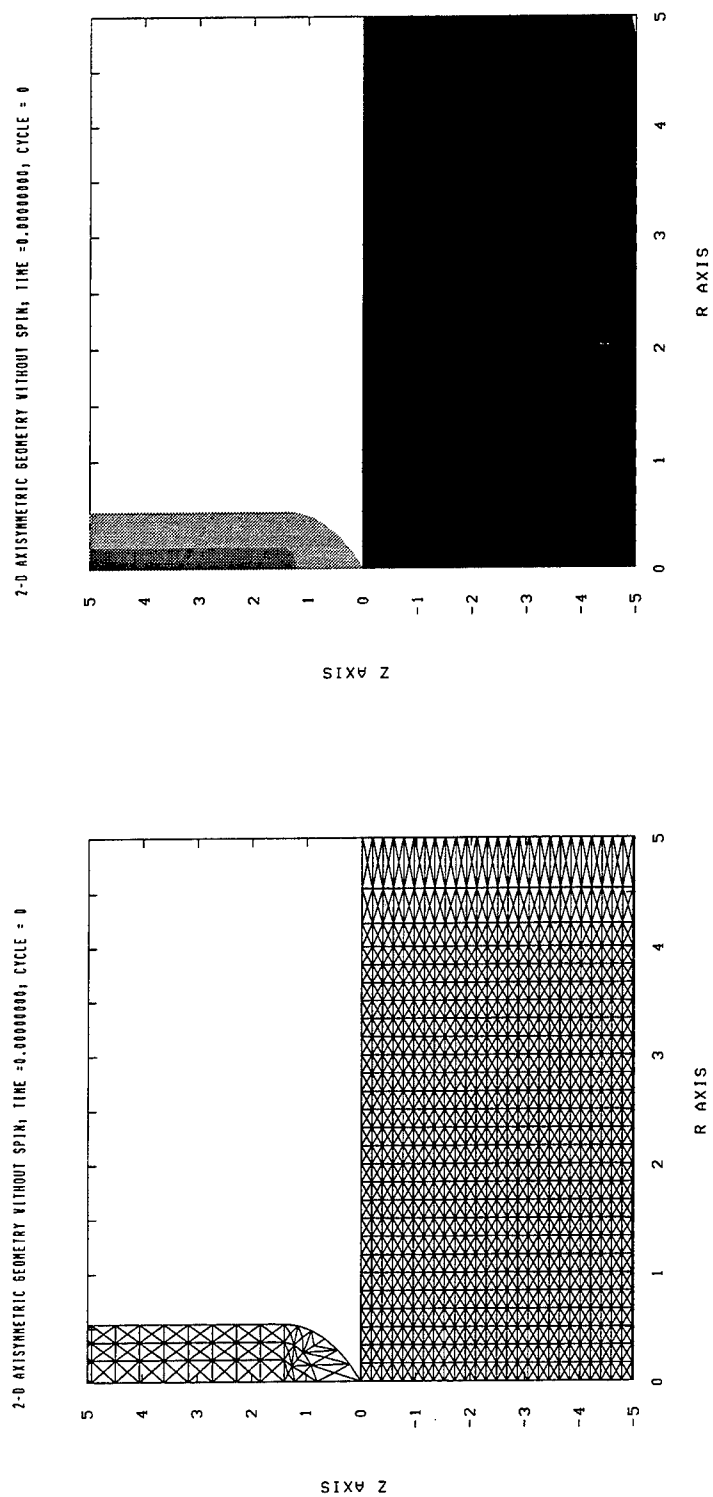
Figure 6.15. Impact (left) and exit (right) crater profiles for the perforation experiments.

### 6.2.1 Penetration Experiments

The AP projectile penetration experiments into CSPC concrete conducted at impact velocities of 277, 499, and 642 m/s will be simulated using the NIF model. A close-up of the initial grid used in the simulations is shown in Figure 6.16.a. Figure 6.16.b shows the materials used in the grid. In the projectile, the outer two columns of the grid make up the steel case of the projectile. Although not shown, a steel end-cap sealed the back of the projectile. The sliding interface algorithm used in the code to separate the projectile case from the concrete target requires that the target elements be about the same size or smaller than the outer elements of the projectile. This aids in ensuring that target elements do not “mix” with the projectile elements. Since the projectile case is relatively thick and no significant deformation is expected, the influence of movement of the fill material on the projectile response should be minor. The fill material was “fixed” to the steel case so that no slideline was required.

The full initial grids for the simulations are shown in Figure 6.17. The same grid was used for both the 277 and 499 m/s simulations. Beyond a radius of 102 mm (4 inches) the grid was gradually expanded to a final radius of 508 mm (20 inches). Similarly, beyond a depth of 559 mm (22 inches) the grid was gradually expanded to a final depth of 1,016 mm (40 inches). The lateral extent of the grid for the 642 m/s simulation was the same as that for the two slower impact velocity simulations. Since the depth of penetration is expected to be greater for the higher impact velocity, the total depth of the grid was extended to 2,032 mm (80 inches) with the expanding grid beginning at a depth of 1,118 mm (44 inches). The grid was expanded to reduce the size of the model and to decrease computation time. Element sizes were kept relatively small within the region of the target influencing the penetration of the projectile.

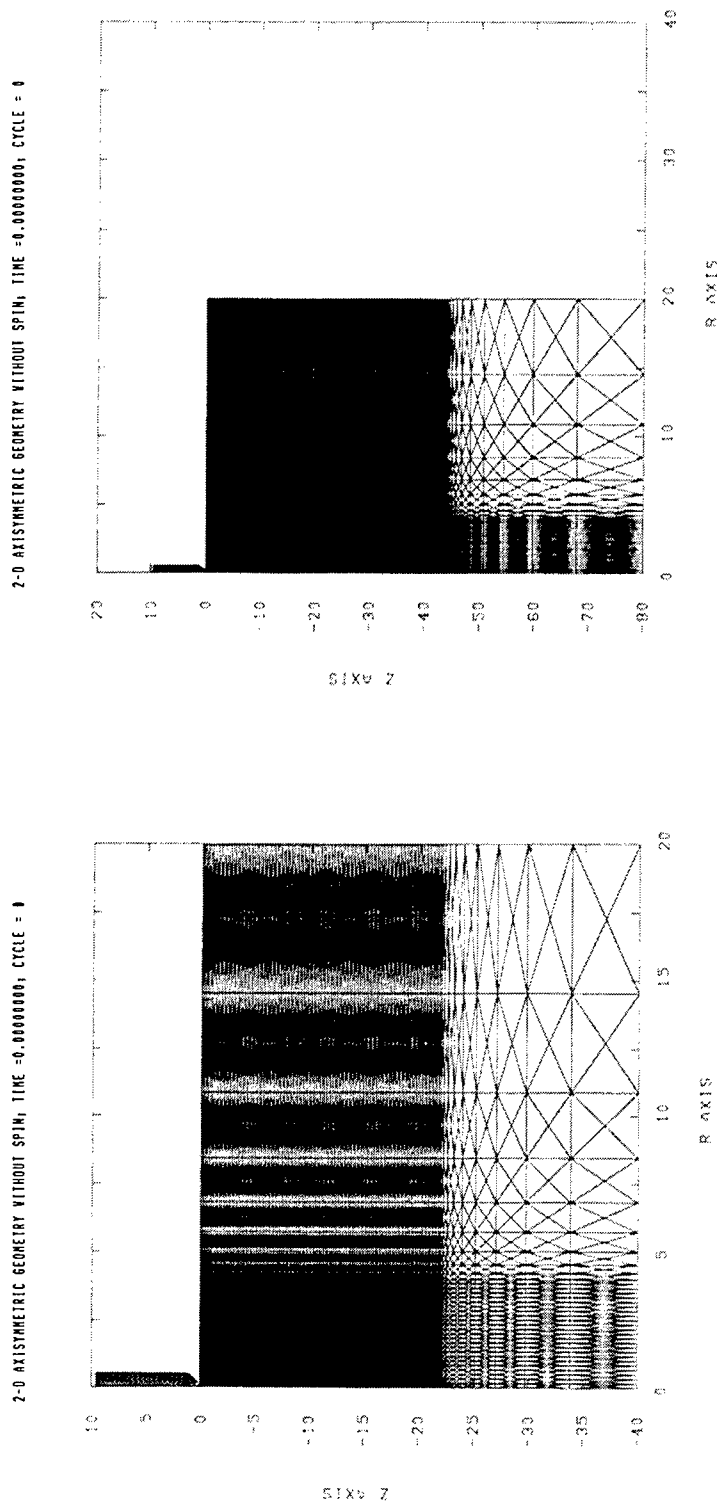
Model parameters presented in Table 4.2 were used in the simulation. The value of DYN applied to the ultimate strength in both shear and hydrostatic tension was 1.25. A



a. Initial grid.

b. Materials: gray - filler, medium gray - steel, black - concrete.

Figure 6.16. Close-up of initial grid and materials used in simulation of the AP projectile impacting CSPC concrete (axis units are inches).



a.  $V_i = 277$  and 499 m/s

b.  $V_i = 642$  m/s

Figure 6.17. Initial grid for simulating the AP projectile penetrating CSPC concrete (axis units are inches).

model parameter that is not defined by mechanical property tests is the critical value of the strain ratio EBAR that was discussed in Section 5.1.2. This value must initially be determined for a given target material by comparing a simulation result with an experiment result. Currently, this must be done through trial-and-error. The critical value of EBAR ( $EBAR_{crit}$ ) was determined to be 400 for the CSPC concrete by simulating the penetration experiment at 277 m/s until a reasonable result (depth of penetration) was obtained. This value of  $EBAR_{crit}$  was then used for the other two impact velocity simulations. During initial simulations with the model, small “sliver” elements that had detached from the grid were overlapping with the remaining target mesh. Although these elements were not influencing the simulation results, they were causing the time step to be unnecessarily small. The strain in these elements was not sufficient to allow normal removal using  $EBAR_{crit}$  criterion. In order to gradually remove these elements, each element was checked to see if its minimum height was less than 1.27 mm (0.05 inches). If this check was true, the value of EBAR for that element was multiplied by 100. If the increased value of EBAR was greater than  $EBAR_{crit}$  then the element was removed from the simulation. This increased computation performance without significantly affecting the simulation results.

Depth of penetration from the simulations is compared to the experiment results in Figure 6.18. Both the simulations and the experiments show an increase in depth of penetration as impact velocity increases. The simulations resulted in slightly greater depth of penetration than the experiments. The depths from the simulations are approximately 20 percent greater than the depths from the experiments at impact velocities of 277 and 499 m/s and 40 percent greater at 642 m/s. It is possible that the simulation results could be improved by modifying  $EBAR_{crit}$  to better fit the experiment results at one of the other impact velocities.

The deformed grid at several times during the simulation is shown in Figures 6.19, 6.20, and 6.21 for the 277, 499, and 642 m/s impact velocities, respectively. The images

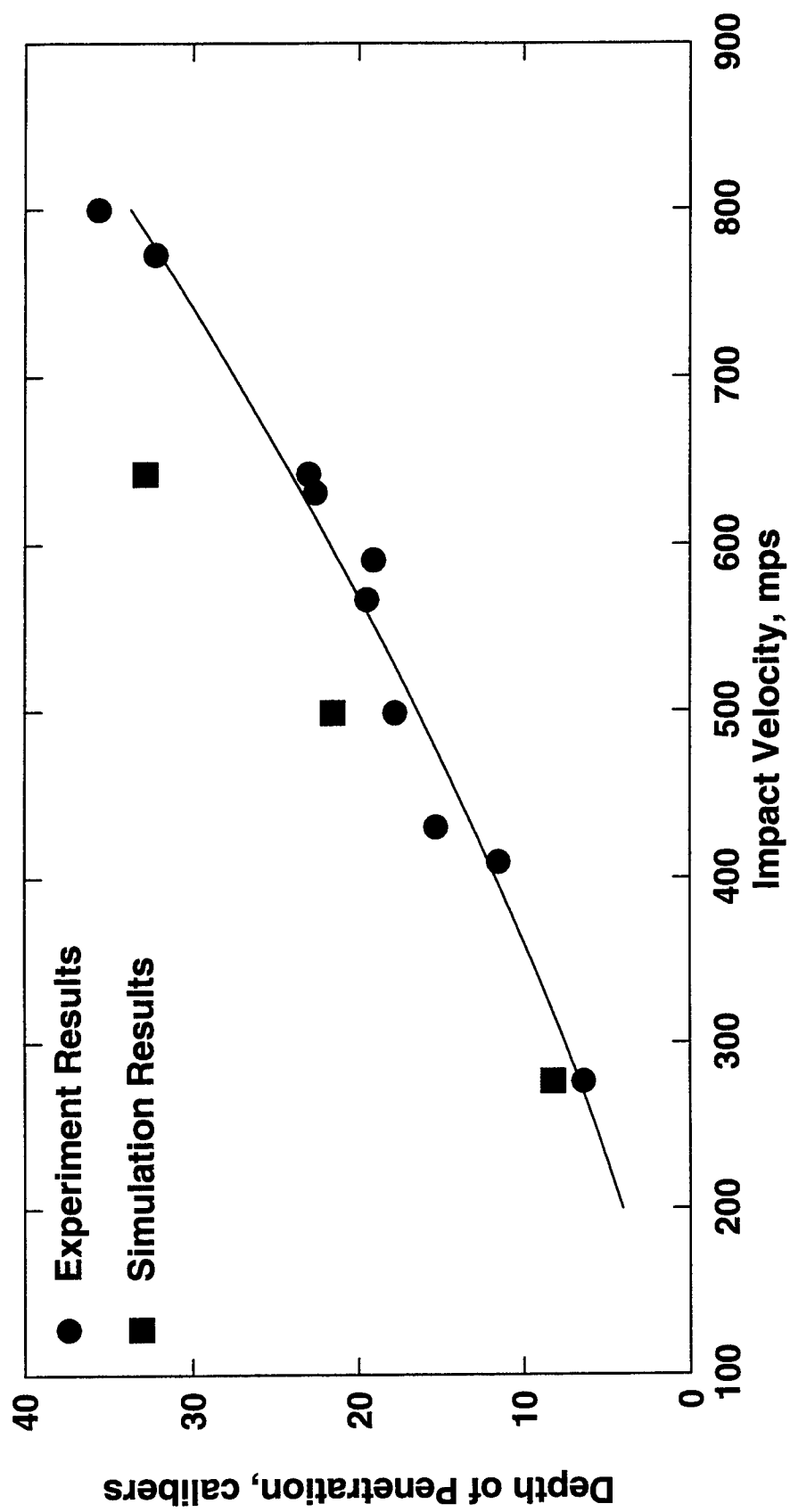


Figure 6.18. Comparison of simulation and experiment results for an AP projectile impacting CSPC concrete.



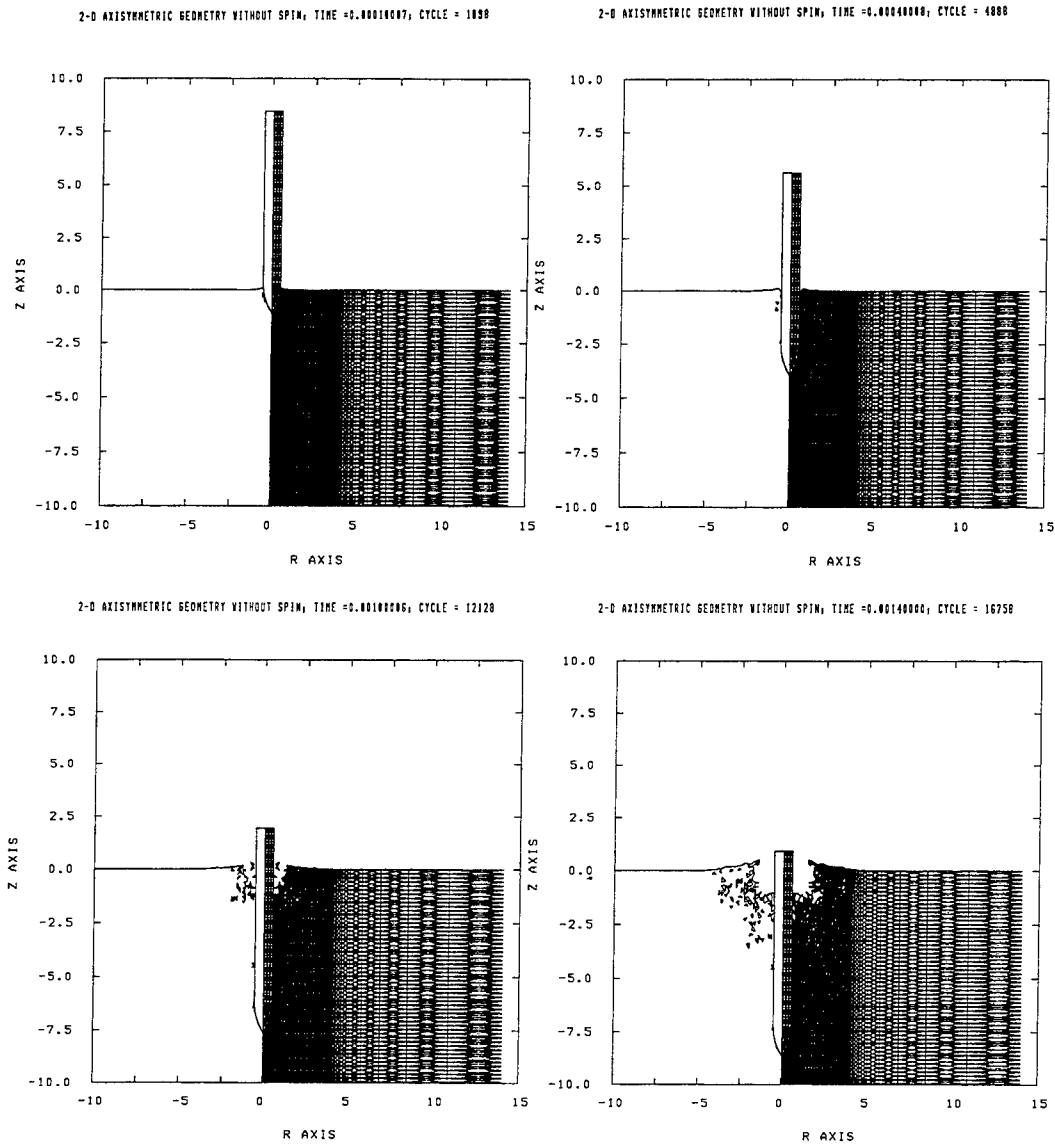


Figure 6.19. Deformed grid for an AP projectile impacting CSPC concrete at 277 m/s (time is in seconds; axis units are inches).

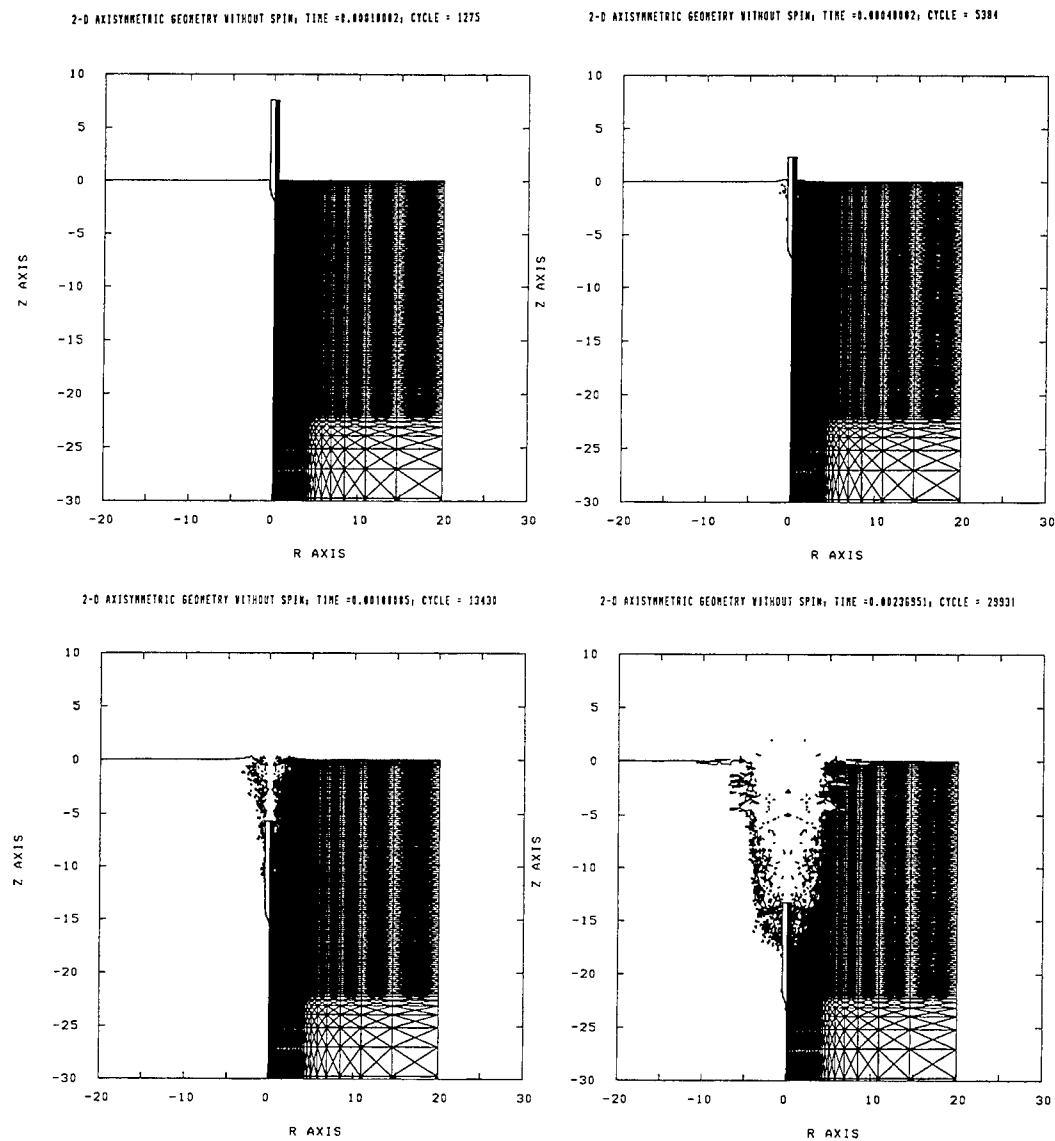


Figure 6.20. Deformed grid for an AP projectile impacting CSPC concrete at 499 m/s (time is in seconds; axis units are inches).

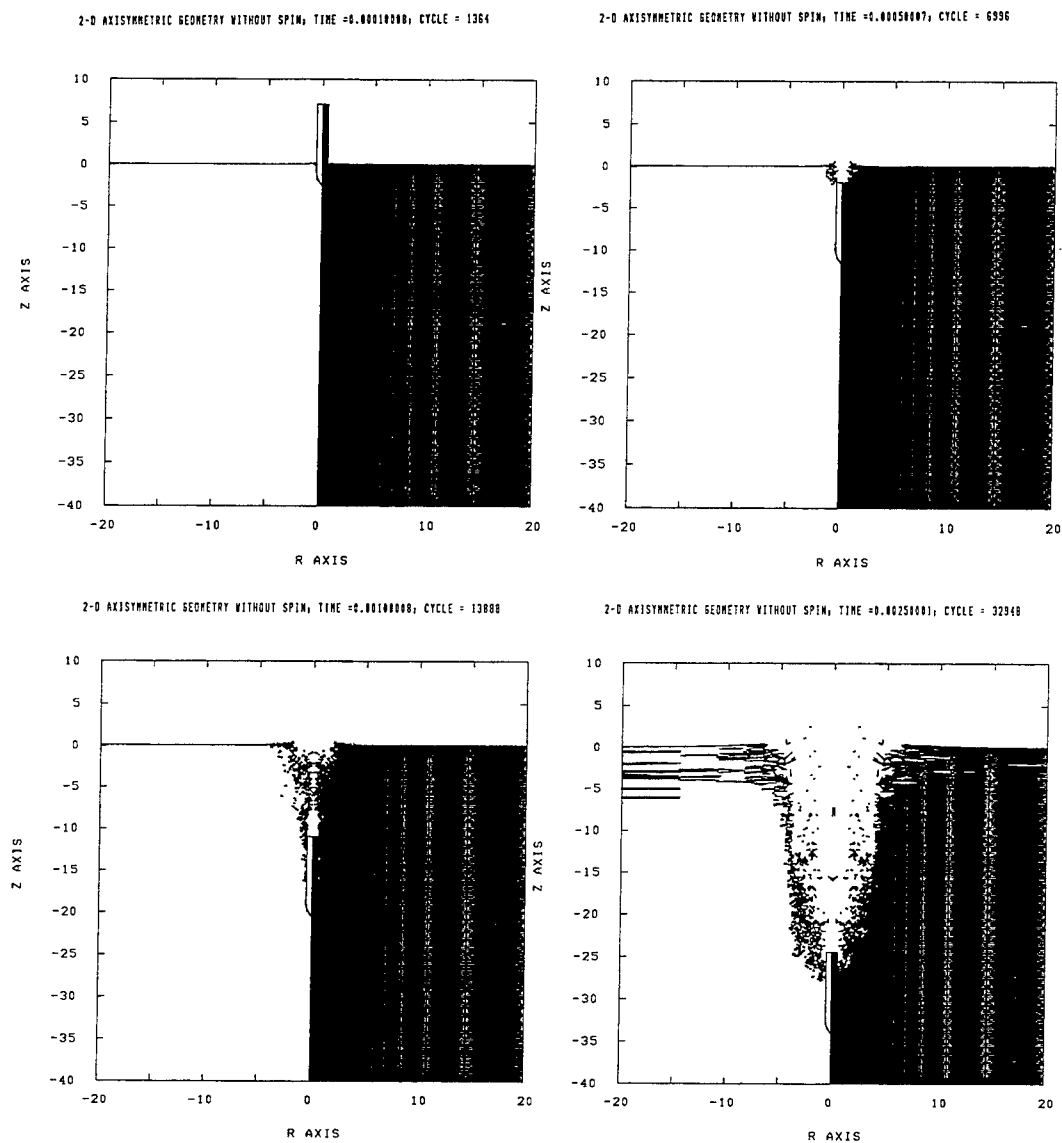


Figure 6.21. Deformed grid for an AP projectile impacting CSPC concrete at 642 m/s (time is in seconds; axis units are inches).

show the gradual formation of the impact crater and penetration tunnel. As the penetration progresses, material around the impact area is ejected in a manner similar to that shown in Figures 2.3 and 6.12. The diameter of the impact crater at the target surface for the 277 m/s impact velocity is about 200 mm (7.9 inches). The crater being generated in the simulation shown in Figure 6.19 is about 254 mm (10 inches) in diameter. After the impact phase, both the simulation and experiment show a tunnel that is the same diameter as the projectile. The deformed grids in Figures 6.20 and 6.21, however, exhibit continued deformation along the penetration path after the projectile has passed. This results in a larger impact crater and tunnel than was seen in the experiments. The cause of this difference is the criteria used in the simulations to delete highly damaged and very small elements from the finite element grid in order to improve computational time. In the simulations the extent of damage and degradation in the target is indicated by the value of the parameter EBAR (strain ratio in the NIF model). Figures 6.22, 6.23, and 6.24 show the progression of the change in EBAR at two times during the simulations for each of the impact velocities. The simulations show high values of EBAR indicating significant damage and degradation of the material where the impact crater and tunnel are being formed and around the aft end of the projectile. The radial extent of the material with high values of EBAR is about four times the diameter of the projectile. Beyond this range, the material is effectively intact and fairly competent. In the simulations, the material that is highly damaged or degraded is eventually removed from the grid if EBAR for the element exceeds  $EBAR_{crit}$ . The impact crater and tunnel continue to grow with removal of the damaged elements and eventually become larger than the impact crater and tunnel observed in the experiments. In the experiments, material along the tunnel is highly damaged but not ejected from the target because it is held in place by its neighboring material due to interlocking and frictional forces. During removal of projectiles from the targets after the penetration experiments, it was noted that material along the penetration path was very weak and easily broken.

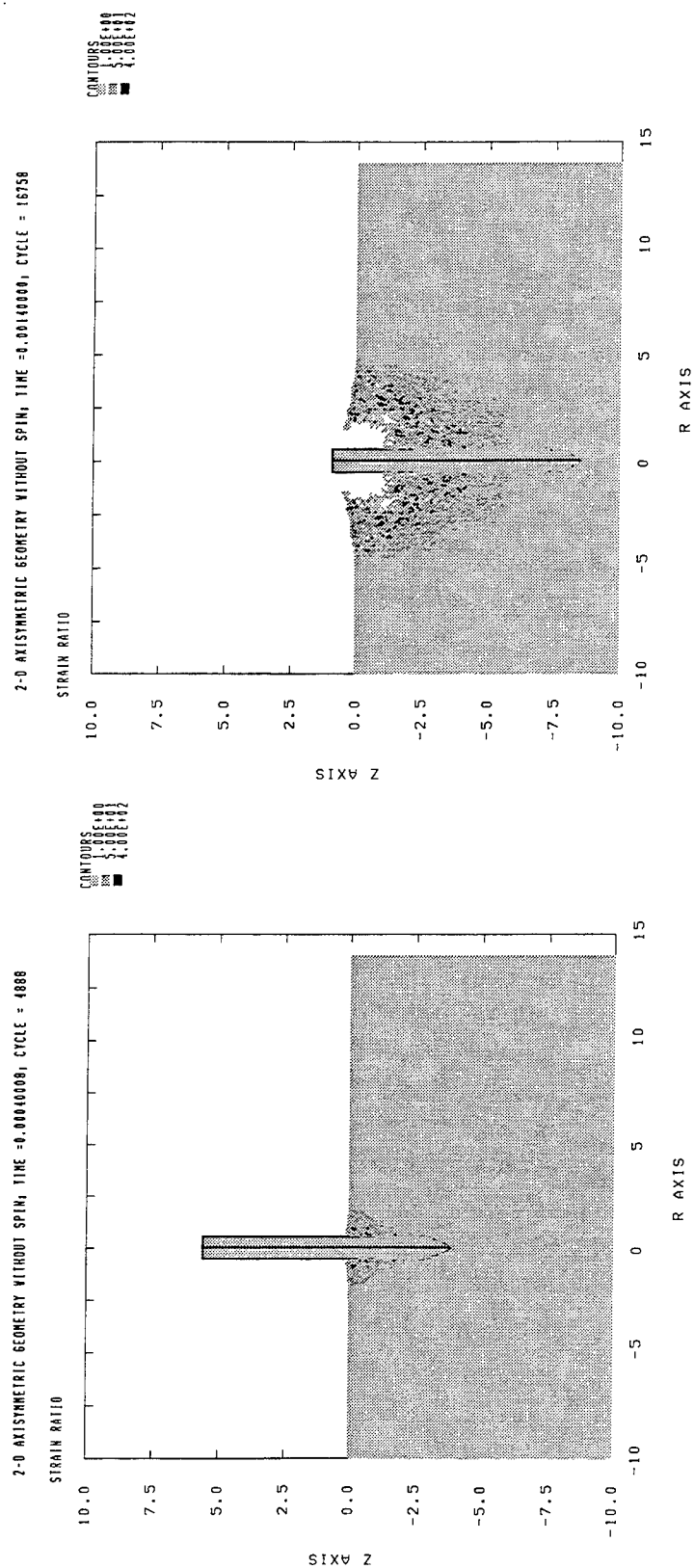


Figure 6.22. EBAR (strain ratio) contours for an AP projectile impacting CSPC concrete at 277 m/s (time is in seconds; axis units are inches; contours are dimensionless).

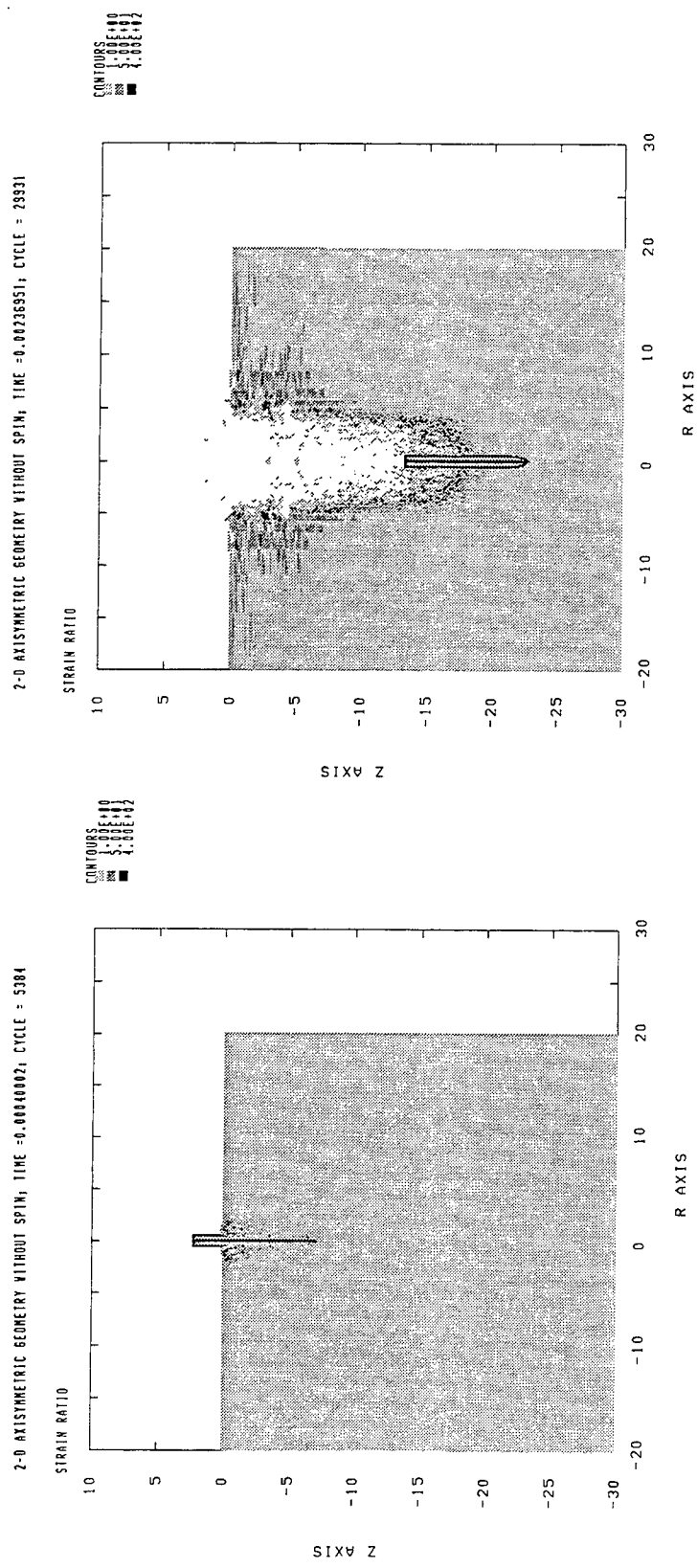


Figure 6.23. EBAR (strain ratio) contours for an AP projectile impacting CSPC concrete at 499 m/s (time is in seconds; axis units are inches; contours are dimensionless).

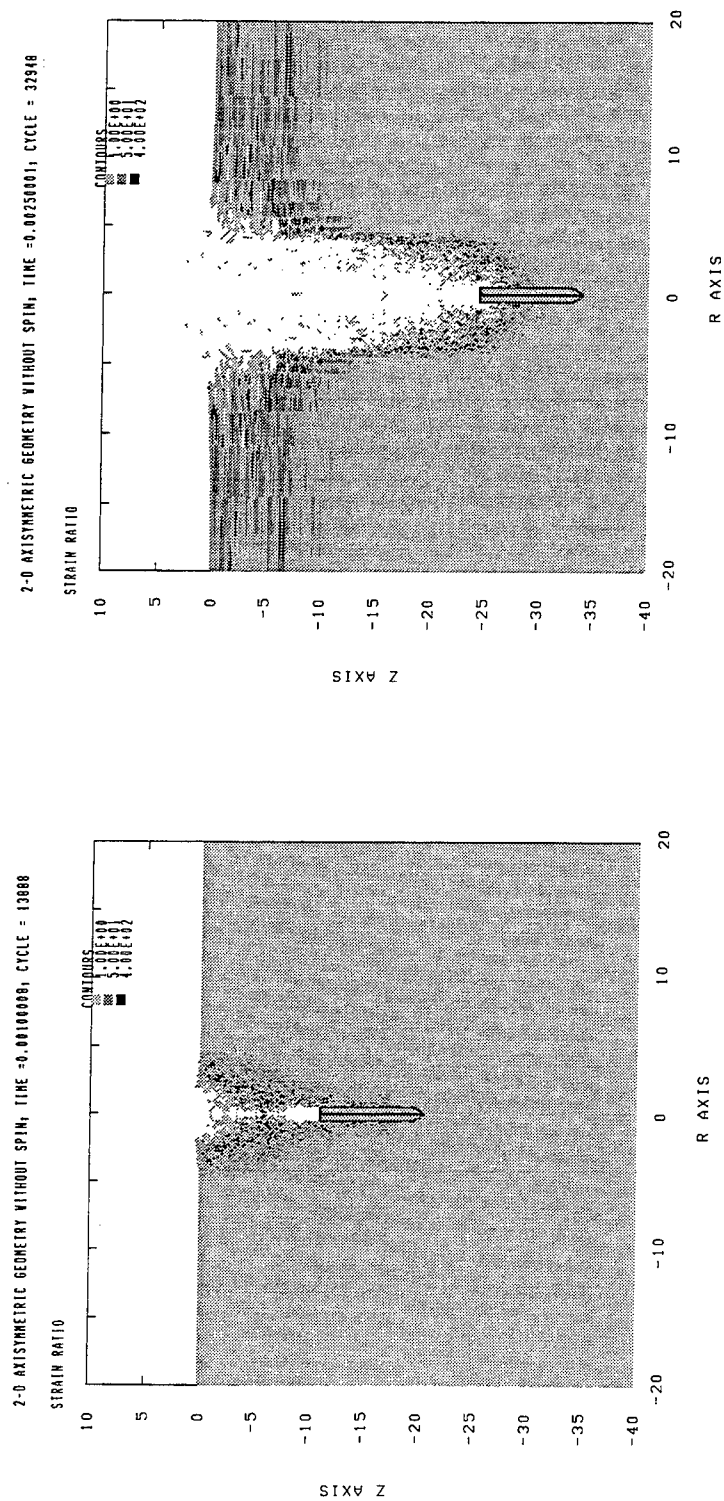


Figure 6.24. EBAR (strain ratio) contours for an AP projectile impacting CSPC concrete at 642 m/s (time is in seconds; axis units are inches; contours are dimensionless).

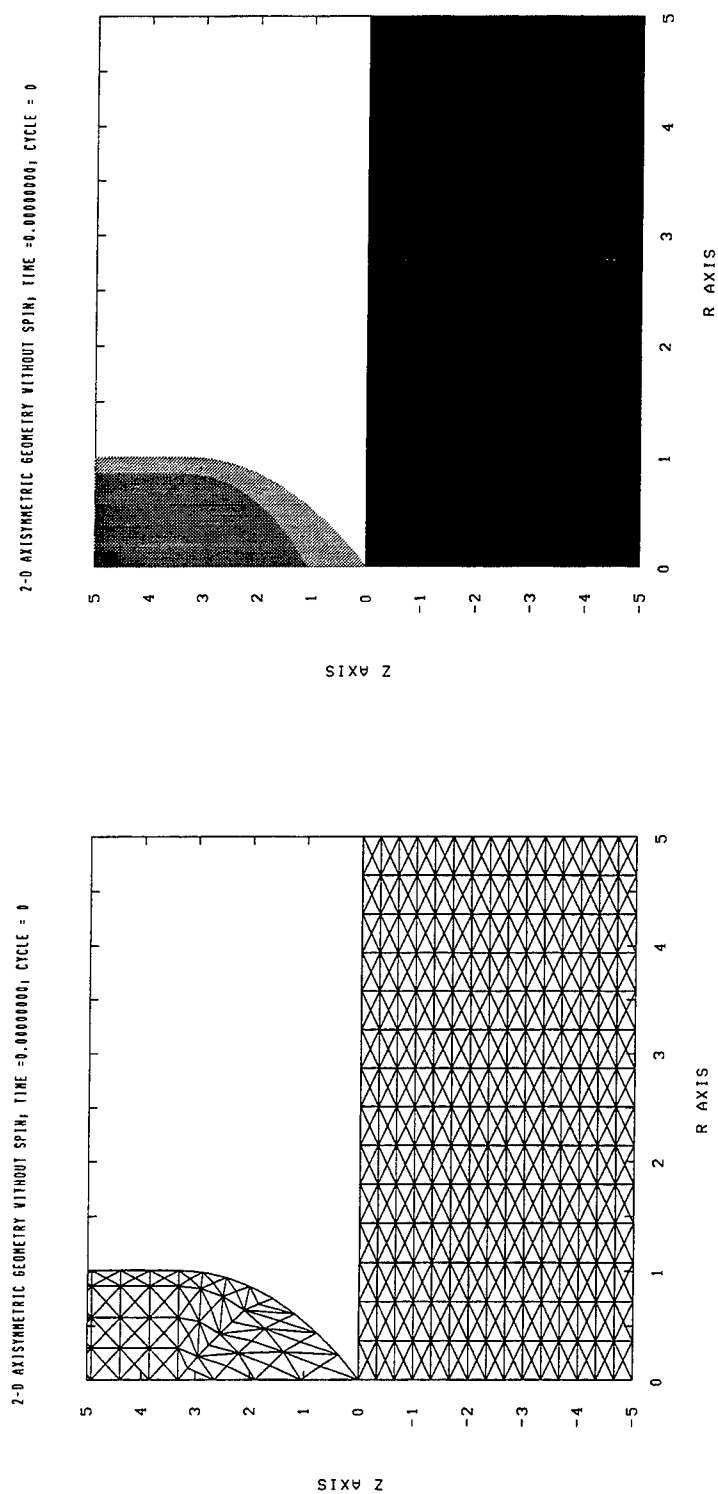
### 6.2.2 Perforation Experiments

Perforation experiments conducted into the 254-, 216-, and 127-mm-thick slabs will be simulated using the NIF for the target response. A close-up of the initial grid used in the simulations of the perforation experiments is shown in Figure 6.25.a. Figure 6.25.b shows the materials used in the grid. In the projectile, the outer column of the grid makes up the steel case of the projectile. Although not shown, a steel end-cap sealed the back of the projectile. No significant deformation of the projectile case is expected, so the influence of movement of the fill material on the projectile response should be minor. The fill material was “fixed” to the steel case so that no slideline was required.

Model parameters presented in Table 4.4 were used in the simulations. The value of DYN applied to the ultimate strength in both shear and hydrostatic tension was 1.25. In order to determine the value of  $EBAR_{crit}$ , a simulation of the SAP projectile impacting a half-space of WES5000 concrete was performed. Experience has shown that the projectile should penetrate approximately 3.7 calibers into this type of concrete. The value of  $EBAR_{crit}$  was determined to be 350 by simulating a penetration experiment at 313 m/s until a reasonable result (depth of penetration) was obtained. The deformed grid from the final simulation is shown in Figure 6.26. The final depth of penetration is about 3.77 calibers. This value was then used for the three simulations of the perforation experiments. Modification to the tension and shear unload/reload responses and the additional check to gradually remove elements with minimum height less than 1.27 mm (0.05 inches) discussed above were also used in these simulations.

The initial grids for the perforation simulations are shown in Figure 6.27. The radius of the grids were all the same and equal to 762 mm (30 inches). Since the size of the targets were relatively small it was not necessary to expand the grids. All elements within the grids were the same size. The impact velocity for all simulations was 313 m/s.





a. Initial grid

b. Materials: gray - filler, medium gray - steel, black - concrete

Figure 6.25. Close-up of initial grid and materials used in simulation of the SAP projectile perforating WES5000 concrete slabs (axis units are inches).

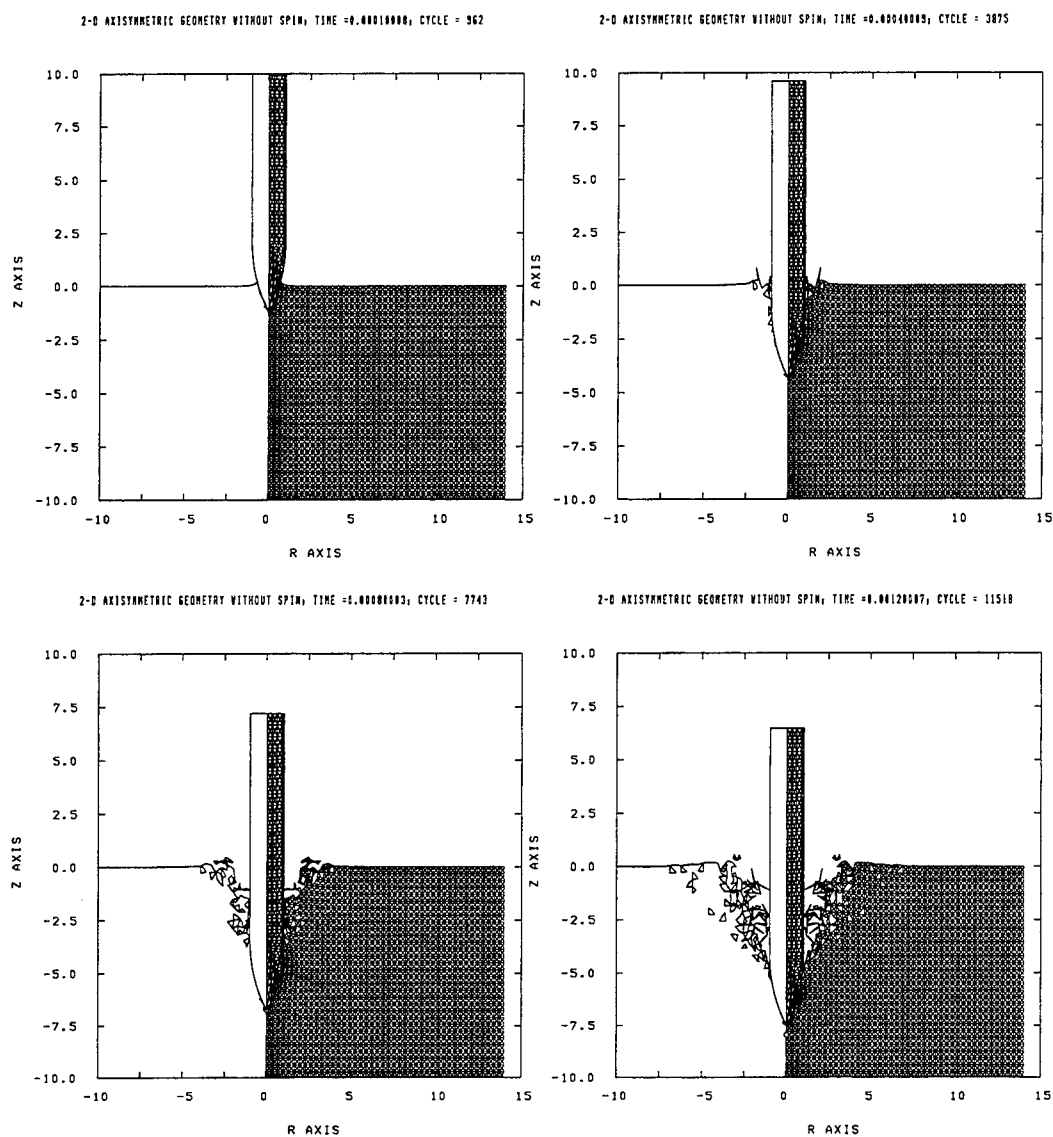


Figure 6.26. Deformed grid for a SAP projectile impacting a half-space of WES5000 concrete (time is in seconds; axis units are inches).

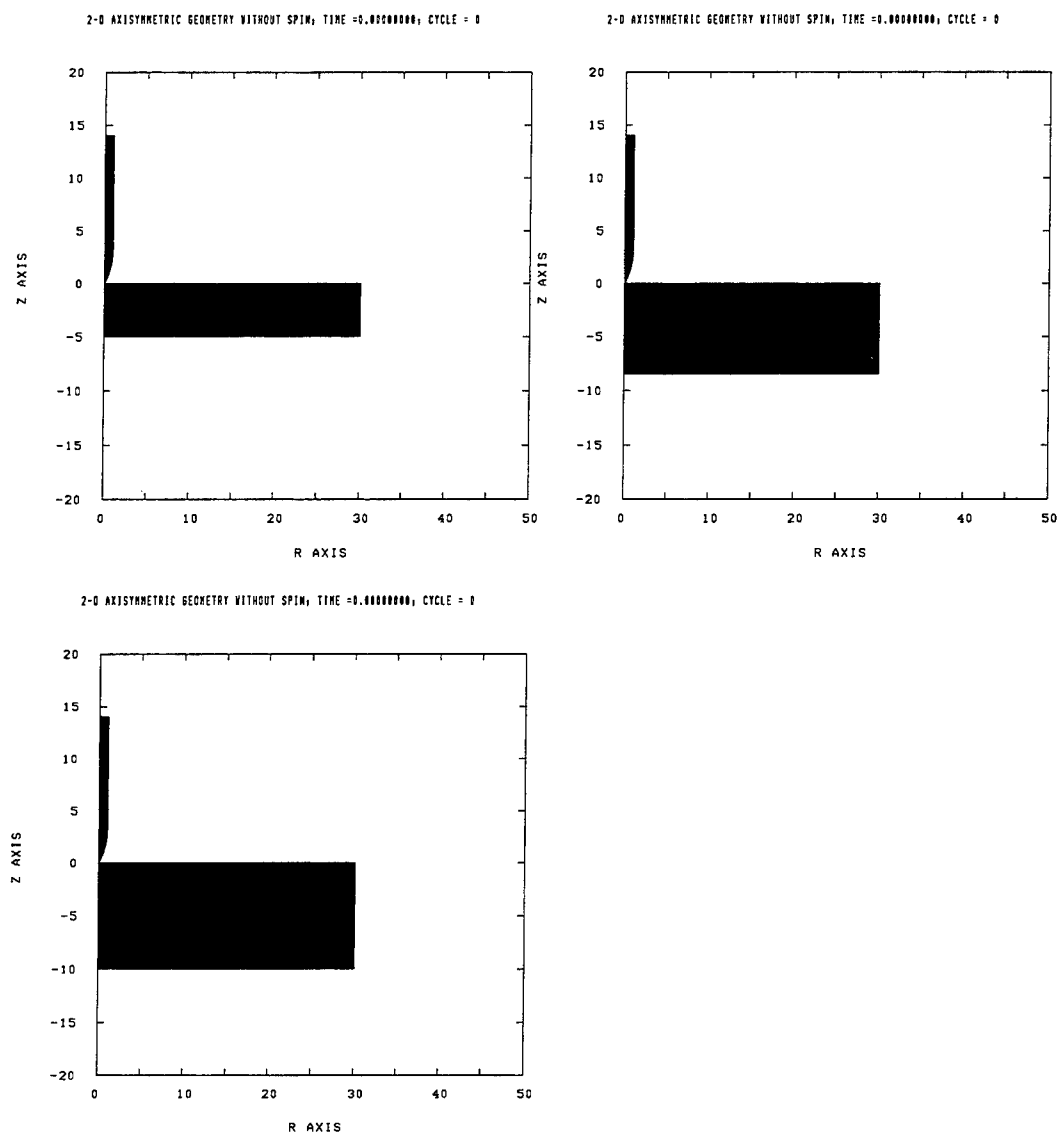


Figure 6.27. Initial grids for simulating the SAP projectile perforating 127-, 216-, and 254-mm-thick (5.0-, 8.5-, and 10.0-inch-thick) WES5000 concrete slabs (axis units are inches).

Each of the simulations exhibited a trend of decreasing velocity with time until a constant exit velocity was achieved. Results from the simulations are compared to the experiment results in Figure 6.28 by comparing the ratio of exit velocity to the impact velocity. The simulation results agree well with the experiment results, with the greatest difference being for the 254-mm-thick slab. The deformed grids at several times during the simulations for each of the slab thicknesses are shown in Figures 6.29, 6.30, and 6.31, respectively. Contour plots of EBAR (strain ratio) for each of the target thicknesses are shown in Figures 6.32, 6.33, and 6.34, respectively. Like the experiment results in Figure 6.12, each simulation shows the formation of the impact crater as material is ejected from the impact area. As the thickness of the slab increases, the size of the exit crater increases as shown in Figures 6.13, 6.14, and 6.15. Simulations for the 216- and 254-mm-thick slabs also show the progressive formation of the exit cone as was described in Section 2.4. As the simulation progresses, the projectile passes through the cone essentially destroying it. Large areas of “damaged” material around the impact crater, projectile, and exit crater are implied by the strain ratio contours in Figures 6.32, 6.33, and 6.34. As with the penetration experiments, material within these regions was easily broken, but farther away, the material was very competent. Again, the highly “damaged” material in the simulations continues to be removed if the value of EBAR exceeds  $EBAR_{crit}$ . The continued removal of these highly “damaged” elements allows the impact and exit craters to continue to grow.

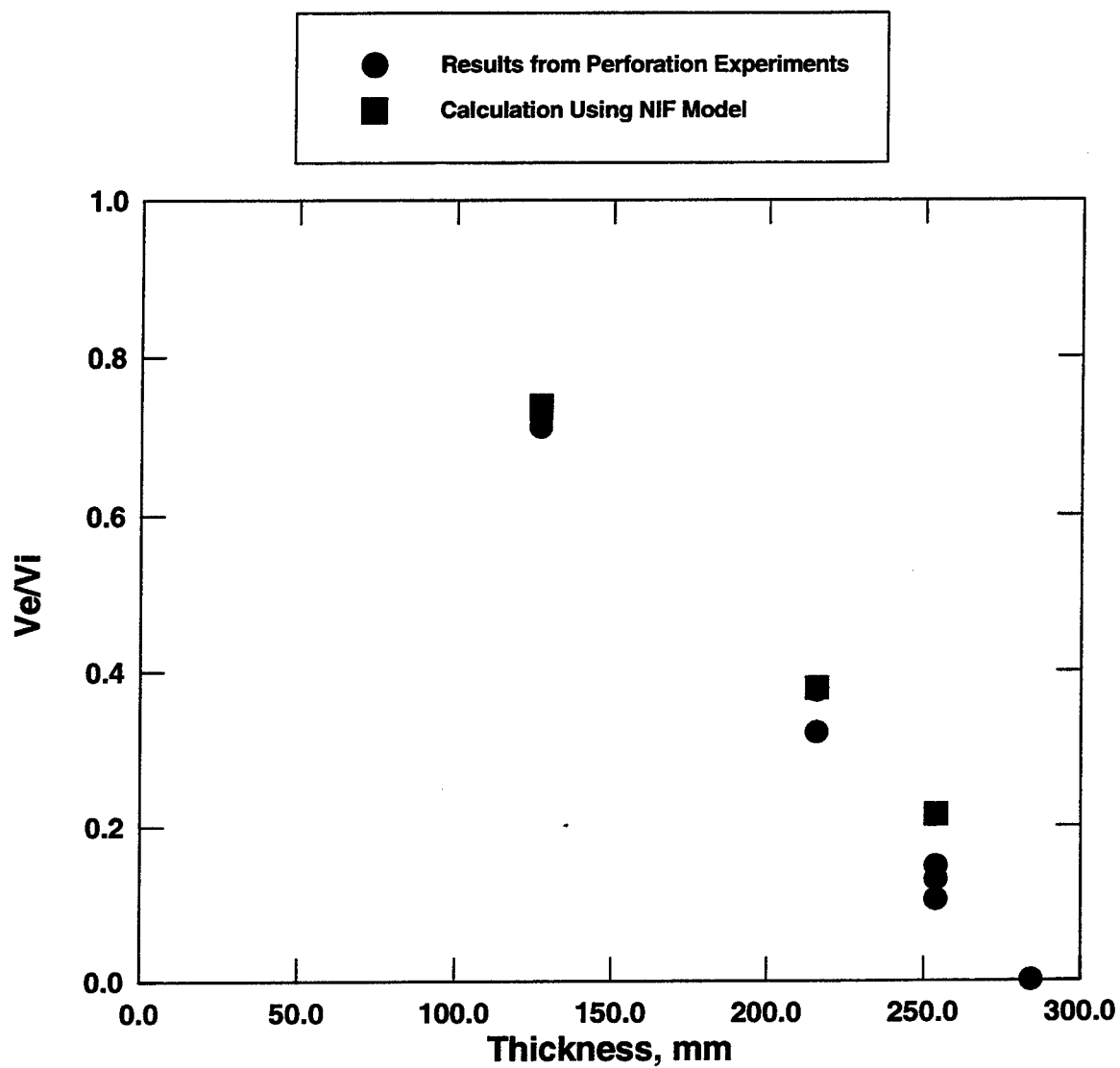


Figure 6.28. Comparison of simulation and experiment results for a SAP projectile perforating WES5000 concrete slabs.

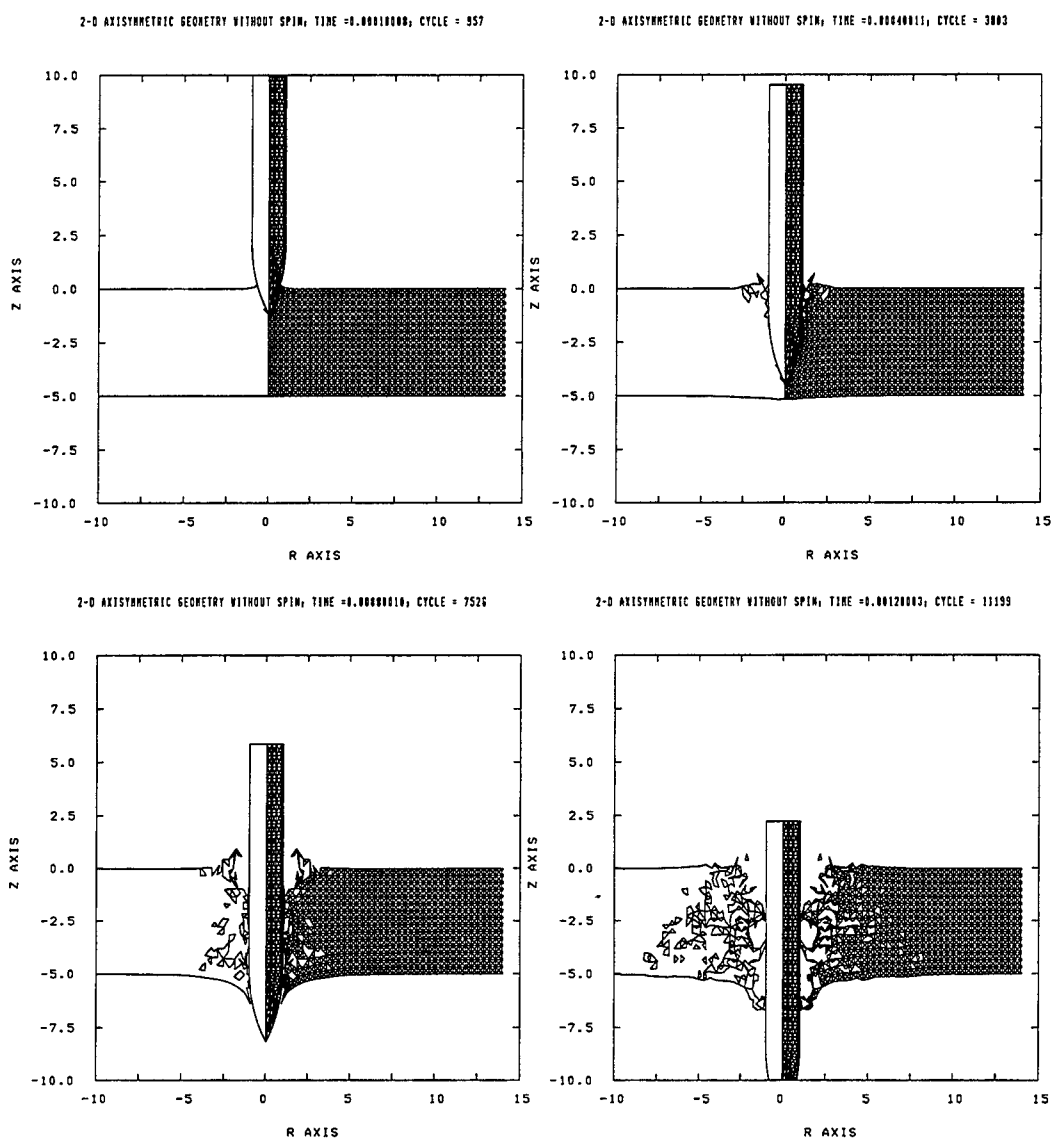


Figure 6.29. Deformed grid for a SAP projectile perforating a 127-mm-thick WES5000 concrete slab (time is in seconds; axis units are inches).

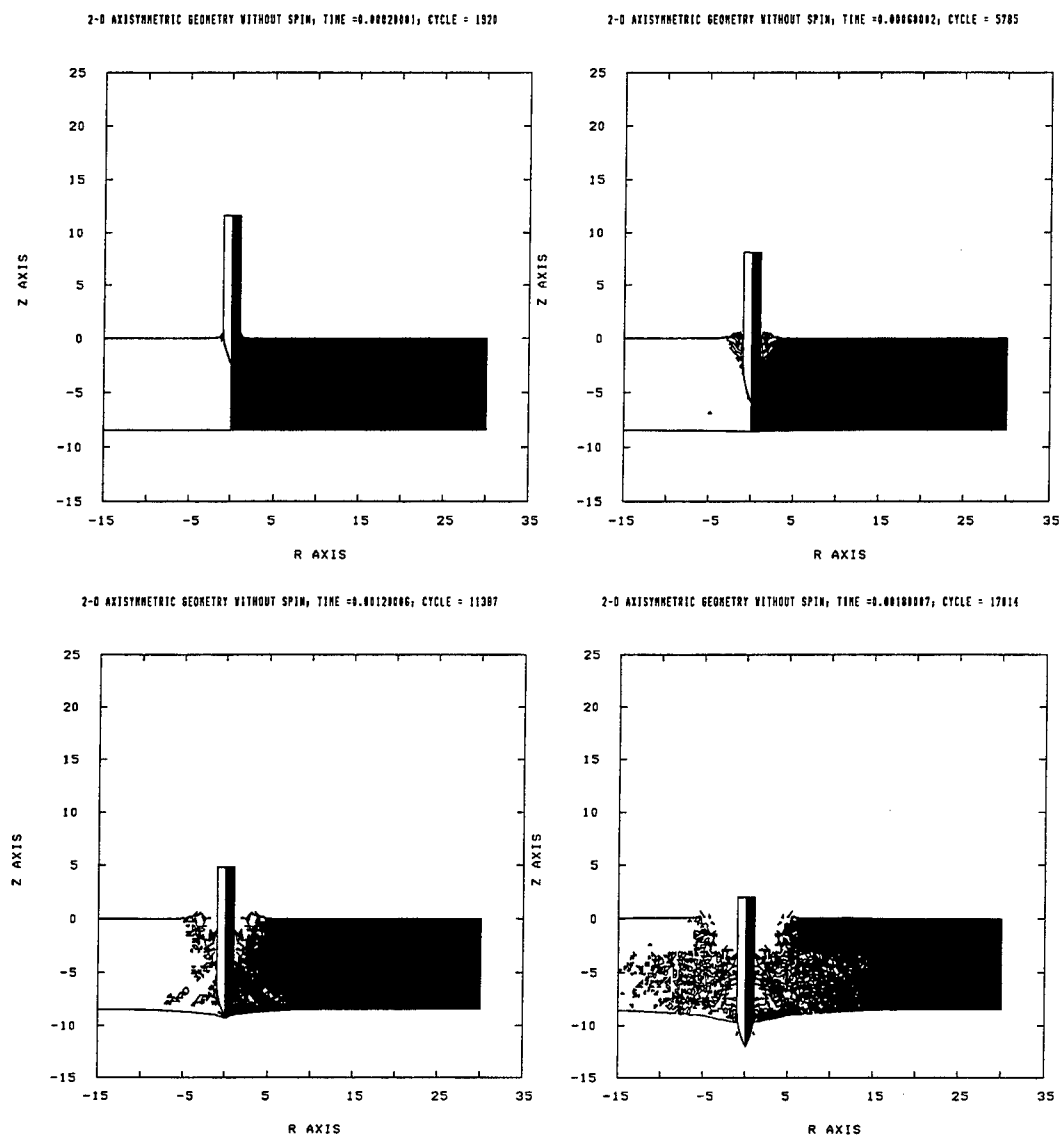


Figure 6.30. Deformed grid for a SAP projectile perforating a 216-mm-thick WES5000 concrete slab (time is in seconds; axis units are inches).

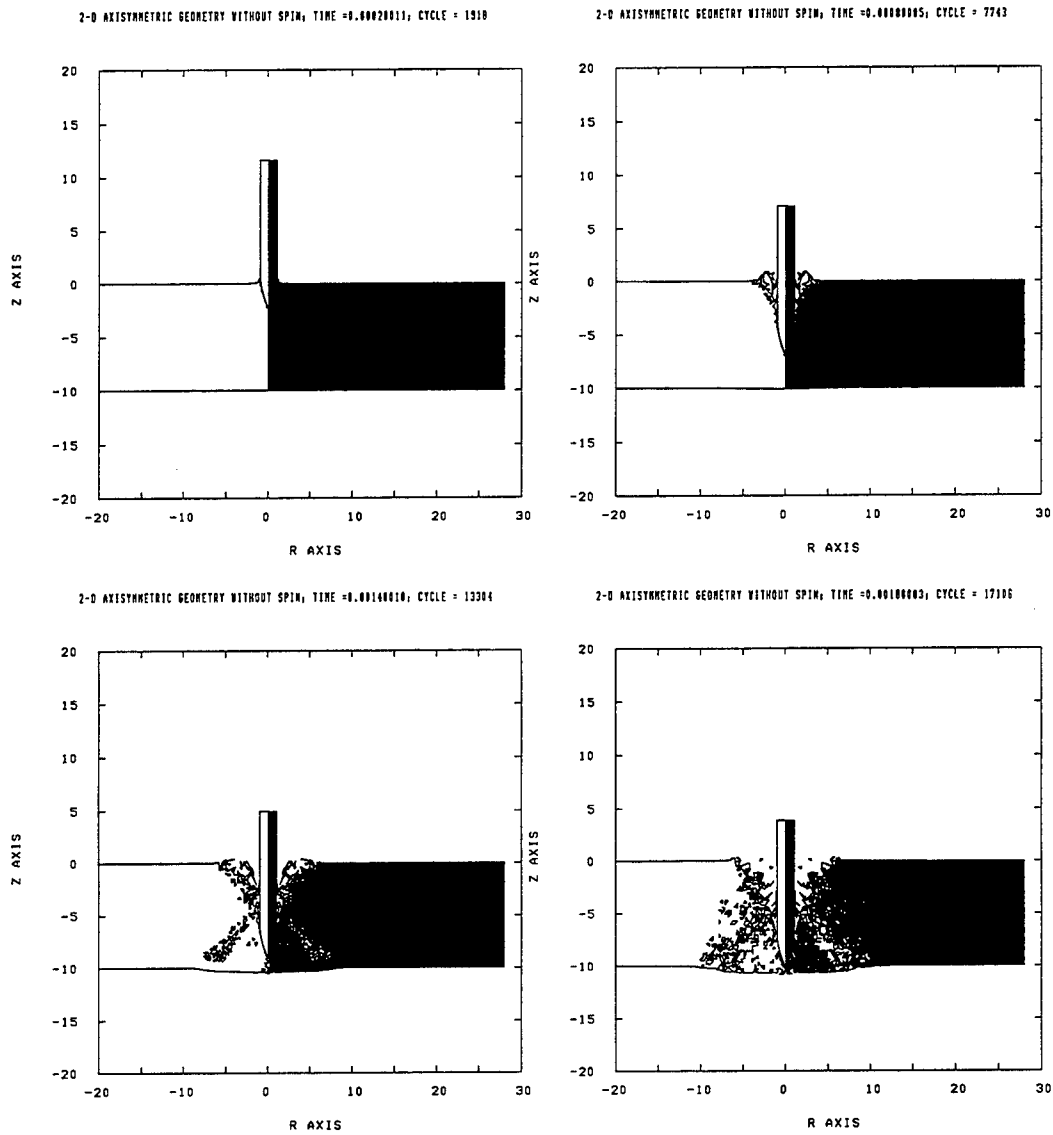


Figure 6.31. Deformed grid for a SAP projectile perforating a 254-mm-thick WES5000 concrete slab (time is in seconds; axis units are inches).



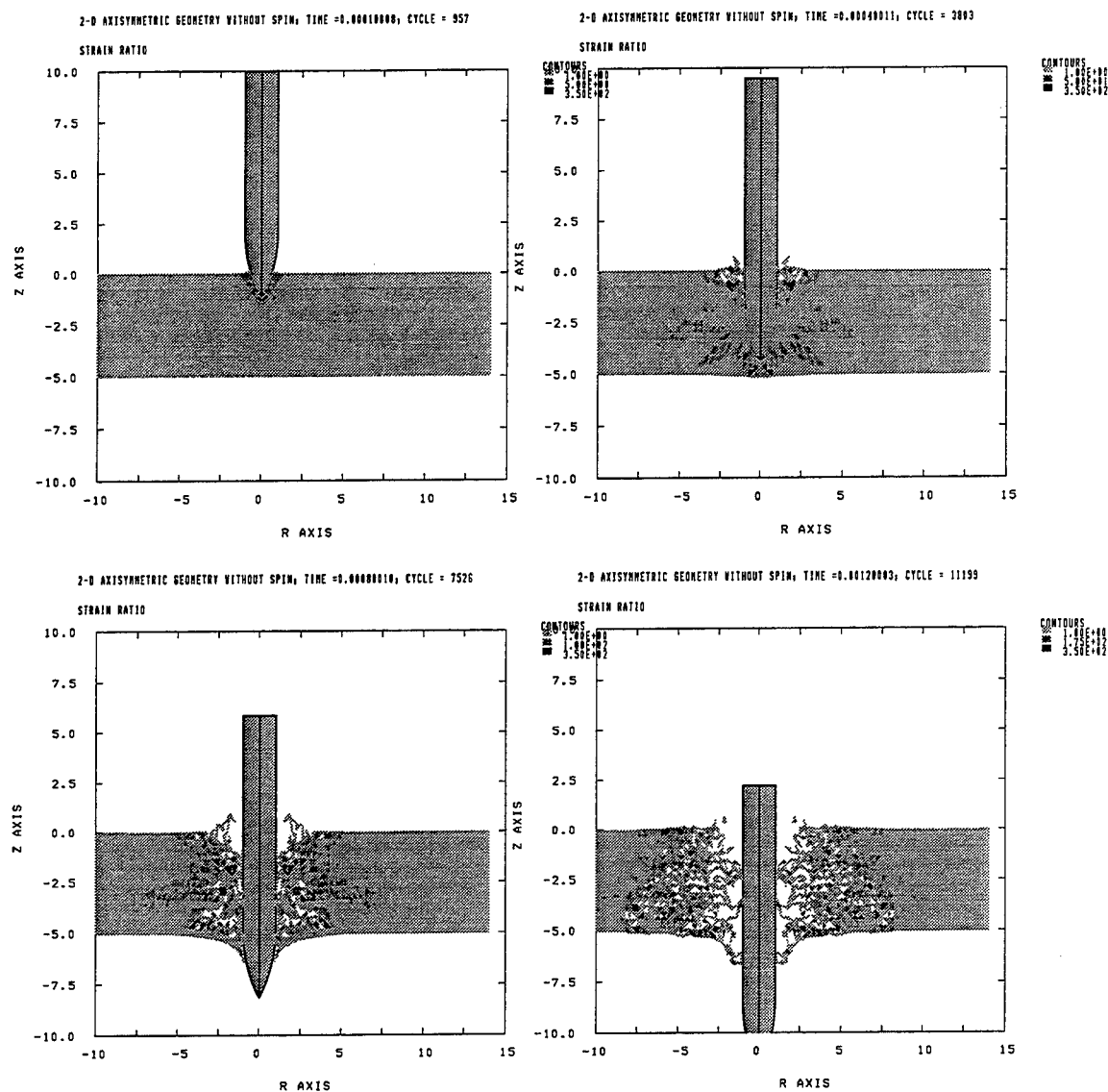


Figure 6.32. EBAR (strain ratio) contours for a SAP projectile perforating a 127-mm-thick WES5000 concrete slab (time is in seconds; axis units are inches; contours are dimensionless).





## CHAPTER 7

### CONCLUSIONS AND RECOMMENDATIONS

#### 7.1 CONCLUSIONS

Simulation of high-velocity projectile penetration into brittle geomaterials is generally performed using either empirical, analytical, or numerical techniques. Only the numerical techniques offer the capability of detailed simulation of the phenomena that occur including the large deformation of the target during formation of craters and the tunneling phase, as well as insight into the response and condition of the target as a result of the penetration event. The loads applied to the target during these events are intense with pressures approaching 1,000 MPa and strain rates up to  $10^4$  /sec.

Laboratory mechanical property tests on brittle geomaterials show a transition in material response from brittle at low pressures to ductile at high pressures. A nonlinear, inelastic fracture (NIF) model was developed that can replicate the brittle response of the material at low pressures and the transition to ductile response at high pressures. The underlying hypothesis of the model is that the shearing response of the material can be resolved into a brittle cohesive component and a ductile frictional component. At very low pressures the cohesive component controls the behavior of the material and the response is brittle. As pressure increases, the cementing bonds between the aggregate particles are broken and the contribution of the cohesive component decreases while the contribution of the frictional component increases. This phase is the transition from brittle to ductile response. The response becomes fully frictional once the cementing bonds are completely broken. This is the fully ductile phase of the response. The NIF model response agreed well with the results from various quasi-static triaxial experiments

on concrete samples and captured all three of the shear phases. Dynamic loading experiments indicate strength enhancement by factors of two or more as loading rate increases. Dynamic strain rate effects were indirectly accounted for in the model by multiplying the ultimate strength of the material in shear and hydrostatic tension by a constant parameter.

The model was implemented into a finite-element wave propagation code. This process involved implementing algorithms to calculate the correct strain input to the model, and to convert the stress output by the model into the form accepted by the code. The model requires the total Lagrangian strain based on the original configuration as input. The Green-Lagrange measure of strain meets this requirement and was selected as the strain input. The strain components were calculated using the deformation-rate and spin tensors from the updated Lagrangian kinematics formulation of the code. The stress output by the model is the Cauchy stress aligned with the original configuration. This stress was rotated to the current configuration of the element to be compatible with the formulation of the code.

A series of laboratory penetration and perforation experiments were conducted to evaluate the performance of the model within the finite-element code. Penetration experiments were conducted by launching a robust, thick-walled steel projectile into semi-infinite concrete targets at impact velocities ranging from 277 to 800 m/s. The data from these experiments included depth of penetration and a mapping of the impact crater and penetration path. Perforation experiments were conducted by launching a robust steel projectile at 313 m/s into concrete slabs with thicknesses ranging from 127 to 284 mm. Data from these experiments included high-speed movies of the impact phase, high-speed movies to capture the evolution of damage to the backface of the slabs and to measure the exit velocity, and the mappings of the impact and exit craters.

Simulation of penetration experiments into thick concrete targets showed the formation of the impact crater and the tunnel during the penetration event. The depth of penetration from the simulations agreed well with the data from the experiments. The simulations showed significant damage and degradation of the material where the impact crater and tunnel were being formed and around the aft end of the projectile. As the simulation continued, the impact crater and tunnel continued to grow and eventually became larger than the impact crater and tunnel observed from the experiments. During posttest examination of the targets from the experiments, it was noted that material along the penetration path was very weak and easily broken. The broken materials were not ejected from the target because they were held in place by interlocking and frictional forces, which were not accounted for in the simulations. Exit velocities from simulation of the perforation experiments agreed well with the data from the experiments. The simulations showed the formation of the impact crater and the progressive formation of the exit cone ahead of the projectile as the backface of the target was approached.

## 7.2 RECOMMENDATIONS

The criteria used to eliminate highly deformed and damaged elements from the simulations need further development. These criteria are needed to allow selection of reasonable computational time increments. Currently, determination of the parameters controlling these criteria is iterative and requires comparison of simulation results with data from penetration experiments. Since values for  $EBAR_{crit}$  were similar for both of the concrete materials used in this research, a value in the range of 350 to 400 may be sufficient, but this requires further investigation. A criterion that does not require this iterative approach or can be based purely on the response and condition of the damaged material is preferable. Use of the model with meshless methods and adaptive grids may eliminate the need for removing highly deformed elements and is a topic for future investigation. Since these methods can require significant computational time, parallel processing may be required.

Additional data on the response of brittle geomaterials to the combined effects of pressure and strain rate are needed. Also, current data is inconclusive as to whether strain rate affects the failure mode of the material or just its ultimate strength.

The ultimate strength in the current model does not distinguish between compression and extension loading. Data from triaxial experiments on brittle geomaterials show that the strength in extension is much lower than the strength in compression. Use of different compression and extension strength surfaces based on the Lode angle would enhance the capabilities of the model.

Other enhancements to the model can include thermal effects and shear induced dilatancy. Significant heat is generated during high-velocity projectile penetration, but it is unclear as to the effect heat may have on the material response. Shear induced dilatancy can be added to the model by including a correction function to account for the volumetric strains produced during deviatoric loadings.

Cause and effect studies can be conducted using the model to investigate the effect of the cohesive and frictional components on the penetration process. Other geomaterials that are as strong as concrete but not as brittle, such as rock, or stronger and more brittle, such as high-strength concrete, should be fit to the model and used in simulations to evaluate the model performance for these materials. Evaluation of the model performance under loading conditions resulting from explosions or quasi-static applications is also of interest.

## LIST OF REFERENCES



## LIST OF REFERENCES

- Adley, M. D., Cargile, J. D., Akers, S. A., and Rohani, B. 1996. "Numerical Simulation of Projectile Penetration into Concrete," Proceedings of the 14th U. S. Army Symposium on Solid Mechanics, October 16-18, Myrtle Beach, SC.
- Ahrens, T. J. and Rubin, A. M. 1993. "Impact-Induced Tensional Failure in Rock," *Journal of Geophysical Research*, Vol. 98, No. E1, pp. 1185-1203.
- Akers, S. A. 1992. Computer program DRIVER, personal communication.
- Anderson, C. E., Cox, P. A., Johnson, G. R., and Maudlin, P. J. 1994. "A Constitutive Formulation for Anisotropic Materials Suitable for Wave Propagation Computer Programs - II," *Computational Mechanics* 15, pp. 201-223.
- Ashby, M. F. and Hallam, S. D. 1986. "The Failure of Brittle Solids Containing Small Cracks Under Compressive Stress States," *Acta Metallica*, Vol. 34, No. 3, pp. 497-510.
- Bangash, M. Y. H. 1993. Impact and Explosion: Analysis and Design, CRC Press, Boca Raton, FL.
- Bazant, Z. P. 1996. "Finite Strain Generalization of Small-Strain constitutive Relations and Volumetric-Deviatoric Split," *International Journal of Solids and Structures*, Vol. 33, No. 20-22, pp. 2887-2897.
- Bazant, Z. P., Adley, M. D., and Xiang, Y. 1996. "Finite Strain Analysis of Deformations of Quasibrittle Material during Missile Impact and Penetration," *Advances in Failure Mechanisms in Brittle Materials*, American Society of Mechanical Engineers, MD-Vol. 75/AMD-Vol. 219, pp. 163-169.
- Bernard, R. S. and Creighton, D. C. 1976. "Projectile Penetration in Earth Materials: Theory and Computer Analysis," November 1976, Technical Report S-76-13, U.S. Army Engineer Waterways Experiment Station, Vicksburg, MS.
- Bernard, R. S. 1977. "Empirical Analysis of Projectile Penetration in Rock," November 1977, Miscellaneous Paper, S-77-16, U.S. Army Engineer Waterways Experiment Station, Vicksburg, MS.

Bischoff, P. H. and Perry, S. H. 1986. "Compressive Strain Rate Effects of Concrete," proceedings of the Cement-Based Composites: Strain Rate Effects on Fracture Symposium, Boston, MA, December 4-5, 1986, edited by Mindess, S. and Shah, S. P.

Bruno, M. S. and Nelson, R. B. 1991. "Microstructural Analysis of Inelastic Behavior of Sedimentary Rock," *Mechanics of Materials* (12), pp. 95-118.

Cargile, J.D. 1998. "Recommended Material Properties for a Conventional Strength Portland Cement (CSPC) Concrete," personal files.

Cargile, J. D. 1986. "Laboratory Test Results for Nellis Baseline Sand," Technical Report SL-86-15, September 1986, US Army Engineer Waterways Experiment Station, Vicksburg, MS.

Cargile, J. D., Giltrud, M. E. and Luk, V. K. 1993. "Perforation of Thin Unreinforced Concrete Slabs," Proceedings of the Special Session during the Sixth International Symposium on Interaction of Nonnuclear Munitions with Structures, Panama City Beach, FL, May 3-7, 1993.

Chen, E. P. 1989. "Penetration into Dry Porous Rock: A Numerical Study on Friction Simulation," in Computational Techniques for contact, Impact, Penetration and Perforation of Solids, Winter Annual Meeting of the American Society of Mechanical Engineers, San Francisco, CA, December 10-15, 1989.

Chen, W. F. 1982. Plasticity in Reinforced Concrete, McGraw-Hill, Inc., New York, NY.

Chen, W. F. and Saleeb, A. F. 1982. Constitutive Equations for Engineering Materials, Volume 1: Elasticity and Modeling, John Wiley and Sons, Inc., New York, NY.

Chen, W. F. and Baladi, G. Y. 1985. Soil Plasticity: Theory and Implementation, Elsevier Science Publishers B. V., Amsterdam, The Netherlands.

Desai, C. S. and Siriwardane, H. J. 1984. Constitutive Laws for Engineering Materials with Emphasis on Geologic Materials, Prentice-Hall, Inc., Englewood Cliffs, NJ.

Desai, C. S., Kundu, T., and Wang, G. 1990. "Size Effect on Damage Parameters for Softening in Simulated Rock," *International Journal for Numerical and Analytical Methods in Geomechanics*, Vol. 14, pp. 509-517.

Ehrgott, J. Q. 1971. "Calculation of Stress and Strain from Triaxial Test Data on Undrained Soil Specimens," Miscellaneous Paper S-71-9, U.S. Army Engineer Waterways Experiment Station, Vicksburg, MS.

Elfgren, L. 1989. Fracture Mechanics of Concrete Structures: From Theory to Applications, RILEM, Technical Committee 90 FMA, London.

Elwi, A. A. and Murray, D. W. 1979. "A 3D Hypoelastic Concrete Constitutive Relationship," ASCE Journal of the Engineering Mechanics Division, Vol. 105, No. EM4, August, pp. 623-641.

Forrestal, M. J. 1986. "Penetration into Dry Porous Rock," International Journal of Solids and Structures, Vol. 22, No. 12, pp. 1485-1500.

Forrestal, M. J. and Luk, V. K. 1992. "Penetration into Soil Targets," International Journal of Impact Engineering, Vol. 12, No. 3, pp. 427-444.

Forrestal, M. J., Altman, B. S., Cargile, J. D., and Hanchak, S. J. 1994. "An Empirical Equation for Penetration Depth of Ogive-Nose Projectiles into Concrete Targets," International Journal of Impact Engineering, Vol. 15, No. 4, pp. 395-405.

Forrestal, M. J. and Tzou, D. Y. 1997. "A Spherical Cavity-Expansion Penetration Model for Concrete Targets," International Journal of Solids and Structures, to be published.

Frew, D. J., Cargile, J. D., and Ehrigott, J. Q. 1993. "WES Geodynamics and Projectile Penetration Research Facilities," Advances in Numerical Simulation Techniques for Penetration and Perforation of Solids, ASME Winter Annual Meeting, New Orleans, LA, November 28 - December 3, 1993.

Fu, H. C., Erki, M. A., and Seckin, M. 1990. "Review of Effects of Loading rate on Concrete in Compression," ASCE Journal of Structural Engineering, Vol. 117, No. 12, December, pp. 3645-3659.

Goldsmith, Werner. 1960. Impact: The Theory and Physical Behaviour of Colliding Solids, Edward Arnold (Publishers) Ltd., London.

Gran, J. K., Florence, A. L., and Colton, J. D. 1989. "Dynamic Triaxial Tests of High-Strength Concrete," ASCE Journal of Engineering Mechanics, Vol. 115, No. 5, May, pp. 891-904.

Henderson, D. and Stephens, R. L. 1972. "Impact and Penetration Technology," presented at the Fuze/Munitions Environmental Characterization Symposium, November 28, Picatinny Arsenal, Dover, NJ.

Heuze, F. E. 1989. "An Overview of Projectile Penetration into Geological Materials, with Emphasis on Rocks," in Computational Techniques for contact, Impact, Penetration and Perforation of Solids, Winter Annual Meeting of the American Society of Mechanical Engineers, San Francisco, CA, December 10-15, 1989.

Hordijk, D. A., Van Mier, J. G. M., and Reinhardt, H. W. 1989. "Chapter 4: Material Properties," in *Fracture Mechanics of Concrete Structures: From Theory to Applications*, Edited by L. Elfgren, RILEM, Technical Committee 90-FMA Fracture Mechanics to Concrete - Applications, published in US by Chapman and Hall, New York, NY.

Hughes, M. L., Tedesco, J. W., and Ross, C. A. 1993. "Numerical Analysis of High Strain Rate Splitting-Tensile Tests," *Computers and Structures*, Vol. 47, No. 4/5, pp. 653-671.

Jansen, D. C. and Shah, S. P. 1997. "Effect of Length on Compressive Strain Softening of Concrete," *ASCE Journal of Engineering Mechanics*, Vol. 123, No. 1, January 1997, pp. 25-35.

Jeng, Y. S. and Shah, S. P. 1987. "Fracture Mechanics and Constitutive Modeling of Concrete," in *Constitutive Laws for Engineering Materials: Theory and Applications*, edited by Desai, C. S., Krempl, E., Kioussis, P. D., and Kundu, T., Elsevier, New York, NY.

Johnson, G. R., Colby, D. D., and Vavrick, D. J. 1978. "Further Development of the EPIC-3 computer Program for Three-Dimensional Analysis of Intense Impulsive Loading," contract report AFATL-TR-78-81, to Air Force Armament Laboratory, Armament Development and Test Center, Eglin Air Force Base, FL.

Johnson, G. R., Stryk, R. A., Petersen, E. H., Holmquist, T. J., Schonhardt, J. A., and Burns, C. R. 1994. "User Instructions for the 1995 Version of the EPIC Research Code," November 1994, Alliant Techsystems, Hopkins, MN.

Jonas, G. H. and Zukas, J. A. 1978. "Mechanics of Penetration: Analysis and Experiment," *International Journal of Engineering Science*, Vol. 16, pp. 879-903.

Kormeling, H. A. and Reinhardt, H. W. 1987. "Strain Rate effects on Steel fibre concrete in Uniaxial Tension," *International Journal of Cement Composites and Lightweight Concrete*, Vol. 9, No. 4, pp. 197-204.

Krajcinovic, D. 1984. "Continuum Damage Mechanics," *Applied Mechanics Reviews*, Vol. 37, No. 1, January 1984, pp. 1-6.

Ladanyi, B. and Aubertin, M. 1990. "Rate Effects in the Deformation of Rocks," *Proceedings of the First Materials Engineering Congress, Serviceability and Durability of Construction Materials*, edited by B. A. Suprenant, published by American Society of Civil Engineers, August 13-15, 1990, Denver, CO.

Lee, Y.-H. and Willam, K. 1996. "Mechanical Properties of Concrete in Uniaxial Compression," American Concrete Institute Materials Journal, Vol. 93,

Livingston, C. W. and Smith, F. L. 1951. "Bomb Penetration Project," Report by Colorado School of Mines Research Foundation, Inc., Golden, CO, to Albuquerque District, US Army Corps of Engineers, Albuquerque, NM.

Lubarda, V. A., Mastilovic, S., and Knap, J. 1996. "Brittle-Ductile Transition in Porous Rocks by Cap Model," ASCE Journal of Engineering Mechanics, Vol. 122, No. 7, July.

Luk, V. K. and Forrestal, M. J. 1987. "Penetration into Semi-Infinite Reinforced-Concrete Targets with Spherical and Ogival Nose Projectiles," International Journal of Impact Engineering, Vol. 6, No. 4, pp. 291-301.

McGlaun, J. M., Thompson, S. L., and Elrick, M. G. 1990. "CTH: A Three-Dimensional Shock Wave Physics Code," Proceedings of the 1989 Hypervelocity Impact Symposium, December 12-14, 1989, published in International Journal of Impact Engineering, Vol. 10, No. 1-4, 1990.

Nichols, R. M. and Ko, H.-Y. 1996. "Behavior of Plain Concrete Under Multiaxial Stresses Including True Triaxial Tension," report submitted to US Army Engineer Waterways Experiment Station under Contract Nos. DACA 39-93-C-0057 and DACA 39-94-C-0061.

Pahl, Hermann. 1989. "Penetration of Projectiles into Finite Thick Reinforced Concrete Targets," Proceedings of the Fourth International Symposium on the Interaction of Non-Nuclear Munitions with Structures, Panama City Beach, FL, April 17-21.

Rohani, B. and Thompson, L. J. 1970. "A Nonlinear Elastic-Viscoplastic Constitutive Relationship for Earth Materials," Technical Report for Project 678-1, Texas A&M Research Foundation, College Station, TX.

Rossi, P., Wu, X., Le Maou, F., and Belloc, A. 1994. "Scale Effect on Concrete in Tension," Materials and Structures, 27, pp. 437-444.

Sears, F.W., Zemansky, M. W., and Young, H. D. 1976. University Physics, Fifth Edition, Addison-Wesley Publishing Company, Reading, MA.

Sierakowski, R. L. 1984. "Dynamic Effect in Concrete Materials," Proceedings of Application of Fracture Mechanics to Cementitious Composites, NATO-ARW, edited by Shah, S. P., Northwestern University, September 4-7, 1984.

Sulem, J. and Vardoulakis, I. 1988. "Bifurcation Analysis of the Triaxial Test on Rock Specimens," Proceedings of the France-US Workshop on Strain Localization and size Effect due to Cracking and Damage, edited by Mazars, J. and Bazant, Z. P., Cachan, France, September 6-9, 1988.

Tang, T., Malvern, L. E., and Jenkins, D. A. 1992. "Rate Effects in Uniaxial Dynamic Compression of Concrete," ASCE Journal of Engineering Mechanics, Vol. 118, No. 1, January, pp. 108-124.

Van Vliet, M. R. A. and Van Mier, J. G. M. 1996. "Experimental Investigation of Concrete Fracture Under Uniaxial Compression," Mechanics of Cohesive-Frictional Materials, Vol. 1, pp. 115-127.

Weerheijm, J., van Doormaal, J. C. A. M., and Sluys, L. J. 1993. "Fracture Energy of Concrete Under Dynamic Tensile Loading," Proceedings of the Sixth International Symposium on the Interaction of Non-Nuclear Munitions with Structures, Panama City Beach, FL, May 3-7, 1993.

Wilbeck, J. S. 1985. "Classification of Impact Regimes," Internal Research Report, SwRI Project 06-9304, Southwest Research Institute, San Antonio, TX.

Yamaguchi, E. and Chen, W. F. 1987. "On Micro-Mechanics of Fracture and Constitutive Modeling of Concrete Materials," in Constitutive Laws for Engineering Materials: Theory and Applications, edited by Desai, C. S., Krempl, E., Kioussis, P. D., and Kundu, T., Elsevier, New York, NY.

Yamaguchi, H., Fujimoto, K., and Nomura, S. 1989. "Strain Rate Effect on Stress-Strain Relationships of Concrete," Proceedings of the Fourth International Symposium on the Interaction of Non-Nuclear Munitions with Structures, Panama City Beach, FL, April 17-21, 1989.

Young, C. W. 1972. "Empirical Equations for Predicting Penetration Performance in Layered Earth Materials for Complex Penetrator Configurations," Development Report SC-DR-72.0523, December 1972, Sandia National Laboratories, Albuquerque, NM.

Zukas, J. A., Nicholas, T., Swift, H. F., Greszczuk, L. B., and Curran, D. R. 1982. Impact Dynamics, John Wiley & Sons, Inc., New York, NY.

## APPENDIX

### LISTING OF SUBROUTINES NIF, INVERS, REMDA, AND RSMDA

```

* $
SUBROUTINE NIF(L1, LN, INCOMP, DVBAR, EDEV, EDOT, EXDOT, EXYDOT,
2      ENSUM, EXZDOT, EYDOT, EYZDOT, EZDOT, SBAR, SMAX, SPINRZ,
3      SS2, XSPIN, YSPIN, ZSPIN, EBAR, EP, EPDOT, ES,
4      ICHECK, M, NODE3, NODE4, SX, SY, SZ, SXY, SXZ, SYZ,
5      BULK, DVOL, U, HMIN, Q, QMAX)
*
C NIF computes the stresses for the JDC Nonlinear, Inelastic Fracture
C model
C
C called by USTRES
* Packaged in EPIC5
C
* IMPLICIT NONE
INTEGER L1, LN, INCOMP, M, NODE3, NODE4
* L1 = first element of block
* LN = last element of block
* M = the material number
* INCOMP flags incompressible materials
INCLUDE 'VECTMX'
REAL DVBAR (MXLB), EDEV (MXLB), EDOT (MXLB), EXDOT (MXLB),
2      EXYDOT (MXLB), EXZDOT (MXLB), EYDOT (MXLB), EYZDOT (MXLB),
3      EZDOT (MXLB), SBAR (MXLB), SMAX (MXLB),
4      SPINRZ (MXLB), XSPIN (MXLB), YSPIN (MXLB),
5      ZSPIN (MXLB), ENSUM (MXLB), U (MXLB), HMIN (MXLB),
6      Q (MXLB), QMAX (MXLB)
* EDOT(I) = total strain rate
REAL EBAR (MXLB), EP (MXLB), EPDOT (MXLB),
2      ES (MXLB), SX (MXLB), SY (MXLB), SZ (MXLB),
3      SXY (MXLB), SXZ (MXLB), SYZ (MXLB), BULK (MXLB),
4      SS2 (MXLB), DVOL (MXLB)
* EBAR(I) = plastic strain
INTEGER ICHECK (MXLB)
INCLUDE 'MATERL'
INCLUDE 'MATERC'
INCLUDE 'MISC'
INCLUDE 'FILES'
INCLUDE 'NBSPHC'
C
REAL C2D9, DENV, DT2, GDT, GDTI, TDT, TGDT, TGDTI, THIRD, GV, CGV
* variables ending in V are temporaries for vector quantities
* which are constant in the current element block
INTEGER I, J
* I is an index into vector arrays
* J is an index into element arrays
REAL DSX (MXLB), DSXY (MXLB), DSXZ (MXLB),
2      DSY (MXLB), DSYZ (MXLB), DSZ (MXLB), SX1 (MXLB),
3      SXY1 (MXLB), SXZ1 (MXLB), SY1 (MXLB), SZ1 (MXLB), SYZ1 (MXLB)
PARAMETER (THIRD = 1.0/3.0)
PARAMETER (C2D9 = 2.0/9.0)
REAL TWO3RD
PARAMETER (TWO3RD = 2.0/3.0)
C *****

```



```

C * Nonlinear, Inelastic Fracture Model *
C * * *
C * DONALD CARGILE *
C * USAE WATERWAYS EXPERIMENT STATION *
C * VICKSBURG, MISSISSIPPI *
C * *****
C
C REAL VHMDAV(MXLJDC), LDWMDA(3,3), FDGMDA(3,3), ROTMDA(3,3),
1 DRMDA(3,3), DRIMDA(3,3), DETMDA(3,3), ETMDA(3,3)
C REAL DEMDA(6), SIGMDA(6), EMDA(6), EJDC(6), DEJDC(6)
C REAL SBMDA(MXLB), HISJDC(8)
C REAL EPSKKM, ATYCP, AGAMCP, GMOCTM, FLGJDC, AK, AEPSC, AAH, ABH, ACH,
1 AEP SL, AKL, ASIGS, ASIGF, AEPSS, AEP SF, AA, AB, AC, AB0, AB1, AMUC,
2 E1E2, E1E3, E2E3, EPS12, EPS13, EPS23, GAMOCT, SIGM,
3 EPSKKP, EPSKK0, SIGMSU, DSIGM, RNUM, RDEN, R, A, B, X, GAM,
4 FALULT, PCRUSH, PFRIC, ATYC, FACTRF, FALJDC, FRIC, AGAMC, REDUC,
5 HARD, COHSN, DEV, TOCTM, GULRL, RATIO, TAUOCT, GMOCT0,
6 AKULRL, GMOD, ANGAMC, DEVEPS, EPSKKV, Q1V, Q2V, SMALL,
7 EBARP, EBARS, AKLAK, AEPSLC, AAAC, FRICDEN, EPSKKD,
8 ATYCUR, ATYCPUR, AGAMCUR, DT22, EFAILV, SIGML, AKEPSC
C REAL DF(3,3), EIN(3,3), DEIN(3,3), LDW2(3,3), LDW3(3,3),
1 DLF(3,3), STEMP1(3,3), STEMP2(3,3)
C REAL E0, AUX, AUX1, AUX2, SIGMG, DETF, CGVJDC, BLKJDC, EPSKK, EPSKKT,
1 CMODJDC, STRFCT
C INTEGER IIN, JIN, KIN, K, IHYP0
C
C DIR$ NOVECTOR
C DENV= DEN(M)
C TDT = 2.0*DT
C DT2 = 0.5*DT
C GV = G(M)
C CGV = 4.0*GV/3.0
C GDT = GV*DT
C TGDT = 2.0*GDT
C GDTI = 1.0/GDT
C TGDTI = 1.0/TGDT
C Q1V = Q1(M)
C Q2V = Q2(M)
C SMALL = -EPSLON
C
C
C ASSIGN MATERIAL CONSTANTS
C
C VOLUMETRIC PART
C
C STRFCT = C18(M)
C AK = C0(M)
C AEPSC = C1(M)
C AAH = C2(M)
C ABH = C3(M)
C ACH = C4(M)
C AEPSL = C5(M)
C AKL = C6(M)
C ASIGS = C7(M)*STRFCT
C ASIGF = C17(M)
C AEPSS = C9(M)*STRFCT
C AEPSF = C10(M)
C ANGAMC = 4.0

```

```

      AEPSF = ANGAMC * AEPSS
      AKLAK = AKL - AK
      AEPSLC = AEPSL - AEPSC
      AKEPSC = AK * AEPSC
      SIGML = AKEPSC + AAH * AEPSLC + ABH * AEPSLC*AEPSLC
&      + ACH * AEPSLC**3.0
C
C      Calculate pressure at crush and pressure at start of
C      friction only
C
      PCRUSH = AKEPSC
      PFRIC = AKEPSC - AAH * ABH/(3.0*ACH)
1      + (2.0*ABH*ABH*ABH)/(27.0*ACH*ACH)
C
C      DEVIATORIC PART
C
      AA = C11(M)*STRFCT
      AB = C12(M)
      AC = C13(M)*STRFCT
      AB0 = C14(M)
      AB1 = C15(M)
      AMUC = C16(M)
      AAAC = AA - AC
      EFAILV = EFAIL(M)
C
      IF (IGEOM.LE.7) THEN
        I = 0
C        DIR$ VECTOR
C        VD$ VECTOR
        DO 15, J=L1, LN
          I = I + 1
          SBAR(I) = (SX(I)+SZ(I)+SY(I)) * THIRD
          SX1(I) = SX(I) - SBAR(I)
          SZ1(I) = SZ(I) - SBAR(I)
          SY1(I) = SY(I) - SBAR(I)
          SXZ1(I) = SXZ(I)
          SXY1(I) = SXY(I)
          SYZ1(I) = SYZ(I)
          DSX(I) = -SXZ1(I)*SPINRZ(I)*TDT
          DSY(I) = 0.0
          DSZ(I) = -DSX(I)
          DSXY(I) = 0.0
          DSXZ(I) = (SX1(I)-SZ1(I))*SPINRZ(I)*DT
          DSYZ(I) = 0.0
          EDOT(I) = AMAX1(EDOT(I), 0.0001)
15      CONTINUE
C      enddo
      ELSE
*      here IGEOM.EQ.8
        I = 0
        DO 16, J=L1, LN
          I = I + 1
          SBAR(I) = (SX(I)+SY(I)+SZ(I))*THIRD
          SX1(I) = SX(I) - SBAR(I)
          SY1(I) = SY(I) - SBAR(I)
          SZ1(I) = SZ(I) - SBAR(I)
          SXY1(I) = SXY(I)
          SXZ1(I) = SXZ(I)
          SYZ1(I) = SYZ(I)

```

```

        DSX(I) = (YSPIN(I)*SXZ1(I) - ZSPIN(I)*SXY1(I))*TDT
        DSY(I) = (ZSPIN(I)*SXY1(I) - XSPIN(I)*SYZ1(I))*TDT
        DSZ(I) = (XSPIN(I)*SYZ1(I) - YSPIN(I)*SXZ1(I))*TDT
        DSXY(I) = (ZSPIN(I)*(SX1(I)-SY1(I)) + YSPIN(I)*SYZ1(I)
1          - XSPIN(I)*SXZ1(I))*DT
        DSXZ(I) = (YSPIN(I)*(SZ1(I)-SX1(I)) + XSPIN(I)*SXY1(I)
1          - ZSPIN(I)*SYZ1(I))*DT
        DSYZ(I) = (XSPIN(I)*(SY1(I)-SZ1(I)) + ZSPIN(I)*SXZ1(I)
1          - YSPIN(I)*SXY1(I))*DT
        EDOT(I) = AMAX1(EDOT(I),0.0001)
16      CONTINUE
C      enddo
      ENDIF
C
C      DIR$ NOVECTOR
C
C
      I=0
      DO 100 J=L1, LN
        I=I+1
        SS2(I) = 0.0
C
        IF(ICHECK(I).LT.0) GOTO 100
C
        DO 110 K=1, MXLJDC, 1
          VHMDAV(K)=VHMADA(J,K)
110      CONTINUE
C
C      L=D+W
C
        IF(IGEOM.LE.7) THEN
C
C          LDWMDA(1,1)=(EXDOT(I)+ENSUM(I))
          LDWMDA(1,2)=(EXYDOT(I)*0.5)
          LDWMDA(1,3)=(EXZDOT(I)*0.5) - SPINRZ(I)
          LDWMDA(2,1)=(EXYDOT(I)*0.5)
          LDWMDA(2,2)=(EYDOT(I)+ENSUM(I))
          LDWMDA(2,3)=(EYZDOT(I)*0.5)
          LDWMDA(3,1)=(EXZDOT(I)*0.5) + SPINRZ(I)
          LDWMDA(3,2)=(EYZDOT(I)*0.5)
          LDWMDA(3,3)=(EZDOT(I)+ENSUM(I))
C
          DETMDA(1,1)=(EXDOT(I)+ENSUM(I))*DT
          DETMDA(1,2)=(EXYDOT(I)*0.5)*DT
          DETMDA(1,3)=(EXZDOT(I)*0.5)*DT
          DETMDA(2,1)=(EXYDOT(I)*0.5)*DT
          DETMDA(2,2)=(EYDOT(I)+ENSUM(I))*DT
          DETMDA(2,3)=(EYZDOT(I)*0.5)*DT
          DETMDA(3,1)=(EXZDOT(I)*0.5)*DT
          DETMDA(3,2)=(EYZDOT(I)*0.5)*DT
          DETMDA(3,3)=(EZDOT(I)+ENSUM(I))*DT
C
          DRMDA(1,1)= 1.0
          DRMDA(1,2)= 0.0
          DRMDA(1,3)= -0.5*SPINRZ(I)*DT
          DRMDA(2,1)= 0.0
          DRMDA(2,2)= 1.0
          DRMDA(2,3)= 0.0

```

```

DRMDA(3,1)= 0.5*SPINRZ(I)*DT
DRMDA(3,2)= 0.0
DRMDA(3,3)= 1.0

```

C

```

DRIMDA(1,1)= 1.0
DRIMDA(1,2)= 0.0
DRIMDA(1,3)= 0.5*SPINRZ(I)*DT
DRIMDA(2,1)= 0.0
DRIMDA(2,2)= 1.0
DRIMDA(2,3)= 0.0
DRIMDA(3,1)= -0.5*SPINRZ(I)*DT
DRIMDA(3,2)= 0.0
DRIMDA(3,3)= 1.0
CALL INVERS(DRIMDA,3)

```

C

ELSE

C

```

LDWMDA(1,1)=(EXDOT(I)+ENSUM(I))
LDWMDA(1,2)=(EXYDOT(I)*0.5) - ZSPIN(I)
LDWMDA(1,3)=(EXZDOT(I)*0.5) + YSPIN(I)
LDWMDA(2,1)=(EXYDOT(I)*0.5) + ZSPIN(I)
LDWMDA(2,2)=(EYDOT(I)+ENSUM(I))
LDWMDA(2,3)=(EYZDOT(I)*0.5) - XSPIN(I)
LDWMDA(3,1)=(EXZDOT(I)*0.5) - YSPIN(I)
LDWMDA(3,2)=(EYZDOT(I)*0.5) + XSPIN(I)
LDWMDA(3,3)=(EZDOT(I)+ENSUM(I))

```

C

```

DETMDA(1,1)=(EXDOT(I)+ENSUM(I))*DT
DETMDA(1,2)=(EXYDOT(I)*0.5)*DT
DETMDA(1,3)=(EXZDOT(I)*0.5)*DT
DETMDA(2,1)=(EXYDOT(I)*0.5)*DT
DETMDA(2,2)=(EYDOT(I)+ENSUM(I))*DT
DETMDA(2,3)=(EYZDOT(I)*0.5)*DT
DETMDA(3,1)=(EXZDOT(I)*0.5)*DT
DETMDA(3,2)=(EYZDOT(I)*0.5)*DT
DETMDA(3,3)=(EZDOT(I)+ENSUM(I))*DT

```

C

```

DRMDA(1,1)= 1.0
DRMDA(1,2)= -0.5*ZSPIN(I)*DT
DRMDA(1,3)= 0.5*YSPIN(I)*DT
DRMDA(2,1)= 0.5*ZSPIN(I)*DT
DRMDA(2,2)= 1.0
DRMDA(2,3)= -0.5*XSPIN(I)*DT
DRMDA(3,1)= -0.5*YSPIN(I)*DT
DRMDA(3,2)= 0.5*XSPIN(I)*DT
DRMDA(3,3)= 1.0

```

C

```

DRIMDA(1,1)= 1.0
DRIMDA(1,2)= 0.5*ZSPIN(I)*DT
DRIMDA(1,3)= -0.5*YSPIN(I)*DT
DRIMDA(2,1)= -0.5*ZSPIN(I)*DT
DRIMDA(2,2)= 1.0
DRIMDA(2,3)= 0.5*XSPIN(I)*DT
DRIMDA(3,1)= 0.5*YSPIN(I)*DT
DRIMDA(3,2)= -0.5*XSPIN(I)*DT
DRIMDA(3,3)= 1.0
CALL INVERS(DRIMDA,3)

```

END IF

C

```

C      RECOVER CURRENT DEFORMATION GRADIENT
C
      FDGMDA(1,1)=VHMDAV(1)
      FDGMDA(1,2)=VHMDAV(2)
      FDGMDA(1,3)=VHMDAV(3)
      FDGMDA(2,1)=VHMDAV(4)
      FDGMDA(2,2)=VHMDAV(5)
      FDGMDA(2,3)=VHMDAV(6)
      FDGMDA(3,1)=VHMDAV(7)
      FDGMDA(3,2)=VHMDAV(8)
      FDGMDA(3,3)=VHMDAV(9)
C
      ROTMDA(1,1)=VHMDAV(20)
      ROTMDA(1,2)=VHMDAV(21)
      ROTMDA(1,3)=VHMDAV(22)
      ROTMDA(2,1)=VHMDAV(23)
      ROTMDA(2,2)=VHMDAV(24)
      ROTMDA(2,3)=VHMDAV(25)
      ROTMDA(3,1)=VHMDAV(26)
      ROTMDA(3,2)=VHMDAV(27)
      ROTMDA(3,3)=VHMDAV(28)
C
      CALL REMDA(DRMDA,DRIMDA,ROTMDA)
C
C      CONVERT EPIC (CAUCHY) STRAIN TO GREEN-LAGRANGE STRAIN
C
C      CALC DF TO SECOND ORDER TERM LEVEL
      DO IIN=1,3
        DO JIN=1,3
          AUX=0.0
          DO KIN=1,3
            AUX=AUX+LDWMDA(IIN,KIN)*FDGMDA(KIN,JIN)
          END DO
          DLF(IIN,JIN)=AUX*DT
        END DO
      END DO
      DO IIN=1,3
        DO JIN=1,3
          AUX=DLF(IIN,JIN)
          DO KIN=1,3
            AUX=AUX+DT2*LDWMDA(IIN,KIN)*DLF(KIN,JIN)
          END DO
          DF(IIN,JIN)=AUX
        END DO
      END DO
C
C      Calculate Green-Lagrange finite strain E and DE
C      (only the upper triangular part)
      DO IIN=1,3
        DO JIN=1,3
          AUX1=0.0
          AUX2=0.0
          DO KIN=1,3
            AUX1=AUX1+FDGMDA(KIN,IIN)*FDGMDA(KIN,JIN)
            AUX2=AUX2+DF(KIN,IIN)*FDGMDA(KIN,JIN)
            +FDGMDA(KIN,IIN)*DF(KIN,JIN)+DF(KIN,IIN)*DF(KIN,JIN)
          END DO
        END DO
      END DO

```

```

        END DO
        EIN(IIN,JIN)=AUX1/2.0
        DEIN(IIN,JIN)=AUX2/2.0
    END DO
    EIN(IIN,IIN)=EIN(IIN,IIN)-0.50
END DO

C
C
C      Extract the strains and strain increments into column matrices
C
    DO IIN=1,3
        EJDC(IIN)=EIN(IIN,IIN)+DEIN(IIN,IIN)
    END DO
    EJDC(4)=EIN(1,2)+DEIN(1,2)
    EJDC(6)=EIN(1,3)+DEIN(1,3)
    EJDC(5)=EIN(2,3)+DEIN(2,3)

C
C      Update the deformation gradient F
    DO JIN=1,3
        DO IIN=1,3
            FDGMDA(IIN,JIN)=FDGMDA(IIN,JIN)+DF(IIN,JIN)
        END DO
    END DO

C
C
C      CONVERT EJDC(I.NE.J) TO GAMMA
C
    DO 120 K=4,6,1
        EJDC(K)=EJDC(K)*2.0
120  CONTINUE

C
C      NONLINEAR, INELASTIC FRACTURE MODEL
C      EJDC - strain
C      sigmda - stress returned by the model
C      There are five history quantities.
C
    DO IHYP0=10,15,1
        HISJDC(IHYP0-9) = VHMDAV(IHYP0)
    END DO

C
C      CALCULATE VOLUMETRIC STRAIN
C      DVOL = VOLUMETRIC STRAIN CALCULATED BY EPIC; TENSION +
C
    EPSKK = -DVOL(I)
    EPSKK = -EJDC(1) - EJDC(2) - EJDC(3)

C
C      ASSIGN HISTORY VARIABLES
C
    EPSKKM = HISJDC(1)
    ATYCP = HISJDC(2)
    AGAMCP = HISJDC(3)
    GMOCTM = HISJDC(4)
    FLGJDC = HISJDC(5)

C
C
C      INITIALIZE SOME VARIABLES

    EPSKK0 = 0.0
    AKULRL = AK
    COHSN = 0.0

```

```

FRIC      = 0.0
DEV       = 0.0
SIGM      = 0.0
SIGMG     = 0.0
FACTRF    = 1.325
ATYC      = 0.0
AGAMC     = 0.005
EBARP     = 0.0
EBARS     = 0.0
GMOD      = 0.0
GULRL     = 400000.0 + AMUC
BLKJDC    = AK

```

C  
C  
C

# CALCULATE OCTAHEDRAL SHEAR STRAIN

```

E1E2 = (EJDC(1) - EJDC(2))**2.0
E1E3 = (EJDC(1) - EJDC(3))**2.0
E2E3 = (EJDC(2) - EJDC(3))**2.0
EPS12 = EJDC(4) * EJDC(4)
EPS13 = EJDC(6) * EJDC(6)
EPS23 = EJDC(5) * EJDC(5)

```

C \*\*\*\*\* use 1.5 instead of 6.0 since eps = gamma / 2 and current  
C \*\*\*\*\* values of EJDC(4-6) are gamma and this eqn assumes eps  
GAMOCT = TWO3RD \* SQRT(E1E2 + E1E3 + E2E3  
1 + 1.5 \* (EPS12 + EPS13 + EPS23))

C  
C  
C

# HYDROSTATIC PART

```

EPSKKV = AMAX1(EPSKK, EPSKKM)

```

C  
C  
C  
C  
C  
C

# HYDROSTATIC COMPRESSION PART

# LOADING IN COMPRESSION

```

IF (EPSKKV.LT.AEPSC) THEN
  SIGM = AK * EPSKKV
  BLKJDC = AK
ELSEIF (EPSKKV.GT.AEPSL) THEN
  SIGM = SIGML + (EPSKKV - AEPSL) * AKL
  BLKJDC = AKL

```

C  
C  
C  
C

```

ELSE
  EPSKKP = EPSKKV - AEPSC
  SIGM = AKEPSC + AAH * EPSKKP + ABH * EPSKKP*EPSKKP
  & + ACH * EPSKKP**3.0
  BLKJDC = AK + AKLAK*EPSKKP/AEPSLC

```

C  
C

```

ENDIF

```

C  
C  
C  
C

# UNLOAD/RELOAD IN COMPRESSION

```

IF (EPSKKM.GT.EPSKK) THEN
  IF (EPSKKM.LT.AEPSC) THEN
    AKULRL = AK
  ELSEIF (EPSKKM.GT.AEPSL) THEN

```

```

      AKULRL = AKL
    ELSE
      AKULRL = AK + AKLAK*(EPSKKM - AEPSC)/AEPSLC
    END IF
    EPSKK0 = EPSKKM - (SIGM/AKULRL)
    EPSKKT = EPSKK0 - (ASIGS/AKULRL)
    SIGM = SIGM - AKULRL * (EPSKKM - EPSKK)
    BLKJDC = AKULRL
    IF (EPSKK.LT.EPSKKT) THEN
      EPSKKT = EPSKKT - EPSKK
    ELSE
      EPSKKT = 0.0
    END IF
    IF (SIGM.LT.-ASIGS) SIGM = -ASIGS
    EBARP = 1.0 * EPSKKT / AEPSS
  END IF

  C
  C      LOADING IN TENSION
  C
  ca IF (EPSKK.LT.0.0 .OR. SIGM.LT.0.0) THEN
  C
  C      EPSKK0 IS STRAIN AT PRESSURE = ZERO
  C
  ca EPSKKT = ABS(EPSKK - EPSKK0)
  ca RNUM = AKULRL * (ASIGS / ASIGF - 1.0)
  ca RDEN = ASIGS/AEPSS * (AEPSP/AEPSS - 1.0) ** 2.0
  ca R = RNUM / RDEN - AEPSS/AEPSP
  ca A = R + AKULRL*AEPSS/ASIGS - 2.0
  ca B = 2.0 * R - 1.0
  ca X = EPSKKT / AEPSS
  ca SIGM = - AKULRL * EPSKKT / (1.0 + A*X - B*X*X + R*X*X*X)
  C
  C      NO SOFTENING WITH FOLLOWING LINE
  ca IF (EPSKKT.GT.AEPSS) SIGM = -ASIGS
  ca IF (SIGM.LT.-ASIGS) SIGM = -ASIGS
  ca BLKJDC = AKULRL
  C
  C      Check for failure in tension
  ca EBARP = EPSKKT / AEPSS
  C
  ca END IF
  C
  IF (GAMOCT.GT.GMOCTM) THEN
    SIGMG = SIGM
  ELSE
    SIGMG = HISJDC(6)
  END IF
  SIGMG = SIGM

  C
  C      BEGIN DEVIATORIC PART
  C
  GAM = AMAX1(GAMOCT,GMOCTM)

  C
  C      LOADING
  C
  C      FRICTION SUBPART
  C
  C      Calculate ultimate surface

```



```

C      IF (SIGMG.GT.0.0) THEN
          FALULT = AA - AC * EXP(AB * SIGMG)
        ELSE
          FALULT = AAAC * (1.0 + SIGMG/ASIGS)
        END IF

C      IF (TIME.LE.DT) ATYCP = AAAC * FACTRF

C      Calculate cohesion yield stress; to be subtracted from
C      FALULT to give friction yield stress

C      Increase yield stresses by FACTRF to account for hyperbolic

C      IF (SIGMG.GT.PFRIC) THEN
          FACTRF = 1.1
          ATYC = 0.0
        ELSE
          IF (SIGMG.LT.0.0) THEN
              ATYC = FALULT
              FACTRF = 1.325
            ELSEIF (SIGMG.GT.PCRUSH) THEN
              ATYC = AAAC*(1.0-(SIGMG - PCRUSH)/(PFRIC - PCRUSH))
              FACTRF = 1.1 + 0.225 * (1.0 - (SIGMG - PCRUSH)
1              / (PFRIC - PCRUSH))
            ELSE
              ATYC = AAAC
              FACTRF = 1.325
            END IF
          END IF
          ATYC = ATYC * FACTRF
          ATYCP = AMIN1(ATYCP,ATYC)
          FALJDC = FALULT * FACTRF

C      Calculate friction subpart
C      AND
C      Calculate agamc at fail(fric)

C      IF (SIGMG.GT.0.0) THEN

C      Can have friction with sigm < 0.0

          GMOD = 400000.0 + AB0 * SIGMG**AB1
          AGAMC = FACTRF*(FALJDC - ATYCP)*(FALJDC/FACTRF - ATYCP)/
1          AMAX1(ABS(SMALL), (GMOD*FALJDC*(FACTRF - 1.0)))
        ELSE
          GMOD = 400000.0
          AGAMC = 0.005
        END IF

C      Limit AGAMC to be greater than 0.005 (0.5%)
C      AGAMC = AMAX1(AGAMC,AGAMCP,0.005)

C      FRICDEN = FALJDC - ATYCP + GAM * GMOD
      IF (FALJDC-ATYCP.LT.ABS(SMALL)) THEN
          FRIC = 0.0
        ELSE

```

```

FRIC = (FALJDC - ATYCP) * GMOD / FRICDEN
END IF

C
C      COHESION SUBPART
C
C
IF (ATYCP.GT.ABS(SMALL)) THEN
REDUC = 1.0

C
C      Reduction in cohesion subpart
C
IF (GAM.GT.AGAMC) THEN
REDUC = 1.0 - (GAM - AGAMC)/(AGAMC*(ANGAMC - 1.0))
END IF
REDUC = AMAX1(REDUC,0.0)

C
C      NO SOFTENING WITH FOLLOWING LINE
C      REDUC = 1.0
C
C      Calculate cohesion subpart prior to reduction
C
1      COHSN = ATYCP * AGAMC * AMUC * REDUC /
      (ATYCP*AGAMC + (AMUC*AGAMC - ATYCP)*GAM)
ELSE
COHSN = 0.0
END IF

C
C      Add friction and cohesion subparts
C
DEV = FRIC + COHSN
IF (SIGM.LE.-ASIGS) DEV = 0.0
C      GULRL = DEV
IF (SIGMG.LE.0.0) THEN
GULRL = 400000.0
ELSE
GULRL = 400000.0 + AB0*SIGMG**AB1
END IF
GULRL = GULRL + AMUC

C
C      UNLOAD/RELOAD
C
ca REMOVE ca COMMENT CHARACTERS TO RETURN TO USE NONLINEAR
ca UNLOADING/RELOADING
C
IF (GAMOCT.LT.GMOCTM) THEN
TOCTM = DEV * GMOCTM
ca IF (TOCTM.LT.0.001*FALJDC) THEN
ca TAUOCT = TOCTM
ca ELSE
c Initial unloading modulus based on pressure at start of unloading
IF (SIGMG.LE.0.0) THEN
GULRL = 400000.0
ELSE
GULRL = 400000.0 + AB0*SIGMG**AB1
END IF
GULRL = GULRL + AMUC
GULRL = GULRL * 1.20
ca GMOCT0 = GMOCTM - TOCTM / GULRL
ca IF (GAMOCT.GE.GMOCT0) THEN

```

```

ca      TAUOCT = ABS(TOCTM - (GMOCTM - GAMOCT)*GULRL)
ca      ELSE
ca      GAM = GMOCT0 - GAMOCT
ca      IF (SIGM.GT.0.0) THEN
ca      FALULT = AA - AC * EXP(AB * SIGM)
ca      ELSE
ca      FALULT = AAAC * (1.0 + SIGM/ASIGS)
ca      END IF

c
c      Calculate cohesion yield stress; to be subtracted from
c      FALULT to give friction yield stress
c
c      Increase yield stresses by FACTRF to account for hyperbolic
c
ca      IF (SIGM.GT.PFRIC) THEN
ca      FACTRF = 1.1
ca      ATYCUR = 0.0
ca      ELSE
ca      IF (SIGM.LT.0.0) THEN
ca      ATYCUR = FALULT
ca      FACTRF = 1.325
ca      ELSEIF (SIGM.GT.PCRUSH) THEN
ca      ATYCUR = AAAC*(1.0-(SIGM-PCRUSH)/(PFRIC-PCRUSH))
ca      FACTRF = 1.1 + 0.225 * (1.0 - (SIGM - PCRUSH)
1      / (PFRIC - PCRUSH))
ca      ELSE
ca      ATYCUR = AAAC
ca      FACTRF = 1.325
ca      END IF
ca      END IF
ca      ATYCUR = ATYCUR * FACTRF
ca      ATYCPUR = AMIN1(ATYCP,ATYCUR)
ca      FALJDC = FALULT * FACTRF

c
c      Calculate friction subpart
c      AND
c      Calculate agamcur at fail(fric)
c
ca      IF(SIGM.LE.0.0) THEN
c
c      Can have friction with sigm < 0.0
c
ca      GMOD = 400000.0
ca      AGAMCUR = 0.005
ca      ELSE
ca      GMOD = 400000.0 + AB0 * SIGM**AB1
ca      AGAMCUR = FACTRF*(FALJDC - ATYCPUR)
ca      1      *(FALJDC/FACTRF - ATYCPUR)/
ca      2      AMAX1(ABS(SMALL), (GMOD*FALJDC*(FACTRF - 1.0)))
ca      END IF
c      Limit AGAMCUR to be greater than 0.005 (0.5%)
c
ca      AGAMCUR = AMAX1(AGAMCUR,AGAMCP,0.005)
c
ca      FRICDEN = FALJDC - ATYCPUR + GAM * GMOD
ca      IF (FALJDC-ATYCPUR.LE.0.0) THEN
ca      FRIC = 0.0
ca      ELSE
ca      FRIC = (FALJDC - ATYCPUR) * GMOD / FRICDEN

```

```

ca          END IF
C
C          COHESION SUBPART
C
ca          IF (ATYCPUR.GT.0.0) THEN
C
C          NO SOFTENING WITH FOLLOWING LINE ALLOWED IN UNLOAD/RELOAD
C
ca          REDUC = 1.0
C
C          Calculate cohesion subpart prior to reduction
C
ca          COHSN = ATYCPUR * AGAMCUR * AMUC * REDUC
ca          1      / (ATYCPUR*AGAMCUR + (AMUC*AGAMCUR - ATYCPUR)*GAM)
ca          ELSE
ca          COHSN = 0.0
ca          END IF
C
C          Add friction and cohesion subparts
C
ca          TAUOCT = AMIN1((FRIC + COHSN) * GAM,FALULT)
ca          END IF
ca          END IF
ca          DEVU = -TAUOCT/GAMOCT
ca          DEV = DEVU
ca          DEV = ABS(DEV)
ca          Following line added with ca changes
ca          IF (TAUOCT.GT.0.0) THEN
ca          TAUOCT = AMIN1(TAUOCT,FALULT)
ca          ELSE
ca          TAUOCT = AMAX1(TAUOCT,-FALULT)
ca          END IF
ca          DEV = TAUOCT/GAMOCT
ca          IF (SIGM.LE.-ASIGS) DEV = 0.0
C
C          END IF
C
C          STRESS CALCUALTION
C
C          EBARS = GAMOCT / AGAMC
C          If EBARP or EBARS GT EFAILV then
C          set EBARS and EBARP to be big
C          allow pressure only, i.e., DEV=0.0
C          IF (AMAX1(EBARP,EBARS).GT.EFAILV) THEN
C          EBARS = EBARS*100.0
C          EBARP = EBARP*100.0
C          DEV = 0.0
C          ENDIF
C          IF (HMIN(I).LT.0.05) THEN
C          EBARS = EFAILV*100.0
C          EBARP = EFAILV*100.0
C          ENDIF
C          EPSKCD = EJDC(1) + EJDC(2) + EJDC(3)
C          DEVEPS = DEV * EPSKCD * THIRD
C          SIGMDA(1) = -SIGM + 2.0*(DEV * EJDC(1) - DEVEPS)
C          SIGMDA(2) = -SIGM + 2.0*(DEV * EJDC(2) - DEVEPS)
C          SIGMDA(3) = -SIGM + 2.0*(DEV * EJDC(3) - DEVEPS)
C          VHMDA(J,19) = (SIGMDA(1) + SIGMDA(2) + SIGMDA(3)) * THIRD
C          SIGMDA(4) = DEV * EJDC(4)

```

```

      SIGMDA(5) = DEV * EJDC(5)
      SIGMDA(6) = DEV * EJDC(6)
C *****
      HISJDC(7) = SIGMG
      HISJDC(8) = DEV
C *****
C
C      UPDATE HISTORY PARAMETERS
C
      HISJDC(1) = EPSKKV
      HISJDC(2) = ATYCP
      HISJDC(3) = AGAMC
      HISJDC(4) = AMAX1(GAMOCT,GMOCTM)
      HISJDC(5) = AMAX1(EBARP,EBARS)
      EBAR(I) = HISJDC(5)
      HISJDC(6) = SIGMG
C
      VHMDA(J,29) = EJDC(1)
      VHMDA(J,30) = EJDC(2)
      VHMDA(J,31) = EJDC(3)
C ***** convert gamma back to eps *****
      VHMDA(J,32) = EJDC(4) / 2.0
      VHMDA(J,33) = EJDC(5) / 2.0
      VHMDA(J,34) = EJDC(6) / 2.0
      VHMDA(J,35) = SIGM
      VHMDA(J,36) = SIGMDA(1)
      VHMDA(J,37) = SIGMDA(2)
      VHMDA(J,38) = SIGMDA(3)
      VHMDA(J,39) = SIGMDA(4)
      VHMDA(J,40) = SIGMDA(5)
      VHMDA(J,41) = SIGMDA(6)
C
C
C      Rotate stresses back to current orientation
C
      CALL RSM DA(ROTM DA,SIGMDA)
C
C      CALCULATE "4G/3" FOR SOUND SPEED CALCULATION
C
      CGVJDC = 4.0 * GULRL * THIRD
C
C      SOUND SPEED
C
      CMODJDC = 1.0*(BLKJDC + CGVJDC)
      BULK(I) = BLKJDC
      SS2(I)=ABS(CMODJDC/(DENV/(1.+DVOL(I))))
      SS2(I) = AMAX1(SS2(I),1.0)
C
C      ! TOTAL STRESSES !
C
      SX(I) = SIGMDA(1)
      SY(I) = SIGMDA(2)
      SZ(I) = SIGMDA(3)
      SKY(I) = SIGMDA(4)
      SYZ(I) = SIGMDA(5)
      SXZ(I) = SIGMDA(6)
      IF (IGEOM.LT.7) THEN
        SYZ(I) = 0.0
        SKY(I) = 0.0

```

```

      ENDIF
C
      SBMDA(I) = (SX(I) + SY(I) + SZ(I))*THIRD
C
C      CONVERT TO "DEVIATORIC" STRESS
C
      SX(I) = SX(I) - SBMDA(I)
      SY(I) = SY(I) - SBMDA(I)
      SZ(I) = SZ(I) - SBMDA(I)
C
C      STORE UPDATED DEFORMATION GRADIENT
C
      VHMDAV(1)=FDGMDA(1,1)
      VHMDAV(2)=FDGMDA(1,2)
      VHMDAV(3)=FDGMDA(1,3)
      VHMDAV(4)=FDGMDA(2,1)
      VHMDAV(5)=FDGMDA(2,2)
      VHMDAV(6)=FDGMDA(2,3)
      VHMDAV(7)=FDGMDA(3,1)
      VHMDAV(8)=FDGMDA(3,2)
      VHMDAV(9)=FDGMDA(3,3)
C
      VHMDAV(20) = ROTMDA(1,1)
      VHMDAV(21) = ROTMDA(1,2)
      VHMDAV(22) = ROTMDA(1,3)
      VHMDAV(23) = ROTMDA(2,1)
      VHMDAV(24) = ROTMDA(2,2)
      VHMDAV(25) = ROTMDA(2,3)
      VHMDAV(26) = ROTMDA(3,1)
      VHMDAV(27) = ROTMDA(3,2)
      VHMDAV(28) = ROTMDA(3,3)
C
      DO 130 K=1,9,1
        VHMDA(J,K)=VHMDAV(K)
130    CONTINUE
      DO 131 K=20,28,1
        VHMDA(J,K)=VHMDAV(K)
131    CONTINUE
C      *****
C      changed from 10,14,1 to 10,13,1 for corant check for failure
C
      DO IHYP0=10,15,1
        VHMDA(J,IHYP0)=HISJDC(IHYP0-9)
      END DO
C      *****
      VHMDA(J,16) = GULRL * DT
      VHMDA(J,17) = HISJDC(8)
      VHMDA(J,18) = HISJDC(5)
C      *****
C
100  CONTINUE
C
C      TEMPORARY APPROXIMATION
C
      IF (IGEOM.LE.7) THEN
        I = 0
C        DIR$   VECTOR
C        VD$    VECTOR

```

```

DO 150, J=L1, LN
  I = I + 1
  EDEV(I) = ( (SX(I)+SX1(I))*EXDOT(I)
1          + (SZ(I)+SZ1(I))*EZDOT(I)
2          + (SY(I)+SY1(I))*EYDOT(I)
3          + (SXZ(I)+SXZ1(I))*EXZDOT(I)
4          + (SXY(I)+SXY1(I))*EXYDOT(I)
5          + (SYZ(I)+SYZ1(I))*EYZDOT(I))
6          * (1.0+DVBAR(I))*DT2
  EXDOT(I) = EXDOT(I) - (SX(I) - SX1(I) - DSX(I))*TGDTI
  EZDOT(I) = EZDOT(I) - (SZ(I) - SZ1(I) - DSZ(I))*TGDTI
  EYDOT(I) = EYDOT(I) - (SY(I) - SY1(I) - DSY(I))*TGDTI
  EXZDOT(I) = EXZDOT(I) - (SXZ(I) - SXZ1(I) - DSXZ(I))*GDTI
  EXYDOT(I) = EXYDOT(I) - (SXY(I) - SXY1(I) - DSXY(I))*GDTI
  EYZDOT(I) = EYZDOT(I) - (SYZ(I) - SYZ1(I) - DSYZ(I))*GDTI
  IF(ICHECK(I).GE.0)THEN
    EPDOT(I) = SQRT(C2D9*( (EXDOT(I)-EZDOT(I))**2
1                + (EXDOT(I)-EYDOT(I))**2
2                + (EZDOT(I)-EYDOT(I))**2
3                + 1.5*( EXZDOT(I)*EXZDOT(I)
4                  + EXYDOT(I)*EXYDOT(I)
5                  + EYZDOT(I)*EYZDOT(I))))
C    EBAR(I) = EBAR(I) + EPDOT(I)*DT
    EP(I) = EP(I) + ( (SX(I)+SX1(I))*EXDOT(I)
1                + (SZ(I)+SZ1(I))*EZDOT(I)
2                + (SY(I)+SY1(I))*EYDOT(I)
3                + (SXZ(I)+SXZ1(I))*EXZDOT(I)
4                + (SXY(I)+SXY1(I))*EXYDOT(I)
5                + (SYZ(I)+SYZ1(I))*EYZDOT(I))
6                * (1.0+DVBAR(I))*DT2
  ENDIF
150 CONTINUE
C enddo
IF(IGEOM.EQ.4)THEN
  INCOMP = 1
ENDIF
IF(IGEOM.GE.5 .AND. NODE3.EQ.0)THEN
  INCOMP = 2
ENDIF
ELSE
* here 3-D
  I = 0
  DO 170, J=L1, LN
    I = I + 1
    EDEV(I) = ( (SX(I)+SX1(I))*EXDOT(I)
1            + (SY(I)+SY1(I))*EYDOT(I)
2            + (SZ(I)+SZ1(I))*EZDOT(I)
3            + (SXY(I)+SXY1(I))*EXYDOT(I)
4            + (SXZ(I)+SXZ1(I))*EXZDOT(I)
5            + (SYZ(I)+SYZ1(I))*EYZDOT(I))
6            * (1.0+DVBAR(I))*DT2
    EXDOT(I) = EXDOT(I) - (SX(I) - SX1(I) - DSX(I))*TGDTI
    EYDOT(I) = EYDOT(I) - (SY(I) - SY1(I) - DSY(I))*TGDTI
    EZDOT(I) = EZDOT(I) - (SZ(I) - SZ1(I) - DSZ(I))*TGDTI
    EXYDOT(I) = EXYDOT(I) - (SXY(I) - SXY1(I) - DSXY(I))*GDTI
    EXZDOT(I) = EXZDOT(I) - (SXZ(I) - SXZ1(I) - DSXZ(I))*GDTI
    EYZDOT(I) = EYZDOT(I) - (SYZ(I) - SYZ1(I) - DSYZ(I))*GDTI
    IF(ICHECK(I).GE.0)THEN
      EPDOT(I) = SQRT(C2D9*( (EXDOT(I)-EYDOT(I))**2

```

```

1          + (EXDOT(I)-EZDOT(I))**2
2          + (EYDOT(I)-EZDOT(I))**2
3          + 1.5*( EXYDOT(I)*EXYDOT(I)
4              + EXZDOT(I)*EXZDOT(I)
5              + EYZDOT(I)*EYZDOT(I)))
C          EBAR(I) = EBAR(I) + EPDOT(I)*DT
          EP(I)    = EP(I) + ( (SX(I)+SX1(I))*EXDOT(I)
1              + (SY(I)+SY1(I))*EYDOT(I)
2              + (SZ(I)+SZ1(I))*EZDOT(I)
3              + (SXY(I)+SXY1(I))*EXYDOT(I)
4              + (SXZ(I)+SXZ1(I))*EXZDOT(I)
5              + (SYZ(I)+SYZ1(I))*EYZDOT(I))
6          * (1.0+DVBAR(I))*DT2
          ENDIF
170      CONTINUE
C      enddo
          IF (NODE3.EQ.0) THEN
              INCOMP = 3
          ELSEIF (NODE4.EQ.0) THEN
              INCOMP = 4
          ENDIF
      ENDIF
C
C      Convert to total stresses
C
C      DIR$ NOVECTOR
C      I = 0
      DO 200, J=L1, LN
          I = I + 1
          IF (ICHECK(I).LT.0) GOTO 200
          SX(I) = SX(I) + SBMDA(I)
          SY(I) = SY(I) + SBMDA(I)
          SZ(I) = SZ(I) + SBMDA(I)
          SBAR(I) = SBMDA(I)
200  CONTINUE
C
      RETURN
      END
*$
      SUBROUTINE INVERS(D,NE)
C *****
C *
C * INVERS - TO COMPUTE THE INVERSE OF A MATRIX USING
C *          GAUSS ELIMINATION
C *
C *****
      REAL CI(3,6), D(3,3)
      REAL TMIJ, SUM
      INTEGER NE, I, J, NN, K
      CDIR$ NOVECTOR
C
      DO 3 I=1, NE, 1
          DO 5 J=1, NE, 1
              CI(I,J)=D(I,J)
              D(I,J)=0.0
              CI(I,J+NE)=0.0
5          CONTINUE
              CI(I,NE+I)=1.0
3          CONTINUE

```



```

C
C      *** START THE GAUSS ELIMINATION PROCEDURE ***
C
      NN=2*NE
      DO 10 J=1,NE-1,1
        DO 40 I=J+1,NE,1
          TMIJ=CI(I,J)/CI(J,J)
          DO 50 K=J+1,NN,1
            CI(I,K)=CI(I,K)-TMIJ*CI(J,K)
50      CONTINUE
40      CONTINUE
10      CONTINUE
C
C      *** UTILIZE BACK-SUBSTITUTION TO OBTAIN THE INVERSE ***
C
      DO 55 K=1,NE,1
        DO 60 I=NE,1,-1
          SUM=0.0
          DO 70 J=I+1,NE,1
            SUM=SUM+CI(I,J)*D(J,K)
70      CONTINUE
          D(I,K)=(CI(I,NE+K)-SUM)/CI(I,I)
60      CONTINUE
55      CONTINUE
C
C
999    RETURN
      END
*$
C *****
C *** SUBROUTINE REMDA - TO ROTATE STRAIN INCREMENT TO INITIAL CONFIG. *
C *****
      SUBROUTINE REMDA(DRMDA,DRIMDA,ROTMDA)
      REAL DRMDA(3,3),DRIMDA(3,3),ROTMDA(3,3)
      REAL DELTAR(3,3),T1(3,3),T2(3,3),C(3,3)
      INTEGER I,J,K
CDIR$ NOVECTOR
C
C
C      DELTAR = DRIMDA*DRMDA
C
      DO I=1,3
        DO J=1,3
          DELTAR(I,J)=0.0
          DO K=1,3
            DELTAR(I,J)=DELTAR(I,J)+DRIMDA(I,K)*DRMDA(K,J)
          END DO
        END DO
      END DO
C
C      ROTMDA_T+1 = DELTAR*ROTMDA_T
C
      DO I=1,3
        DO J=1,3
          T1(I,J)=0.0
          DO K=1,3
            T1(I,J)=T1(I,J)+DELTAR(I,K)*ROTMDA(K,J)
          END DO
        END DO
      END DO

```

```

      END DO
C
C      COMPUTE ROTMDA_TRANSPOSE*DETMDA
C
      DO I=1,3
        DO J=1,3
          ROTMDA(I,J) = T1(I,J)
        END DO
      END DO
999 RETURN
      END
*$
C *****
C *** SUBROUTINE RSMDA - TO ROTATE STRESSES TO CURRENT CONFIGURATION *
C *****
      SUBROUTINE RSMDA(ROTMDA,SIGMDA)
      REAL ROTMDA(3,3),T1(3,3),T2(3,3),SIGMDA(6)
      INTEGER I,J,K
C$DIR$ NOVECTOR
C
C      insert the stresses into square matrices
C
      T1(1,1)=SIGMDA(1)
      T1(1,2)=SIGMDA(4)
      T1(1,3)=SIGMDA(6)
      T1(2,1)=SIGMDA(4)
      T1(2,2)=SIGMDA(2)
      T1(2,3)=SIGMDA(5)
      T1(3,1)=SIGMDA(6)
      T1(3,2)=SIGMDA(5)
      T1(3,3)=SIGMDA(3)
C
C      COMPUTE ROTMDA*STRESS
C
      DO I=1,3
        DO J=1,3
          T2(I,J)=0.0
          DO K=1,3
            T2(I,J)=T2(I,J)+ROTMDA(I,K)*T1(K,J)
          END DO
        END DO
      END DO
C
C      COMPUTE (ROTMDA*STRESS)*ROTMDA_TRANSPOSE
C
      DO I=1,3
        DO J=1,3
          T1(I,J)=0.0
          DO K=1,3
            T1(I,J)=T1(I,J)+T2(I,K)*ROTMDA(J,K)
          END DO
        END DO
      END DO
C
C      INSERT THE STRESSES INTO A VECTOR
C
      SIGMDA(1)=T1(1,1)
      SIGMDA(2)=T1(2,2)
      SIGMDA(3)=T1(3,3)

```

```
SIGMDA(4)=T1(1,2)  
SIGMDA(5)=T1(2,3)  
SIGMDA(6)=T1(1,3)
```

C

```
999 RETURN  
END
```

## DISTRIBUTION LIST

### DEPARTMENT OF DEFENSE

Director  
Advanced Research Project Agency  
ATTN: Library  
3701 N. Fairfax Drive  
Arlington, VA 22203-1714

Director  
Defense Intelligence Agency  
ATTN: Unclassified Library  
Washington, DC 20340

Defense Technical Information Center  
ATTN: TC (2 cys)  
8725 John Kingman Road  
Suite 0944  
Fort Belvoir, VA 22060-6218

Director  
Defense Threat Reduction Agency  
ATTN: CPW (Mr. Cliff McFarland)  
CPWE (Dr. L. A. Wittwer)  
CPWS (Mr. M. E. Giltrud)  
Technical Library  
6801 Telegraph Road  
Alexandria, VA 22310-3398

Commander  
Field Command, Defense Threat Reduction Agency  
ATTN: CPT (Dr. G. Y. Baladi)  
CPTP (Dr. E. J. Rinehart)  
CPTP (Dr. E. L. Tremba)  
1680 Texas St., SE  
Kirtland AFB, NM 87117-5669

### DEPARTMENT OF THE ARMY

Commander  
US Army Corps of Engineers  
ATTN: CERD-ZA (Dr. L. E. Link)  
CERD-M (Dr. D. J. Leverenz)  
CERD-M (Mr. J. R. Lundien)  
CEMP-ET (Mr. Mohan Singh)  
CEMP-ET (Mr. Ray Navidi)  
CEIM-SL (2 cys)  
Washington, DC 20314-1000

Director  
US Army Engineer Research and Development Center  
Cold Regions Research and Engineering Laboratory  
ATTN: Technical Library  
72 Lume Road  
Hanover, NM 03755-1290

Director  
US Army Engineer Research and Development Center  
Construction Engineering Research Laboratories  
ATTN: Technical Library  
P.O. Box 9005  
Champaign, IL 61826-9005

Director  
US Army Engineer Research and Development Center  
Topographic Engineering Center  
ATTN: Technical Library  
7701 Telegraph Road  
Alexandria, VA 22315-3864

Commander  
US Army Engineer District, Omaha  
ATTN: CENWO-ED-S (Mr. Bruce Walton)  
CENWO-ED-S (Mr. Tim Knight)  
215 North 17<sup>th</sup> Street  
Omaha, NE 68102-4978

Commander  
US Army Engineer School  
ATTN: Technical Library  
Fort Leonard Wood, MO 65473-5000

Director  
US Army Research Laboratory  
ATTN: Technical Library  
Aberdeen Proving Ground, MD 21005-5066

### DEPARTMENT OF THE NAVY

Naval Air Warfare Center  
Weapons Division  
ATTN: Technical Library  
1 Administration Circle  
China Lake, CA 93555-6000

Naval Facilities Engineering Command  
ATTN: Technical Library  
200 Stovall Street  
Alexandria, VA 22332-2300

Commander  
Naval Surface Warfare center  
Dahlgren Division  
ATTN: Technical Library  
17320 Dahlgren Road  
Dahlgren, VA 22448-5100

DEPARTMENT OF THE AIR FORCE

Air Force Institute of Technology  
Air University  
ATTN: Technical Library  
Wright-Patterson AFB, OH 45433

Air Force Office of Scientific Research  
Technical Library  
Bolling AFB, DC 20332

Air Force Research Laboratory  
ATTN: Technical Library  
101 W. Eglin Blvd.  
Eglin AFB, FL 32542-6810

Air Force Research Laboratory  
ATTN: MLQC (Mr. Dick Vickers)  
139 Barnes Dr., Suite 2  
Tyndall AFB, FL 32403-5323

DEPARTMENT OF ENERGY

Lawrence Livermore National Laboratory  
ATTN: L-53 (Technical Library)  
P.O. Box 808  
Livermore, CA 94550-0622

Los Alamos National Laboratory  
ATTN: M/S P364 (Report Library)  
P.O. Box 1663  
Los Alamos, NM 87545

Sandia National Laboratories  
ATTN: Dept 9823 (Dr. M. J. Forrestal, M/S 0312)  
Dept 7141 (Technical Library, M/S 0889)  
P.O. Box 5800  
Albuquerque, NM 87185

Sandia National Laboratories  
ATTN: Technical Library, M/S 9211  
Livermore, CA 94550

DEPARTMENT OF DEFENSE CONTRACTORS

Dr. J. G. Jackson, Jr.  
5024 Nailor Road  
Vicksburg, MS 39180

Dr. Gordon Johnson  
Alliant Techsystems, Inc.  
M/S MN11-1614  
600 2d Street, NE  
Hopkins, MN 55343

Dr. James K. Gran  
SRI International  
Poulter Laboratory  
333 Rowenswood Avenue  
Menlo Park, CA 94025

Dr. Y. Marvin Ito  
Mr. H. D. Zimmerman  
Titan Research & Technology  
9410 Topanga Canyon Blvd., Suite 104  
Chatsworth, CA 91311-5771

Dr. Zdenek Bazant  
Northwestern University  
Civil Engineering Department  
2145 Sheridan Road  
Evanston, IL 60208-3109

**REPORT DOCUMENTATION PAGE**Form Approved  
OMB No. 0704-0188

Public reporting burden for this collection of information is estimated to average 1 hour per response, including the time for reviewing instruction, searching existing data sources, gathering and maintaining the data needed, and completing and reviewing the collection of information. Send comments regarding this burden estimate or any other aspect of this collection of information, including suggestions for reducing this burden, to Washington Headquarters Services, Directorate for Information Operations and Reports, 1215 Jefferson Davis Highway, Suite 1204, Arlington, VA 22202-4304, and to the Office of Management and Budget, Paperwork Reduction Project (0704-0188), Washington, DC 20503.

<b>1. AGENCY USE ONLY (Leave blank)</b>		<b>2. REPORT DATE</b> September 1999	<b>3. REPORT TYPE AND DATES COVERED</b> Final Report
<b>4. TITLE AND SUBTITLE</b> Development of a Constitutive Model for Numerical Simulation of Projectile Penetration into Brittle Geomaterials			<b>5. FUNDING NUMBERS</b>
<b>6. AUTHOR(S)</b> J. Donald Cargile			
<b>7. PERFORMING ORGANIZATION NAME(S) AND ADDRESS(ES)</b> U.S. Army Engineer Research and Development Center U.S. Army Engineer Waterways Experiment Station 3909 Halls Ferry Road Vicksburg, MS 39180-6199			<b>8. PERFORMING ORGANIZATION REPORT NUMBER</b>  Technical Report SL-99-11
<b>9. SPONSORING/MONITORING AGENCY NAME(S) AND ADDRESS(ES)</b> U.S. Army Corps of Engineers Washington, DC 20314-1000			<b>10. SPONSORING/MONITORING AGENCY REPORT NUMBER</b>
<b>11. SUPPLEMENTARY NOTES</b> Available from National Technical Information Service, 5285 Port Royal Road, Springfield, VA 22161.			
<b>12a. DISTRIBUTION/AVAILABILITY STATEMENT</b> Approved for public release; distribution is unlimited.			<b>12b. DISTRIBUTION CODE</b>
<b>13. ABSTRACT (Maximum 200 words)</b> <p>A nonlinear, inelastic fracture model for brittle geomaterials has been developed for simulating the response of these materials to high-velocity projectile penetration. Laboratory mechanical property experiments show a transition in the shearing response for these materials from brittle at low pressures to ductile at high pressures. The model has the underlying assumption that the shearing response can be resolved into a brittle cohesive component and a ductile frictional component. At low pressures, the cohesive component controls the behavior and the material response is brittle. As pressure increases, the cementing bonds that hold the aggregate particles together are broken and the contribution of the cohesive component decreases while the contribution of the frictional component increases. Once the bonds are completely broken, the material response is determined only by the ductile frictional component. The model response agreed well with the results from various quasi-static triaxial experiments on concrete samples. The model is implemented into a finite-element code and used to simulate high-velocity projectile penetration events.</p> <p>A series of laboratory penetration and perforation experiments were conducted and used to evaluate the model within the finite-element wave propagation code. Penetration experiments were conducted by launching robust steel projectiles into semi-infinite concrete targets to obtain depth of penetration and crater profiles at impact velocities ranging from 277 to 800 m/s. Perforation experiments were conducted by launching robust steel projectiles at 313 m/s into concrete slabs measuring 127 to 284 mm thick to obtain exit velocity and crater profiles. High-speed movies of the impact and exit faces of the targets showed the evolution of surface damage during the perforation event. Depth of penetration and exit velocity from simulations of the penetration and perforation experiments agree well with the experiment results. The simulations show the break-up and damage to the target during formation of the impact crater and tunnel in the deep penetration experiments and the impact and exit craters in the perforation experiments.</p>			
<b>14. SUBJECT TERMS</b> See reverse.			<b>15. NUMBER OF PAGES</b> 228
			<b>16. PRICE CODE</b>
<b>17. SECURITY CLASSIFICATION OF REPORT</b> UNCLASSIFIED	<b>18. SECURITY CLASSIFICATION OF THIS PAGE</b> UNCLASSIFIED	<b>19. SECURITY CLASSIFICATION OF ABSTRACT</b>	<b>20. LIMITATION OF ABSTRACT</b>

#### **14. SUBJECT TERMS.**

Brittle geomaterials  
Concrete  
Constitutive model  
Material response  
Nonlinear inelastic fracture model  
Numerical simulations  
Penetration mechanics  
Projectile